

Development of Terahertz Photonic Crystal Quantum Cascade Lasers and Investigation on III-V&SOI Photonic Structures at Near-Infrared Wavelength

THÈSE N° 4809 (2010)

PRÉSENTÉE LE 17 SEPTEMBRE 2010
À LA FACULTÉ SCIENCES DE BASE
INSTITUT DE PHOTONIQUE ET D'ÉLECTRONIQUE QUANTIQUES
PROGRAMME DOCTORAL EN PHOTONIQUE

ÉCOLE POLYTECHNIQUE FÉDÉRALE DE LAUSANNE

POUR L'OBTENTION DU GRADE DE DOCTEUR ÈS SCIENCES

PAR

Hua ZHANG

acceptée sur proposition du jury:

Prof. H. P. Herzig, président du jury
Dr R. Houdré, directeur de thèse
Prof. R. Delarue, rapporteur
Dr A. Dunbar, rapporteur
Prof. J. Faist, rapporteur



ÉCOLE POLYTECHNIQUE
FÉDÉRALE DE LAUSANNE

Suisse
2010

Contents

ABSTRACT.....	V
RÉSUMÉ.....	VII
PREFACE	IX
1. BASIC PROPERTIES OF THE PHOTONIC CRYSTALS.....	1
1.1 INTRODUCTION TO PHOTONIC CRYSTALS	1
1.2 ONE DIMENSIONAL PHCs AND THE ORIGIN OF THE PBG	2
1.3 TWO DIMENSIONAL PHCs	4
1.3.1 Ideal two dimensional PhCs	4
1.3.2 Slab waveguide two dimensional PhCs	5
1.3.3 PhC lattice parameters.....	7
1.3.4 Dispersion relation of the bulk photonic crystal and light cone issues.....	8
1.3.5 Defects, waveguides and cavities	10
1.4 THREE DIMENSIONAL PHCs.....	11
2. THEORY, MODELLING TECHNIQUES AND CONCEPTS.....	17
2.1 THE MAXWELL'S EQUATIONS FOR THE ELECTROMAGNETIC FIELD	17
2.1.1 The master equation.....	17
2.1.2 The scalability of photonic crystal.....	18
2.1.3 The Bloch-Floquet Theorem.....	20
2.2 MODELLING TECHNIQUES	21
2.2.1 The Plane Wave Expansion (PWE) method.....	21
2.2.2 Finite element method (FEM).....	23
2.2.3 Finite Difference Time Domain (FDTD)	28
2.3 SLOWLIGHT	29
2.3.1 Slow light introduction.....	29
2.3.2 Passive Slow light PhC line defect waveguide.....	31
2.3.3 Active Slow light PhC band-edge lasers	32
3. FABRICATION TECHNIQUES	35
3.1 GENERAL FABRICATION PRINCIPLE FOR SEMICONDUCTOR FABRICATION.	36
3.2 THE MATERIALS NEEDED FOR NIR PHC DEVICES.	39
3.2.1 Silicon on Insulator (SOI)	39

3.2.2	SOI thickness variation	40
3.2.3	Indium phosphide (InP).....	41
3.3	PROCESS STEPS FOR NIR PASSIVE PHC DEVICES	42
3.3.1	EBL system in EPFL (Hardware).....	42
3.3.2	Data processing and CATS (Software).....	45
3.3.3	Deeper understanding of CATS in EBPB.....	45
3.3.4	CATS Conditional Figure Assignment (CFA).....	49
3.3.5	Sample processing with EBL PMMA on InP and ZEP-520A on SOI	50
3.3.6	Dry etching of SOI	52
3.3.7	Si Membrane wet etching	55
3.4	FABRICATION TECHNOLOGY FOR THz PHC QC LASERS*	56
3.4.1	Motivation of pillar type PhC lasers.	57
3.4.2	Fabrication processes.....	57
3.4.3	Multi-layer BCB planarization	61
4.	EXPERIMENTAL INVESTIGATION OF PASSIVE SLOW LIGHT PHC DEVICES IN NEAR	
	INFRA-RED.....	65
4.1	FOURIER SPACE IMAGING SETUP.....	67
4.2	LIGHT TRANSPORT REGIMES IN SLOW LIGHT PHOTONIC CRYSTAL WAVEGUIDES*	70
4.2.1	Introduction	70
4.2.2	Light transport identification	71
4.2.3	Structures.....	72
4.2.4	Dispersive regime and diffusive regime	73
4.2.5	Frequency scanning of the modes	75
4.2.6	Comparison between the transmissions and dispersion properties.....	76
4.2.7	Conclusion.....	77
4.3	EXPERIMENTAL INVESTIGATION OF SLOW LIGHT PHOTONIC CRYSTAL COUPLED CAVITY WAVEGUIDES AND	
	THEIR INTRINSIC LIMITATIONS*	77
4.3.1	CCW theory background.	78
4.3.2	Design, fabrication and characterization.	81
4.3.3	Experimental investigation of the CCW.	84
4.3.4	Delay Bandwidth Product and its upper limit	87
4.3.5	Summary	89
5.	EXPERIMENTAL INVESTIGATION OF PHC NANO-CAVITY DEVICES IN NEAR INFRA-RED	91
5.1	GENERAL RULES FOR DESIGNING HIGH Q FACTOR CAVITIES.....	92
5.1.1	The Gaussian envelope function and the Fourier transform.	92

5.1.2	High Q factor cavity designs.....	95
5.2	EXPERIMENTAL INVESTIGATION OF HIGH Q FACTOR PHC CAVITIES	101
5.2.1	Local filling factor modulation cavity	101
5.2.2	The cavity-waveguide coupling role.....	103
5.2.3	Nonlinear and bistable effects	105
5.2.4	Summary	107
5.3	AIR-SLOT PHOTONIC CRYSTAL NANOCAVITY*	107
5.3.1	The air-slot waveguide and air-slot cavity	107
5.3.2	The air-slot cavity modelling, fabrication.....	109
5.3.3	The cavity characterization	111
5.3.4	The gas sensing experiment.....	112
5.3.5	Summary.....	114
6.	TERAHERTZ PHOTONIC CRYSTAL QUANTUM CASCADE LASERS.....	115
6.1	INTRODUCTION OF THZ QUANTUM CASCADE LASERS	117
6.1.1	The Terahertz technology.	117
6.1.2	From semiconductor laser to the intersubband engineering	121
6.1.3	THz QCL Active-region designs.....	124
6.1.4	The waveguide	126
6.1.5	From Fabry Perot to Slow light photonic crystals.	127
6.2	CHARACTERIZATION TECHNOLOGY FOR THz PHC QC LASERS	129
6.2.1	Electroluminescence and laser emission measurements	129
6.2.2	Far-field characterization	130
6.3	EXPERIMENTAL INVESTIGATION OF HIGH PERFORMANCE IN-PLANE EMITTING TERAHERTZ PHOTONIC CRYSTAL QUANTUM CASCADE LASERS*	131
6.3.1	First band slow light photonic crystal pillars	131
6.3.2	Electro-Luminescence and lasing measurement.	134
6.3.3	Measurement results and discussion.....	136
6.3.4	Conclusions	139
6.4	SURFACE EMITTING PILLAR TYPE PHOTONIC CRYSTAL QUANTUM CASCADE LASERS WORKING AT Γ BAND-EDGE POINT*	140
6.4.1	Introduction	140
6.4.2	Design of surface emitting PhC QCLs with large extractors	141
6.4.3	Large surface emitting extractors	143
6.4.4	Experimental results and discussion	144
6.4.5	Conclusions	146

6.5	HIGH POWER SURFACE EMITTING PILLAR TYPE PHOTONIC CRYSTAL TERAHERTZ LASERS WITH SUB-WAVELENGTH EXTRACTORS*	147
6.5.1	Introduction	147
6.5.2	Solutions on the band splitting	147
6.5.3	Loss modulation by positioning the extractors	148
6.5.4	Experimental results on circular pillars	150
6.5.5	Experimental results of elliptical pillars	151
6.5.6	Conclusion	153
7.	CONCLUSIONS AND FUTURE WORKS	155
	ACKNOWLEDGMENTS	157
	GLOSSARY AND ACRONYMS (ALPHABETICAL ORDER)	159
	REFERENCES	161
	LIST OF PUBLICATIONS AND PRESENTATIONS	179
	CURRICULUM VITAE	183

Abstract

Photonic crystals (PhC) are periodically structured electromagnetic media, in which light within some frequency ranges cannot propagate through the structure. Such frequency ranges are commonly referred as photonic band gaps (PBG). The length scale of the periodicity of the dielectric map is comparable to the wavelength of light propagating in the structure. This is an electromagnetic analogue of a crystalline atomic lattice, where the latter acts on the electron wavefunction to produce the familiar band gaps. It has been known since 2001 that the strong dispersion in specific PhC structures can generate slow propagating electromagnetic modes often but not exclusively in the vicinity of the photonic band-edge. Slow light, with small group velocity (v_g), is one of the most promising features of the two-dimensional (2D) PhCs.

It is therefore very interesting to study the slow light behaviours as well as other PhC properties for both the passive devices for integrated optics applications and active devices for light sources. This thesis investigates both aspects, on one hand we studied the slow light dispersion properties of passive structures. All the passive devices are operating in the Near-Infrared (NIR) wavelengths. This part of work was first started by the building-up of the entire fabrication platform with state of the art Electron Beam lithography (EBL) on Silicon-On-Insulator (SOI) material system. Various slow light PhC structures based on dispersion band-edges were investigated, *e.g.* PhC line defect waveguides and PhC coupled cavity waveguides.

On the other hand, we investigated active slow light structures constituting in band-edge lasers in the Terahertz (THz) frequency range. The active layers of the THz sources are inter-subband quantum cascade (QC) structures. Due to its intrinsic TM polarised emission, we investigated electrical pumped pillar-type PhC QC lasers that have complete PBGs in TM. We developed a BCB planarization technique to enable the metallization and electrical pumping on these isolated pillars.

Keywords:

Photonic crystals, slow light, silicon on insulator, fabrication, Electron Beam lithography, coupled cavity waveguide, quantum cascade laser, Terahertz, BCB planarization technique.

Résumé

Les cristaux photoniques (PhC) sont des matériaux, dont la structure périodique interdit aux ondes électromagnétiques de se propager sur certaines gammes de fréquences. Ces bandes de fréquences sont généralement appelées Bandes Interdites Photoniques (PBG). Les dimensions de la période de la carte diélectrique sont comparables à la longueur d'onde de la lumière se propageant dans la structure. Il faut y voir une analogie avec les réseaux atomiques dans les cristaux dont l'action sur la fonction d'onde des électrons permet l'apparition des bandes interdites. On sait depuis 2001 que la forte dispersion observée dans certaines structures à PhC permet la propagation de modes électromagnétiques lents, souvent mais pas nécessairement dans le voisinage du bord de bande photonique. La lumière lente, avec une faible vitesse de groupe (v_g), est une des caractéristiques les plus prometteuses des cristaux photoniques bidimensionnels (2D PhCs)

Il est donc particulièrement intéressant d'étudier les comportements de la lumière lente mais aussi d'autres propriétés des structures à PhC en vue de leur application pour les composants passifs pour l'optique intégrée d'une part, et les composants actifs des sources de lumière d'autre part. Cette thèse développe les deux aspects : d'une part nous avons étudié les propriétés de dispersion de la lumière lente dans les structures passives. Elles opèrent toutes dans le proche infrarouge (NIR). Cette partie du développement a débuté par la mise en place de l'entière plateforme de fabrication, avec l'état de l'art en matière de Lithographie à Faisceau d'Electron (EBL) sur des matériaux Silicium sur Isolant (SOI). Diverses structures de type lumière lente basée sur la dispersion de bord de bande ont été étudiées, par exemple des guides d'ondes PhC à défaut de ligne et des guides d'ondes PhC à cavités couplées.

D'autre part, nous avons étudié des structures actives à lumière lente, constitutives de lasers à bord de bande, opérant dans les fréquences TeraHertz (THz). Les couches actives des sources THz sont des structures à Cascade Quantique Inter-Sousbande (QC). Du fait de leur émission intrinsèquement polarisée TM, nous nous sommes consacrés à l'étude de lasers PhC QC de type pilier, pompé électriquement, qui possèdent une bande interdite complète en polarisation TM. Nous avons développé une technique de planarisation pour permettre la métallisation et le pompage électrique des piliers isolés.

Mots-clefs:

Cristaux photoniques, lumière lente, silicium sur isolant, fabrication, Lithographie à Faisceau d'Electron, Guides d'ondes à Cavités Couplées, Lasers à Cascade Quantique, Terahertz, technique de planarisation BCB.

Preface

Structures exhibiting a periodic modulation of the dielectric permittivity and/or the magnetic permeability of the media are called photonic crystals. In these structures the periodicity affects the propagation of light with a wavelength comparable to the period of the modulation in a way similar in which a crystal structure affect the properties of electrons. As a result the photonic band structure consists in photonic bands and band gaps (similar to the electronic structures in semiconductor or metal crystals). Two-dimensional photonic crystals are considered among the key components of modern and future integrated optics because they open many new possibilities of light control and can be fabricated using well-developed technologies with high accuracy and reproducibility.

Complex dispersion structure of the light states opens many possibilities to control the light propagation in the photonic crystals. Proper design of the photonic crystal allows tailoring light properties for the desired application. If the light frequency is inside the band gap, the propagation of the light modes is forbidden and the photonic crystal acts as a photonic insulator. Such structures can be used to reflect all incident light in case of a bulk PhC structure. They can also be used to guide light with desired direction in the case when a line defect (called W_1 in case of 1 missing row of holes in 2D PhC) is introduced to the PhC structures, or to confine light in a small volume in the case when a point defect (one or several missing holes in 2D PhC) is introduced to the PhC structures. When a series of defect cavities are coupled to form a coupled cavity waveguide (CCW), we can consider it as a new 1D PhC whose periodicity is the cavity separation. A slow light dispersion band can be formed by the CCW. For the line defect and point defect PhC structures, we studied their corresponding slow light PhC W_1 waveguide dispersion and coupled cavity waveguide dispersion at NIR frequency. In terms of bulk 2D PhC structures, we studied the PhC band engineering with combination of quantum cascade inter-subband engineering for slow light band-edge lasing application at THz frequency.

The manuscript is divided into 6 chapters.

In Chapter 1 the basic properties of the photonic crystals are introduced and discussed. This chapter defines the concepts that are used throughout the manuscript.

Chapter 2 describes the theory behind the photonic crystal. The modelling techniques, as well as the slow light concepts are introduced in this chapter.

In Chapter 3, the detailed fabrication procedures, for both the NIR passive photonic crystal devices and THz active photonic crystal quantum cascade lasers are described in detail.

Chapter 4 and Chapter 5 focus on the NIR passive devices and Chapter 6 focus on the THz active devices.

Chapter 4 details the design as well as experimental characterization results of NIR passive devices for two types of slow light structures: PhC W_1 waveguide and CCW.

In Chapter 5, prior to fabricate and investigate coupled cavity waveguides it was necessary to study its constitutive blocks: the single cavity. The design principle of high quality factor (Q-factor) PhC cavities has been reviewed, and experimentally measured high Q cavities up to half a million will be reported. Nonlinearities, bistable effects were observed, however they were accomplished with self-pulsing behaviours.

In Chapter 6, we focus on the design, modelling, and characterization results of various slow light pillar-type PhC lasers based on quantum cascade active layers. For in-plane emitting PhC QCL, we demonstrated performance enhancement in all aspects comparing with the best performance Fabry-perot (FP) lasers. For vertical emitting purposes, we developed a complex-coupled PhC QCL scheme that can modulate the refractive index and loss independently. Based on such scheme, very high vertical emitting power was achieved.

This thesis has been performed in the framework of the Swiss National Centre of Competence in Research (NCCR) in Quantum Photonics and two National Science Foundation projects (200021-109845 and 200020-122099). For the passive devices on SOI material system in NIR wavelengths, the works were performed with collaboration inside the group. For the Indium Phosphide (InP) material system in NIR wavelength, the work was performed with close collaboration with Dr. Anne Talneau in Laboratory for Photonics and Nanostructures (LPN), National Center for Scientific Research (CNRS), France. For the active devices in THz frequencies, the works were performed with close collaboration with Prof. Jérôme Faist's Quantum Opto Electronics group in Swiss Federal Institute of Technology Zurich (ETHZ).

Lausanne, July 2010.

Chapter 1

1. Basic properties of the photonic crystals

1.1 Introduction to photonic crystals

In 1887, Lord Rayleigh studied the electromagnetic wave propagation in periodic media. The study was in connection with the peculiar reflective properties of a crystalline mineral with periodic planes. These structures should be called with nowadays' name: one-dimensional (1D) photonic crystals. Lord Rayleigh identified that there is a narrow band gap prohibiting light propagation through the planes. This band gap is angle-dependent, due to the different periodicities experienced by light propagating at non-normal incidences, producing iridescent reflected colour patterns that vary sharply with angle.

A similar effect is responsible for many other iridescent colours in nature, such as butterfly wings, sea mouse threads, natural opals and peacock feathers shown in Fig. 1.1.1. Their corresponding scanning electron microscope (SEM) images or optical microscope images indicate the periodic arrangement of the structures. All these beautiful colour examples have microscopic structures known as photonic crystals. Unlike pigments, which absorb or reflect certain frequencies of light as a result of their chemical composition, the way that photonic crystals reflect light is given by their physical structure.

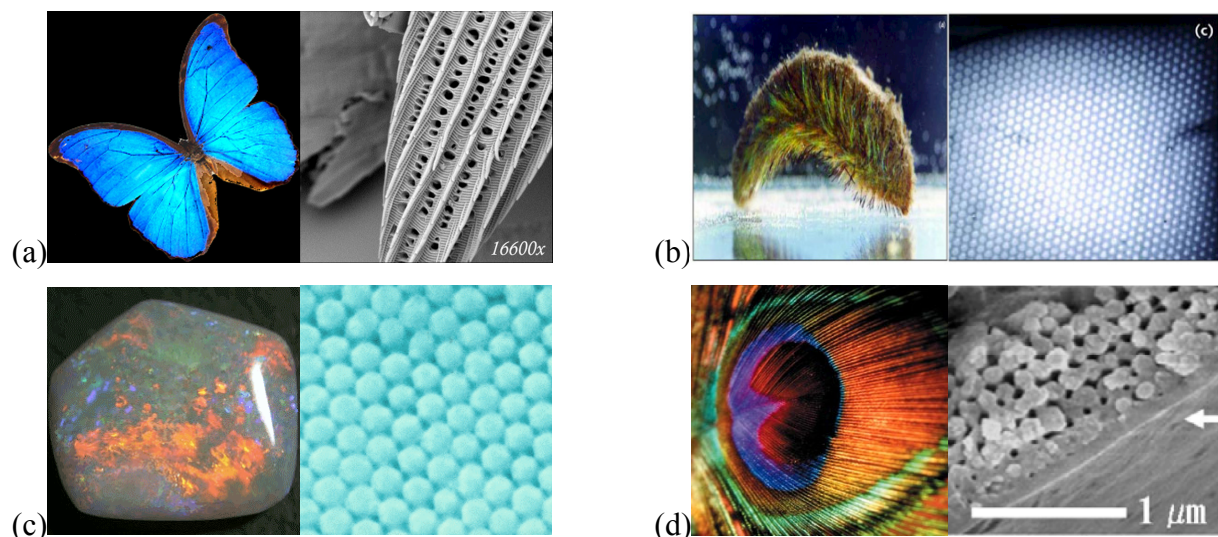


Fig. 1.1.1. (a), *Mopho Didus* butterfly and its SEM structure. (from [1]) (b), Sea mouse with its iridescent threads and the SEM cross-section of a spine, (from [2]). (c) Coober pedy opal with red fire flash and its SEM (from [3]). (d) Peacock feather and its SEM (from [4]).

Periodic arrangement of atoms in crystal lattices determines the periodic potential for the valence electrons and set the behaviour of the electrons in the crystal. Materials with different crystalline structures exhibit broad range of physical properties, and according to their electronic structures they can be metals, insulators, semiconductors and *etc.* The developed ability to control electrons in crystals and to design devices with many important properties inspired the interest to create artificial structures which can control the photons in a way similar to electrons in crystals. Photonic crystals (PhCs) were originally proposed independently and simultaneously in 1987 by two researchers, in order to realise two fundamental optical principles: the localization and trapping of light in a bulk material [5] and the complete inhibition of spontaneous emission over a broad frequency range [6]. Sajeev John was investigating whether Anderson localization of electrons in a disordered solid can be extended to photons in a strongly scattering medium, and predicted that localised states of the electromagnetic field can be created in a periodic dielectric medium. At the same time, Eli Yablonovitch was trying to address the possibility of suppressing the unwanted spontaneous emission affecting the semiconductor lasers, and predicted that a 3D periodic dielectric can produce a forbidden gap in the electromagnetic spectrum. This generalization, which inspired the name “photonic crystal,” led to many subsequent developments [7-9] in the fabrication, theory, and applications from passive devices, active devices, integrated optics to optical fibres that guide light in air.

1.2 One dimensional PhCs and the origin of the PBG

The PhCs can be coarsely distinguished according to whether their dielectric function is periodic in one, two or three dimensions (1D, 2D and 3D, as schematically shown in Fig. 1.2.1). A full photonic band gap (PBG) can exist only in 3D system where light is forbidden for any direction and polarization. However, 2D or even a 1D (pseudo) PBG is sufficient for many applications. There are also incomplete gaps, which only exist over a subset of all possible wavevectors, polarizations, and/or symmetries.

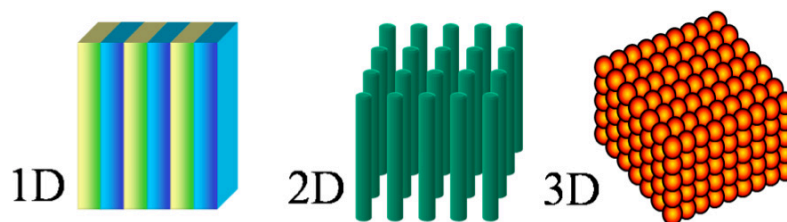


Fig. 1.2.1. Schematic illustration of 1D, 2D and 3D photonic crystals.

The origins of both the complete PBG and incomplete PBG are the same, and can be understood by examining the consequences of periodicity for a simple 1D system: a Bragg stack of dielectric planes. Let us consider first the case of a plane wave with wavevector k impinging at normal incidence on a Bragg mirror with period a (see Fig. 1.2.2).

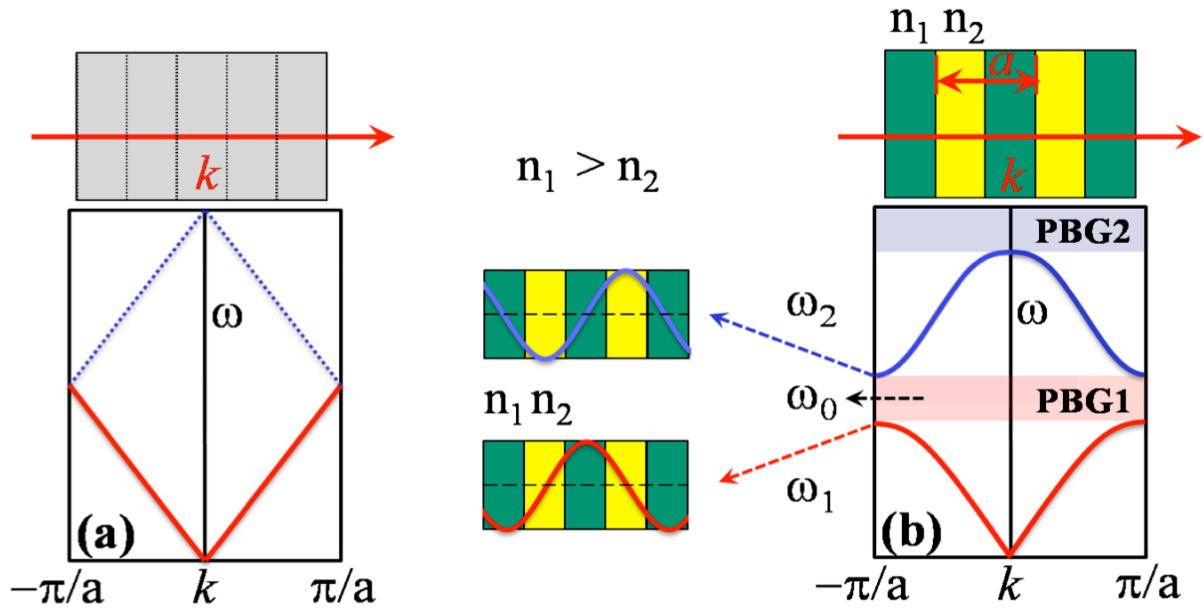


Fig. 1.2.2. (a): Dispersion relation $\omega(k)$ of a uniform medium at normal incidence: The dashed lines represent the 'folding' effect of applying Bloch theorem [10] with an artificial periodicity a . (b): Dispersion diagram of a 1D periodic dielectric medium at normal incidence, where the anti-crossing between the two counter-propagating modes has opened two PBGs at $k = \pm\pi/a$.

Because of the periodicity in the wave propagating direction, the electromagnetic modes of the stack can be characterised by the wavevector k , with k restricted to $-\pi/a < k < \pi/a$ (Bloch theorem, Ref. [10]). At each interface between different dielectrics a part of the light is reflected, but at every second interface an additional phase-shift of π also occurs upon reflection. The phase difference between two successively reflected waves is $\phi = ka + \pi$. The total amount of reflected light is only important when $\phi \approx 2\pi$, *i.e.* the reflected waves interfere constructively. This is the case at the border of the Brillouin-zone (BZ). The superposition of the incident and the reflected waves: $k = \pm\pi/a$ results in a standing wave pattern. The coupling of the two counter-propagating waves (with the same energy ω_0 by the reciprocal vector $G = 2\pi/a$ of the grating) results in a band-splitting that lifts the degeneracy and generates two standing wave modes with energies ω_1 and ω_2 .

When $n_1 > n_2$, the lower band-edge mode has its E field power maxima in the high index region, on the contrary, the upper band-edge mode has its E field power maxima in the low index region. Such bands are normally called **dielectric band** and **air band**, respectively. In 1D and at normal incidence the bandwidth $\Delta\omega$ of the stop band in the frequency domain depends on the index contrast [11] as:

$$\Delta\omega = \frac{4}{\pi} \omega_0 \sin^{-1} \left(\frac{n_1 - n_2}{n_1 + n_2} \right) \quad (1.1.1)$$

The gap closes continuously with decreasing index contrast. The situation becomes more complex when the light enters the medium with an incidence angle. Assuming the Bloch vector in the (x, y) plane there are two different solutions, which correspond to different light polarizations. The first (called s-polarization) has the electric field only in the z direction and the magnetic field in the (xy) plane. The second (called p-polarization) has the magnetic field only in the z direction and the electric field in the (xy) plane.

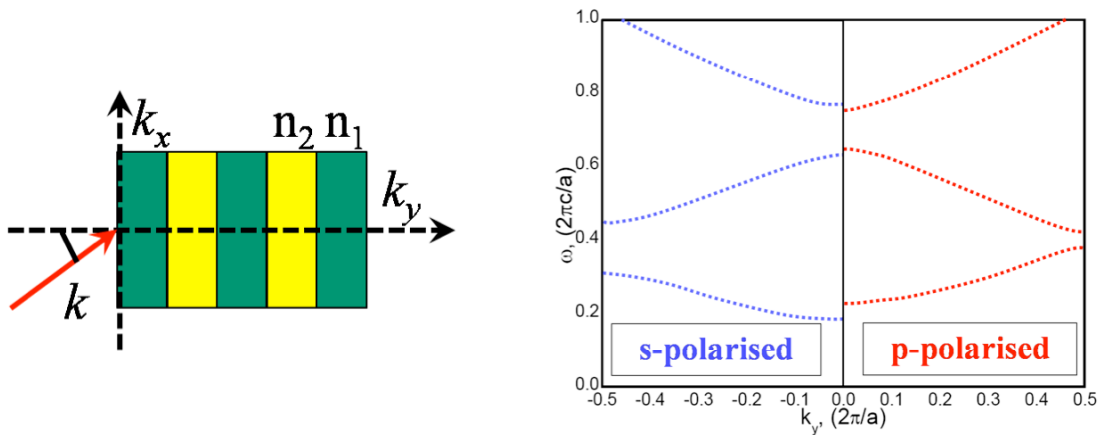


Fig. 1.2.3. Dispersion relations of the Bloch modes with different light polarizations.

The dispersion relations of light with different polarizations are presented in the Fig. 1.2.3. Only propagating states (with real Bloch vectors) are shown. The x component of the Bloch vector $k_x = 0.3(2\pi/a)$. Because of different interaction of the light with these polarizations with the media (and especially with the internal boundaries) they have different dispersion properties: different shape and position of the bands, different position and width of the band gaps.

1.3 Two dimensional PhCs

1.3.1 Ideal two dimensional PhCs

The design freedom of 1D PhC is limited for the integrated circuits purpose. However, after the identification of 1D band gaps, it took a full century to add a second dimension, and three years to add the third. 2D systems exhibit important characteristics in many aspects. It can be used to demonstrate most proposed photonic-crystal devices. A pure 2D PhC would be periodic in the (x, y) plane and infinitely long in the z -direction, *i.e.* k_z is conserved. Such infinite long 2D system does not exist in reality, however a good approximation is attained by PhCs based on macroporous silicon (see Fig. 1.3.1).

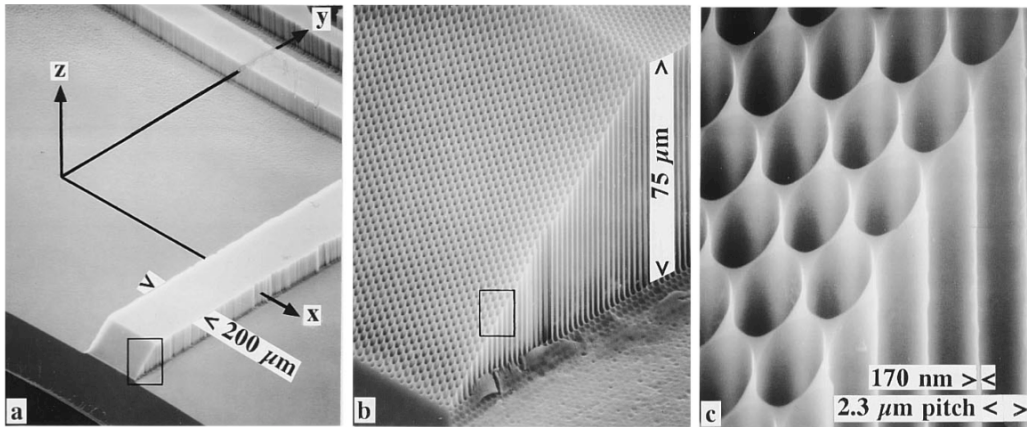


Fig. 1.3.1. Scanning electron micrographs of a patterned and micromachined layer of macroporous silicon forming a 2D PhC. The lattice constant of the macropore array is $2.3 \mu\text{m}$, the pore is $2.13 \mu\text{m}$ in diameter and $75 \mu\text{m}$ in depth. (reprinted from Ref. [12])

A triangular lattice of circular air rods with a lattice constant of $2.3 \mu\text{m}$ was etched $75 \mu\text{m}$ deep in an n-type silicon substrate by electrochemical pore formation in hydrofluoric acid. The porous layer was then micromechanically structured in such a way that $200 \mu\text{m}$ thick free standing bars of porous material were left over on the silicon substrate [12]. The narrow pitch is only 170 nm width, which leads to an extremely high aspect ratio of more than 440:1. Such type of photonic crystal behaves like an ideal 2D structure when working with a plane wave.

1.3.2 Slab waveguide two dimensional PhCs

In this thesis we focused on a different approach called slab waveguides, in which a vertical confinement is provided by **index guiding**, provided that $n_{\text{core}} > n_{\text{clad}}$, has been followed. A PhC slab waveguide provides periodic modulation of index in the (x, y) plane, and confines light vertically within the slab, which can be seen as total internal reflection (TIR) on a first order. The index confinement in the vertical direction is not complete, but still sufficient for many integrated optics applications. Many PhC slab waveguide systems have been successfully developed to demonstrate the PhC effects, such as Silicon-on-insulator (SOI) [13], Si membrane [14], AlGaAs-based waveguides [15], InP membrane [16], or metal-metal waveguides [17]. There are consequences for the light polarisation in case of slab waveguides, because the translational symmetry is broken by the vertical structure. In the ideal 2D PhCs the fields are homogenous in z -direction and the distinction between TE and TM polarisation is exact as shown in Fig. 1.3.2(a).

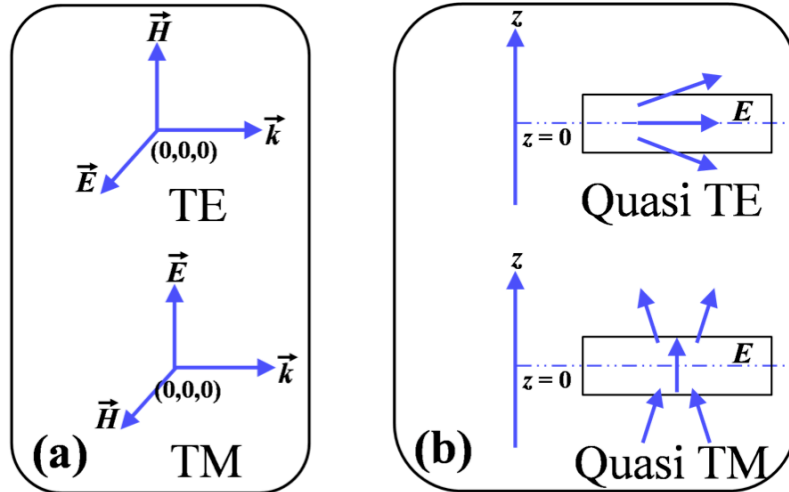


Fig. 1.3.2. The polarisation inside the slab and definition for TE and TM. (a). The polarisation definition in ideal 2D system. (b). The polarisation inside the slab is defined with respect to the mirror plane at $z = 0$. The electrical field distribution may either be even (Quasi TE) or odd (Quasi TM).

However, in slab waveguides the fields vary as a function of the z -coordinate (see Fig. 1.3.2(b)). For example, the field components of a TE PhC slab mode are (H_x, H_y, H_z) for the magnetic field and $(E_x, E_y, 0)$ for the electric field. When considering the mirror plane $z = 0$ in the core layer of the symmetric structure, the even (Quasi TE) and odd (Quasi TM) modes (which are purely TE/TM in the mirror plane itself) can still be distinguished, and the eigenvalue problem for the electromagnetic field can be reduced to a single vertical component, *e.g.* H_z for TE-polarisation. In the case of asymmetric slab structures, this symmetry breaks down and the calculation of modes has to include all three field components due to the potential polarisation mixing. In practice the symmetry braking can be either weak for high index contrast structures (the modes are strongly confined in the slab), or strong for low index contrast structures (the modes are loosely confined in the slab).

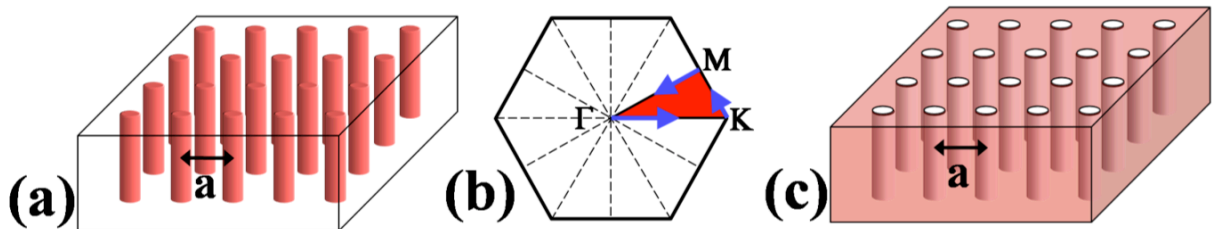


Fig. 1.3.3. Schematic demonstration of hexagonal lattices of high dielectric pillar in air for (a), and air holes in dielectric for (c), where a is the lattice constant. (b), the $\Gamma K M \Gamma$ blue arrows indicate the calculation path in the Brillouin zone for the future dispersion.

The 2D slab PhC systems can be divided into two groups: isolated high index regions and connected high index regions. The corresponding ideal and simplest examples are high index

pillars surrounded by air and low-index holes in high index material as depicted in Figs. 1.3.3(a) and 1.3.3(c), respectively. These two different topologies are suited due to the complete in-plane PBGs for different polarizations: Pillar-type PhC systems have complete in-plane PBG for TM polarised light; hole-type PhC systems have complete in-plane PBG for TE polarised light.

1.3.3 PhC lattice parameters

In 2D PhC systems the most common geometries are the square and the hexagonal lattice (see Fig. 1.3.4). Each of them is described by two direct lattice vectors. Each direct lattice is accompanied by a reciprocal lattice. For a given set a_1, a_2, a_3 of real space lattice vectors (in the 2D case a_3 can be chosen arbitrarily, e.g. $a_3 = (0, 0, 1)$), the corresponding set b_1, b_2, b_3 of reciprocal vectors is defined by $a_i \cdot b_j = 2\pi\delta_{ij}$. The solution to these equations is given as follow:

$$b_1 = 2\pi \frac{a_2 \times a_3}{V_C}, b_2 = 2\pi \frac{a_3 \times a_1}{V_C}, b_3 = 2\pi \frac{a_2 \times a_1}{V_C} \quad (1.1.2)$$

where $V_C = a_1 \cdot (a_2 \times a_3)$ is the volume of the primitive unit cell.

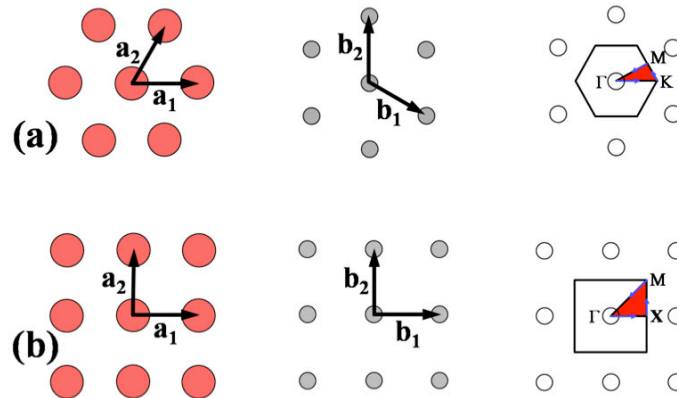


Fig. 1.3.4. Real space lattice, reciprocal lattice and Brillouin zone including symmetry points of the two most common lattices in two dimensions: (a) hexagonal lattice, (b) square lattice.

Filling factor (ff) is considered as another important parameter. It indicates the fraction of the hole or pillar surface with respect to the total surface of the unit cell. In Table 1.1.1, the lattice parameters for both the hexagonal and the square lattice are specified.

	Hexagonal lattice	Square lattice
Real space vectors	$a_1 = (1,0); a_2 = (\frac{1}{2}, \frac{\sqrt{3}}{2});$	$a_1 = (1,0); a_2=(0,1);$
Reciprocal vectors	$b_1 = \frac{2\pi}{a} (1, -\frac{\sqrt{3}}{3}); b_2 = \frac{2\pi}{a} (0, \frac{2\sqrt{3}}{3});$	$b_1 = \frac{2\pi}{a} (1,0); b_2 = \frac{2\pi}{a} (0,1);$
ff	$\frac{2\sqrt{3}\pi R^2}{3a^2}$	$\frac{R^2\pi}{a^2}$
Unit cell surface	$\frac{\sqrt{3}a^2}{2}$	a^2

Table. 1.1.1. Basic properties of the hexagonal lattice and square lattice.

1.3.4 Dispersion relation of the bulk photonic crystal and light cone issues

The dispersion of the 2D PhC system has many similarities with the dispersion of the 1D PhC system, but is more complex, because in this case the frequency is a function of the Bloch vector $\omega = \omega(\mathbf{k})$, instead of the scalar k as for 1D photonic crystals. For a given \mathbf{k} vector there are several possible values of frequencies: $\omega = \omega_n(\mathbf{k})$. These values define surfaces in the (ω, \mathbf{k}) space, called the photonic bands of the photonic crystal. The examples of dispersions for both pillar-type and hole-type 2D PhC are shown in the Fig. 1.3.5.

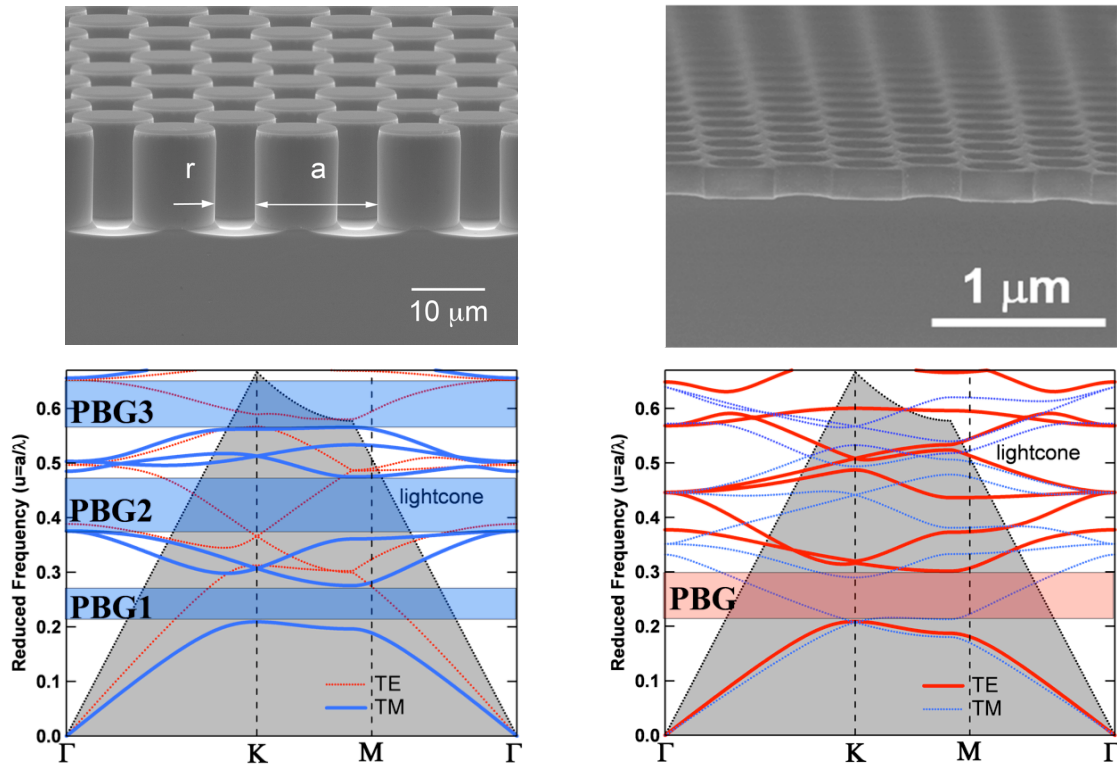


Fig. 1.3.5. SEM images of pillar-type (topleft) and hole-type (topright) PhC systems. Their band diagrams are shown for high dielectric pillar in air ($n = 3.56$, $ff = 40\%$, bottom left), and air holes in dielectric ($n = 3.56$, $ff = 40\%$, bottom right). The frequencies are plotted according to $\Gamma K M \Gamma$ direction (referring to Brillouin zone plot in Fig, 1.3.3). The pillar- and hole-type PhC systems have complete bandgaps for TM (blue lines) and TE (red lines) polarizations in bottom left and bottom right figures, respectively.

Here, we use a hexagonal lattice, to calculate the bulk PhC dispersion. As mentioned in section 1.3.2, the pillars are best suited to TM light, and the holes are best suited to TE light. This preference is reflected in the band diagrams, shown in Fig. 1.3.5, in which the pillars/holes (top left/right SEM images) have a strong TM/TE band gap, for ff of 40% and high/low index is 3.56/1. Such dispersion band structures are based on 2D Plane wave expansion (PWE) that will be explained in Chapter 2.

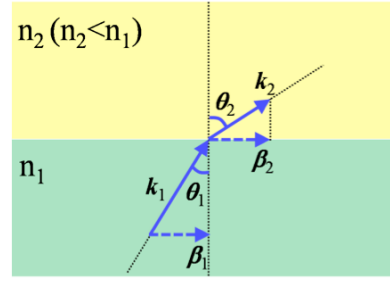


Fig. 1.3.6. Schematic representation of Snell-Descartes' law

When considering the influence of the third dimension in the case of 2D photonic crystals in slab waveguide, the light line is a very important concept to be introduced. It is a reformulation of total internal reflection (TIR) condition in terms of wavevector conservation. Snell-Descartes' law states that the parallel wavevector component is conserved at the interface (see Fig. 1.3.6):

$$\beta_1 = \beta_2 \rightarrow k_0 n_1 \sin \theta_1 = k_0 n_2 \sin \theta_2 \rightarrow \frac{\sin \theta_1}{\sin \theta_2} = \frac{n_2}{n_1} \quad (1.1.3)$$

The critical angle is given by the condition $\theta_2 = \pi/2$.

$$\beta_1 = k_0 n_2 \sin \frac{\pi}{2} = \frac{\omega}{c} n_2 \rightarrow \omega(\beta_1) = \frac{c \beta_1}{n_2} \quad (1.1.4)$$

where β_1 is the wavevector inside the core, parallel to the interface, n_2 denotes the refractive index of the cladding and $\omega(\beta_1)$ identifies the light line. In the case of 2D PhCs the lightline is defined by $\omega(k) = |k|c/n$, where $k = (k_x, k_y)$ is traced along the main symmetry directions (see Fig. 1.3.5).

Here if we come back to the comparison between high-index contrast structures and low index contrast structure, with the consideration of the light line problem one would rather favour high-index contrast structures. In high-index contrast structures, such as SOI and Si membrane, InP membrane, double metal waveguides, can be considered to exhibit strong PhC effects, where lossless Bloch modes propagate well below the light line [17, 18]. This can be understood in the sense that the scattered waves of different holes interfere destructively. However, the Bloch mode is only lossless as long as there is translational symmetry. A reason for a symmetry breaking could be a cavity or a bend, these elements will be presented naturally in a photonic integrated circuit. In this case also the strong confinement waveguides will exhibit losses. Additionally, the high-contrast structure is more sensitive to fabrication imperfections (e.g. roughness). On the contrary, the low-index contrast structures, such as Air/GaAs/Al_xO_y, double/single metal hybrid waveguides [19], can be considered to exhibit weak PhC effects, where all the modes propagate above the light line.

1.3.5 Defects, waveguides and cavities

When there is a perturbation in the PhC lattice (*e.g.*, missing hole, bend), the translation symmetry is destroyed and optical properties of the PhC will be modified. In perfect PhCs, Bloch modes with different frequencies and/or different Bloch vectors are orthogonal. The presence of defects introduces coupling between the different Bloch modes, defects serve as scattering centres for propagating Bloch modes. New photonic states are allowed to exist inside the PBG. The shape and properties of the states are dictated by the nature of the defect, *e.g.*, cavity modes confined in a **point defect** (with 1 or more missing holes), or guided modes propagating in a **line defect** (with a line of missing holes along ΓK direction).

For point defect, we can remove a single hole from the crystal, or replace it with another size, shape, or dielectric constant, or similarly to a number of holes form a cavity. In this case the modes cannot be described by an in-plane wave vector. However, the mirror-reflection symmetry is still intact for $k_z = 0$. Therefore we can still restrict our attention to in-plane propagation, and the TE and TM modes are still decoupled. The point defect may introduce a peak into the electromagnetic density of states (the number of possible modes per unit frequency and per unit volume) within the PBG. The defect mode cannot penetrate into the rest of the crystal, since it has a frequency in the band gap. Any defect states should be localized near the defect core and decay exponentially away from the defect. They are localized in the xy plane, but extended in the z direction.

In the presence of defects, the PhC reflects light of certain frequencies because of its band gap. By removing a single hole from the lattice, we create an optical **cavity** that is effectively surrounded by reflecting walls. If the cavity has the proper size and supports a mode in the band gap, then light cannot escape, and we can pin the mode to the defect mode. The simplest cavity (called H_1 cavity) is presented in the Fig. 1.3.7. and is created by removing one atom from the PhC lattice. The holes around the defects are highlighted by blue colour, while the remaining atoms are shown as red circles. Another type of cavities in 2D PhC is also plotted in the Fig. 1.3.7. These cavities are created by removing the atoms along the line in one of the lattice principal directions (such as ΓK or ΓM directions for the triangular lattice and ΓX and ΓM directions for the square lattice). The L2 and L3 cavities [20], as shown in Fig. 1.3.7, are created by removing two or three adjacent atoms along the ΓK direction from the lattice, respectively.

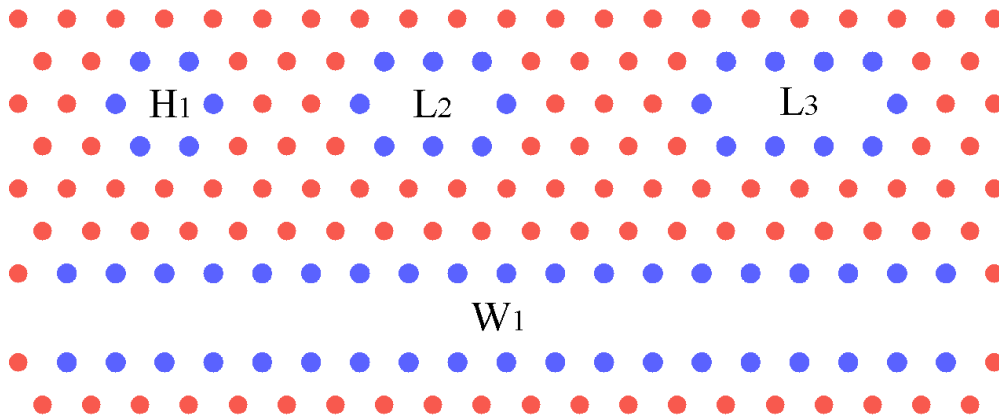


Fig. 1.3.7. Schematic illustration of possible sites of point, line defects. Perturbing one single hole in the bulk of the crystal might allow a defect state to be localized in both x and y . Perturbing one row in the bulk of the crystal might allow a state to be localized in one direction (x). Holes around the defects are highlighted by blue colour.

Increasing the number of the removed atoms in the L-type cavity leads to creation of the 1D defect: the chain of missing atoms along the ΓK direction. This defect is called W_1 waveguide and is shown in the Fig. 1.3.7. Two or three neighbour lines of missing atoms create the W_2 and W_3 waveguides, respectively. As in the previous section, a slab PhC waveguide has a series of guided modes that are confined horizontally by the bandgap, and vertically by the index guiding. However, the presence of such a W_x waveguide has a second category of guided modes, which arises because the waveguide has a higher average dielectric constant than the surrounding air in a particular direction. Modification of the dispersion relation for the Bloch modes propagating along a linear defect can create states with the frequency inside the full PBG of the perfect PhC. Modes with such frequencies cannot propagate inside the PhC and so they are localized near the defect, but they can propagate along the defect.

Parameters of the photonic crystal waveguides determine the dispersion properties and the field distribution of the guided modes. For example, the W_1 waveguide has the mirror symmetry relative to the reflection in the (xz) plane that contains the waveguide axis (the plane $y = 0$). Such waveguide can support the mode which also has even symmetry relative to the reflection in the plane $y = 0$ [21]. The W_2 waveguide doesn't have the mirror symmetry and so the corresponding guided modes have different symmetry properties in comparison with the modes of the W_1 waveguide.

1.4 Three dimensional PhCs

The full 3D PBG has been predicted for structure consisting of the dielectric spheres arranged in the diamond structure [7] and for a face-centered-cubic structure with non-spherical

atoms [8]. The latter structure (called Yablonoivite) is created by etching (or drilling) cylindrical holes in high-permittivity dielectric, its dispersion and schematic drawing are shown Figs. 1.4.1 and 1.4.2(a).

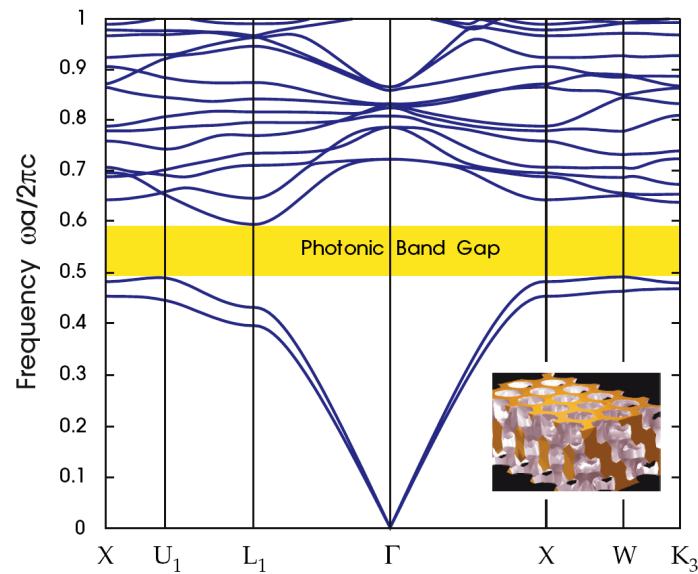


Fig. 1.4.1. The photonic band structure for the lowest bands of Yablonoivite (inset). Wave vectors are shown for a portion of the irreducible Brillouin zone that includes the edges of the complete gap (yellow). Reprinted from Ref. [10]

The PBG has been first demonstrated for this type of PhC in the microwave range [8]. Using ion beam etching allows one to significantly decrease the size of the holes and to demonstrate the PBG effect for infrared light [22]. Drilling holes with a radius of $0.234a$ results in a structure with a complete photonic band gap of 19%, as shown in Fig. 1.4.1. The fabricated sample is shown in the SEM image of Fig. 1.4.2(b).

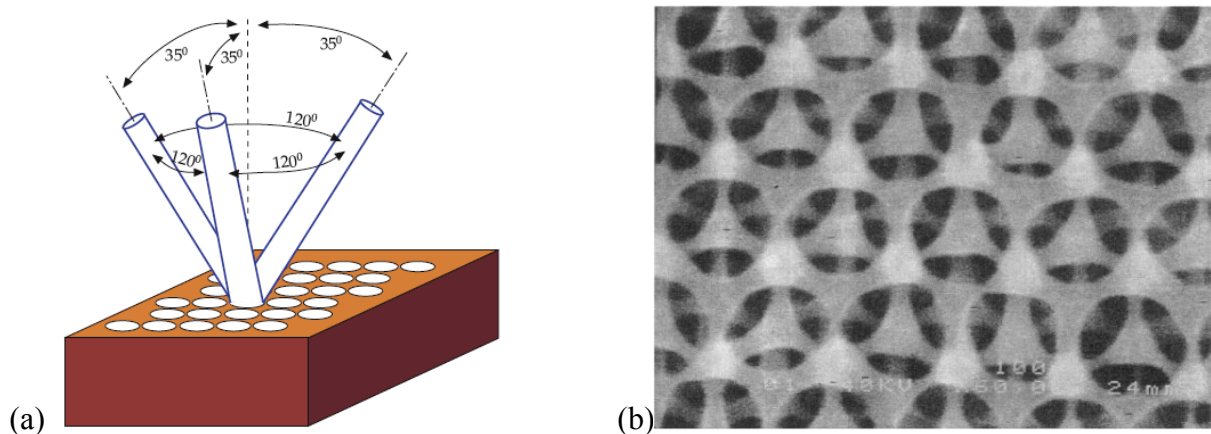


Fig. 1.4.2. (a) The photonic crystal structure proposed by Yablonoivitch et al. in [8]. (b) Yablonoivite structure fabricated by the ion beam etching (from [22]).

In past years many 3D PhC structures have been proposed. There are mainly two ways to fabricate 3D PhC structures: self-assembled structures and artificial-fabricated structures. The first is working with the opal structures (closely-packed lattice of SiO_2 spheres in air), which are self-assembled from a water colloid of monodisperse silica spheres [23-28]. By filling the inter-sphere space with high-dielectric material and subsequent etching of the silica, the inverse opal structures can be fabricated [24, 29]. The band structure for a lattice of air spheres within a dielectric medium is shown in Fig. 1.4.3(a). Waveguide in 3D PhC with the inverse opal structure is shown in the Fig. 1.4.3(b). However such opal-based crystals inevitably contain unintentional defects.

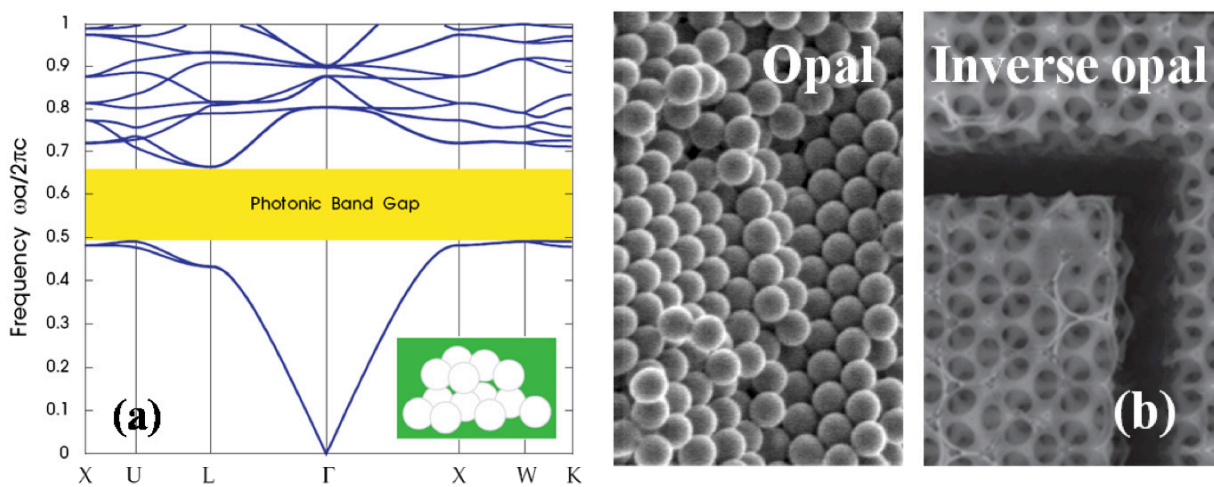


Fig. 1.4.3. (a) The photonic band structure for the lowest bands of a diamond lattice of air spheres in a high dielectric ($\epsilon = 13$) material (inset). A complete photonic band gap is shown in yellow. The wave vector varies across the irreducible Brillouin zone between the labelled high-symmetry points. Reprinted from Ref. [10]. (b) SEM images of self-assembly of colloidal SiO_2 spheres (left panel, from Ref. [23]) and waveguide in inverse opal (right panel, from Ref. [28]).

Apart from the self-assembled 3D PhC structures, many progresses have been made by artificially fabricated 3D PhC structures, such as the layer-by-layer structures [30-32] ('woodpile structures'), holography fabricated structures (as shown in Fig. 1.4.4(c)), and microporous silicon structures (as shown in Fig. 1.4.4(d)).

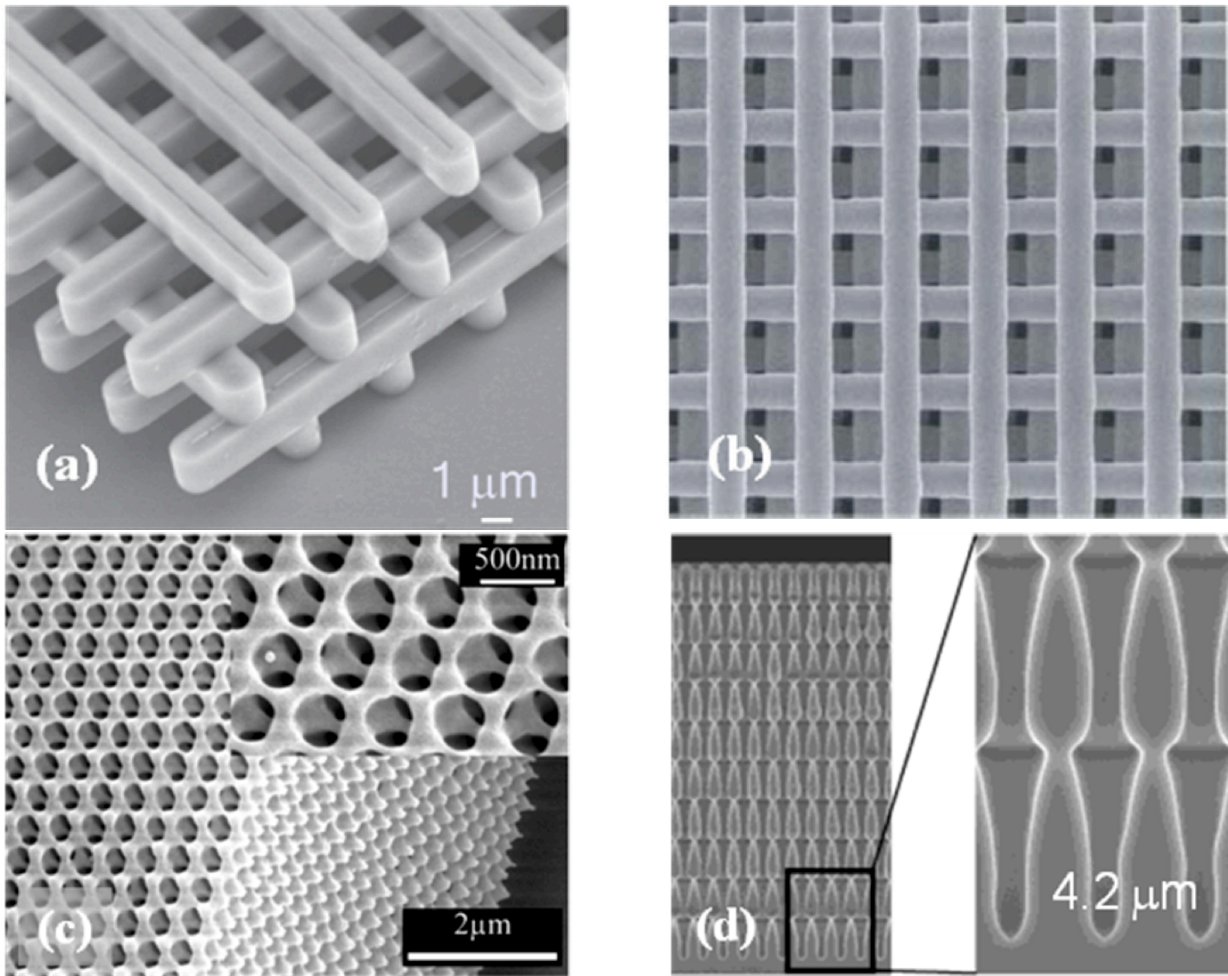


Fig. 1.4.4. (a) 3D photonic crystal consisting a stack of Si bars (from [30]). (b) 3D photonic crystal consisting a stack of Si bars (from [33]). (c) 3D photonic crystal made by laser holography in photo resist (from [34]). (d) SEM cross section of a sample etched with 10 periods of modulated light intensity. The lattice constant a_{xy} in the xy -plane is $4.2 \mu\text{m}$, in the z -direction $a_z = 7.2 \mu\text{m}$ (from [35]).

The woodpile crystal is formed by a stack of dielectric ‘logs’ (normally rectangular) with alternating orthogonal orientations. It can be fabricated as a sequence of layers deposited and patterned by lithographic techniques developed for the semiconductor electronic industry. This lithographic compatibility is considered as the main advantage of woodpile crystal than the opal ones. Examples of fabricated woodpile crystals are given in Figs. 1.4.4(a) and 1.4.4(b) [30][33].

Recently, holographic lithography has emerged as a very promising technique for the inexpensive fabrication of high-quality 3D PhC templates. Together with direct laser writing approaches, holographic lithography offers the attractive possibility of controlled incorporation of functional elements using direct laser writing in a second step [36]. Example of holographic lithography fabricated 3D PhC structure is shown in Fig. 1.4.4(c) [34].

3D PhC on the basis of macroporous silicon consists of a 2D ordered array of air pores which were etched into a silicon wafer. Thanks to the fabrication process macropores with high aspect ratios (ratio between pore depth and pore diameter) of 100 and more can be achieved. To obtain a 3D photonic crystal a periodic index variation along the pores has to be achieved. This may be realized through a periodic variation of the pore diameter with pore depth. By modulating the light intensity during the electrochemical etching with hydrofluoric acid (HF), the number of charge carriers varies which in turn modifies the dissolution of the Si. Thus, by modulating the illumination intensity, the internal microstructure, and thus local refractive index of the sample is controlled [35].

The advantage of 3D photonic crystals is that they can control propagation of the light in all three dimensions, which allows, for example, total suppression of the spontaneous emission by creation of the full photonic band gap. However, compare to the 2D PhC, the biggest disadvantage of 3D PhC is still its difficult fabrication process, which limits types of possible structures (lattice symmetry, materials *etc.*) and incorporation of desired defects in the PhC.

Chapter 2

2. Theory, modelling techniques and concepts

The problem of electromagnetic analysis on a macroscopic level consists in solving Maxwell's equations with certain boundary conditions. Maxwell's equations are a set of equations, written in differential or integral form, stating the relationships between the fundamental electromagnetic quantities. These quantities are the electric field, the electric displacement or electric flux density, the magnetic field, the magnetic flux density, the current density and the electric charge density.

This chapter first starts from describing the theory behind the photonic crystal in Section 2.1. Then the simulation tools used for the modelling will be explained in Section 2.2. In this thesis work, two major tools have been used for the modelling of 2D PhC systems: Plane wave expansion method (PWE) and finite element method (FEM). PWE is used for the calculation of PhC band structures (dispersion $\omega(k)$ relationship) and the field distribution of waveguides, cavities, and bulk PhC structures. The FEM is used mainly as an eigenmode solver for specific PhC structures which require complex boundary conditions and three-dimensional modelling. Finally, in Section 2.3, the slow light concept and design rule for the experimental investigated PhC structures will be introduced in detail.

2.1 *The Maxwell's equations for the electromagnetic field*

2.1.1 The master equation

The propagation of light in a photonic crystal is governed by the four macroscopic Maxwell equations. In Gaussian Centimetre-Gram-Second (CGS) units, they are:

$$\begin{aligned}\nabla \cdot B &= 0 \\ \nabla \cdot D &= 4\pi\rho \\ \nabla \times E &= -\frac{\partial B}{c\partial t} \\ \nabla \times H &= \frac{4\pi}{c}J + \frac{\partial D}{c\partial t}\end{aligned}\tag{2.1.1}$$

where respectively, D and B are the displacement and magnetic induction fields, E and H are the macroscopic electric field and the magnetic field, and ρ and J are the free charge and current densities.

For the isotropic materials if the electric field and the magnetic induction strengths are small enough (so that there are no non-linear effects in the media) the electric displacement $D(r)$ and the magnetic field $H(r)$ are given by:

$$D = \varepsilon E \quad (2.1.2)$$

$$H = \frac{B}{\mu} \quad (2.1.3)$$

where $\varepsilon(r)$ is the dielectric permittivity and $\mu(r)$ is the magnetic permeability of the media. Assuming that there are no external charges ($\rho = 0$) and currents ($J = 0$) the Maxwell's equations become:

$$\begin{aligned} \nabla \cdot (\varepsilon E) &= 0 \\ \nabla \cdot H &= 0 \\ \nabla \times E &= -\frac{\mu}{c} \frac{\partial H}{\partial t} \\ \nabla \times H &= \frac{\varepsilon}{c} \frac{\partial E}{\partial t} \end{aligned} \quad (2.1.4)$$

Considering a monochromatic light with the standard time dependence $\exp(-i\omega t)$ the following equations can be derived:

$$\begin{aligned} \frac{1}{\mu(r)} \nabla \times \frac{1}{\varepsilon(r)} \nabla \times H(r) &= \left(\frac{\omega}{c}\right)^2 H(r) \\ \frac{1}{\varepsilon(r)} \nabla \times \frac{1}{\mu(r)} \nabla \times E(r) &= \left(\frac{\omega}{c}\right)^2 E(r) \end{aligned} \quad (2.1.5)$$

According to these equations the electric field and the magnetic field can be decoupled and treated separately. However, if the distribution of the electric field is known, it allows finding the distribution of the magnetic field, and vice versa. The equations (2.1.5) have the structure of an eigenvalue problem. The eigenvalues of the problems provide the allowed light frequencies and the corresponding eigenfunctions give the field distributions.

2.1.2 The scalability of photonic crystal

The scalability is a very useful property of photonic crystals. It is possible to scale all geometrical dimensions of the sample or to scale the values of the dielectric permittivity or magnetic permeability keeping all the features related to the light propagation (but at the corresponding scaled light wavelength). The master equation for the magnetic field is

$$\frac{1}{\mu(r)} \nabla \times \frac{1}{\varepsilon(r)} \nabla \times H_\omega(r) = \left(\frac{\omega}{c}\right)^2 H_\omega(r) \quad (2.1.6)$$

Assume that the distribution of the dielectric permittivity $\varepsilon(r)$ and the magnetic

permeability $\mu(r)$ are shrunken or expanded by a scaling factor α , *i.e.* the new distributions are $\varepsilon'(r) = \varepsilon(r') = \varepsilon(r/\alpha)$ and $\mu'(r) = \mu(r') = \mu(r/\alpha)$. After substituting $r' = r/\alpha$, the nabla operator ∇ turns to $\nabla' = \alpha\nabla$ and Eq. (2.1.6) transforms into:

$$\frac{1}{\mu(r')} \nabla' \times \frac{1}{\varepsilon(r')} \nabla' \times H_{\omega}(r') = \left(\frac{\omega}{\alpha c}\right)^2 H_{\omega}(r') \quad (2.1.7)$$

This means that for the scaling of PhC geometrical parameters by a factor of α , the frequency of the state is multiplied by α , while the profile of the electromagnetic field is just scaled by α . Since the periodicity of the field remains the same the eigenvalue of the translation operator doesn't change:

$$e^{ikR} = e^{ik'R'} = e^{i(\alpha k)\left(\frac{R}{\alpha}\right)} \quad (2.1.8)$$

the scaled period corresponds to the scaled Bloch vector. This scaling property allows to introduce a dimensionless Bloch vector and a dimensionless frequency:

$$\kappa = \frac{a}{2\pi} k \quad (2.1.9)$$

$$u = \frac{a}{2\pi c} \omega = \frac{a}{\lambda} \quad (2.1.10)$$

where a is any characteristic scale of the photonic crystal (usually the lattice constant) and λ is the light wavelength in the vacuum. It also has the meaning of measuring the Bloch vector k in the units $2\pi/a$ and the frequency ω in the units $2\pi c/a$.

The dimensionless Bloch vector κ and the dimensionless frequency u usually are referred to as the **reduced Bloch vector** and the **reduced frequency** or the **reduced energy**, respectively. The reduced Bloch vector and the reduced frequency uniquely identify the Bloch state independently of the spatial scaling of the photonic crystal. Another scaling property is related with the dielectric permittivity (or the magnetic permeability) values and contrast. By changing the permittivity by a factor of β^2 : $\varepsilon'(r) = \beta^2 \varepsilon(r)$ the Eq. (2.1.6) becomes

$$\frac{1}{\mu(r)} \nabla \times \frac{1}{\varepsilon'(r)} \nabla \times H_{\omega}(r) = \left(\frac{\omega}{\beta c}\right)^2 H_{\omega}(r) \quad (2.1.11)$$

This means the mode profile remains the same but the frequency of the state is multiplied by the factor β . Because the refractive index of a media equals the square root of the permittivity, scaling of the permittivity by a factor β^2 corresponds to changing of the refractive index by the factor β . It indicates that the change of the state frequency (for the same Bloch vector) is proportional to the change of the refractive index. Similar relation corresponds to the scaling of the magnetic permeability.

2.1.3 The Bloch-Floquet Theorem

The properties of the light propagating through a periodic media are very similar to the properties of electrons propagate through a crystal with a periodic potential. So, many theories and concepts from solid state physics may be applied for photonic crystals. One of the most useful and important is the Bloch-Floquet theorem, which describes properties of the electron wave function in a crystal with the periodic potential. In solid state physics the Bloch-Floquet theorem is deduced by expanding the periodic crystal potential $V(x) = V(x+a)$ into a Fourier series summed over all reciprocal lattice vectors, *i.e.* $V(x) = \sum_G c_G e^{jGx}$. Such potential is then inserted into the stationary Schrödinger equation $\hat{H}\Psi = \varepsilon\Psi$. Here \hat{H} is the Hamiltonian of the electron in a potential field and ε is the energy of the state. The resulting set of algebraic equations is solved by a function of the form [37]:

$$\Psi_k(x) = e^{jkx} u_k(x) \quad \text{and} \quad u_k(x) \equiv \sum_G c_{k-G} e^{-jGx} \quad (2.1.12)$$

where k is the Bloch wavevector lying in the first Brillouin zone. The Bloch theorem states that eigenfunctions of the Hamiltonian operator for a periodic potential are always of the form of Eq. (2.1.12). For instance, $u_k(x)$ is a Fourier series over the reciprocal lattice vectors, it is periodic with respect to a translation by a direct lattice vector, *i.e.* $u_k(r + R) = u_k(r)$. In summary the electron wave functions inside a periodic crystal potential are plane waves modulated by a periodic function.

In the case of photonic crystals, the periodic potential has to be replaced by the periodic dielectric map $\varepsilon(r)$. Meanwhile the Schrödinger equation has to be replaced by the Master equation of the magnetic field:

$$\hat{\theta}H(r) = \lambda H(r) \quad (2.1.13)$$

$$\text{where} \begin{cases} \hat{\theta} = \nabla \times \left(\frac{1}{\varepsilon(r)} \nabla \times \right. \\ \left. \lambda = \frac{\omega^2}{c^2} \right. \end{cases}$$

It is convenient to introduce the translation operator \hat{T}_d which shifts the argument of an arbitrary test function by the vector d , *i.e.* $\hat{T}_d f(r) = f(r+d)$. The eigenfunctions of the translational operator are plane waves and the eigenvalues complex numbers with modulus one:

$$\hat{T}_d e^{jkr} = e^{jk(r+d)} = \underbrace{e^{jkd}}_{\lambda} e^{jkr} \quad (2.1.14)$$

In the case of a translation by a direct lattice vector Eq. (2.1.14) writes:

$$\hat{T}_R e^{jkr} = e^{jkR} e^{jkr} \quad (2.1.15)$$

The eigenfunctions are specified by the wavevector k ; however, there are degenerate eigenfunctions that yield the same eigenvalue. In fact all modes with wavevectors of the form $k' = k + G$ are degenerate, where G is an arbitrary reciprocal lattice vector. Applying the theorem that a linear combination of degenerate eigenfunctions is itself an eigenfunction to the same eigenvalue, the general solution of Eq. (2.1.15) is

$$H_\omega(r) = \sum_n c_{k,n} e^{j(k+Gn)r} = e^{jkr} \underbrace{\sum_n c_{k,n} e^{jGnr}}_{\equiv u(r)} \quad (2.1.16)$$

where $u(r)$ is by construction a periodic function with $u(r + R) = u(r)$ and $H_k(r)$ thus has the form of a Bloch mode. Due to the discrete translation symmetry of the dielectric map, $\hat{\theta}$ commutes with \hat{T}_R . Accordingly, the two operators possess a common set of eigenvectors and we have proven that the solutions to Eq. (2.1.13) are of the Bloch form.

2.2 Modelling techniques

2.2.1 The Plane Wave Expansion (PWE) method

The Plane-wave expansion method refers to a computational technique in electromagnetism to solve an eigenvalue problem from the Maxwell's equations. It was initially proposed by Maradudin *et al.* [38] in 1991, and by now becomes a standard tool for calculating the dispersion properties of photonic crystals [39, 40]. The advantages of this method are simplicity and high flexibility. It allows one to describe not only the bulk photonic crystals with perfect periodicity but also point defects (PhC cavities) and line defects (W_1 or W_x PhC waveguides).

The Bloch theorem is applied in the PWE to develop the magnetic and electric fields. For a 2D PhC with periodicity in the (x, y) , the magnetic and electric fields (E and H) can be written with their Fourier coefficients (\tilde{E} and \tilde{H}) as:

$$\begin{aligned} H(r_{\parallel}) &= \sum_G \tilde{H}(G) e^{i(k_{\parallel}+G)r_{\parallel}} \\ E(r_{\parallel}) &= \sum_G \tilde{E}(G) e^{i(k_{\parallel}+G)r_{\parallel}} \end{aligned} \quad (2.2.1)$$

where $k_{//}$ and $r_{//}$ are the wave vector and real space vector in the (x, y) plane, respectively. G is a reciprocal lattice vector in the plane.

The inverse of the dielectric constant can also be decomposed into a Fourier series:

$$\frac{1}{\varepsilon(r_{//})} = \sum_G \frac{e^{iG_{//}r_{//}}}{\tilde{\varepsilon}(G)} \quad (2.2.2)$$

this expression can be used in the following equations:

$$\begin{aligned} \nabla \times \left(\frac{1}{\varepsilon(r)} \nabla \times H(r) \right) &= \left(\frac{\omega}{c} \right)^2 H(r) \\ \nabla \times (\nabla \times E(r)) &= \left(\frac{\omega}{c} \right)^2 \varepsilon(r) E(r) \end{aligned} \quad (2.2.3)$$

Then we obtain an eigenvalue problem for the Fourier components $\tilde{H}(G)$. If the number N of plane waves is truncated beyond a certain standard G_{\max} , we obtain a linear $N \times N$. Moreover, this vector problem can be split into two scalar problems for the transverse component of the field in each of the TE and TM polarizations (Figure 1.3.2):

$$\sum_{m=1}^N (k_{//} + G_n) \cdot (k_{//} + G_m) \cdot (\tilde{\varepsilon}(G_n - G_m))^{-1} \cdot \tilde{H}_m(k_{//}) = \left(\frac{\omega}{c} \right)^2 \tilde{H}_n(k_{//}) \quad \text{'TE'} (2.2.4)$$

$$\sum_{m=1}^N |k_{//} + G_n| \cdot (\tilde{\varepsilon}(G_n - G_m))^{-1} \cdot |k_{//} + G_m| \cdot |k_{//} + G_m| \cdot \tilde{E}_m(k_{//}) = \left(\frac{\omega}{c} \right)^2 (|k_{//} + G_n|) \cdot \tilde{E}_n(k_{//}) \quad \text{'TM'} (2.2.5)$$

The standard plane wave expansion uses unit cell (Fig. 2.2.1(a)) and it only allows one to calculate the band diagrams of bulk photonic crystal. In this case a single hole/pillar is sufficient to calculate the complete photonic dispersion diagram due to its periodical boundary condition along a_1 and a_2 directions (a_1 and a_2 refer to the real space lattice vectors). In case of calculation of more complex structures, such as PhC cavities with point defects or waveguides with line defects, this method should be adapted: the unit cell of the crystal should be replaced by a supercell containing a proper combination of several unit cells. Figs. 2.2.1(b) and 2.2.1(c) shows the supercells adapted for the PhC cavities and waveguides, respectively.

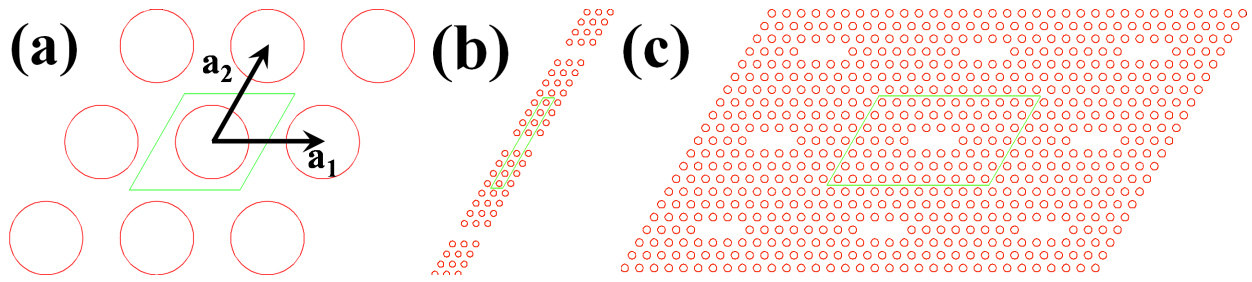


Fig. 2.2.1. Illustrations of different unit cell or supercells used for the dispersion calculation in PWE: (a) standard unit cell for bulk photonic crystal; (b) supercell of PhC W_1 waveguide with 1 missing line along ΓK direction; (c) supercell of a PhC cavity with 3 missing holes along the ΓK direction. The unit cell and supercell are labeled with green colour. All the three figures are plotted with 3×3 of their unit cells (or supercells).

For the calculation of dispersion relations of PhC straight waveguides with one or multiply missing holes along ΓK direction (so called W_1 or W_x waveguides), a supercell with variation along only a_2 direction is sufficient. However, in case of more complex structure, e.g., a PhC cavity with 3 missing holes along ΓK direction (so called L3 cavity), a supercell with variation along both a_1 and a_2 directions are needed. The unit cell and the supercells are repeated periodically in both a_1 and a_2 directions in the calculation. It needs to be mentioned that the distance between defects must be sufficient to prevent the coupling of cavity modes. The number of rows of holes between the cavities must be increased until the value of clear energy converges to a stable value, such as the cavity computed with a large supercell in Fig. 2.2.1(c).

2.2.2 Finite element method (FEM)

Finite element method (FEM) is a general numerical technique widely used to obtain numerical solutions to engineering and mathematical physics problems. It can be used to solve any partial differential equations (PDEs). The method was first developed in 1940's by Richard Courant for use in structural analysis [41], and soon after that, it was used in a wide variety of engineering disciplines, including electromagnetics.

In this method, an entire continuous domain is replaced by a number of subdomains, that is **finite elements**, in which the unknown function is represented by simple interpolation functions with unknown coefficients [42]. This makes the original problems with infinite number of degrees of freedom converted into a problem with a finite number of degrees of freedom. The accuracy of the FEM method is closely related to the way of discretization. By refining the mesh, the accuracy can be improved. After the discretization, then those equations, together with applicable physical considerations, are applied to each element. In this case a system of simultaneous equations is constructed which minimises the error. Finally the system of equations

is solved for unknown values using techniques of linear algebra or nonlinear numerical schemes, as appropriate.

The finite element software used during the thesis is COMSOL Multiphysics [43]. The application fields of this software are very diverse, we only focus on the ‘lossy eigenmode solver’ in the RF module to model photonic crystal structures with complex boundary conditions. For dispersion diagram computation, PWE is a better tool as accurate results can be obtained in a fast way. The COMSOL software is installed in a linux based workstation with 16 GB memories in ETHZ. The whole modelling consists of the following steps:

- Geometry modelling
- Physics settings to setup boundary conditions and subdomain settings
- Mesh generation
- Computing the solution
- Postprocessing and visualization.

2.2.2.1 Boundary conditions and Perfectly Matched Layers (PMLs)

One of the challenges in finite element modelling is how to treat open boundaries in radiation problems. The RF Module offers two closely related types of absorbing boundary conditions, the **scattering boundary condition** and the **matched boundary condition**. The former is perfectly absorbing for a plane wave, whereas the latter is perfectly absorbing for guided modes, provided that the correct value of the propagation constant is supplied. However, in many scattering and antenna-modelling problems, one cannot describe the incident radiation as a plane wave with a well-known direction of propagation. In such situations, **perfectly matched layers** (PMLs) should be used. In COMSOL, a PML is strictly speaking not a boundary condition but an additional domain that absorbs the incident radiation without producing reflections. It provides good performance for a wide range of incidence angles and is not particularly sensitive to the shape of the wave fronts. The PML formulation can be deduced from Maxwell’s equations by introducing a complex-valued coordinate transformation under the additional requirement that the wave impedance should remain unaffected [42]. The following section describes how to create PMLs in the RF Module for 3D simulation in Cartesian coordinate directions.

This RF Module uses the following coordinate transform for the general coordinate variable t .

$$t' = t \frac{\lambda}{\delta t} (1 - i) \quad (2.2.6)$$

The coordinate, t , and the width of the infinite element region, δt , are input parameters for each

region. These parameters get a default setting according to the drawn geometry.

2.2.2.2 Lossy Eigenvalue Calculations

In mode analysis and eigenfrequency analysis, it is usually the primary goal to find a propagation constant or an eigenfrequency. Ideally eigenfrequencies are real (due to the Hermitian operator and energy conservation) [44], however formal extension to lossy system can be done with introduction of complex eigenvalues. Such as in case of a nonzero conductivity or an open boundary, the eigenvalue is complex. In such situations, the eigenvalue is interpreted as two parts:

- the propagation constant or eigenfrequency
- the damping in space and time.

The ‘eigenfrequency analysis’ is available for all application modes in the RF Module, it solves the eigenfrequency of a designed model. Time-harmonic representation of the fields is more general and includes a complex parameter in the phase:

$$E(r, t) = \text{Re}(\bar{E}(r) e^{j\omega t}) = \text{Re}(\bar{E}(r) e^{-\lambda t}) \quad (2.2.7)$$

where the eigenvalue, $(-\lambda) = \delta + j\omega$, has an **imaginary** part (ω) representing the eigenfrequency, and a **real** part (δ) responsible for the damping. It is often more common to use the quality factor or **Q-factor**, which is derived from the eigenfrequency and damping:

$$Q = \frac{\omega}{2|\delta|} \quad (2.2.8)$$

2.2.2.3 The 3D tetrahedral mesh quality measure.

In COMSOL Multiphysics, the convergence of a numerical solution of one or several partial differential equations generally depends on various characteristics of the problem, on the numerical algorithm, on the mesh refinement and on the mesh quality. The **mesh quality measure (q)** is a very important concept, it means that anisotropic elements can obtain a low quality measure even though the element shape is reasonable. The value of q is a number between 0 and 1. When the value of q is sufficiently high, the mesh quality is considered as ideal and it should not affect the solution’s quality. Table 2.1.1 shows the summery of mesh quality q expressions in case of different meshing elements.

Elements	Mesh quality measure	q range	Ideal q	Remarks
Triangular	$q = \frac{4\sqrt{3}A}{h_1^2 + h_2^2 + h_3^2}$	$0 < q < 1$	$q > 0.3$	$q = 1$ for an equilateral triangle. A is the area.
Quadrilateral	$q = \frac{4A}{h_1^2 + h_2^2 + h_3^2 + h_4^2}$	$0 < q < 1$		$q = 1$ for a square.
Tetrahedral	$q = \frac{72\sqrt{3}V}{(\sum_{i=1}^6 h_i^2)^{\frac{3}{2}}}$	$0 < q < 1$	$q > 0.3$	$q = 1$ for a regular tetrahedron. V is the volume.
Hexahedron	$q = \frac{24\sqrt{3}V}{(\sum_{i=1}^{12} h_i^2)^{\frac{3}{2}}}$	$0 < q < 1$		$q = 1$ for a cube.
Prism	$q = \frac{36\sqrt{3}V}{(\sum_{i=1}^9 h_i^2)^{\frac{3}{2}}}$	$0 < q < 1$		$q = 1$ for right-angled prism where all edge lengths are equal.

Table. 2.1.1. Summary of mesh quality measures.

In order to know the capacity and accuracy of the desired configuration, we started the 3D modelling meshing test by finding the PhC band-edge frequency and its loss (defined in Equation 2.2.7) at different number of elements. Such test was performed on a dual core 64-bit Macintosh computer with 8 GB memory. For simplicity, the structure was chosen as 4x4 hexagonal pillar type bulk PhC with refractive index of 3.56 and surrounding refractive index of 1.6. The top and bottom boundaries are perfect electric conductors that are assumed to be the ideal double metal waveguide configuration. In such case there is no out of plane loss. The in-plane boundaries are specified as scattering boundary conditions (as defined in section 2.2.2.1). By changing the number of meshing elements under **tetrahedral** condition, different results are recorded. The band-edge frequency and loss as a function of number of meshes are compared in Table 2.1.2 and Fig 2.2.2.

No of meshes.	2,996	19,427	24,480	46,667	58,068	67,231
Degree of freedom	20,474	128,304	162,262	307,686	384,404	440,410
Q_{\min_global}	0.1422	0.2005	0.2237	0.2880	0.2708	0.2813
Q_{\min_CD}	0.1607	0.2807	0.3096	0.3514	0.3384	0.4092
Frequency (THz)	3.17149	3.14582	3.14716	3.14762	3.14758	3.14704
Loss (cm^{-1})	3.9005	1.7352	1.7363	1.7305	1.7397	1.73

Table. 2.1.2. Comparison of calculation results (frequency and loss) and mesh quality measures as a function of number of meshes.

The Q_{\min_global} represents the minimum element quality globally. However, in most of the cases, this value doesn't determine the solution's accuracy, *e.g.*, when the Q_{\min_global} occurs intentionally far away from the centre structure. Therefore, here we introduce a more useful and accurate concept called Q_{\min_CD} (critical dimension), which is used to describe the minimum element quality for the smallest features (normally the most important features, like a slot cavity) in the system. For the bulk photonic crystal structure case, such value was measured on a plane which is parallel to the surface and taken from the middle of the pillar. A good approximation of a reasonable minimum element quality on critical dimension is $Q_{\min_CD} \geq 0.2$.

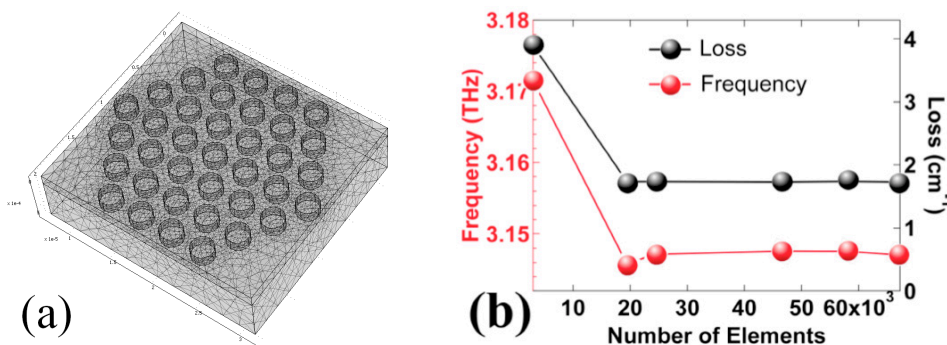


Fig. 2.2.2. (a) 3D meshing results of 4x4 hexagonal PhC structure with 67231 number of tetrahedral meshes. (b) Band-edge frequency and loss as a function of number of meshes.

As can be seen from both Table 2.1.2 and Fig. 2.2.2(b), for this specific simulation, when the number of meshes is more than 20,000, the mesh quality is high enough ($Q_{\min_CD} > 0.3$) to obtain a clear convergence of the solution.

2.2.2.4 The 3D structures with metal.

There have been successful attempts with finite element solver (Comsol Multiphysics) to simulate the complex eigenvalue problems on THz ridge waveguides or Distributed Feedback (DFB) Lasers with double metal waveguide configuration. Drude model was used at these calculations for the active region, heavily doped contact layer, and Au metal [45-47]. However such method is impractical for the simulation of our pillar type photonic crystal. A simply full 3D simulation of planar photonic crystal pillars (10 – 15 μm) embedded in the double metal waveguide (500 - 1500 nm) requires extremely large amount of meshes already. When more complicated structures are investigated, *e.g.*, adding holes in the metal layer above or between the pillars, the calculation capacity becomes unreasonable even the cluster can barely run it.

A good approximation of the double metal waveguide is to use the **perfect metal conductor** boundary to replace the thin Au layer [48]. Holes can be drilled by using the **Embed** function therefore both the top plasmon layer and the holes possess zero thickness, hence the meshing load can be dramatically reduced. The meshing result, the H_z field profile of the PhC

band-edge mode and its associated far field (calculated from E_x and E_y fields via the small surface holes, details will be discussed in Chapter 7) are shown in Figs. 2.2.2(a), 2.2.2(b) and 2.2.2(c), respectively.

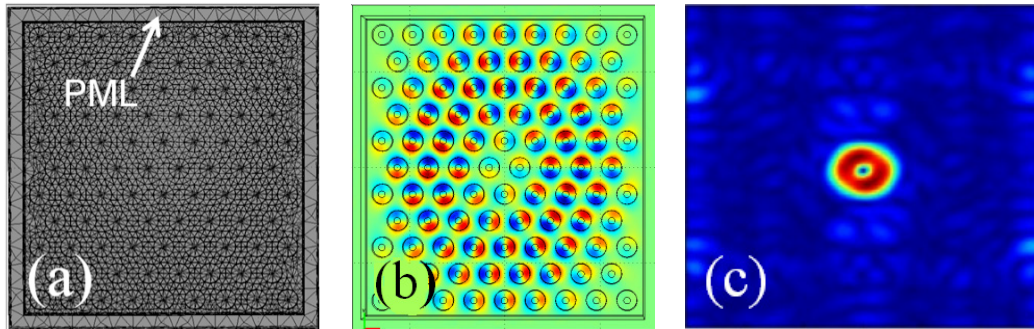


Fig. 2.2.3. (a), 3D meshing results in COMSOL of planar photonic crystal pillars embedded in the double metal waveguide. External regions (indicated by the arrow) are the perfect matching layer. (b), Calculated H_z field profile of the PhC band-edge mode has a rotational symmetry due to the boundaries. (c). Far field results of this PhC band-edge mode (calculation methods are detailed in Chapter 7).

2.2.3 Finite Difference Time Domain (FDTD)

Despite the fact that the FDTD technique has not been used during this thesis work, it is still necessary to mention such a technique. In this method the Maxwell's equations for the electromagnetic field are discretized over a regular grid in space, and time evolution of the field in each grid site is calculated using the finite difference formulas. The basic FDTD space grid and time-stepping algorithm trace back to a seminal 1966 paper by Kane Yee [49]. The descriptor "Finite-difference time-domain" and its corresponding "FDTD" acronym were originated by Allen Taflove in 1980 [50].

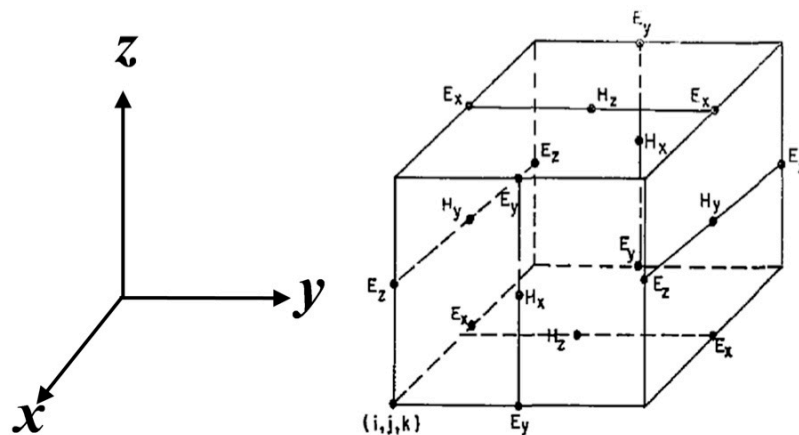


Fig. 2.2.4. Illustration of a standard Cartesian Yee cell used for FDTD. The E -components are in the middle of the edges and the H -components are in the center of the faces. From Ref. [49].

The computational domain was first established, in order to determine the physical region within which the calculation will be performed. The Electric field, E , and the magnetic field, H , are distinguished at every point within the domain by specifying the material used at each domain point (in xyz directions, as shown in Fig. 2.2.4). The materials involved could be air, metal or dielectric material. A light source in the form of a plane wave is then impinging on the chosen material. The FDTD method is a brute force method which can be used to calculate light evolution in almost any structure, periodic or not, and provides direct information about the electromagnetic field distribution. Among the disadvantages are: high demands for the computational resources (calculation time and required memory), especially in the 3D case; special treatment for the boundaries with discontinuous dielectric permittivity and/or magnetic permeability to suppress approximation errors; the method provides a raw data for the field distribution, special sophisticated treatment is required to extract necessary information like frequency and Bloch vector of a mode, transmission coefficient of a device *etc.*

2.3 Slowlight

2.3.1 Slow light introduction.

The interesting property of PhCs is that they support so-called **slow light**: light in a certain range of frequencies will propagate at velocities a few orders of magnitude slower than in vacuum [51-53]. Slow light has numerous and diverse practical applications. The related phenomena include enhancement of various light-matter interactions. With enhanced optical gain/absorption as well as linear [54] and non-linear effects [55] per unit length, various optical devices, such as lasers, amplifiers, detectors, absorption modulators and wavelength converters, switches, optical delay lines and all-optical storages could be miniaturized. Initially, slow light was generated using extremely strong material dispersion. However, in this thesis we focus on the dispersion arising from engineered structures, in particular PhC devices, which offer a promising approach for the on-chip integration of slow-light devices.

It has been known since 2001 that the strong dispersion in this waveguide generates slow light in the vicinity of the photonic band-edge [14-17, 51-54, 56-60]. The dispersion relations discussed in the previous sections show that the wavevectors are strongly dependent on the optical frequency in a PhC waveguide. Non-patterned structures would show merely straight or slightly bent modes in the dispersion relation [61, 62]. The slope of the dispersion relation determines the group velocity (v_g) of the propagating light:

$$v_g \equiv \frac{d\omega}{dk} = \frac{c}{n_g} \quad (2.3.1)$$

where k , ω and n_g are the wavenumber, angular frequency and group index, respectively.

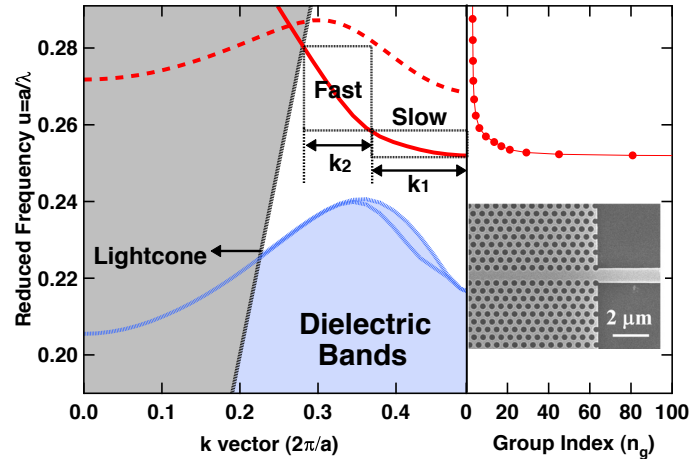


Fig. 2.3.1. PhC W_1 waveguide, photonic bands and group-index characteristics. Left: Dispersion bands of W_1 PhC waveguide. PWE is used to calculate the TE polarised dispersion with $n_{high}/n_{low} = 2.8/1$ at $ff = 24\%$. W_1 waveguide mode is labelled as red curve. The blue and gray shadows represent the dielectric band and the lightcone, respectively. Right: Group index of the W_1 waveguide mode. Inset: SEM image of W_1 waveguide fabricated on SOI.

As can be seen in the dispersion relations in Fig. 2.3.1, two regions with different slopes are highlighted, which correspond to the fast light regime with steep slope and slow light regime with shallow slope. In another word, the slow light is excited in a frequency range where the dispersion is smooth and flat over a broad k vector range and light will propagate at a very low group velocity. In the extreme case, *e.g.*, at the Brillouin zone boundary, the dispersion relation is completely flat, hence light will theoretically be frozen in the waveguide (with infinite group index n_g).

Slow light has an intriguing effect on the E-field amplitude of a wave packet [55]. To illustrate this effect, we consider a pulse of light impinging on a slow-light medium from air. The pulse has a certain spatial extend in air. As a result of the low v_g , the spatial extend of the pulse in the slow-light medium will be smaller than that in air. The energy density of the pulse is determined by the energy of the pulse and its spatial extend. If we now assume that all the energy of the pulse has been transmitted into the medium, this results in a higher energy density in the medium. In a photonic crystal, this results in an increase of the E-field intensity in the medium, roughly proportional to the group index n_g . Since the group index in photonic crystals can be dramatically increased, these structures are promising for the enhancement of light-matter interaction, especially in the case of nonlinear processes [63]. The resulting second order derivative is called the group velocity dispersion (GVD) [51, 64] and causes a distortion of pulses in time. For processes where the electric field should be high, pulse broadening is

obviously a disadvantageous effect, since the peak power of a pulse decreases due to this broadening.

Another effect that plays a role in slow light propagation is the influence of disorder in the photonic crystal lattice. Any imperfection in the lattice, such as a slight displacement of a unit cell, variations in shape or size of a cell or surface roughness, can cause losses [65]. As both slow light and the increase of the E-field are caused by multiple reflections of the light at the lattice sites, one can intuitively expect higher losses for slow light, since the interaction time with the medium and therefore also the chance of scattering at imperfections increases. Detailed discussion regarding the slow light limits, useful bandwidth issues, *etc.* will be performed in Chapter 6.

2.3.2 Passive Slow light PhC line defect waveguide

Photonic crystal structures are nevertheless promising for both passive and active optical devices, with highly integrated structures with dimensions on the micron-scale and responses in the picosecond time-scales. There are a number of challenges to be resolved, which lie on the forefront of the development of future applications. In this thesis we will investigate the fundamental properties of the passive PhC waveguides and of active PhC structures. The first slow light PhC structure is the line defect hole-type PhC waveguide. Such W_1 waveguides are passive devices based on InP, a general introduction with applications and detailed experimental investigation results will be explained in Chapter 6. The second slow light PhC structure is the bulk PhC pillars. Such band-edge operating structures are active PhC devices based on gain medium at terahertz, detailed experimental investigation results will be explained in Chapter 8.

An example of the dispersion of the TE polarised W_1 waveguide modes and its group index for the triangular lattice photonic crystal is given in the Fig. 2.3.1. Large structure dispersion can be obtained by PhC waveguides [51]. Owing to zone-folding of the guided-mode band and the coupling of forward and backward propagating waves forming a standing wave, the first-order dispersion diverges to infinity, and slow light occurs when approaching the band-edge. Here the photonic crystal consists of the circular air holes etched in the high- ϵ material. One missing row of holes along ΓK direction forms this W_1 PhC waveguide. The effective refractive indices used in the PWE calculation for the high- ϵ dielectric and low- ϵ material are $n_{\text{high-}}/n_{\text{low-}} = 2.8/1$, the air filling factor is 24%. The group index, n_g is calculated and plotted in the same figure, which confirms that at the W_1 mode band-edge ($k = 0.5$), the ideal group index n_g turns to infinity.

General speaking, any horizontal flat dispersion band results in infinite group index. Depending on the purpose of the application, different slow light bands can be engineered to

fulfil the requirement. For example, for slow light bands where the field maximum is centred in the high- ϵ region (normally dielectrics), various enhanced light-matter interactions can be studied. On the other hand, for slow light bands where the field maximum is centred in the low- ϵ region (commonly air), high sensitivity index sensing applications can be performed.

2.3.3 Active Slow light PhC band-edge lasers

Here, an example of the dispersion of the TM polarised Bloch modes and their group indices for the triangular lattice photonic crystal is given in the Fig. 2.3.2. Here the photonic crystal consists of the circular dielectric pillars (surrounded by air or other low- ϵ material) in planar waveguide. The effective refractive indices used for the high- ϵ pillar and low- ϵ material are $n_{\text{pillar}}/n_{\text{low-}\epsilon} = 3.565/1.6$, the pillar filling factor is 40%. As can be seen in Fig. 2.3.2(a), two complete band gaps exist for TM polarization. All the band-edges (*e.g.*, K1 and Γ_2/Γ_3 state), or saddle singularity (such as M point in the first band at $u = 0.195$), have flat dispersion bands over broad k-vector regions and could result in infinite group index. Detailed slow light regimes are zoomed, and the corresponding slow light states (E_z Field distribution, modulus) are calculated with PWE as shown in Figs. 2.3.2(b) and 2.3.2(c).

It was first demonstrated by Dowling *et al.* [66] in 1993 that a 1D photonic band gap structure can be used as an effective approach to the optical gain enhancement. Dowling pointed out that near the band-edge of 1D photonic band gap structure, the photon group velocity approaches zero. This effect implies an exceedingly long optical path length in the structure. If an active medium is present, the optical path length increase near the photonic band-edge can lead to a significant enhancement of the optical gain. Nojima *et al.* reported similar optical-gain-enhancement effects in 2D PhC with active gain medium [67-71]. This optical-gain-enhancement is shown to occur in the vicinity of every photonic band-edge. The optical-gain-enhancement factor is uniquely determined by the product of the time for light to pass a gain rod and the confinement factor of the field energy in the gain rod, irrespective of the choice of dielectric constants, wave numbers, band indices, and polarization directions of light. It has been pointed out that in designing photonic crystals lasers, more gently sloped bands and a larger index contrast between gain and background materials are essential. This is because the former leads to a larger group index, and the latter contributes to a better confinement.

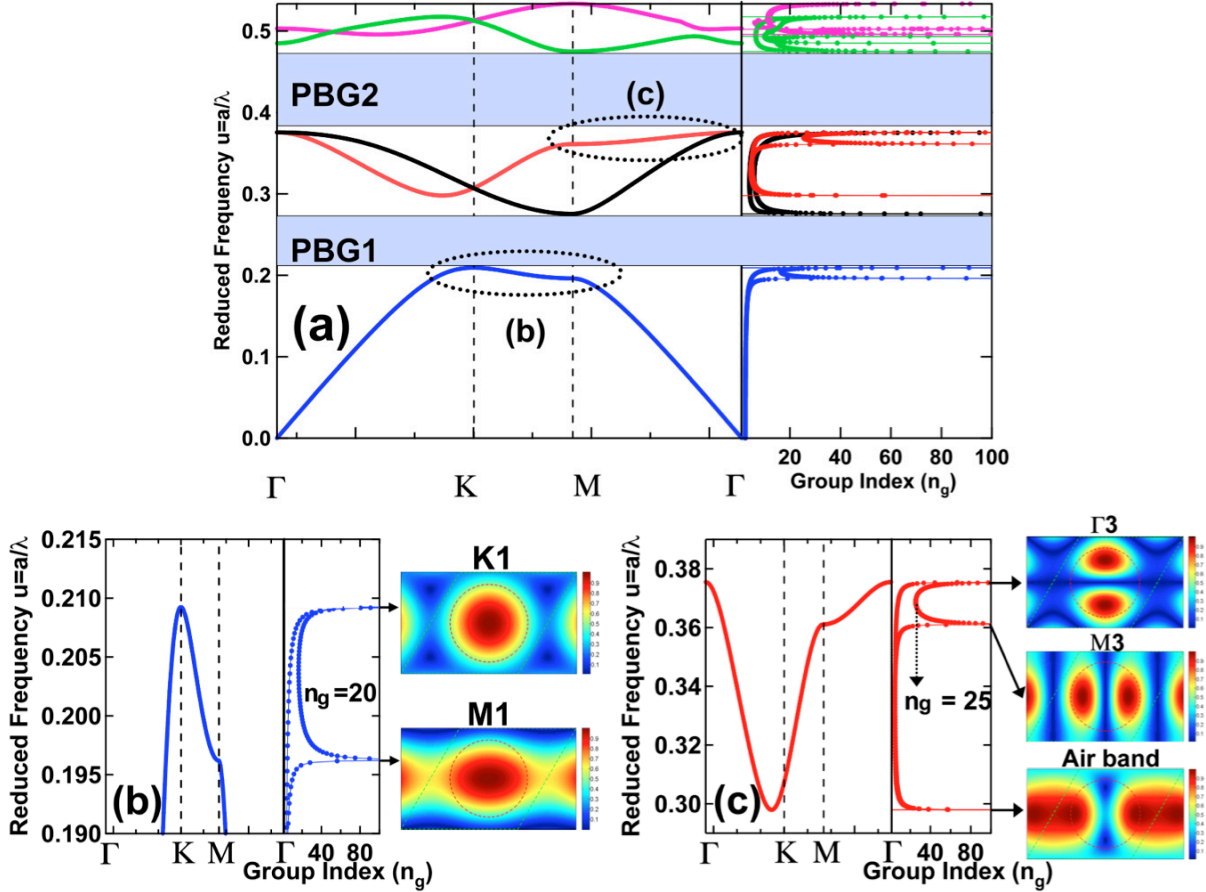


Fig. 2.3.2. (a), left: Full dispersion bands of bulk pillar-type PhCs. PWE is used to calculate the TM polarised dispersion with $n_{high}/n_{low} = 3.565/1$ at $ff = 40\%$. Dashed circle regions are zoomed in details in (b) and (c). Complete 2D band gaps of PBG1 and PBG2 are presented by the semi-transparent blue shadows. Right: Plot of group indices of different modes. (b), zoomed detail of the first band and its group index plot. Between the KM path, the minimum group index is 20, the infinite group index states are K_1 and M_1 as shown in the inserted E_z field distributions. (c), zoomed detail of the third band and its group index plot. Between the $M\Gamma$ path, the minimum group index is 25. The infinite group index states are Γ_3 , M_3 and an air band as shown in the inserted E_z field distributions.

In our case, the optical gain in the pillars is assumed to be created by current injection or optical pumping of all lattice points homogeneously. At the band-edges such as Γ , K or saddle point M , standing waves are formed by the superposition of reflected waves originating from the periodic index variation. Therefore, near these symmetry points, the group velocity (v_g) of the wave approaches to zero, meanwhile the density of photon states and the group index approaches infinity. If the group velocity becomes very slow, photons would have much longer time to interact with the active medium and experiment the enhanced effective gain that proportional to the product of the group index and the confinement factor of the field energy in the gain rod [66].

Therefore, for the first band, the M1 and K1 states in Fig. 2.3.2(b) are all good candidates for lasing due to their high n_g and large mode/pillar overlap. For the third band, the Γ 3 and M3 states in Fig. 2.3.2(b) are both good candidates for lasing due to the same reason. However, the air band state at $u = 0.30$ will not lead to a lasing mode despite its high n_g , this is due to its mode is not confined in the gain rod. Experimental results of such investigation based on slow light PhC lasers will be given in detail in Chapter 6.

Chapter 3

3. Fabrication Techniques

Under the research scope of this PhD thesis, one goal is to investigate and establish a fabrication platform (based on the EBL system in EPFL) of near in-far-red (NIR) passive photonic crystal devices for the group. Another goal is to develop the PhC THz QC lasers based on slow light effects. During the course of the PhD, nearly a third of the time was devoted to the build up of the EBL and optimization of fabrication processes. On one hand, this was motivated by the need to build the fabrication platform for the NIR passive devices, and to fulfill the missing chain: to enable modeling, design, fabrication and characterization of NIR passive structures to be performed locally in EPFL. An EBL system was purchased by the Center of Micronanotechnology (CMI) at EPFL 1 year after the starting of the PhD, therefore I was initially involved in testing the system as the first PhD student. And then continuously, I contributed to the development and establishment of high quality Si ICP dry etching procedures as well as the Si membrane wet etching procedures. On the other hand, I contributed on the continuous development and optimization of BCB planarization technique on pillar type PhC QC material.

The quality of the fabricated devices is vital to the final experimental results. However the fabrication imperfections cannot be completely eliminated but need to be understood, reduced and properly managed, therefore careful and multiple optimizations on the fabrication processes are carried to achieve the desired performance. The minimum feature size (so called critical dimensions, abbreviated as CDs) that are required for NIR PhC passive devices can reach a range as low as the tens of nanometers, therefore Electron Beam Lithography, a technique with the ability to achieve 1.25 nm resolution is the best choice. However for THz PhC active devices, we are dealing with extremely long operation wavelengths ($80 \mu\text{m} < \lambda < 200 \mu\text{m}$), the corresponding CD in this case is in the range of tens of micrometers. Such requirement can be fulfilled easily by the standard photolithography (PL). Due to the material system differences and above-mentioned CD differences, the fabrication techniques of NIR photonic crystal devices are completely different from THz photonic crystal lasers, and they will be explained separately.

In this chapter, the techniques that are employed for the fabrication of both near NIR passive photonic crystal devices and active THz photonic crystal devices will be described. This chapter consists in 4 sections. Section 3.1 starts to introduce the general principles behind the standard micro-nano fabrication processes, including the history of the micro-nano technology,

the lithography tools, and the working principles of different resins. Then, in Section 3.2, the material systems used for the investigation of slow light PhC devices are explained. Section 3.3 explains the process steps of the NIR PhC devices in detail. Finally, in Section 3.4, the detailed fabrication techniques for photonic crystal quantum cascade laser will be explained.

3.1 General fabrication principle for semiconductor fabrication.

After dominating the electronics industry for decades, silicon is on the verge of becoming the material of choice for the photonics industry: the traditional stronghold of III–V semiconductors. The pioneering works of the silicon photonics can be traced back to the late 1980s and early 1990s, when Soref and Petermann reported on Si waveguides at telecommunication wavelengths [72-75]. This early work stimulated activities that resulted in substantial progress, mostly in passive devices, in the 1990s [75-80]. Silicon photonic devices can be made using existing semiconductor fabrication techniques. Because silicon is already used as the substrate for most integrated circuits, it is possible to create hybrid devices in which the optical and electronic components are integrated onto a single microchip [81].

The driving force of the development on silicon photonics is its compatibility with the mature silicon integrated circuit (IC) manufacturing. Creating low-cost photonics for mass-market applications by exploiting the mighty IC industry has been the traditional motivation for the research of the silicon photonics. Another motivation is the availability of high-quality Silicon-on-Insulator (SOI) wafers, an ideal platform for creating planar waveguide circuits. The strong optical confinement offered by the high index contrast between silicon ($n = 3.45$) and SiO_2 ($n = 1.45$) makes it possible to scale photonic devices to the scale of sub-micrometer level. Such lateral and vertical dimensions are required for true compatibility with IC processing. Here we will briefly review the full IC fabrication process to understand how semiconductors are made, or even more specifically, how a photonic crystal structure is fabricated. The IC manufacturing process can be divided into three phases [82]: the Design/Mask creation, the Front-end processing (Wafer fabrication) and the Back-end processing (Assembly and testing).

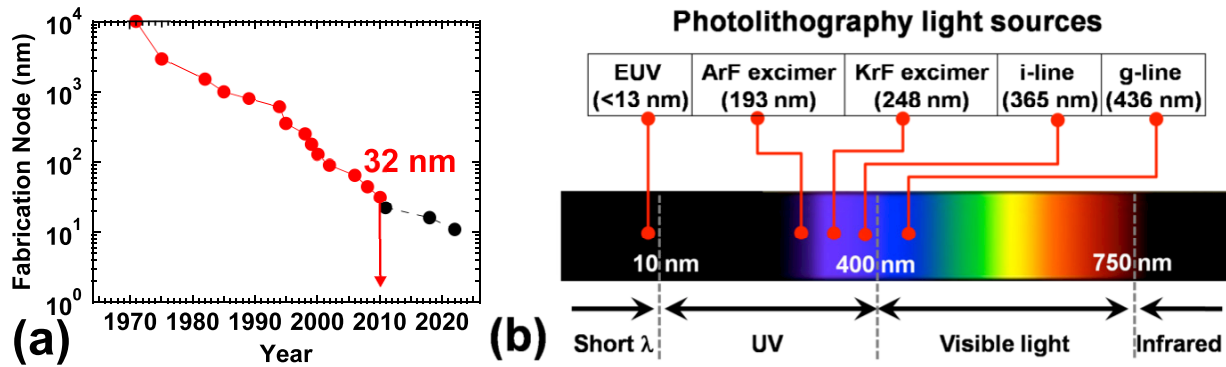


Fig. 3.1.1. (a). Roadmap of minimum resolution for semiconductor fabrication process. (b). Photolithography light sources.

In 1965, Gordon Moore described a long-term trend in the history of computing hardware, in which the number of transistors that can be placed inexpensively on an integrated circuit has doubled approximately every 20 months [83]. A Roadmap of minimum resolution for semiconductor fabrication process is shown in Fig. 3.1.1(a). The main technical driving force behind is the **stepper**, which is the key equipment in the **photolithography**. Previous generations of photolithographic equipment used to expose the entire wafer at once: a stepper, working on a limited area, is capable of higher resolution. The image is focused and reduced by a high NA lens, and projected onto the surface of a silicon wafer that is coated with photoresist which is photosensitive. When the wafer is processed in the stepper, the pattern on the mask is exposed repeatedly across the surface of the wafer in a grid. The stepper gets its name from the fact that it "steps" the wafer from one shot location to another.

Historically, photolithography had used ultraviolet (UV) light from gas-discharge lamps using mercury (Hg), sometimes in combination with noble gases such as xenon (Xe). The initial UV "g-line" (436 nm) of the mercury lamps was used to create lines in the 750 nm range in steppers, as shown in Fig. 3.1.1(b). Several years later systems employed the "h-line" (405 nm) from mercury lamps and then shifted to "i-line" (365 nm) from mercury lamps in the late 80s to create lines as narrow as its wavelength: 350 nm. As the desired line widths approached and eventually became narrower than the wavelength of the light used to create them, a variety of resolution enhancement techniques were developed to make this possible, such as phase shifting mask and various techniques for manipulating the angles of the exposure light in order to maximize the resolving power of the lens. The semiconductor industry then moved towards deep UV (DUV) steppers that employ krypton-fluoride (KrF) excimer lasers producing 248 nm light. Such systems are currently being used to produce lines in the 110 nm range. Lines as low as 32 nm are being resolved by steppers with argon-fluoride (ArF) excimer lasers at a wavelength of 193 nm. Further reduction in the source wavelength (*e.g.*, fluoride (F_2) produces 157 nm light)

are not practical due to their low power and because they quickly degrade the materials used to make the lenses in the stepper.

However, in order to delay as long as possible the vast expense and difficulty of adopting a whole new type of illumination technology, manufacturers have turned to a technique, previously used in microscopes, for increasing the numerical aperture of the lens by allowing the light to pass through water instead of air. This method, called **immersion lithography**, is the current cutting edge of practical production technology. It works because numerical aperture is a function of the maximum angle of light that can enter the lens and the refractive index of the medium through which the light passes. When highly purified liquid (normally water) is employed as the medium, it greatly increases numerical aperture, since it has a refractive index of 1.44 at 193nm, while air has an index of 1. It is being applied to the 45 nm and 32 nm nodes. Several companies, including IBM, Intel and TSMC, have prepared for the continued use of current lithography, using double patterning, for the 22 nm and 16 nm nodes, and extending double patterning beyond 11 nm.

Ultimately, other sources of illumination will have to be put to use, referred as **next-generation lithography (NGL)** [84, 85] for the semiconductor industry. Such as Extreme Ultraviolet Lithography (EUVL) [86], X-ray Lithography [87], Electron Beam Lithography (EBL), Focused Ion Beam lithography (FIB), and Nanoimprint lithography (NIL). NIL is limited mainly by the throughput, while X-ray lithography is limited by implementation and operation costs. Finally, EUVL seems to be the winner in this competition [88-91]. Using the 13.5 nm light source, EUVL systems have the potential to reduce the resolution to below 10 nm. The ultrahigh resolution (1.25 nm) EBL is the method of choice for our research purpose. Detail of the EBL operation will be given in section 3.3.

There are two types of photoresist: positive and negative. For positive resists, the resist is exposed with UV light wherever the underlying material is to be removed. In these resists, exposure to the UV light changes the chemical structure of the resist so that it becomes more soluble in the developer. The exposed resist is then washed away by the developer solution, leaving windows of the bare underlying material. In other words, "whatever shows, goes." The mask, therefore, contains an exact copy of the pattern which is to remain on the wafer.

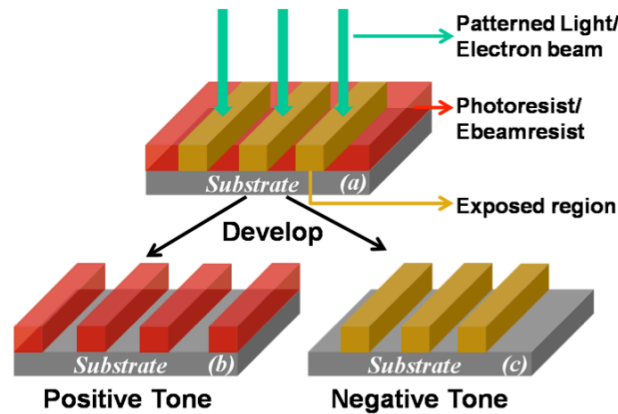


Fig. 3.1.2. Working principle of positive and negative tone resist (for both photo and Ebeam resist).

Negative resists behave in just the opposite manner. Exposure to the UV light causes the negative resist to become polymerized, and more difficult to dissolve. Therefore, the negative resist remains on the surface wherever it is exposed, and the developer solution removes only the unexposed portions. Masks used for negative photoresists, therefore, contain the inverse (or photographic "negative") of the pattern to be transferred. Fig. 3.1.5 shows the pattern differences generated from the use of positive and negative resist. For EBL, Ebeam resist is sensitive to the electron beam exposure and works the same principle as the photoresist.

After reviewing the modern IC manufacturing technology, I would like to focus on the specific fabrication techniques that developed during the past 4 years for the NIR slow light photonic crystal devices. The lithography tool is based on the high resolution EBL system.

3.2 The materials needed for NIR PhC devices.

3.2.1 Silicon on Insulator (SOI)

For the passive NIR photonic crystal devices, two types of material systems were used throughout this work, they are Silicon-on-Insulator (SOI) and Indium Phosphide (InP), GaAs is also commonly used but was not in this work. The SOI wafers were purchased from SOITEC and the InP wafers were obtained through collaboration with LPN-CNRS in France. The SOI wafers are produced with the 'Smart Cut' technique [92-94], which is based on Hydrogen implantation, wafer bonding and atomic level splitting. Ion implantation weakens the silicon crystal at the desired depth. This acts as an atomic scalpel, lifting off a thin layer from the donor substrate and placing it onto a new base wafer of your choice.

The 200 mm diameter SOI wafers used here consist in 3 layers, from the top to the bottom there are: the silicon core layer has a normal thickness of 220 nm with a tolerance of ± 3 nm;

the BOX buffer layer has a normal thickness of $2\ \mu\text{m}$; and the supporting base silicon substrate with a thickness of $\sim 700\ \mu\text{m}$. The PhC designs will be patterned on the top silicon layer only, which acts as the guiding core of the waveguide. Both SOI waveguides and Si Membrane waveguides are used with Air/Si/SiO₂ or Air/Si/Air configurations, respectively. In the later case, Si membrane waveguides are obtained by removing the buffering BOX layer. It is necessary to mention that the SOI wafers are mechanically back polished down to $200\ \mu\text{m}$ thick, in order to improve the cleavage quality.



Fig. 3.2.1. SOI wafer cross section.

3.2.2 SOI thickness variation

For the Si core layer, it is known that there is a couple of nanometers thickness variation from the supplier's document. However, the dimensions of the PhC layout are always less than $1 \times 1\ \text{cm}^2$, therefore we need to dice the entire SOI wafer into small pieces, such as $1 \times 1.4\ \text{cm}^2$. Such dimension is chosen for easy mounting of the sample on the piece-part EBL holder. Assuming that the waveguide width is constant, and the Si core layer thickness is varied, the effect index for the fundamental mode will still be affected. Such change should be avoided, in particular for the slow light structures.

A specific example is: 1 nm thickness variation in a 500 nm wide ridge waveguide can cause the effective refractive index change of the fundamental TE mode by as large as 0.2%. Such variation could destroy the optical design (*e.g.* slow light design) completely and make the device useless. Therefore it is important to know exactly and accurately the real core layer thickness variation for the piece selected for fabrication. All the following Si processes are performed in EPFL's center of micronanotechnology (CMI).

In order to measure the thickness variation on multilayer structures of our SOI wafer, a technique that combines both spectroscopic ellipsometer [95-97] and spectro-reflectometer [98] is used. Due to the slow operation mode of the SOPRA GES 5E Spectroscopic ellipsometer (one detected point needs approximately half an hour to obtain the desired thickness parameter), we used it first to measure the SiO₂ BOX thickness. Then we fixed this BOX thickness parameter in the NANOSPEC 6100 spectro-reflectometer, which is a fast tool to do a complete mapping of thickness measurement on the 200 mm SOI wafer.

The measurement was performed with 360 individual detection points. It presents a full

mapping of the Si core layer thickness on the 200 mm diameter SOI wafer as plotted in Fig. 3.2.2. It is found that the thickness change is not a linear function across the entire wafer. Instead, concentric circles with quasi-sine shape can be expressed for the thickness variation. This may take place during the sliding process from the manufacture. The average thickness is found to be 221.99 nm (presented by light green color), which is 2 nm thicker than the specification. However, the largest variation is found around the wafer borders (presented by pink, red, and browns colors), which counts 7 nm changes in the total 9.2 nm variation.

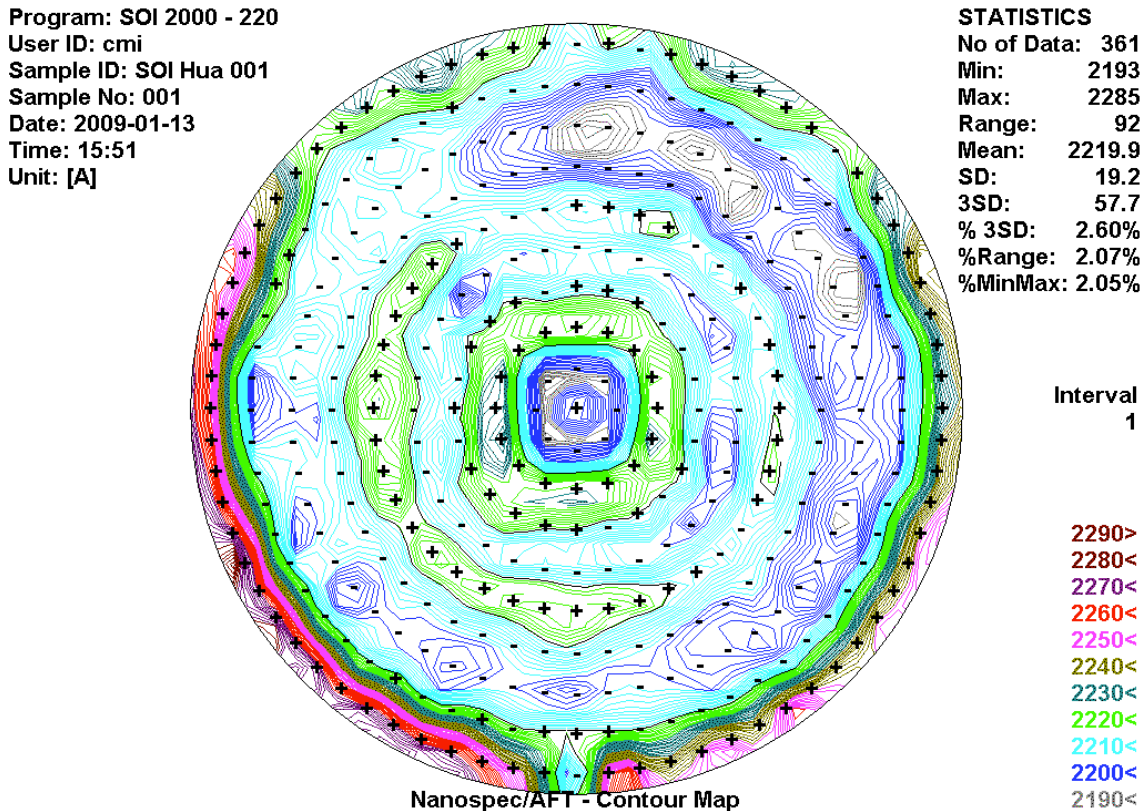


Fig. 3.2.2. SOI surface smoothness mapping.

After the SOI wafer mapping, we used the Disco DAD321, an automatic dicing saw [99] is used to cut the 200 mm wafer into $1 \times 1.4 \text{ cm}^2$ as mentioned before for further EBL patterning purpose. This dicing machine is also used to cut the fabricated photomask that will be mentioned in Section 3.4.2.1. The samples are then carefully selected regarding the thickness mapping results with minimum thickness variation, and then backside (Si substrate) polished down to 200 μm for easy cleavage purpose (performed with the help of Hans Jörg Buehlmann).

3.2.3 Indium phosphide (InP)

Some of our research works on slow light Photonic crystal waveguides were based InP wafers, which were obtained within the framework of a collaboration with Dr. Anne Talneau in Laboratory for Photonics and Nanostructures (LPN), National Center for Scientific Research

(CNRS), France. The 2 inches InP material system also consists in 3 layers as shown in Fig. 3.2.3. The optical structure is similar but the material are very different and processing has to be completely redeveloped. From the top to the bottom there are: a 260 nm thick InP guiding layer is grown on top of a 1.5 μm $\text{In}_y\text{Ga}_{1-y}\text{As}$ sacrificial layer, on an InP substrate with $\sim 500 \mu\text{m}$ thickness. The PhC designs will be patterned only on the top InP layer, which acts as the guiding core of the waveguide. InP membrane waveguides are obtained by removing the $\text{In}_y\text{Ga}_{1-y}\text{As}$ sacrificial layer.



Fig. 3.2.3. InP wafer cross section.

3.3 Process Steps for NIR passive PhC devices

3.3.1 EBL system in EPFL (Hardware)

The fabrication procedures used for different material systems are all based on Electron Beam Lithography. I performed the EBL patterning jobs for all the results presented in this thesis, using a Vistech EBPG 5000+ES Electron Beam writing system in EPFL [100]. An EBL system uses a small electron beam spot (**Beam size**) that is moved with respect to the wafer to create a pattern in an electron sensitive resist on the wafer one pixel at a time. The beam is scanned across the wafer using an electromagnetic deflection system. Direct writing systems can be classified as raster scan or vector scan, with either fixed or variable beam geometry. The machine in EPFL uses a vector scan system (as illustrated in Fig. 3.3.2(a)) rather than raster scan system [101, 102], which means the beam is only deflected to the areas where it needs to expose and never to areas where there is nothing to expose.

The advantages of the EBL are resolution, beam placement accuracy and flexibility. The machine allows one to access length scales not practically available with any other lithography technique. It also allows overlying different levels of lithography very accurately $<20 \text{ nm}$. The pattern is defined only as a software mask, which means it is very easy to change designs without having to make a new mask. The disadvantage is that it is slow compared to photolithography. This is because EBL is inherently a sequential process; with the pattern having to be exposed 1 pixel at a time. A schematic drawing of the EBL system is plotted in Fig. 3.3.1.

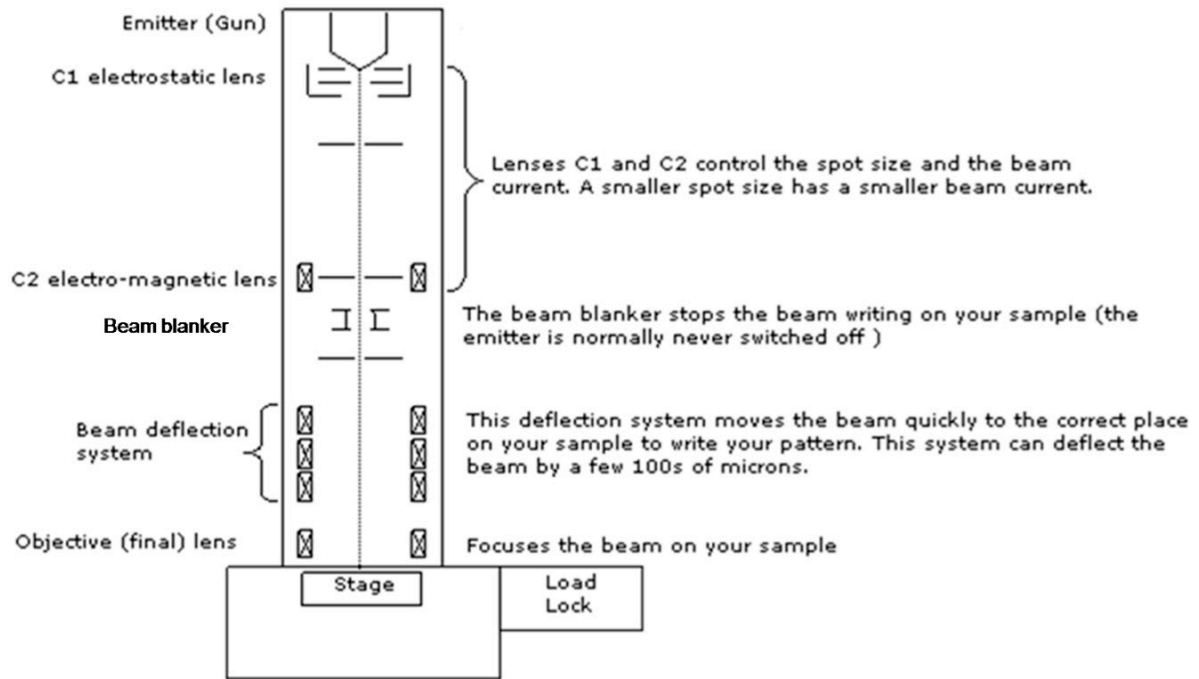


Fig. 3.3.1. Schematic drawing of the EBL system. (Reprint from Ref. [103]).

The key features of our EBPB 5000+ES system are listed as follow:

- 20 to 100 keV Thermal Field Emission Gun
- High Resolution Gaussian Beam System
- 50 MHz Intelligent Pattern Generator
- 1.25 nm minimum pixel size
- Robust Direct Write Mark Detection & Alignment Software
- 2 position load lock for batch processing of multiple substrates
- Holders for 50 mm, 100 mm, 150 mm wafers and smaller piece parts
- Housed in a class 100 cleanroom which maintains a temperature of $21^{\circ}\text{C} \pm 0.1^{\circ}\text{C}$

An Ebeam system writes on the sample by deflecting the electron beam with a set of electromagnetic deflection coils. These coils can only deflect the beam by a few hundreds of microns. To make larger patterns on a wafer, once the deflection reaches this maximum value, the stage then has to be moved to start writing the next bit. The machine will always finish writing a block before moving the stage because deflecting the beam electronically is fast, whereas moving the stage is relatively slow. The maximum area that can be written without moving the stage is called the **block size**. This varies depending on how the machine is configured; at 100 keV Ebeam acceleration condition our machine can deflect the beam up to a maximum of $256\ \mu\text{m}$. When the stage is moved to continue the writing, the matching together of the two writing blocks is called **stitching** [104]. If the machine is calibrated correctly the machine should stitch the writing blocks together almost perfectly. Fig. 3.3.2(b) shows the

border between 2 blocks of writing. The stitching error in aligning the 2 blocks is <10 nm. Typically our machine stitches the blocks (fields) together with an accuracy of 18 nm [103].

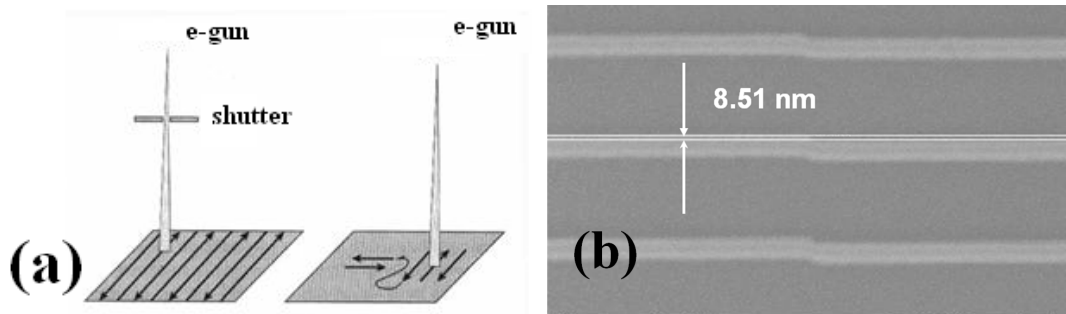


Fig. 3.3.2. (a) A comparison of scanning methodologies of EBL systems; raster scan (left) and vector scan (right). (b) SEM image of the stitching error [103].

The **resolution** of an EBL machine defines the distance where the minimum two pixels can be written. The **Beamstepsize** (BSS = trapezium deflection resolution \times multiple stepping factor (MSF)) is the distance between two adjacent pixels and defines the writing accuracy. By default it equals the resolution, however it can be set to be integer number of the resolution. To achieve a clear exposure, the beam size is ranged from 4.5 nm to 20 nm for beam current ranging from 100 pA to 40 nA, as can be seen from Table 3.3.1 and Fig. 3.3.3.

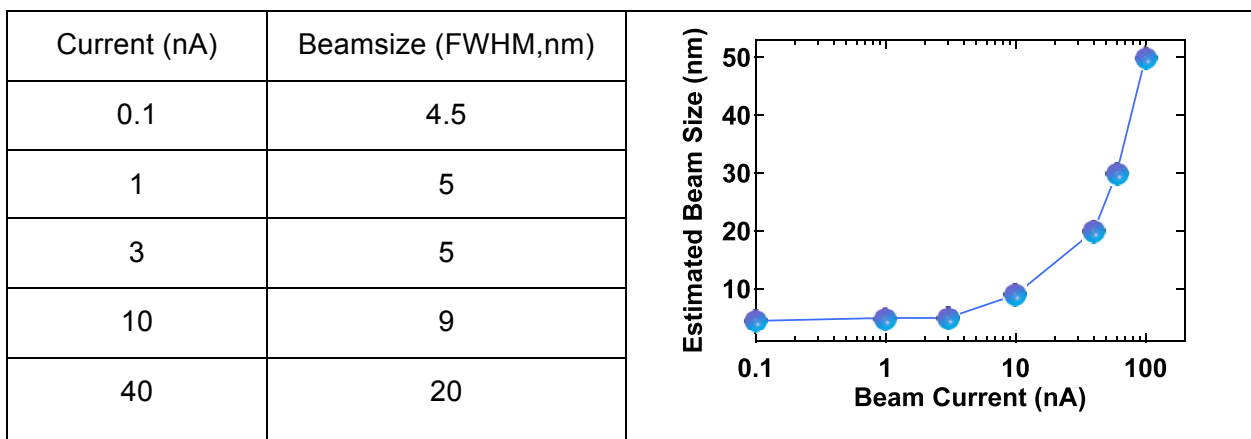


Table 3.3.1. and Fig. 3.3.3. Vistech EBPG Ebeam system beam current and beam size correlation.

On our EBPG5000 the minimum step size is 1.25 nm and can be varied continuously after that. The **writing frequency (F)** is the frequency with which the beam is stepped from one pixel to another when writing a pattern and can vary from 0.5 kHz to 50 MHz. The higher frequency, the faster writing speed. It is calculated from the measured beam current, the resolution and the proper dose:

$$F[\text{MHz}] = 0.1 \times \frac{\text{Current}[\text{nA}]}{\text{Dose}[\frac{\mu\text{C}}{\text{cm}^2}] \times \text{BSS}^2[\mu\text{m}]} \quad (3.2.4)$$

Dose can be calculated by rearranging this formula:

$$\text{Dose}[\frac{\mu\text{C}}{\text{cm}^2}] = 0.1 \times \frac{\text{Current}[\text{nA}]}{F[\text{MHz}] \times \text{BSS}^2[\mu\text{m}]} \quad (3.2.5)$$

Note that the units in brackets correspond to the units of the numbers entered into this formula. The answers will then be in either MHz or $\mu\text{C}/\text{cm}^2$ which are the normal units for used in EBL.

3.3.2 Data processing and CATS (Software)

Data processing is needed prior to the sample processing. A complete data process flow chart is plotted in Fig. 3.3.4. Here we use **L-Edit** to design the standard GDSII (acronym for Graphic Database System II stream format) mask, and then use Raith/CleWin to verify the design. CATS (Computer Aided Transcription System) is used to fracture the data. During the fracturation, all the necessary parameters needed for EBL are entered, *e.g.*, resolution, BSS, layer information as well as data type. After the data fracturation, either Unix based scripts or **Cjob** (a graphical user interface to generate the scripts) is used to generate a job file that defines the expose parameters on the wafer. As a last step, the EBPG runs this job and start the pattern exposure.

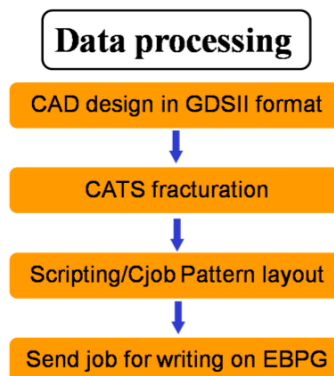


Fig. 3.3.4. Data process flow chart for EBL system.

3.3.3 Deeper understanding of CATS in EBPG.

In EBPG system, a CATS **flat** file contains rectangles, trapezoids, arrayed rectangles and arrayed trapezoids, each of which can be as large as the block size. However, an EBPG can only write so-called elementary shapes whose sizes are determined by the trapezoid field. The process of fracturing large rectangles and trapezoids into elementary shapes is often referred to as final

fracturing. It occurs during **WRITEFILE**. It is also viewable in CATS without making the target file; CATS shows the exact shapes in the target format.

An EBPB uses two deflection systems; one moves the beam from one shape to the other (main deflection), and the second (trapezium deflection) writes the actual shape. The fields are referred as main field and trapezium field, respectively. A large pattern is normally divided into several main fields, therefore the substrate has to move for each next main field (as shown in Fig. 3.3.5(a) where stitching error occurs). The Ebeam is centered in the main field with center height compensation, and the deflection is calibrated to the state movement and the height. In the trapezium field the beam is moved with the trapezium deflection without substrate movement. CATS will always use the maximum trapezoid field size during the final fracturing in order to minimize the number of final shapes.

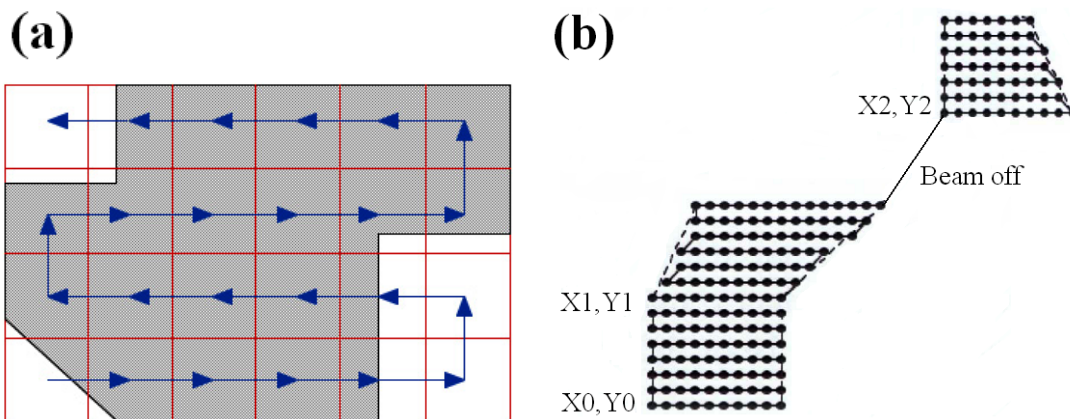


Fig. 3.3.5. (a). Meander style write order of main field. (b). Trapezium wise beam stepping in main field. Here each (x_i, y_i) is a new start of a new trapezium.

Older formats require users to choose between using the trapezium deflection unit or main deflection unit to fracture data, and to specify the desired MSF value. The EBPB5000 brought a simpler method of selecting a resolution that separated the main and trapezium deflections, allowing users to specify the actual writing resolution. Actual writing resolution is used to fracture all data. CATS can automatically select the deflection units and MSF values to obtain maximum block size. However, both the main deflection resolution and trapezium deflection resolution can be chosen with smaller values that differ from CATS, thus smaller blocksize and trapezium field size in order to have less field distortion. CATS will check if the specified main deflection resolution or trapezium deflection resolution can be used to realize the specified resolution, if not a message will be given and the request will be denied. In some other EBL systems, CATS may support the main field and subfield format, instead of trapezium field.

After CATS fracturation, the input GDSII file is reconfigured to GPF (acronym for Generic Pattern Format) file. The GPF explicitly sets the parameters for creating files used for

fracture. In most situations, the GPF commands are not needed. One can simply set the resolution and beamstepsize, and CATS will use the correct settings. The typical resolution range is 1.25 nm to 2 μm , depending on the selected resolution. The main and trapezium field resolution are calculated, where the mainResolution is approximated by:

$$\text{MainResolution} = \text{resolution} / \mathbf{m}$$

and the trapezium field resolution is given by:

$$\text{TrapResolution} = \text{beamstepsize} / \mathbf{n}$$

m and **n** are the number of main bits and number of sub bits. A detailed example is given in Table 3.3.2, which compares different parameters of the same pattern after CATS fracturation with different resolutions.

Actual Res	1.25 nm	2.5 nm	5 nm	100 nm
BeamStepSize	1.25 nm	2.5 nm	5 nm	100 nm
MainRes	1.25 nm	2.5 nm	5 nm	7.692308 nm
m	1	1	1	13
TrapRes	0.416667 nm	0.416667 nm	0.454545 nm	0.487805 nm
n	3	6	11	205
max main field size	81.920 μm	163.840 μm	256.000 μm	256.000 μm
max trapezium size	4.525 μm	4.525 μm	4.525 μm	4.524878 μm

Table 3.3.2. CATS fracturation parameters with different resolutions for same pattern.

The attempt is made to minimize the m and n as much as possible. The maximum field sizes for main and trapezium fields are derived from these resolutions. These are typically $2^{\text{nrbits}} - 1$. For example, if you have a 10 nm main resolution, this would result in a $(2^{16} - 1) * 10 \text{ nm} = 655.35 \mu\text{m}$.

If we modify the resolution or the beamstepsize, the mainResolution and trapResolution changes. If one of the mainResolution, trapResolution, or hightension changes, the corresponding field size may also change. CATS attempts to maximize the main and trapezium field resolution, and thus the main and trapezium field size. However, for certain resolutions, other combinations are possible that might be more suitable for the data.

No proximity correction was used, this is because the extremely high electron acceleration voltage (100 keV) penetrates more than 100 μm thick into substrate and causes negligible proximately effect [105].

The deep understanding of these technical points for EBL system is crucial for the achievement of high performance PhC devices, in particularly when the writing patterns are at the limit of the system capability. Careful optimizations of EBL parameters have to be performed in order to maximize both the main field size and the trapezium field size. Otherwise there will

be mainly two large impacts, even if the errors are barely observable by SEM.

The first impact comes from the previously mentioned stitching error, which is the product of limited main field size. The stitching error is normally large (tens of nanometers) and can be observed by SEM (Fig. 3.3.2(b)). If the patterns were written with many main fields, a large ‘residual grating’ will be generated. Such errors introduce large propagation loss to the waveguide due to the large mode mismatch. This problem can be minimized by maximizing the main field size, in another word, by properly choosing the EBL resolution and beam step size.

The second impact comes from a falsely chosen the small trapezium field (or subfield for some other EBeam systems). Such small trapezoidal write subfields can be a problem when the EBeam exposure dosages are low. In this case, ‘small’ residual grids with periodicity identical to the trapezium field size will be generated. Such errors are normally very small (subnanometer) and cannot be observed by SEM. Fig. 3.3.6 shows an example of the impacts from non-optimized EBL procedure which induces residual grids (reprinted from Ref. [106]).

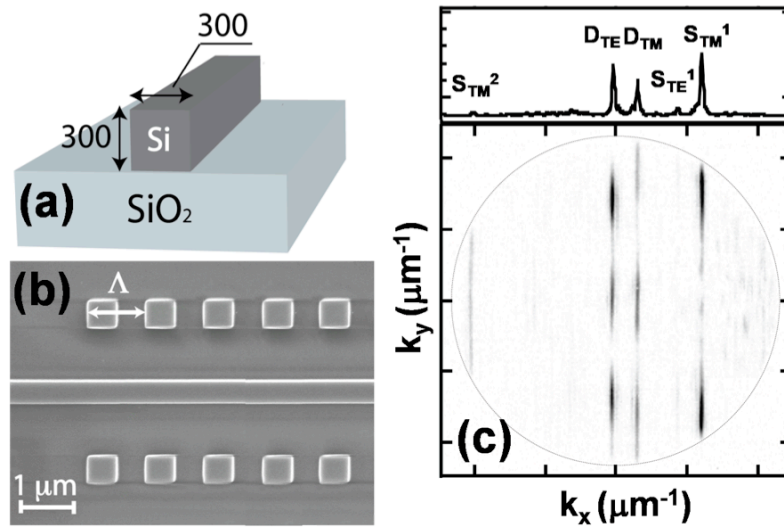


Fig. 3.3.6. (a) Layout of the photonic wire waveguide. (b) SEM image of the photonic wire waveguide with intentional linear grating ($\Lambda = 1 \mu\text{m}$). (c). Optical Fourier space images of the photonic wire waveguide at $\lambda = 1620 \text{ nm}$ (reprinted from Ref. [106]).

Figures 3.3.6(c) shows the optical Fourier space image of light scattered from the 300 nm wide rectangular photonic wire waveguide with 1 μm side grating. The Fourier space image technique will be explained in detail in Chapter 4. The pattern exhibits two groups of sharp straight lines S_{TM}^1 , S_{TE}^1 , S_{TM}^2 , and D_{TE} , D_{TM} . The ‘D’ lines are attributed to the radiated fields of the fundamental TE and TM modes of the wire waveguides scattered by the 1 μm side grating. The spacing between the S_{TM}^1 and S_{TM}^2 is constant when the wavelength is tuned, and it corresponds to a spatial modulation of 1.28 μm that is exactly the dimension of the trapezoidal write subfield pattern used in the EBL process. Therefore, we attribute these ‘S’ lines to the first

and second orders of a small corrugation grating on each sidewall of the wire waveguides resulting from the Ebeam patterning [106]. Such problem can be minimized by maximizing the trapezium field size using the relation between TrapResolution, beamstepsize and number of sub bits in CATS.

3.3.4 CATS Conditional Figure Assignment (CFA)

It is very common to have Ebeam exposure patterns with different Critical Dimensions that require identical resolution, BSS and beam current, but different dosages. For example, if we want to write PMMA (a positive resist) on InP substrate with 1.25 nm resolution, we would like to assign dose of $900 \mu\text{C}/\text{cm}^2$ for the ridge waveguide and $1800 \mu\text{C}/\text{cm}^2$ for photonic crystal waveguide. There are two ways to do it. One is to assign the two patterns with two sets of dosages and to do two CATS fracturations separately, however in this case the machine will calibrate twice according to the reference point hence will introduce definite alignment errors. Another solution is to using the CFA function to expose the two regions on a single batch with different dose assigned to targeted pattern regions.

The CATS Conditional Figure Assignment (CFA) feature attaches a value to figures depending upon various selection rules. The attached value corresponds to the concept of dosage, which varies from machine to machine. Currently, CFA can be used not only for Vistec EBPG formats, but also for Cambridge, Hitachi, JEOL formats. With this CFA function, CATS offers a means for users of vector-scan electron beam systems to assign doses on a figure-by-figure basis. As shown in Fig. 3.3.7, a dose index value is assigned to each figure in the file based on the figure's geometric properties. Figures are sorted into categories corresponding to clock frequencies using a series of CATS select rules. The data containing the dose assignment can be viewed in the Flying CATS Graphics viewport before fracturing. Index numbers are displayed within each figure, and figures of different index values may be drawn in different colors.

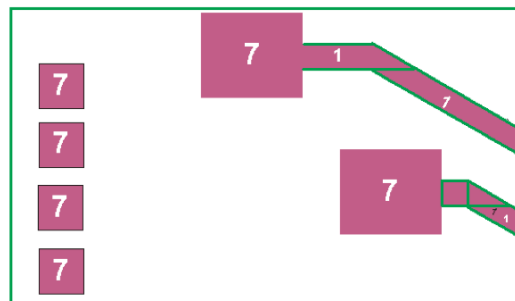


Fig. 3.3.7. Example of CFA Dosage Index numbers. Different index values are assigned depending on the geometrical qualities of the figures.

After a fracture, a CFA number is attached to each figure in the flat file, which also stores

layer and datatype identifiers. The Options menu enables the CFA button for draw mode and color to access these values for immediate feedback during pre-fracture and post-fracture work. To use CFA with CATS or with WRITEFILE/WRITETAPE, the user must create an ASCII file with the extension ".CCFA". This file has one or two parts. The first part is called "Index_Table" and the second is called the "Rule_Selection". For some formats only the second part is necessary. For Leica EBPG formats both parts are required. An example of using CFA to expose PMMA on ICP substrate is shown in Fig. 3.3.8.

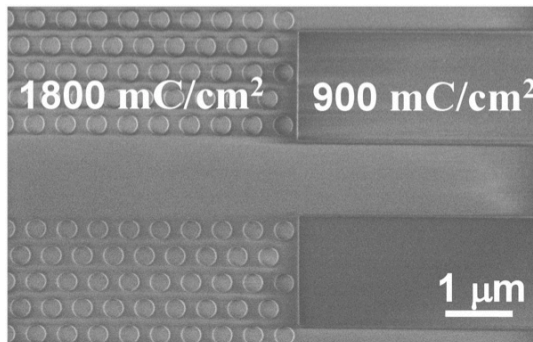


Fig. 3.3.8. SEM image of PMMA resist with PhC pattern. Two different dosages are assigned and exposed at the same time with same resolution.

3.3.5 Sample processing with EBL PMMA on InP and ZEP-520A on SOI

There are a lot of Ebeam resists available, but in the framework of this thesis only two positive tone resists were used: PMMA (poly methyl methacryllate) and ZEP-520A (Based on Styrene Methyl Acrylate). Both PMMA and ZEP-520A have long polymer chains. The chains that are exposed to the Ebeam are cut into shorter pieces (chain scission) which are then more easily dissolved by the developer. Standard PMMA products cover a wide range of film thicknesses and are formulated with 495,000 (495K) & 950,000 (950K) molecular weight resins in either chlorobenzene or the safer solvent anisole [107]. For PMMA, the sidewall profile is normally extremely vertical under high beam energies (100 kV). However the etching selectivity of PMMA is poor when etching is performed with an N_2/BCl_3 plasma (currently used for InP etching), therefore a second hard mask (normally SiO_2 , PMMA is highly selective to this material) is used for the pattern transferring. ZEP-520A can be used mostly as a good dry etch mask for Si, because its resolution as well as dry etching selectivity are higher than PMMA, and it is more sensitive than PMMA (need lower dose) [108]. The process procedures for the ZEP-520A and PMMA are shown in Fig. 3.3.9.

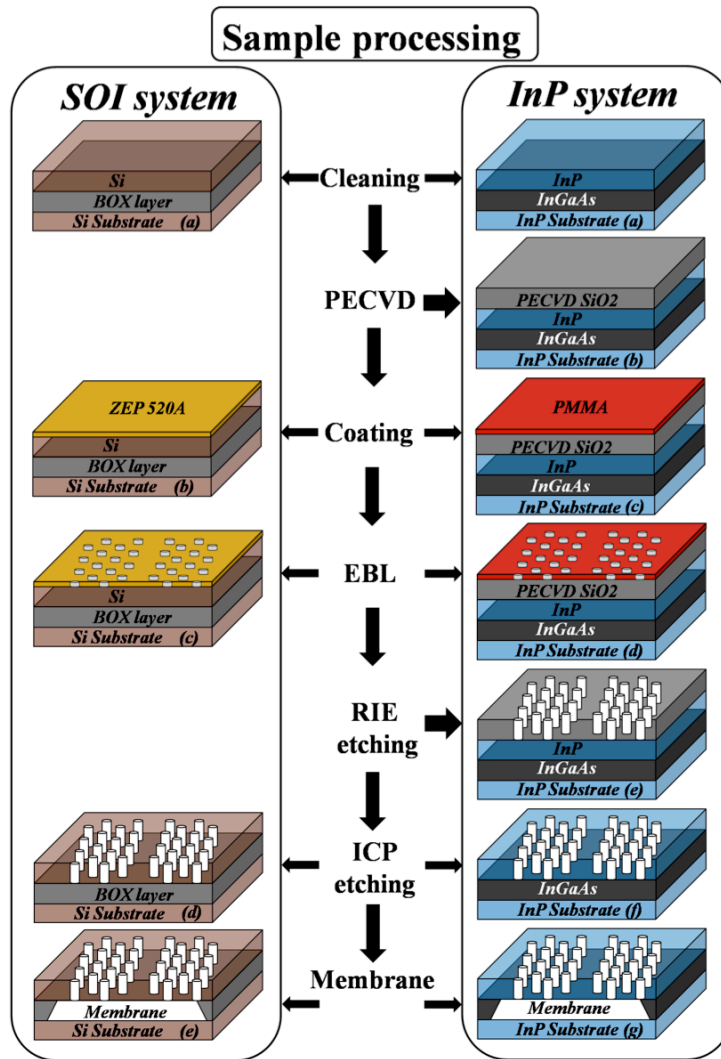


Fig. 3.3.9. Sample fabrication processes flow for SOI (left) and InP (right) systems, respectively.

The process procedures for the ZEP-520A and PMMA are similar therefore they can be compared together in Table 3.3.3. After the standard sample cleaning by Acetone, Methanol and Isopropanol Alcohol (IPA), the sample is blow dried with N_2 flow, and then pre-baked on $115\text{ }^\circ\text{C}$ hotplate for 2 minutes. This step is important as it dehydrates the sample. The sample is then spin-coated with either PMMA or ZEP-520A at 2000 r.p.m. for 30 seconds. The typical film thickness of PMMA or ZEP-520A under such condition is 340nm or 200 nm, respectively. Here sufficient thick resists are chosen in order to etch through the corresponding core layers. The sample is then baked on a $180\text{ }^\circ\text{C}$ hotplate for 3 minutes.

ZEP-520A resist has relatively shorter molecular length compared to PMMA, therefore ZEP-520A resist is highly sensitive to Ebeam exposure and requires an Ebeam dose of $210\text{ }\mu\text{C}/\text{cm}^2$. The PMMA requires 9 times higher dose to achieve a clear exposure ($1800\text{ }\mu\text{C}/\text{cm}^2$). The exposed samples are developed using different developers as detailed in Table 3.3.3. Here MIBK stands for Methyl Isobutyl Ketone. The patterns are divided into high-resolution and

low-resolution layers according to the characteristic feature sizes. Doses as well as exposure currents need to be adjusted according the resolution needed. Removing residues (scum) from a substrate through gentle plasma cleaning is known as **descumming**. The sample will be ready for etching after short time (10-30 s) at low power (30 mW) descumming in O₂ plasma to remove the resist residues after developing.

Tables 3.3.3 shows the detailed preparation, exposure and developing parameters of the two Ebeam resist for the EBPG 5000+ES EBL writing tool.

Sample preparation	Material	InP		SOI	
	Pre-baked on hotplate (seconds/ °C)	120/115		120/115	
	Resist	PMMA 950K A4		ZEP-520A	
	Dilution	4% in Anisole		1:1 with Anisole	
	Hardmask	PECVD SiO ₂		None	
	Spin (rpm/seconds)	2000/30		2000/30	
	Post-baked on hotplate (seconds/ °C)	180/180		180/180	
EBL expose	Parameters	High Res.	Low Res.	High Res.	Low Res.
	Typical structure	holes	waveguides	holes	waveguides
	E- acceleration (keV)	100			
	Resolution (nm)	2.5	100	2.5	100
	Dose (μC/cm ²)	1800	900	210	230
	Beam current (nA)	0.5	200	0.5	200
	Writing field (μm ²)	160×160	256×256	160×160	256×256
Developing	Developer/seconds	1:3 MiBK:IPA/30		n-amyl-acetate/60	
	Rinse/seconds	IPA/30		9:1 MiBK:IPA/30	
	Descumming (seconds)	30		30	

Table 3.3.3. Detailed preparation, exposure and developing parameters of ZEP-520A and PMMA resists for the EBPG 5000+ES EBL tool.

3.3.6 Dry etching of SOI

After the EBL patterning and development, the InP samples were shipped to LPN, CNRS, France for the Inductively coupled Plasma (ICP) dry etching, using N₂/BCl₃ combined gases. Here we will focus only on the optimization of dry etching qualities on SOI performed with ICP in CMI, EPFL. There are three ICP systems available to etch Si in CMI: STS-ICP (short for STS Multiplex ICP), Alcatel 601E and AMS-200 (short for Alcatel AMS 200 DSE). Both STS-ICP and AMS-200 were tested in order to obtain high quality vertical Si sidewall profile. The working principle of all the ICP machines are similar, therefore we plot a global view of the AMS200 processing chamber in Fig. 3.3.10 [109]. Main parts are visible: ICP source, diffusion chamber and Electrostatic Clamping Chuck (ESC). ICP source is made with an antenna

connected to an RF power supply and wrapped around an alumina cylinder. RF power (13.56 MHz and 3 kW maximum) is coupled to the plasma through an inductive mode. The oscillating current in the antenna at 13.56 MHz induces an electromagnetic field (E/B) in the alumina cylinder. For plasma ignition, some primary electrons collect the E/B field energy (ions are too heavy to get the energy from E/B field). Inelastic collisions between hot electrons and neutrals (injected gas mixture) give ions/electrons pairs. This is the way how the main plasma is created inside the cylinder where the gas mixture and pressure are controlled. A coil surrounding the plasma source gives a permanent magnetic field for a better plasma confinement and to avoid wasting too much charged species.

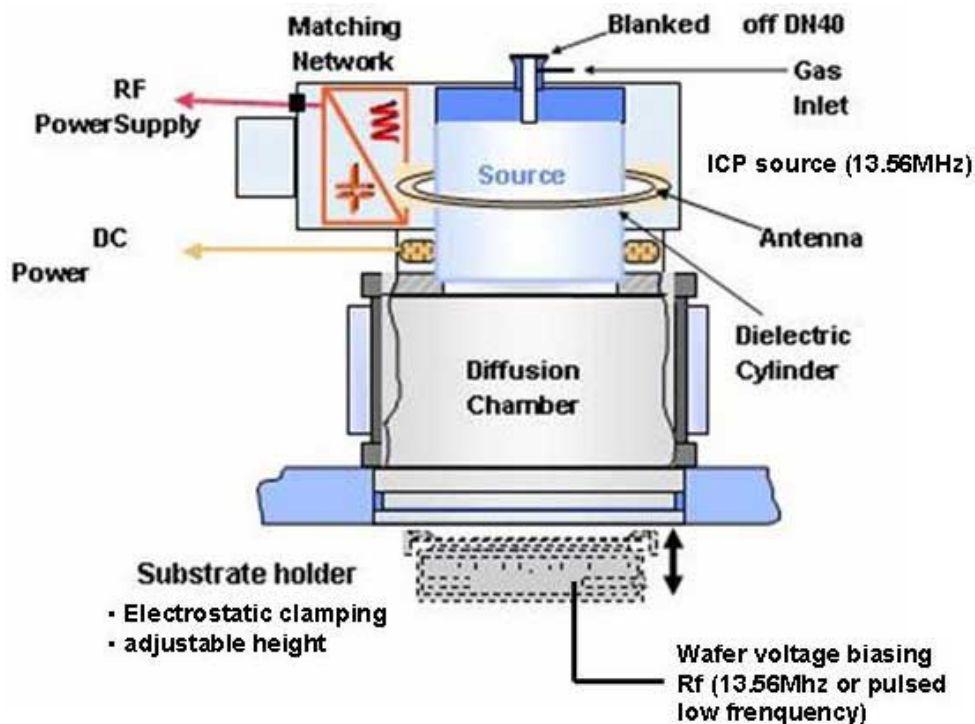


Fig. 3.3.10. AMS200 processing chamber. (reprinted from [109]).

STS-ICP test was performed on 220 nm thick Si layer. Unfortunately, this dry etcher is designated for metal and polymer etching. For the Si etching, only Cl_2 gas can be used. This makes the process a dominate physical bombardment by Cl_2 ions. Hence the etching selectivity is very low (about 1:1), the 200 nm ZEP-520A resist is not thick enough to etch through the entire Si layer. Meanwhile the etching profile shown in Fig. 3.3.11(a) is not vertical due to the absence of isotropic chemical etching components. We also started Si etching test with AMS-200 machine from using the standard **Bosch process** [110-115] with ZEP-520A resist. Note that for the AMS-200, all the test etching samples have a slightly thicker Si core layer (340 nm). The Bosch process, also known as pulsed or time-multiplexed etching, alternates repeatedly with 1 second interval between C_4F_8 and SF_6 in order to achieve very high aspect ratio [109] (upto 50:1) in standard MEMS. However, the etching result (Fig. 3.3.11(b)) was not satisfactory for our PhC

structures on thin Si layer. Within 340 nm thickness, there are three obvious elliptical shapes.

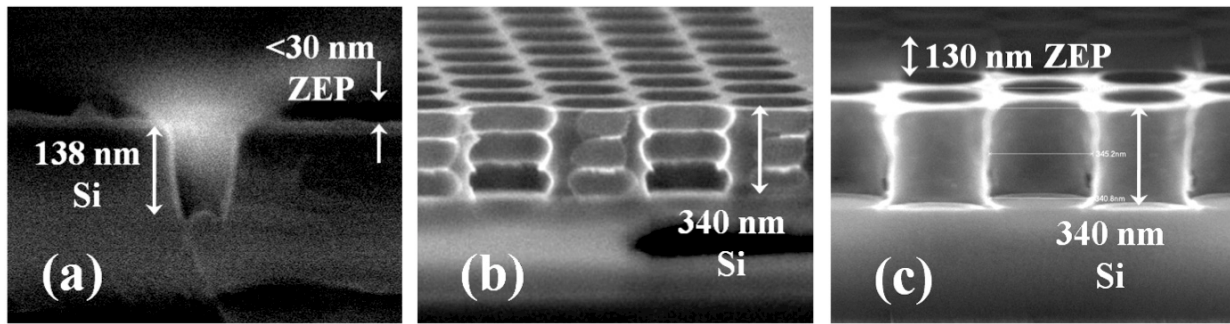


Fig. 3.3.11. (a) Cross section SEM image of Si etching result from STS-ICP machine with standard recipe (21 s). (b) and (c), Cross section SEM images of Si etching results from AMS-200 machine with standard Bosch process recipe (30 s) for (b) and Si-opto-slow recipe (45 s) for (c).

Therefore, we chose a recipe designed for smooth etching by combining C_4F_8 and SF_6 together (40/100 in sccm). During the etch process, the Si sidewalls are coated with polymer from SF_6 dissociation while the bottom of the exposed features are etched by ion bombardment which prevented passivation build up. The result shown in Fig. 3.3.11(c) is still not satisfactory but at least shows improvements. We conclude that the reason for non-vertical sidewall is due to the weak SF_6 dissociation, therefore, further optimization was focused on the role between C_4F_8 dissociation and C_4F_8 passivation.

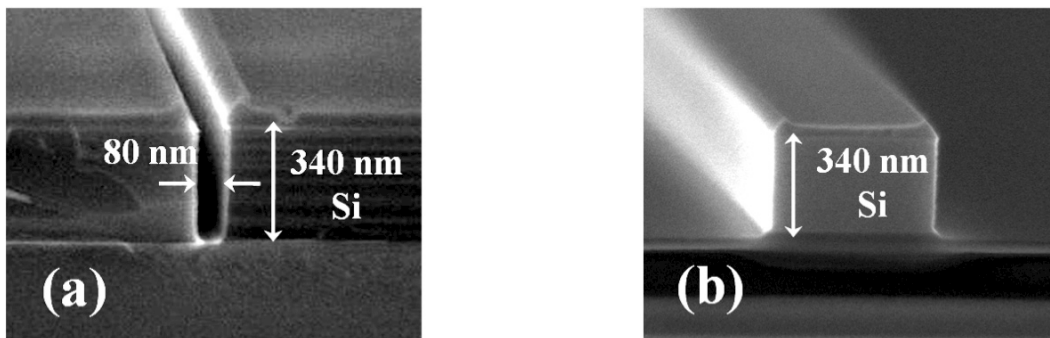


Fig. 3.3.12. (a) and (b), Cross section SEM images of Si etching results from STS-ICP machine with optimized recipe (225 s) for a 80 nm trench in (a), and ridge waveguides in (b).

Finally an optimized Si etching recipe, with SF_6 dissociation and C_4F_8 passivation at a balanced ratio (26/63 in sccm) for AMS-200 machine can achieve vertical sidewall profiles. The etching chamber pressure is to 3×10^{-2} mBar, and the RF generator power is 1500 mW. The etching time is 225 s for the 340 nm thick Si layer. Detailed cross-section profiles of an 80 nm width trench and a ridge waveguide are plotted in Fig. 3.3.12.

3.3.7 Si Membrane wet etching

The sample after ICP dry etching is then prepared for membrane process. By doing this the index contrast can be increased from the SOI case of 1/3.45/1.45 to the Si membrane case of 1/3.45/1, thus increasing the light confinement, and reducing the losses due to the evanescence coupling to the Si substrate via the BOX layer. The detailed fabrication process flow chart is shown in Fig. 3.3.13.

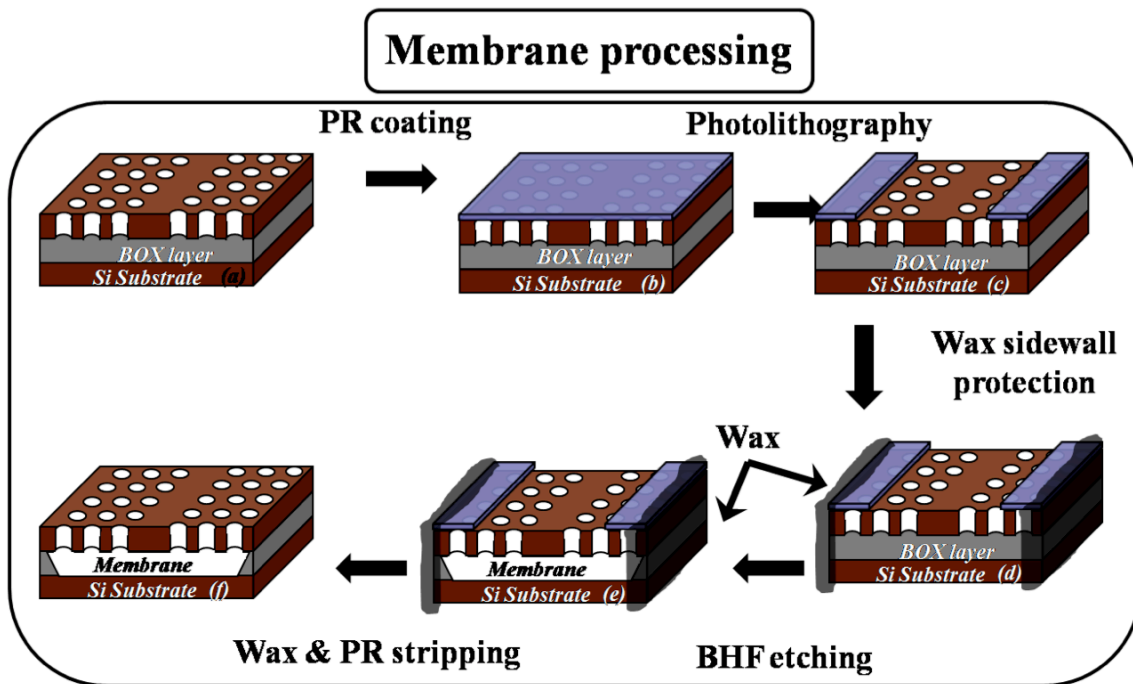


Fig. 3.3.13. Fabrication process flows for Si membrane.

After developing the ICP dry etching recipe for the Si etching, the final step is to develop the Si membrane wet etching recipe. After dry etching the sample is spin-coated with an image-reversible photoresist AZ5214 at 4000 r.p.m for 30 seconds. A 1.4 μm photoresist film is then deposited on top. Standard photolithography is then performed using Suss Microtech MJB3 mask aligner. Here the light source we used is a 350 W multi-wavelength mercury arc lamp and it is calibrated at 20 mW/cm^2 measured h-Line (405 nm). Please note that the lamp emits power at multiple wavelengths, thus the exposure dose should not be judged solely by the 20 mW/cm^2 output at h-Line. An estimation can be obtained by assuming that there is about half dose as i-Line (365 nm) added to the h-Line dose. Thus for this tool a very close estimate would be 30 mW/cm^2 . The patterns are exposed in AZ5214 with chromium mask during 4 seconds. All the chromium masks were fabricated by myself in CMI with the direct writing laser (DWL) tools. The details of the DWL tools will be explained in the Section 3.4.

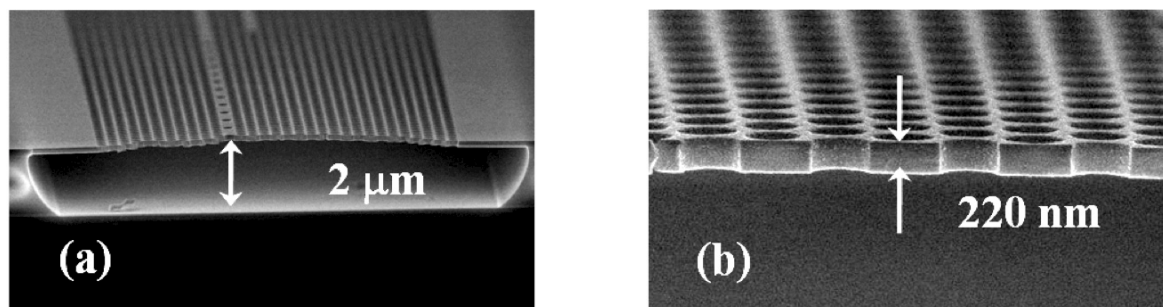


Fig. 3.3.14. Cross-section SEM images of PhC Si membrane structures.

The sample facets are then covered by wax, in order to prevent the wet etching of the waveguide from the wet etching solution. Buffered Hydro fluoride Acid (BHF) is used to selectively wet etch the BOX layer. After 30 minutes, the membrane is completely opened, as shown in the SEM images in Fig. 3.3.14. The etching rate for the BOX SiO₂ in BHF is about 70 nm/min. After the membrane process the sample is cleaned in hot acetone and then dried under hot Isopropanol vapor (called supercritical drying [116, 117]) in order to prevent any strain in the structures caused by water surface tension. CO₂ is another good candidate for supercritical drying however not used in the experiment [118]. The sample after membraning is then ready for optical characterization. For slow light passive devices, the detailed structure designs, and their characterization results will be reported separately in Chapter 4.

3.4 Fabrication technology for THz PhC QC lasers*

*The main results in this section are originally published in "Design and fabrication technology for high performance electrical pumped THz photonic crystal band-edge lasers with complete photonic band gap." (Paper accepted for publication in Journal of Applied Physics.)

In this section, we will describe the detailed fabrication technology that we developed in EPFL for two-dimensional photonic crystal (PhC) band-edge emitting quantum cascade lasers (QCLs) operating at terahertz frequencies. We developed a multi-layer Benzocyclobutene (BCB) planarization technique to achieve electrically pumped QCLs on pillar structures with complete PBG. In comparison to the high contrast structure fabricated using a double wafer bonding techniques [119], we believe our BCB planarization technique brings more freedom in terms of lithography, especially regarding the definition of the top contacts on these non-connected structures. It is necessary to mention that such BCB planarization technique is not limited to the fabrication processes for pillar type TM polarized PhC QCL structures. It can also be used for more general purposes on various material systems where the device surfaces are intrinsically not smooth and require additional lithography, in *e.g.* PhC hole-type structures with TE polarization, DFB lasers.

3.4.1 Motivation of pillar type PhC lasers.

Slow light PhC lasers can be achieved either with a high index modulation scheme or with a low index scheme, leading to strong PhC or weak PhC effects, respectively. The strong PhC effect, which requires high index modulation can be achieved with deeply etched structures [17, 120, 121] that are sandwiched within the two metallic layers, as illustrated in Figs. 3.4.1(a) and 3.4.1(b).

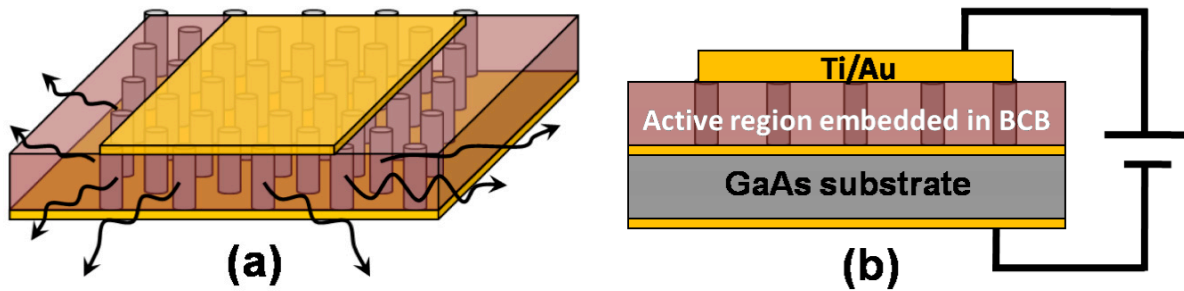


Fig. 3.4.1. (a), Sketch of the lasing mode operation at the bandedges corresponding to the in-plane emitting scheme. The pillar height is about $15\ \mu\text{m}$ and period range is between $14 - 23\ \mu\text{m}$. (b), Side view of the PhC QCL device.

The periodical arrangement of active region material provides a better heat generation, dissipation and distribution budget than the low index modulation case, as it allows a reduction of the active material and a better surface to volume ratio. Under the high index modulation scheme, pillar type PhC lasers are more appealing than the air hole type PhC lasers. One reason for this is that there are several complete photonic bandgaps (PBGs) for the pillar type PhC for TM polarized light, another one is that the pillar type PhC lasers eliminate the risk of electrical leakage in contrast with PhC device with etched holes [120, 121].

In our case for pillar type PhC structures, the entire QCL active layer has been deeply etched to form a triangular lattice PhC. Strong vertical optical confinement is provided by metal-metal plasmon waveguide fabricated with thermo-compression bonding and planarization. Benzocyclobutene (BCB) is employed as a low loss medium to planarize the PhC structure. By tailoring the top metal contact on the planarized PhC structures, electrical current injection pad can also be defined. The lasing properties can be controlled by engineering the photonic band structure.

3.4.2 Fabrication processes

3.4.2.1 Photomask fabrication with DWL technique

Prior to the sample fabrication, the first thing is to design and fabricate the mask, therefore it is necessary to mention the direct writing laser (DWL) technique. Instead of purchasing

photomasks from external suppliers, such as Photronics [122] or Delta Mask [123], I established the photomask fabrication procedure locally in EPFL with such DWL technique (Heidelberg DWL200 [124, 125]).

DWL200 is an optical pattern generator based on a fast laser scanner. The smallest linewidth that can be achieved is 800 nm with 4 mm write Head (4 mm is the focal length). For our purpose we use the DWL to write Cr-blank mask (5x5"), however it is also capable to write 7x7" mask or wafers (100 or 150 mm diameter) for g, h-line photoresist. The Cr-blank consists in a 100 nm thick Cr layer sputtered on the Soda-lime glass. There are two laser sources available: For the 800 nm resolution, the 4 mm writing head with continuous Kr gas source light at $\lambda = 413$ nm is used. For the 2 μm resolution, the 10 mm laser Head with continuous Solid State Diode light at $\lambda = 405$ nm is used. The minimum fabrication grid is 200 nm (can be considered as stitching error referring to the EBL case).

Similar to the EBL fabrication process, the DWL mask fabrication also involves the data processing and sample processing:

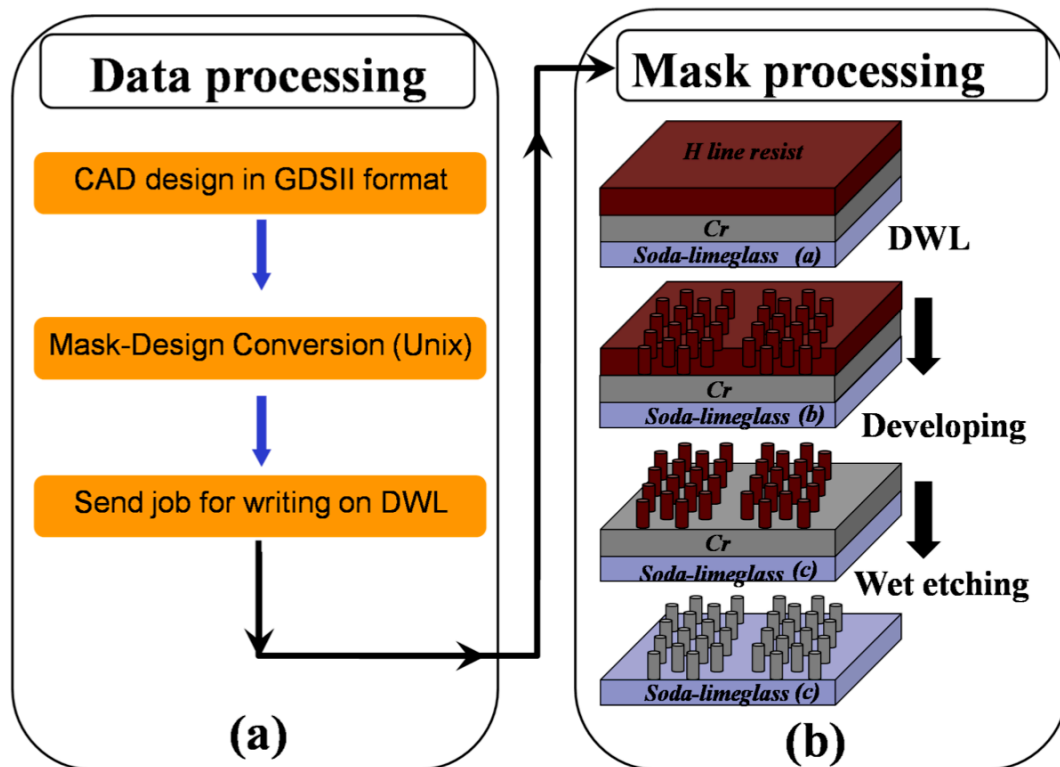


Fig. 3.4.2. (a) and (b), data process and mask process flow charts for DWL system, respectively.

The fabricated mask (shown in Fig. 3.4.3) was then diced using the previous mentioned Disco DAD321 dicing saw [99] into 4 identical pieces. The mask was then used in the III-V cleanroom in IPEQ [126]. I performed all the following QCL fabrications in this III-V cleanroom.

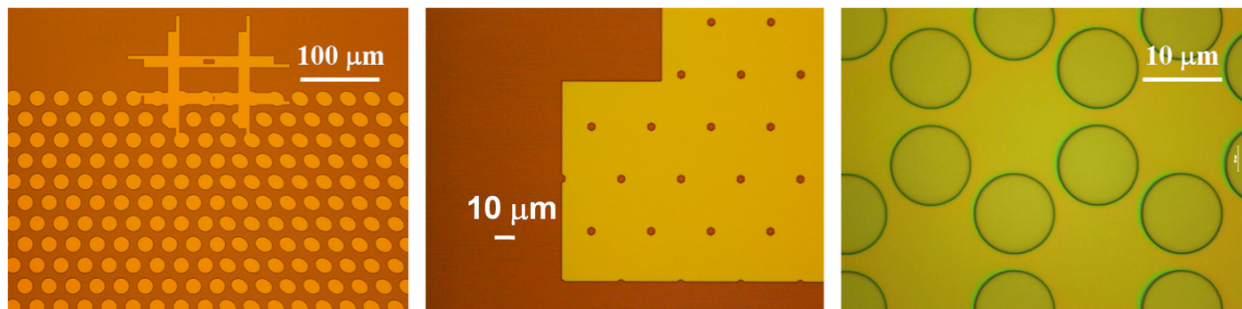


Fig. 3.4.3. Examples of the photomasks fabricated by the DWL technique. Left: Circular and Elliptical pillar mask. Middle: Mask of the top contact pad with 5 μm small holes. Honey comb PhC mask.

3.4.2.2 PhC QCL fabrication process

The active layer used for the fabrication of PhC QCL consists of 120 periods of GaAs/ $\text{Al}_{0.15}\text{Ga}_{0.85}\text{As}$, which is grown by Molecular Beam Epitaxy (MBE) on a semi-insulating GaAs substrate. Details about the QCL active region designs will be given in Chapter 6. A 700 nm thick $\text{Al}_{0.30}\text{Ga}_{0.70}\text{As}$ was grown as an etching stop layer. The flow chart shown in Fig. 3.4.4 illustrates the fabrication process steps for the pillar type PhC lasers. To create the metal-metal confinement, Ti/Au (5 nm/500 nm) layers were evaporated onto both the QCL structure and a n^+ doped substrate, the Au/Au surfaces of these wafers were then bonded together by means of thermo-compression wafer bonding as illustrated in Fig. 3.4.4(a). This wafer-wafer bonding forms the first surface plasmon layer. It is performed in air at 300 $^{\circ}\text{C}$ with 4.5 MPa pressure for 45 minutes. Polishing of the substrate was performed, and then it is followed by the selective wet etching with a mixture solution containing citric acid (citric: H_2O_2 : H_2O = 3:2:3 in weight, Fig. 3.4.4(b)). When the etch stop layer was reached, the sample was then processed with standard photolithography, Reactive Ion Etching (RIE) was used to fabricate the pillars (Fig. 3.4.4(c)). The structure was planarized using BCB (Fig. 3.4.4(d)). A new metallic layer was deposited and lifted off (Fig. 3.4.4(e)) to form the second surface plasmon layer and the top contact as well. The bottom contact layer was formed by depositing metal on the n^+ GaAs substrate, as plotted in Fig. 3.4.4(f).

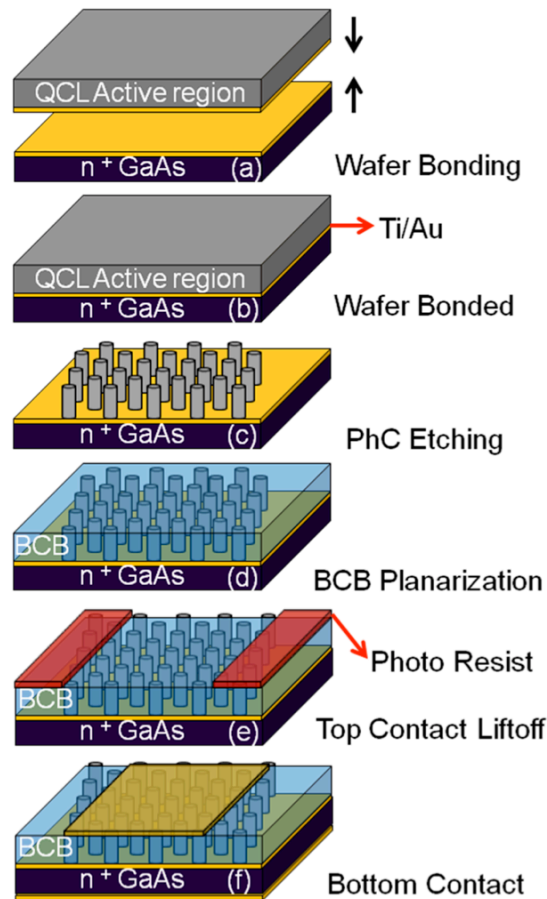


Fig. 3.4.4. Complete fabrication flow chart of photonic crystal pillar type QCLs.

Detailed fabrication information after wafer bonding is given below: A 900 nm thick SiO_2 was deposited by Plasma Enhance Chemical Vapor Deposition (PECVD, Oxford PlasmaLab100 [127]) on the epilayer, to form the hard mask for the following photolithography. In order to obtain smooth side wall profile of the pillar, it is necessary to obtain smooth hard mask profile. We used AZ5214 image reversal resist as a positive tone photoresist (Fig. 3.4.5(a)) to define the PhC pattern. The pattern was then transferred into the SiO_2 hard mask using a CHF_3/Ar based plasma mixture in RIE (Oxford Plasma80Plus [128, 129]). The CHF_3/Ar plasma mixture with ratio of 25/25 (unit in sccm) was used for the RIE step. The chamber pressure was kept at 30 mTorr with a radio frequency (RF) power of 200 W. Under such conditions, the etching rate is about 31 nm/min. A 29-minute etching time is required to etch through the entire 900 nm SiO_2 layer. The reason to choose the image reversible photoresist AZ5214 rather than a positive resist such as S1818 (Fig. 3.4.5(b)) will be discussed below and the results will be compared in detail. The key issue during the etching is that the in-plane roughness of the photoresist is more important than its vertical shape. During the first etching of SiO_2 hard mask, both AZ5214 and S1818 transfer almost the same angle to the SiO_2 hard mask (Middle images in Figs. 3.4.5(a) and 3.4.5(b)). However, the AZ5214 intrinsically transfers a much smoother in-plane profile to the

SiO₂ layer than S1818, despite the vertical profile of AZ5214 resist that has a donut shape. This in-plane roughness on the SiO₂ introduced by the S1818 will be further amplified during the second etching, where the ~13.5 μm thick QCL active region is etched through. (Right hand side images in Figs. 3.4.5(a) and 3.4.5(b)). Detailed zooms on the edge of the pillars processed with the two resists are provided in the insert images. Such comparison demonstrates that the AZ5214 is a better choice for the SiO₂ mask etching.

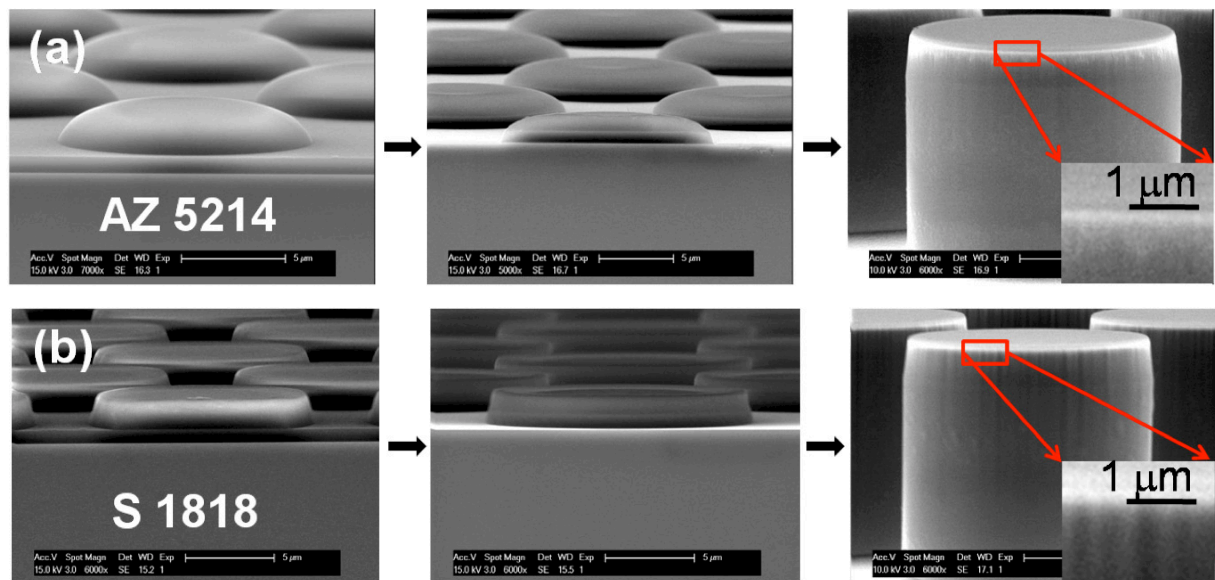


Fig. 3.4.5. (a) Resist profile of AZ5214 (left), after SiO₂ mask transferring (middle), and after active region core etching (right). (b) Resist profile of S1818 (left), after SiO₂ mask transferring (middle), and after active region core etching (right).

After the first SiO₂ mask transfer, the sample was cleaned in warm acetone (40°C) ultrasonic bath, and then processed with oxygen plasma cleaning to remove the resist residues before the QCL core etching. For the second QCL active region etching, SiCl₄/Ar/Cl₂ plasma mixture with ratio of 46/6/1 (unit in sccm) in the RIE (Oxford Plasma90) was used. The chamber pressure was kept at 10 mTorr with a RF power of 100 W. Under such conditions, the etching rate is about 125 nm/min. A 120-minute etching time is required to etch through the entire 13.5 μm active region. The PhC pillars after etching have nearly perfect vertical profiles, with very smooth sidewall across the entire active region (right hand side image in Figs. 3.4.5(a) and Fig. 3.4.7(a)). Such high quality etching leads to a considerable reduction of the propagation loss and scattering loss, and hence it should effectively contribute to a lower threshold current density.

3.4.3 Multi-layer BCB planarization

The biggest challenge in the fabrication of pillar type PhC QCL is to form the top

plasmon/contact layer for the light confinement and uniform current injection purpose. Furthermore the planarization provides freedom on the definition of surface plasmon patterns, and potentially it forms a better heat-conducting environment surrounding the QCL material than air [119]. A multi-layer planarization technique based on BCB (CYCLOTENE 3022-46) was applied to address this issue. The BCB's low refractive index, low curing temperature, low loss, and ability to be dry etched are the most important features for this purpose. The standard single layer BCB planarization recipe, which suits for large piece wafer scale process, was modified with multi-layer curing for small piece QCL devices. The single layer of thick BCB always results in much thicker resin at the edge than in the wafer center, this effect is critical when the BCB is coated on small device pieces. Moreover, one single layer coating of thick BCB cannot achieve smooth surface on 13.5 μm pillar after curing. An adhesive promoter (Dowing AP3000) was spin-coated on the sample before the first BCB layer to enhance the adhesion. The BCB was cured each time after the spin coating. N_2 purge is required when the curing temperature ramps higher than 180 $^\circ\text{C}$ to prevent the BCB oxidation.

Detailed curing information is listed in Table. 3.4.1 and Fig. 3.4.6.

Number of curing	Spin Speed (RPM)	Approximate Thickness (μm)	Maximum Curing temperature ($^\circ\text{C}$)	Curing time (hours)
1	5000	4	210	1
2	4000	6	210	1
3	4000	6	250	1

Table. 3.4.1. Multi-layer BCB curing information.

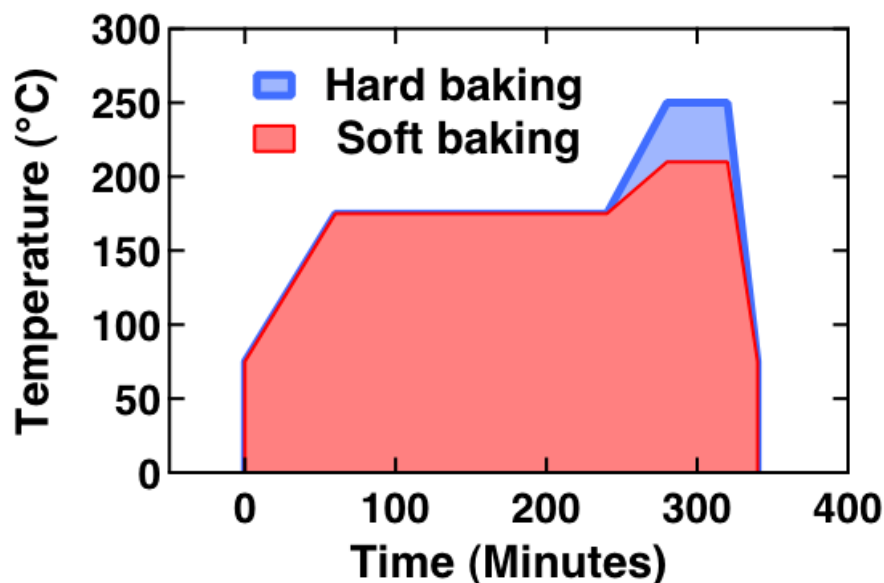


Fig. 3.4.6. BCB curing information. Red: soft baking, blue: hard baking.

After 3 layers of spin coating and curing (two soft baking and one hard baking), the entire sample was completely covered with BCB with a smooth surface as seen in Fig. 3.4.7(b). The measured surface roughness is only ± 28 nm (using α -step profiler), which is negligible comparing to the 15 μm total thickness. The BCB was etched without any surface preparation on the sample using a CF_4/O_2 plasma mixture with sccm ratio of 40/60 in the RIE. The chamber pressure was kept at 100 mTorr with a radio frequency (RF) power of 200 W. The BCB was etched to a depth a little bit lower than the top of the pillar, e.g., ~ 800 nm (Fig. 3.4.7(c)), in order to guarantee that the remaining SiO_2 mask can be easily removed through the following wet etching. The etching rate of the BCB strongly depends on the curing conditions; e.g., for a typical multi-layer planarization process (two soft baking at 210 $^\circ\text{C}$ and one hard baking at 250 $^\circ\text{C}$ as shown in Fig. 3.4.6), the etching rate is 700 nm/min. This number can be slowed down to 370 nm/min in the case of a 3 hard baking curing process.

When the BCB layer was ~ 800 nm over etched, *i.e.* below than the top of the pillar, the sample was then dipped in the Buffered Hydrofluoric acid (BHF) to remove the remaining SiO_2 mask. Note that this step is very important because it determines the quality of the top metal contact; in another word it impacts on the laser current/voltage (IV) performance. A new pattern with negative photoresist TI35ES was written on the sample with ~ 4 μm thick undercut profile for thick metal contact lift-off. Very thick Ti/Au (5 nm/1200 nm) was evaporated on the device and then lifted off to generate a thick enough surface plasmon layer (Figs. 3.4.7(c), 3.4.7(d), 3.4.7(e), 3.4.7(f)), this thick layer compensates for the BCB over etching and surface roughness. The bottom contact was achieved by deposition of Ti/Au (5 nm/500 nm) on the bottom of the n^+ GaAs substrate. The sample was then cleaved and mounted on copper supporter with conductive glue and bonded with 25 μm gold wires (Figs. 3.4.7(g), 3.4.7(h)).

It is necessary to mention that such BCB planarization technique is not limited to the fabrication processes for pillar type TM polarized PhC QCL structures. It can be also used for more general purposes on various material systems where the device surfaces are intrinsically not smooth and require additional lithography, in *e.g.* PhC hole-type structures with TE polarization, DFB lasers.

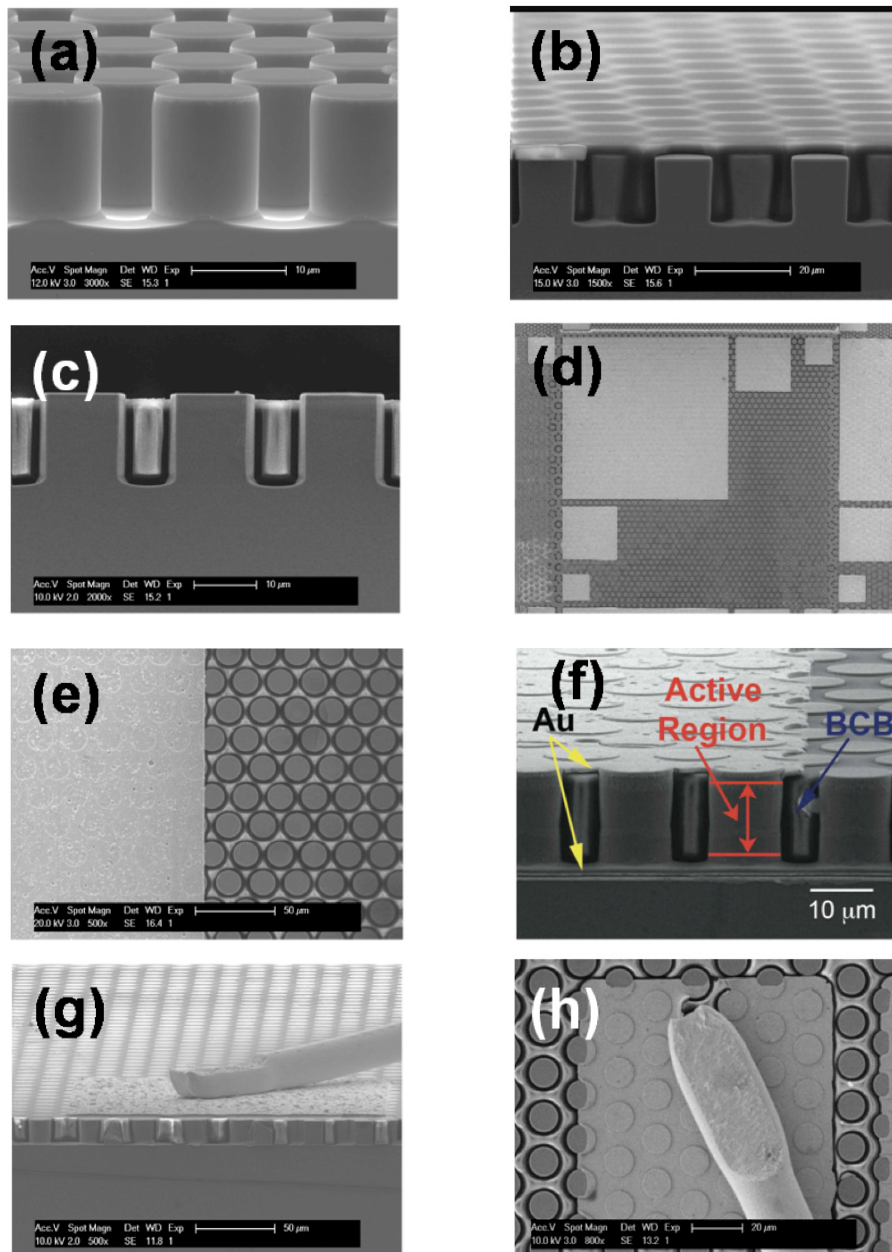


Fig. 3.4.7. (a) SEM image of PhC pillars after RIE core etching. (b) Side view SEM image of the sample after multi-layer BCB planarization. (c). Side view SEM image of the sample after BCB etching and SiO₂ removal. (d) SEM top view of metal contacts. (e) Detail of double-plasmon and single-plasmon interface. (f) Side view of PhC pillars embedded in double metal waveguides with BCB filling material. (g). Side view of PhC pillar lasers after cleaving with bonding pad. (h). Top view of bonding pad on small contact (100×100 μm²).

After the deposition of bottom contact, the sample was shipped to ETHZ and then cleaved, wire bonded and then mounted on copper holder with conductive glue. All the fabricated PhC QC lasers were characterized in collaboration with the group of Prof. J. Faist in ETHZ. The detail about the characterization technique and experimental results will be given in Chapter 6.

Chapter 4

4. Experimental investigation of passive slow light PhC devices in Near Infra-Red

The Near Infra-red (NIR) PhC devices studied under the scope of this PhD thesis can be cataloged into two groups based on their functionalities. The first type is the slow light PhC device, where light speed (group velocity v_g) is significantly slowed down by means of engineering of the dispersion structure. The second type is high Quality (Q) factor PhC cavity, where photons are confined intensively in a extremely small volume with a long photon life time. In this thesis our interest for high-Q cavities lies in the fact that they are elementary constituents of coupled cavity waveguide. The experimental investigation of different slow light photonic crystal devices operating in NIR will be described systematically in this chapter. The investigation of different high Quality (Q) factor photonic crystal cavities will be described systematically in chapter 5.

Slow light devices are attracting more and more attention as key components for practical and meaningful applications in future optical networks. For example, ultra-compact optical delay lines [64, 130], optical memories [131], optical buffers [132, 133] and lasers [17, 134] are based on photonic crystal (PhC) waveguides with low group velocity (v_g). These have been reported and extensively investigated. The most common slow light PhC device is the PhC slab waveguide with one or multiple line defects (W_1 or W_x waveguides) [16, 54, 135-139], which exhibits a large dispersion over a broad k-vector range near the mode cut-off. However, in W_x waveguides, the reported group indices do not exceed 35 [54, 135-140]. Short optical pulses and high bit-rate signals with a wide frequency spectrum are seriously distorted by the group velocity dispersion (GVD) [141, 142].

To overcome this GVD problem, dynamic controls (electrically, mechanically or optically) of the dispersion characteristics have been discussed [143], but such phase modulation of input signals method operates like a one-bit optical memory rather than an optical buffer, because it cannot store continuous signals without mutual interference [144]. The photonic crystal coupled waveguides (PCCW) [64, 141, 145, 146], both chirped and unchirped, are called dispersion-compensated slow-light devices because they can couple two PhC waveguides with opposite dispersion characteristics. They have been reported to effectively eliminate the

distortion due to GVD. The drawback of such scheme is that it strongly suffers from fabrication induced imperfection [59], which causes large reflection loss, and such scheme is achieved at a cost of limited nonlinear enhancement [141].

Another approach to slow down short optical pulses while suppressing the higher-order dispersion is to use the so-called zero-dispersion slow-light devices, *i.e.*, coupled cavity waveguide (CCW) based on concatenated PhC cavities or microrings [14, 132, 147-157]. Light propagates through the CCW chain via the evanescent coupling between the neighboring cavities [132, 158]. Depending on the quality factor (Q factor) of the constituting cavities, either high Q factor [155, 159] ($Q > 10^5$) or moderate-Q factor [14] ($Q < 10^4$) tightly confined eigenmodes can be generated. Such modes form a flat dispersion band, where the group index in the middle of the band can be tuned by the adjusting interaction between the neighboring cavities. Such CCW slow light system achieves larger experimental group index ($n_g \geq 50$) than the W_x line defect waveguide. Meanwhile the GVD is strongly reduced. However, neither the low Q nor the high Q PhC CCWs had shown continuous transmission over a broad bandwidth. The transmission properties of the low Q CCWs are limited by strong out-of-plane radiation loss. While the high Q CCWs suffer from a narrow passband which accompanied with discretized characters. This is owing to the intrinsic high Q and large impedance mismatch between the cavity chain and the external waveguides [155, 157].

Two types of slow light PhC devices are investigated under the scope of the PhD thesis. The first type is the common PhC slab waveguide with one or multiple line defects (W_1 or W_x waveguides) fabricated on InP material system. This investigation was performed under close collaborations: Dr. Anne Talneau (CNRS, France) designed the PhC slow light structure and provided the InP wafer, I was in charge of the Ebeam insolation with different resolutions. The sample was then etched and membraned in France, then the optical characterisation was performed by Dr. Nicolas Le Thomas in EPFL. The second type is the coupled photonic-crystal cavity (CCW) waveguide fabricated on SOI material system. The CCW devices were designed by Miss Jana Jágerská (PhD student) and me. Then I fabricated the sample, and performed optical characterisation together with J. Jágerská.

This chapter consists of 3 sections. Section 4.1 first starts with the description of the experimental setup[160] which was used to carry out the optical characterizations for all the NIR range PhC devices under the scope of this thesis. The experimental setup was developed by Dr. Nicolas Le Thomas in 2006, it is based on the standard end-fire setup and combined with a near field/far field imaging technique. In Section 4.2, slow light photonic crystal W_1/W_x waveguides based on InP material system are investigated. In the vicinity of a band-edge, different light transport regimes are identified by direct measurement of the dispersion curve in k space. The

transition of the guided mode of these regimes is determined as whether a group velocity, n_g , can be defined from a ω vs. k dispersion relation. In Section 4.3, slow light coupled photonic crystal cavity waveguides are investigated systematically. The radiation profile of the constitutive single cavity is found to be directly related to the radiation loss and the Q-factor of the CCWs. The transmission and dispersion properties as well as intrinsic limitations of coupled-cavity waveguides (CCW) are studied. Referring to the experimental data, the impact of residual disorder on CCW systems is studied, showing that the CCWs are more robust than slow light line defect waveguides.

4.1 Fourier space imaging setup

There are mainly three types of techniques for the optical characterization of photonic crystals (PhC). The first type of optical measurement techniques is based on an external light source, typical example is the end-fire setup used for transmission measurement. The second type relies on the presence of a light source inside the PhC under investigation, such as Internal Light Source (ILS) setup [161-163]. The third type of techniques is based on more advanced techniques like scanning near field optical microscopy (SNOM) [164], atomic force microscope (AFM) [165] and Fourier space (FS) imaging [160].

The standard first two types of characterization techniques consist in the measurement of the optical response or light emission from the PhC structures. Although a large number of important information can be accessed, they are still ‘black box’ approaches. The standard techniques do not directly investigate light propagation inside the PhC and the fundamental quantities such as dispersion curve or equi-frequency surfaces (EFS) are only inferred after data analysis. This has motivated the development of SNOM and heterodyne SNOM to achieve real space and Fourier space high-resolution imaging. However these methods can be cumbersome and time consuming. Imaging directly the Bloch mode in real and reciprocal space with old-fashioned classical optics is currently re-discovered in plasmonic [166, 167], and with nano-objects [160].

During the thesis, all the fabricated NIR PhC devices were characterised under the Fourier imaging (FS) setup (as illustrated in Fig. 4.1.1). Such setup is a combination of standard end-fire setup and the Fourier space imaging technique [160]. The end-fire setup allows transmission measurement, while the Fourier space imaging technique allows direct measurement in k-space. The principle is to image the out of plane scattered light from the PhC in a standard end-fire experiment by using a high numerical aperture microscope objective ($NA = 0.9$). A direct measurement already provides high-resolution optical images, such images will be referred as real space (RS). Moreover, by imaging the back focal plane of the collecting lens (Fourier plane), one can access to the far field, k-space or Fourier space (FS) images. In this plane every point is

uniquely related to a direction of emission, thanks to geometrical optics. Such a single point is also uniquely related to an in-plane wave vector of the PhC Bloch mode, thanks to in-plane wave vector conservation law. A set-up where the insertion or removing of a single lens allows switching from real and Fourier space is detailed in Fig. 4.1.2. Detailed discussion of the technique, largely developed at EPFL, is provided in Ref. [160].

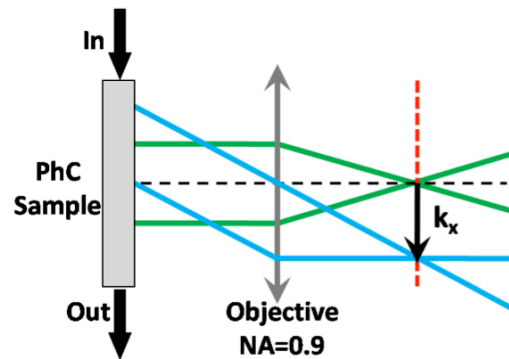


Fig. 4.1.1. Principle of Fourier imaging. In the back focal plane of the collecting lens every point is uniquely related to a direction of emission. Such point is also uniquely related to a unique in-plane wave vector of the PhC Bloch mode due to in-plane wave vector conservation law.

All the fabricated NIR PhC structures are excited using a monochromatic laser source tuneable within the wavelength range of 1470 – 1660 nm through a lensed fiber and adiabatically tapered access waveguides. The wavelength resolution of the Tunics is 1 pm. For each wavelength of excitation, the transmitted TE-polarized signal is detected using an InGaAs photodiode (Fig. 4.1.2(a)). At the same time, light emitted from the sample surface is collected by the high numerical aperture microscope objective and projected onto an infrared CCD camera. Direct imaging of the sample surface yields the real space image (Fig. 4.1.2(b)).

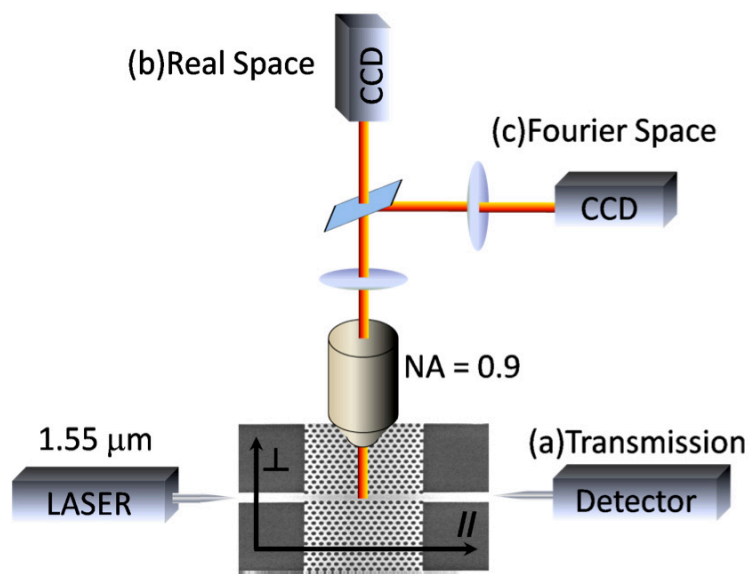


Fig. 4.1.2. End-fire setup based Fourier space imaging technique.

By projecting the back-focal plane of the collecting lens on the CCD, we obtain the Fourier-space image (Fig. 4.1.2(c)), which yields the k -vector distribution of the emitted light from the sample. Such far field image provides us with comprehensive information about all spatial components contained in the radiated field. The experimental dispersion curve $\omega(k)$ is obtained by integrating the Fourier space images along k_x for each frequency and by stacking the corresponding profiles.

However, this technique appears inherently limited to wavevector value inside the air light cone, while most of the present interesting structures are designed to operate below the light line in order to minimize propagation losses. An approach called linear probe gratings (LPG) [136] has been implemented to break the light line limit. This approach consists in adding a vanishingly weak extra periodicity that folds back the Brillouin zone into the light cone. This is intrinsically the case when measuring coupled cavity waveguide as shown in Ref. [136] where the supercell periodicity folds back the entire dispersion curve inside the air light cone. The extra periodicity can also be deliberately included, as it is demonstrated on a measurement of slow light dispersion curve in a modified W_1 PhC waveguide as it can be seen in Fig. 4.1.3(reprinted from Ref. [136]).

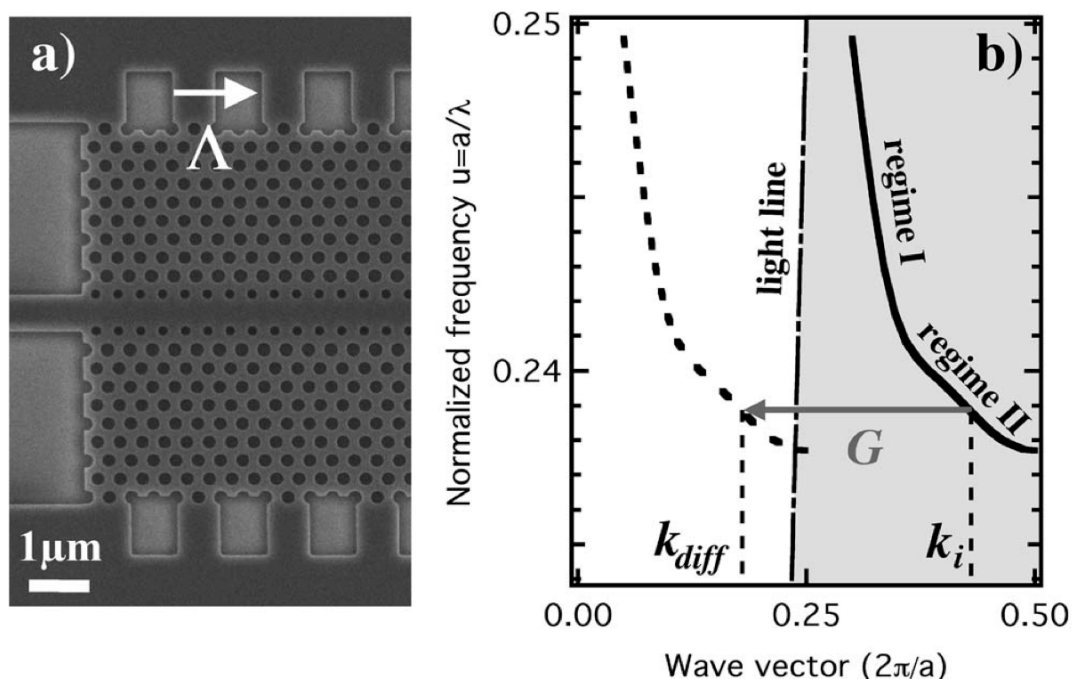


Fig. 4.1.3. (a) SEM image of a modified W_1 waveguide with the linear probe gratings at the waveguide boundaries. (b) Illustration of the folding of the dispersion curve dark line into the light cone dash line. Reprinted from Ref. [136].

4.2 *Light transport regimes in slow light photonic crystal waveguides**

*The main results in this section are originally published in "Light transport regimes in slow light photonic crystal waveguides", Physical Review B 80 (12), 125332 (2009).

4.2.1 Introduction

The transport properties of waves, such as electromagnetic waves, matter waves, electronic waves, or acoustic waves, are strongly affected by the disorder present in the propagating medium [168, 169]. The different regimes of wave propagation that can set up due to disorder-induced scattering depend on the relative values of the mean-free path l of the wave, the sample size L and the wavelength λ . When $l \gg L$ the medium can be considered as homogeneous and the propagating wave undergoes rare scattering events: the corresponding wave transport regime is often ambiguously called the “coherent” regime [168, 169]. In this case, wave equations such as the Schrödinger or the Helmholtz equations offer a straightforward determination of the eigenstates of the wave field, with the wave number k as a good quantum number. This gives access to a well defined dispersion relations $\omega(k)$ between k and the frequency ω . We will prefer here to name this propagating regime the “dispersive” regime. The dispersive regime is favoured for information transmission in modern communication systems.

When $\lambda \ll l \ll L$, the spatial phase of the field is strongly affected by the disordered potential in the medium. After propagation over several mean-free paths, the multiple scattering regime takes place. This regime will be called the “diffusive” regime. Anomalous diffusive transmission and reduction of the diffusion constant near the band-edge of partially disordered PhCs were reported in Ref. [170] and [171], respectively.

As mentioned before in Chapter 2, the ideal W_x PhC waveguides exhibit slow light regime where the group velocity of guided Bloch modes theoretically vanishes at band-edges. Nevertheless, as shown in Refs. [172] and [139], the presence of residual disorder in actual structures strongly affects the group velocity at the band-edges. Some of the first experimental investigations of the speed of light in line-defect PhC waveguides reported group velocity of $c/50$ and $c/150$ [51, 53], whereas in other types of experiments group velocities lower than $c/1000$ were claimed [52, 173]. Time-of-flight experiments revealed that the lower group velocity was only $c/7$ near band-edges in 2D PhC structures [174]. More recently, some theoretical calculations predicted that group velocities smaller than $c/100$ could not be achieved in so-called W_1 or W_3 waveguides, with the current state-of-the-art technology [139, 175]. In addition Engelen *et al.* highlighted two regimes of light propagation featuring a “*group-velocity range of $c/7$ down to $c/200$* ” in chirped W_1 waveguides [176].

In this work, we identify the light transport regimes between dispersive and diffusive regime in the vicinity of a PhC W_1 waveguide band-edge. In the dispersive regime, where the dispersion as well as the group index can be effectively defined. However in the diffusive regime, the group index is no longer able to be identified and the group velocity loses its meaning. In this case the energy transport velocity v_E should be the proper description of the light speed. The largest group index achieved among our W_1 membrane PhC waveguides with different amounts of disorder is around 25.

4.2.2 Light transport identification

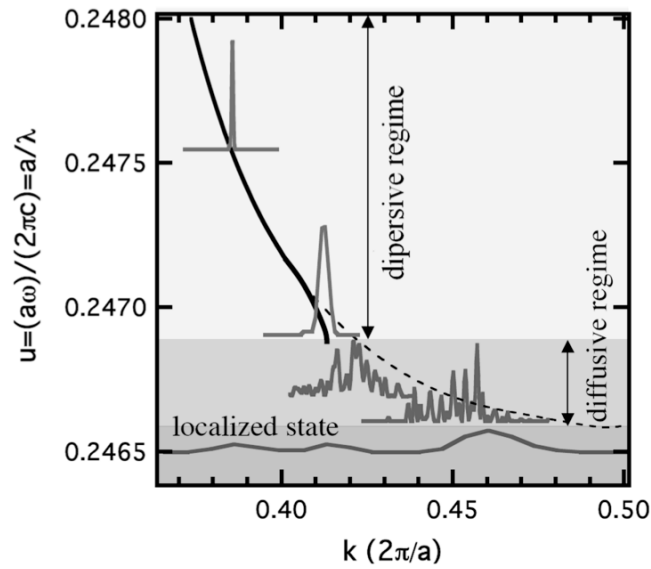


Fig. 4.2.1. Definition of the light transport regimes according to their dispersion properties in an actual W_1 photonic crystal waveguide. From top to bottom, the different grey shadows represent the dispersive, diffusive, and localized regimes, respectively. Dashed line: dispersion band diagram of the fundamental mode of an ideal W_1 waveguide. Black line: schematic representation of the modified dispersion curve due to residual disorder. The corresponding expected angular spectra in the dispersive, diffusive, and localized regimes are superimposed in gray.

In Fig. 4.2.1, we show the theoretical dispersion curve of the fundamental guided mode (dashed line) propagating in an ideal W_1 photonic crystal waveguide near the boundary of the first Brillouin zone. With this Figure, we also give a schematic representation of the expected dispersion curve modified due to an arbitrary residual disorder (dark line) as well as the corresponding Fourier space spectrum (represented in gray). The dispersive, diffusive and the strongly spatially localized regimes are correlated with the different regions of the modified dispersion curve.

The dispersive regime, which corresponds to a well defined v_g , is located far enough from the band-edge at $k < 0.4 \times 2\pi/a$ where a is lattice constant. In this regime, the Fourier space

spectrum is approximated by a Dirac δ function. When the normalized frequency $u = a/\lambda$ approaches the band-edge, the effect of the disorder becomes significant as a result of the slowing down of the light [169]. It follows that the slope of the dispersion curve is modified, which sets a lower bound for v_g . Moreover the linewidth of the real space spectrum broadens as a result of the decrease of the mean-free path l , due to the random spatial dephasing of the field.

The diffusive regime corresponds to a region where the dispersion curve cannot be defined. It results in the formation of speckle-like spatial frequency spectra for frequencies close to the band-edge ($k > 0.42 \times 2\pi/a$). The disappearance of a dispersion relation between ω and k does not mean that the wave transport vanishes in the diffusive regime. Although the spectral correlations are too weak to generate a clear dispersion curve, the diffusive energy transport can still be efficient in contrast to the spatially localized regime [177] which appears at frequencies ω located below the ideal band-edge (shown as localized states in Fig. 4.2.1).

4.2.3 Structures

The W_1 waveguides were fabricated on indium phosphide (InP) semiconductor suspended membrane. A 260 nm thin InP guiding layer was grown on top of a 1.5 μm InGaAs sacrificial layer, on InP substrate. The W_1 PhC waveguides have been patterned in polymethylmethacrylate (PMMA) resist with an ultrahigh-resolution (1.25 nm) Vistec Ebeam lithography performed at EPFL as shown in Fig. 4.2.2(a) and Fig. 4.2.2(b). Recall that here we used two dose factors, high dose of 1800 $\mu\text{C}/\text{cm}^2$ for the PhC and basic dose of 900 $\mu\text{C}/\text{cm}^2$ for the ridge waveguide.

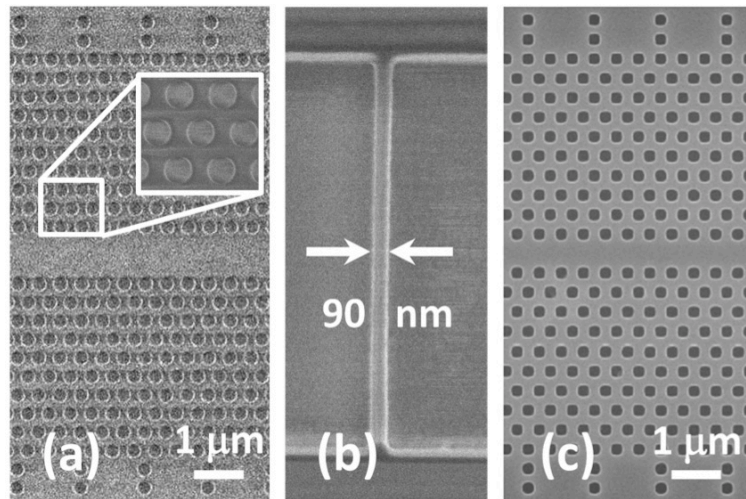


Fig. 4.2.2. SEM images of PhCs patterns at different fabrication phases. (a) SEM images of PhC W_x waveguide pattern in PMMA resist. (b) SEM images in PMMA resist of extremely narrow supporting nanowires (90 nm after EBeam exposure) for access waveguides. (c) SEM image of PhC W_x waveguide pattern in InP membrane.

Fig. 4.2.2 shows the SEM results of PMMA resist after EBL patterning on InP substrate. The dimensions of the PhC holes in PMMA resist are as close as the design in GDSII, which is in the error range of the SEM resolution (typically 2.5 nm). The pattern designed on PMMA was then transferred into a SiO₂ layer at CNRS-LPN. The SiO₂ layer is used as a hard mask for N₂/BCl₃ inductive coupled plasma (ICP) dry etching process, as shown in Fig. 4.2.2(c). Here the membrane processes are slightly different from the SOI case: after ICP etching and cleaving, the sacrificial underlying InGaAs layer was selectively etched away to produce the membrane. Supercritical drying in CO₂ was performed to prevent any strain in the structures [116]. Extremely narrow nanowires (90 nm after EBeam exposure) were defined to prevent the access waveguides from falling after membrane, as shown in Fig. 4.2.2(b). The PhC structural parameters were chosen to operate near a wavelength of 1.55 μm. Typical losses reported for W₁ waveguides are around 25 dB/cm [178]. As mentioned before, the dispersive part of the Fourier space spectrum of the investigated W₁ PhC waveguide is located below the light cone, additional linear probe gratings (LPG), designed as two extra holes with 3a period along ΓM direction (Figs. 4.2.2(a) and 4.2.2(c)), have been implemented along the outer edges of the photonic crystal structure in order to fold the spatial spectrum into the light cone with minimal perturbation as explained in Ref. [60].

4.2.4 Dispersive regime and diffusive regime

To experimentally determine the dispersion curve and the Fourier space spectrum of the modes excited in the structure, we have used the Fourier-space imaging technique as mentioned in section 4.1. Direct 2D intensity plots of the real space images show the field emitted from the surface of the sample (Figs. 4.2.3(a)–4.2.3(d)).

The real-space image of the field excited in the W₁ PhC waveguide (Fig. 4.2.2(a)) shows that the radiated parts mainly come from the centre of the waveguide and the probe gratings. The intensity of these contributions is in the same order of magnitude. For this specific image (Fig. 4.2.3(a)), the excitation wavelength corresponds to a Bloch mode in the dispersive fast light regime (see Fig. 4.2.1). This mode is located below the light cone, which implies that ideally no emission from the central part of the waveguide is expected.

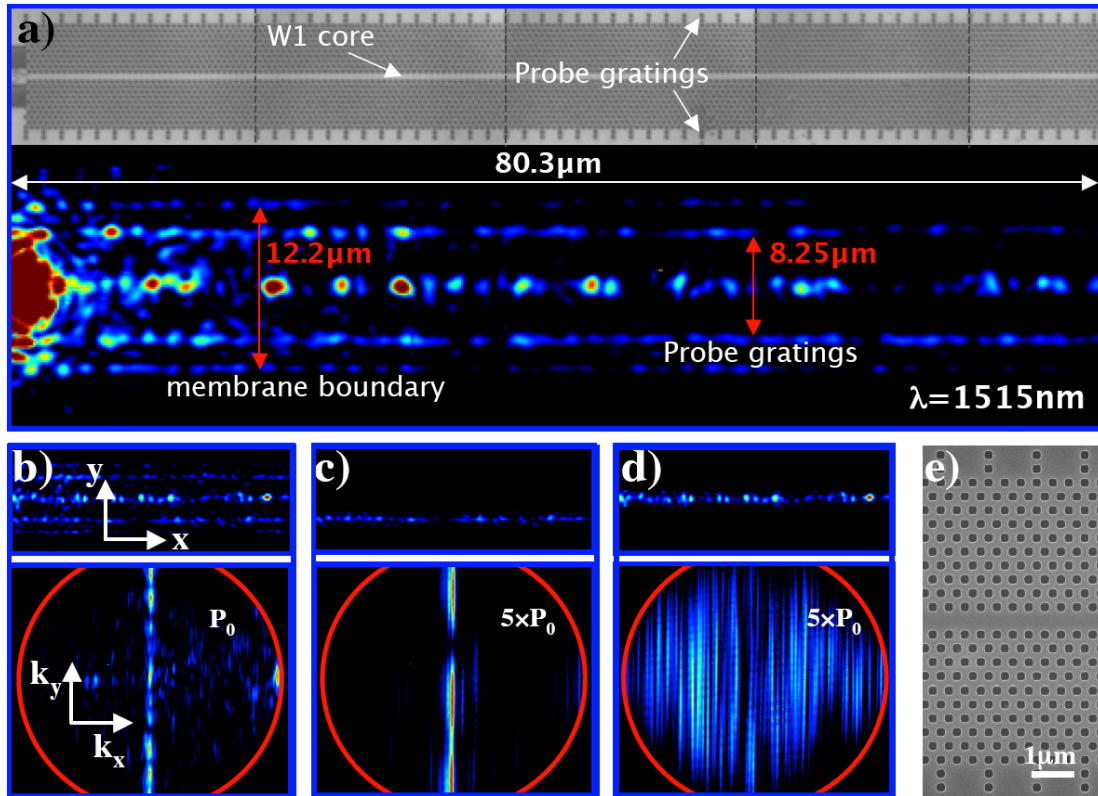


Fig. 4.2.3. Far field imaging of the light propagation in a W_1 waveguide with identification of the light transport nature in k space. (a) Real space pattern radiated from the W_1 waveguide (bottom) as well as the optical microscope image at high numerical aperture ($NA=0.9$) of a typical W_1 structure (top). The thin dashed lines mark the optical image stitchings. The high intensity scattered at the input results from the impedance mismatch at the interface between the access waveguide and the PhC waveguide. (b)–(d) correspond to the real space (top) and Fourier-space (bottom) images of the infrared light radiated from the entire waveguide (b), from only one probe grating (c), and from only the waveguide centre (d), respectively. The excitation power P_0 has been increased fivefold in the Fourier images of (c) and (d). (e) SEM image of the W_1 waveguide ($a = 440$ nm). The linear probe gratings (LPGs) consist of a series of two lines of holes periodically spaced with three times the PhC lattice constant (see (a) and (e)). They are located ten lines apart from the waveguide core to ensure minimal perturbation of the mode whose transverse intensity profile exponentially decreases away from the core.

However, as shown in the bottom images of Figs. 4.2.3(b)–4.2.3(d), direct imaging of the real space spectrum corresponding to the emission either from the probe gratings or from the centre of the waveguide, enlightens the nature of the scattering processes involved in the centre of the W_1 waveguide. In Fig. 4.2.3(b) the Fourier space spectrum of all the contributions is measured: it consists of a sharp line and a speckle background that is formed by a random field [179, 180]. In order to understand the origin of such Fourier space image, an experimental spatial filtering is used (Fig. 4.2.3(c)) to retrieve only the real space spectrum of the field

scattered above the probe gratings, whereas in Fig. 4.2.3(d) only the real space spectrum of the central waveguide is measured. The outcome of this procedure indicates that the sharp line is associated with the field scattered off the probe grating as expected from the folding process of the dispersive part of the field [160], while the central part corresponds only to the speckle part of the spectrum, associated with a random spatial phase of the field.

4.2.5 Frequency scanning of the modes

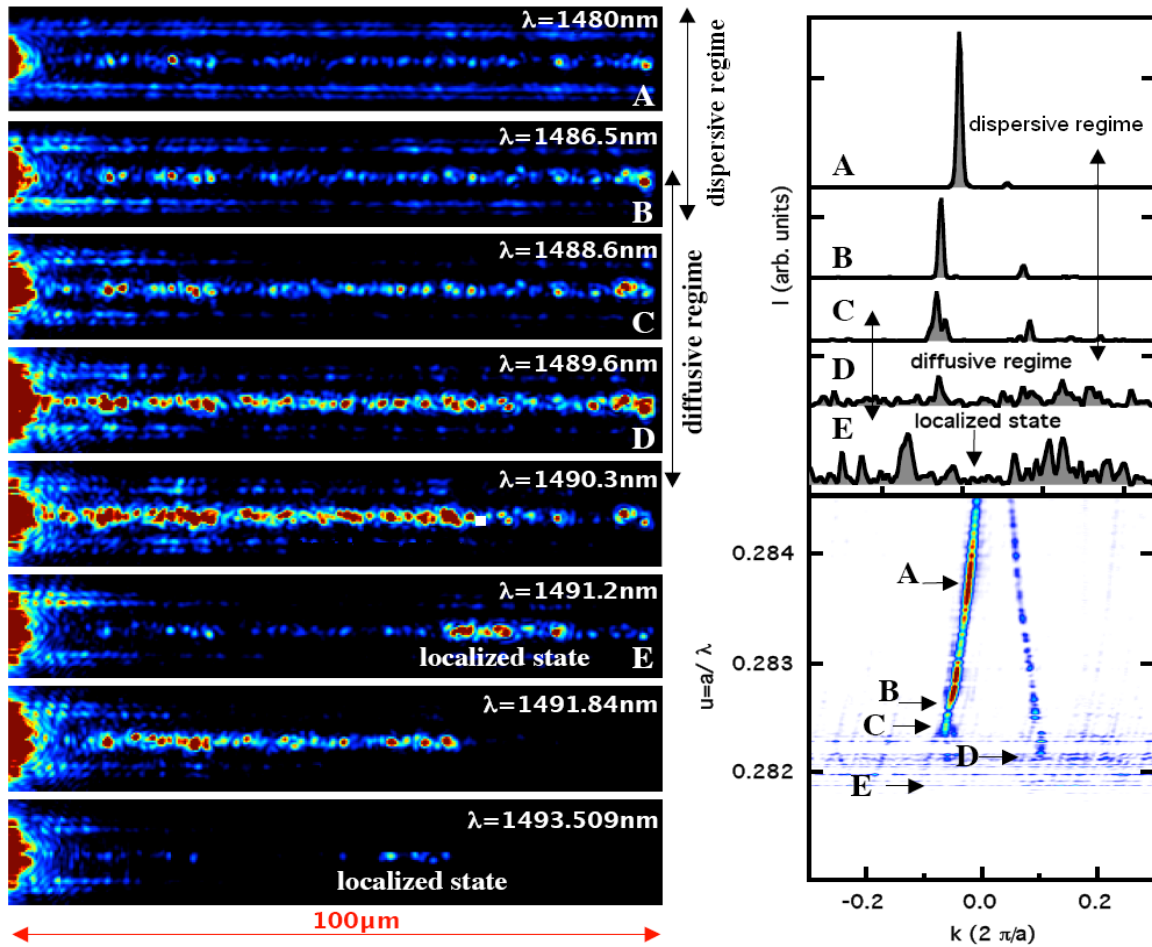


Fig. 4.2.4. Scanning of the light transport regimes along the dispersion curve. Left: the different light propagation regimes in the W1 photonic crystal waveguide highlighted with the real-space images of the radiated infrared field. Right: the corresponding 2D map representation of the dispersion diagram (at the bottom) as well as some of the real space spectrum profiles (at the top). The 2D representation consists in stacking the angular spectra measured at different frequencies. The position of the intensity maximum (color coded) reproduces the dispersion curve.

In Fig. 4.2.4, the signatures between the different light propagation regimes are highlighted both with the real space images and with the Fourier space spectra. These regimes are progressively scanned over by decreasing the frequency ω along the dispersion curve towards the band-edge. From the top to the bottom real space images (A to E), we can observe a gradual

decreasing of the dispersive contribution from the probe grating, and an increasing contribution from the central waveguide. The intensity pattern of the central part extends along all the waveguide length ($L \approx 200 \mu\text{m}$), until the frequency reaches the localize regime where pure random localized states appears. Some of these localized states can be located more than $50 \mu\text{m}$ away from the input of the waveguide with very large Q factors ($Q > 105$). The creation of spatially localized defect mode inside the W_1 waveguide can be considered as similar to the perturbation successfully introduced to create high Q heterostructure PhC cavities [181]. A second kind of localized states has been identified as necklace states [182], for instance at $\lambda = 1490.3 \text{ nm}$ and $\lambda = 1491.84 \text{ nm}$: their particularity is to exhibit an intensity pattern that begins at the input of the waveguide but abruptly stops at a random position.

4.2.6 Comparison between the transmissions and dispersion properties

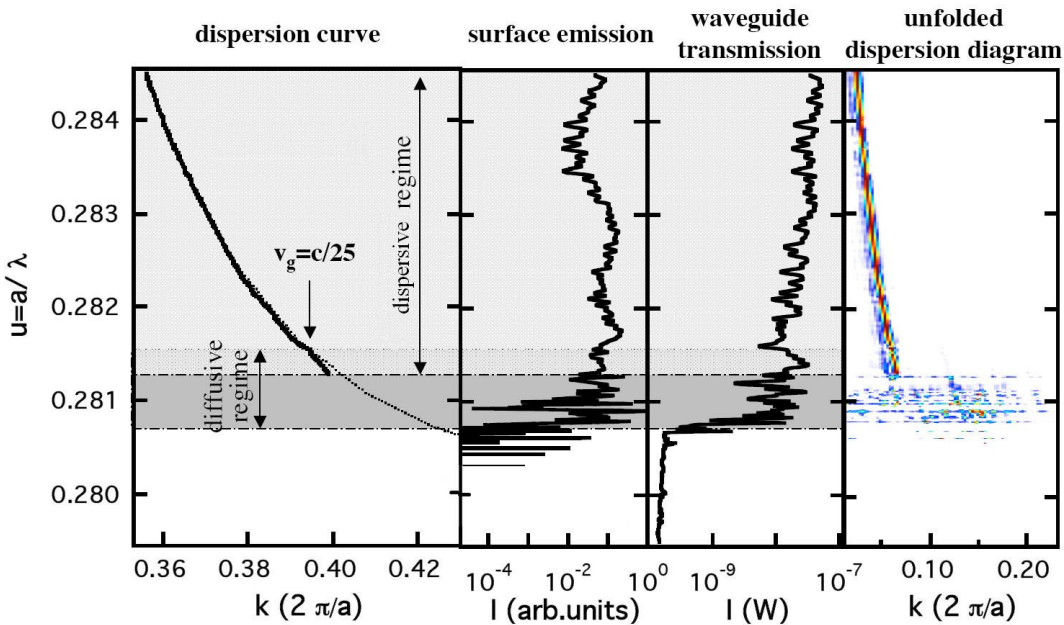


Fig. 4.2.5. From left to right: experimental dispersion curve (black line), total intensity scattered from the surface of the waveguide at different normalized frequencies u , in-line transmission and the 2D map representation of the unfolded dispersion diagram for a W_1 waveguide with lattice constant $a=420 \text{ nm}$ and filling factor $ff=0.295$. The dotted line on the left panel corresponds to the theoretical dispersion curve calculated with the guided mode expansion method. The dispersive regime and the diffusive regime are highlighted in light and dark gray, respectively.

The dispersion curve $\omega(k)$, the total intensity $I_S(\omega)$ of the emission scattered from the surface along the waveguide as well as the transmitted intensity from the input to the output port of the waveguide $I_S(\omega)$ are presented in Fig. 4.2.5 for a W_1 waveguide with lattice constant $a = 420 \text{ nm}$ and $ff = 29.5\%$. The bandwidth of $\Delta u = 0.0006$ for the diffusive regime and a group velocity as low as $v_{g\text{min}} = c/25$ are obtained from Fig. 4.2.5. The frequency bandwidths

corresponding to the pure dispersive regime and the pure diffusive regime are highlighted in light gray and dark gray shades, respectively. The intermediate gray level region points out the frequency range where the dispersion curves starts to deviate from the theoretical dispersion curve of the underlying ideal structure. The theoretical curve is the outcome of a calculation based on the guided mode expansion model [183].

4.2.7 Conclusion

In conclusion, the presence of residual disorder generates different light transports near a band-edge depending on the value of the group velocity of the underlying ideal structure. In the pure dispersive regime the Fourier space spectrum consists of a sharp peak that follows the variation of the dispersion curve of the ideal structure. In the pure diffusive regime, the peak that allows us to determine the dispersion curve disappears and the Fourier space spectrum becomes a speckle pattern. As a result, no dispersion curve can be retrieved, whereas the inline transmission is still efficient. In the intermediate frequency range where the dispersion curves starts to deviate from the theoretical dispersion curve, the Fourier space peak broadens from sharp peak to a speckle pattern. A light transport regime associated with a continuous transmission band is present even when the dispersion curve vanishes. Therefore, a careful distinction between v_g and v_E is required to determine the actual slow-down capability of a specific device for data information management. The direct imaging of the k space in the Fourier space is a reliable approach in order to investigate the lowest group velocity achievable in a photonic structure.

4.3 *Experimental investigation of slow light photonic crystal coupled cavity waveguides and their intrinsic limitations**

* The main results in this chapter are originally published in "Radiation loss of photonic crystal coupled-cavity waveguides", Applied Physics Letters 95 (11), 111105 (2009), and presented in "Experimental investigation of slow light photonic crystal coupled cavity waveguides and their intrinsic limitations". (Paper in preparation.)

As previously reported in section 4.2, the line defect PhC waveguides can strongly suffer from minute residual fabrication disorder when reaching large group index. Diffusive regime is found for frequencies close to the band-edge (n_g around 15~20) where the wave number k cannot follow the ideal dispersion relation anymore. The practical useful slow light bandwidth and group index are unavoidably limited in the W_x waveguide case. Therefore a new type of slow light structure is investigated to achieve larger group index, which shows less sensitivity to the fabrication disorders. Such structure is based on coupling a chain of identical PhC resonators and is called photonic-crystal coupled cavity waveguide (CCW). The supercell length of the CCW

(or the period of the constituent cavity) is defined as $\Lambda = m \times a$, where a is the PhC lattice constant, m is the number of photonic crystal lattice constant. The PhC CCW systems should be less impacted by the same amount of fabrication disorder, because the CCW states are formed with localized states that have already averaged the disorder over their cavity size, typically more than four lattice constants. The PhC CCW schemes we have investigated here are based on point defect L3 cavities [20] of moderate Q factor within the range of 10^3 to 10^4 .

This section is structured as follows: We start from reminding the theoretical background of the PhC CCWs dispersion properties. We further give a systematic description of the design, simulation, fabrication, and experimental techniques [160] used for characterization of the CCW system. This is followed by a detailed experimental investigation of the CCW structures. The transmission and dispersion properties of PhC CCW systems are investigated systematically. Finally, the last section discusses theoretical intrinsic limitations on achievable group index and the energy bandwidth of slow light devices in periodic structures (such as PhC W_x waveguides and CCW). The intrinsic limits of PhC slow light applies with a large generality to slow light structures designed in periodic systems.

4.3.1 CCW theory background.

4.3.1.1 CCW theory with Tight Binding Approximation.

Let us first define the quantities that are used in this section:

λ	Wavelength in vacuum	a	Lattice constant
$\Lambda = ma$	CCW Period	$L = N \times \Lambda = Nma$	CCW total length
$u = \frac{a}{\lambda}$	Frequency reduced units (a)	$u' = \frac{\Lambda}{\lambda} = mu$	Frequency reduced units (Λ)
$\kappa = \frac{ak}{2\pi}$	Wavevector in reduced unit (a)	$\kappa' = \frac{\Lambda k}{2\pi} = m\kappa$	Wavevector in reduced unit (Λ)
$\Delta k, \Delta \kappa, \Delta \kappa'$	Wavevector bandwidth	$\Delta \omega, \Delta u, \Delta u'$	Frequency bandwidth
$\delta k, \delta \kappa, \delta \kappa'$	Individual mode linewidth in wavevector	$\delta \omega, \delta u, \delta u'$	Individual Mode linewidth in frequency
$dk, d\kappa, d\kappa'$	Mode separation in wavevector	$d\omega, du, du'$	Mode separation in frequency
$n_g = \frac{\Delta \kappa}{\Delta u} = \frac{\Delta \kappa'}{\Delta u'} = \frac{dk}{d\omega}$	Group index n_g	$Q = \frac{u}{\delta u} = \frac{u'}{\delta u'} = \frac{\omega}{\delta \omega}$	Quality factor

Table 4.3.1. Quantity definitions in slow light CCW system, refer also to fig. 4.3.1.

A general chain of coupled optical resonators is depicted in Fig. 4.3.1(a), where Λ denotes the period, Q_i the quality factor of the isolated cavities and Γ the coupling constant. The total length is $L = N \times \Lambda$ in the case of a finite chain of N cavities.

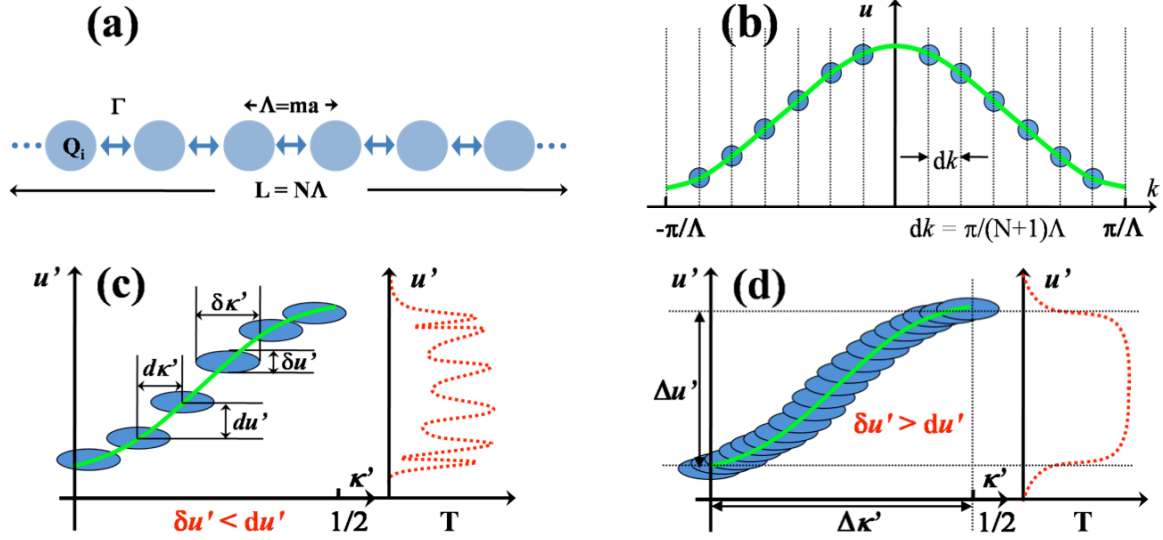


Fig. 4.3.1. (a) Illustration of a CCW chain: Λ denotes the period, Q_i the quality factor of the isolated cavities and Γ the coupling constant, the total length of a finite chain of N cavities is $L = N \times \Lambda$. (b) For chains made of N ($N=6$) cavities, the dispersion curve is sampled in N states with a constant spacing in k . (c) Schematic plot of the dispersion curve sampling and its corresponding transmission in case of discretised dispersion condition of $\delta u' < du'$. (d) The same as in (c) for smooth dispersion condition of $\delta u' > du'$.

The dispersion of such a chain of coupled resonators can be conveniently modeled by the Tight Binding Approximation (TBA) [132, 157, 159, 184-187], which is well known in solid state physics as a means to describe the formation of electronic bands in the crystals [188]. In most PhC CCW structures, the cavity separation is large enough so that the coupling strength between the two neighbors is sufficient to yield the dispersion curve, which is fully characterized by a few overlap integrals (namely S , R and T referred as shift, overlap and transfer integrals). The dispersion curve [188-190] of the infinite chain takes the well-known following form [191]:

$$\omega_i = \omega_0 + \frac{S + 2T \cos k_i \Lambda}{1 + 2R \cos k_i \Lambda} \quad (4.3.1)$$

which can often be approximated as:

$$\omega_i \approx \omega_0 + 2T \cos k_i \Lambda = \omega_0 + \Gamma \cos k_i \Lambda \quad (4.3.2)$$

where $k_i = i\pi/(N+1)\Lambda$ is the wavenumber, ω is the frequency of the state with index i ($i = 1 \dots N$), the bandwidth is 2Γ , and ω_0 is the resonance frequency of the isolated cavity. For slow light applications the operating point of interest is the inflection point at ω_0 . Although the group velocity v_g is maximum at this point ($v_g = \Gamma\Lambda$), the group velocity dispersion vanishes and dispersion can be considered linear with a good approximation.

4.3.1.2 CCW with discrete spectrum.

For chains of finite length of N cavities, the dispersion curve is sampled in N states with a constant spacing in k : $dk = \pi/(N+1)\Lambda$, as it can be inferred from *e.g.* periodic boundary conditions (Fig. 4.3.1(b)). The spacing in energy $d\omega$, is not constant: $d\omega = cdk/n_g$. If the linewidth of the CCW mode (δu) is narrower than the energy spacing du ($\delta u < du$), the dispersion curve will consist in N isolated points with equidistant k interval (dk) as illustrated in Fig. 4.3.1(c). Concomitantly, the optical transmission shall exhibit N well separated sharp peaks [157, 159]. Analogous conditions also apply along the k -axis between the CCW modes broadening in k -space (δk) and their separation dk (*i.e.* $\delta k < dk$). Such regime with sharp peaks in transmission or discrete energy spectrum occurs when the cavity number is small in regard of the cavity quality factor, Q , like *e.g.* in the work of Notomi *et al.* [155] where a finite chain of high intrinsic Q cavities ($Q_i > 10^5$) was discussed.

4.3.1.3 CCW with continuous dispersion.

In order to be able to define a group velocity and to achieve a flat transmission band, a continuous mode spectrum must be ensured, both along k and u , *i.e.* $\delta k > dk$ and $\delta u > du$. Remarkably, continuity in k is **always** fulfilled: the mode broadening (δk) due to the finite size of the coupled states that extend over L is always greater than the mode separation due to the finite number of cavity dk : $\delta k \geq \frac{2\pi}{L} = \frac{2\pi}{N\Lambda} > dk$.

However the continuity in frequency: $\delta u > du$, is not necessarily fulfilled. Elementary algebra leads to the condition: $mNn_g\delta u > 1$, which can be also written as: $mNn_g u > Q_N(\kappa)$ or alternatively $Nn_g\delta u' > 1$ and $Nn_g u' > Q_N(\kappa')$, where $Q_N(\kappa)$ is the CCW mode quality factor. The quality factor depends on both the number of cavities and the location of the mode wavevector within the Brillouin zone (with respect of the far field radiation pattern of the isolated cavity) as demonstrated in Ref. [14]. In a first approximation we will consider the quality factor constant. It is independent from N and κ , and of comparable magnitude as the isolated cavity quality factor, Q_i . Such approximation is exact for an isolated cavity whose quality factor is not limited by the out of plane radiation, like it would be for coupled micro-ring resonators. This leads to the frequency continuity condition among the group index, the number of coupled cavities and the quality factor:

$$mNn_g u > Q \quad (4.3.3)$$

Relation (4.3.3) provides a quantitative condition of the intuitive fact that the better the cavity (larger Q), the more cavities (larger N) must be coupled to achieve a relevant group index

n_g . A schematic illustration of frequency continuity is plotted in Fig. 4.3.1(d).

4.3.2 Design, fabrication and characterization.

4.3.2.1 Structure Design

To experimentally illustrate the regimes of discretized and continuous dispersion, we will focus on two different types of constituent PhC cavities with different Q factors. The first type is a standard L3 cavity, which is defined by removing three holes in Γ -K direction and is characterized by moderate Q factor of approximately 4500. Another type of PhC cavity is a modified L3 with a relatively high unloaded Q factor of approximately 8000. The latter was achieved by decreasing the diameter of adjacent holes by a factor of 0.8 with respect of the bulk PhC. In the current CCW designs, the neighbouring cavities are separated by one or two-hole barriers, for the standard L3 and modified L3 cavities, respectively. In both cases we assume cavities are weakly coupled due to the sufficient large separation between the individual cavities. However, the number of holes in the barriers determines the coupling strength between the individual cavities (*i.e.* the magnitude of overlap integrals R in Eq. 4.3.1), and hence the bandwidth of the coupled-cavity mode. The number of cavities: N varies from $N = 1$ to 100.

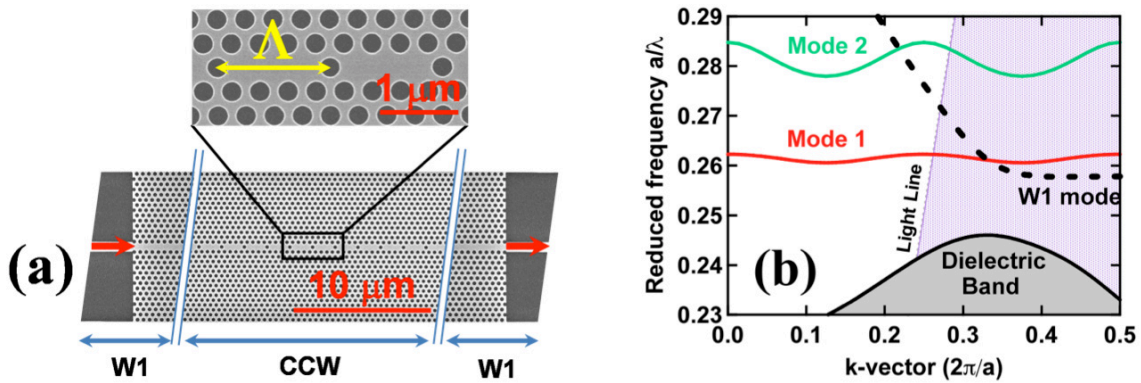


Fig. 4.3.2. (a) Top view SEM image of a CCW sample with 1-hole in the barriers coupled in-line to $15 \mu\text{m}$ long W_1 access waveguides. Insert image shows a detailed zoom of CCW cavity. (b) Theoretical dispersion calculated with Guided Mode Expansion method showing the dielectric band (gray shadow), W_1 mode (dashed black curve), first order (red curve) and second order (green curve) CCW mode.

For the design with one-hole long barrier, an example of a CCW is shown in the SEM image of Fig. 4.3.2(a). Coupling between the access waveguides and the CCW chain was achieved by a 25 period long W_1 waveguide section in so called inline configuration, which improves the coupling efficiency and typically allows for high transmission through the resonator [155]. The corresponding theoretical dispersion diagram is shown in Fig. 4.3.2(b) and calculated by the guided mode expansion (GME) method [183]. The 1st order CCW mode is

found at the reduced frequency $u = 0.261$, and is well separated from both the dielectric band ($u < 0.245$) and the 2nd order CCW mode ($u > 0.28$). In agreement with the TBA theory, the fundamental CCW mode is characterized by flat and sinusoidal dispersion curve, centred at the resonance frequency of an isolated L3 cavity. The calculated mode bandwidth is wider than 8 nm, and a group index value of $n_g \approx 50$ is predicted at the inflection point. The 2nd order CCW mode plotted in Fig. 4.3.2(b) is not interesting, due to the fact that its odd symmetry doesn't allow an efficient light in-coupling from the waveguide. For the two-hole barrier design, the GME simulations predict even flatter dispersion curve with the group index $n_g \approx 100$, which is achieved at the expense of a reduced bandwidth ~ 5.5 nm.

4.3.2.2 Fabrication and characterization technique.

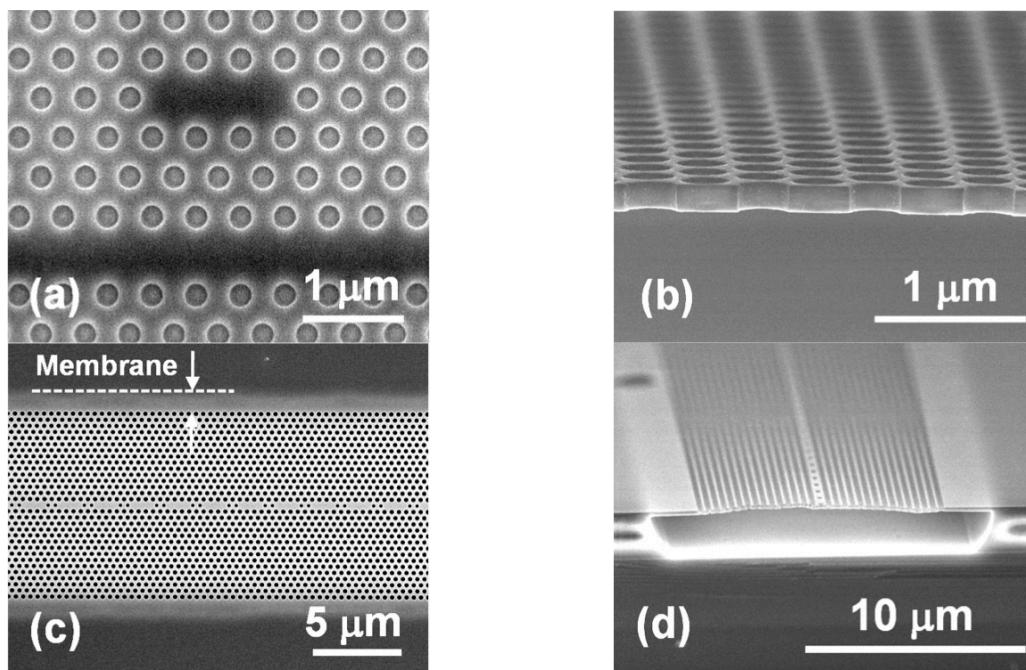


Fig. 4.3.3. (a) Top view SEM image of a standard PhC L3 cavity on ZEP resist (after development). (b) Side view SEM image of Si membrane structure after direct ICP dry etching and BHF wet etching. It exhibits vertical and smooth sidewall profiles. (c) Top view SEM image of Si air membrane after BHF release of the BOX layer showing the membrane border. (d) Side view SEM image of Si air membrane structures after releasing the BOX layer in the BHF.

The CCW devices of the above described design were fabricated on a 220 nm-thick Silicon-on-Insulator (SOI from Soitec, France) wafer with 2 μm BOX layer. The bulk photonic crystal filling factor was set to 35% on the design mask, and the lattice constant a was scanned between 430 and 450 nm to ensure that the fundamental CCW mode falls in the 1.55 μm wavelength range. The fabrication technique employed here is the same as described in Chapter 3. The air hole radii (r) of the PhC after fabrication are 266, 275 and 287 nm for lattice

constants of 430, 440 and 450 nm, respectively, yielding an air filling factors of 36%, which is very close to the design.

The transmission properties of the CCW devices were characterized using the setup as mentioned in section 4.1.1. Direct imaging of the sample surface (Fig. 4.3.4(a)) yields the near field, or real space image. Although the spatial resolution of the infrared imaging doesn't make it possible to resolve the detailed features of the field distribution, it still allows one to closely visualize the light propagation along the coupled cavity chain, as shown in Fig. 4.3.4(a). The optical propagation loss can be determined by the light scattering method [192, 193]. Assuming the scattering in the films is uniform, the intensity $I(x)$ of the guided mode is therefore proportional to the scattering intensity $I_{SC}(x)$ at the same position, and the attenuation coefficient α (in dB/cm) will be:

$$\alpha = -\frac{10 \log\left[\frac{I(x)}{I(0)}\right]}{x} = -\frac{10 \log\left[\frac{I_{SC}(x)}{I_{SC}(0)}\right]}{x} \quad (4.3.4)$$

A statistical linear fit of the data to the logarithm of the scattered light intensity versus the distance propagated down the waveguide yielded a waveguide loss as a slope. From the exponential decay of the collected light intensity as shown in Figs. 4.3.4(a) and 4.3.4(b) we can retrieve that the propagation loss is around 200 dB/mm at 1584 nm. The real-space imaging allows us to identify the regions of increased structural disorder at positions where the light propagation is abruptly decreased or terminated. Thus the effects of out-of-plane radiation loss and disorder can be distinguished. This cannot be done by a simple transmission experiment.

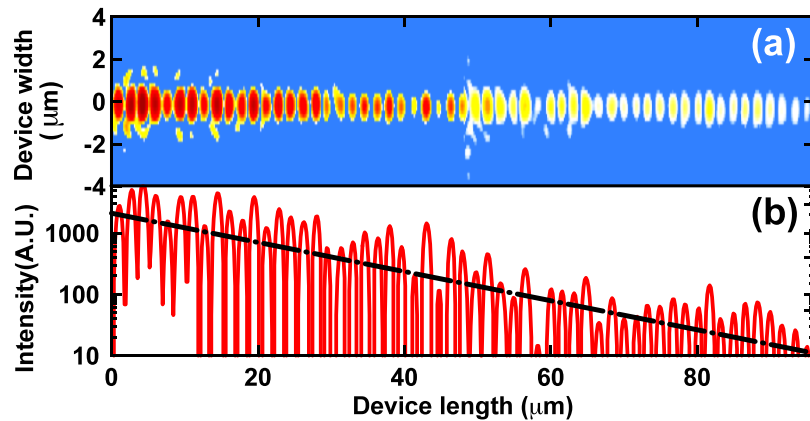


Fig. 4.3.4. (a) 2D logarithmic (log) scale plot of real space intensity at wavelength 1584 nm for 1-hole barrier CCW device with more than 55 cavities coupled. (b) Corresponding 1D log scale plot shows linear light intensity decay along the propagation direction at zero position (along the device width axis of Fig. 4.3.4(a)).

4.3.3 Experimental investigation of the CCW.

In Fig. 4.3.5, we show the full experimental dispersion curve of a CCW made of 6 cavities. As expected from the TB model, the number of sampling points of the dispersion curve is equal to the number of coupled cavities: 6 distinct Bloch modes are observed and are distributed along the theoretical dispersion curve. The inter cavity coupling strength defined by 2 holes in the barrier results in a bandwidth of $\Delta u = 0.0011$ ($\Delta\lambda = 6.3$ nm). And the group index extracted from the linear part of the underlying ideal dispersion curve (dashed black curve in Fig. 4.3.5) is around 90.

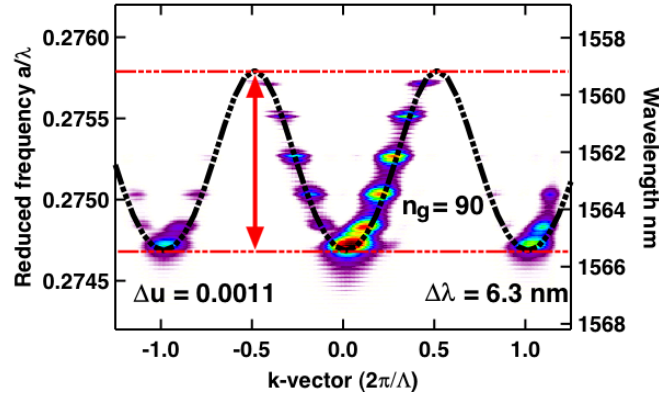


Fig. 4.3.5. Experimental dispersion curve of a CCW made of 6 cavities. Black dashed line shows the calculated dispersion with GME method.

However, note that the spacing in k between the respective coupled cavity states is not constant as predicted by the TB theory. The deviation between the experimental k_i and the ideal sampling positions (vertical dash lines) is highlighted in Fig. 4.3.6. The closer to the BZ centre band edge ($k = 0$), the larger discrepancy. The main reason of such discrepancy is to the finite number of cavities in the chain: the CCW chain creates different boundary conditions for the first cavity and the cavity in the middle of the chain.

The far field intensity profiles of the six resonant states as well as their Q-factors are plotted versus the k-vector in Fig. 4.3.6. It can be observed that the intensity of the emitted light is extremely weak at the BZ boundary and it increases as the $k_{//}$ vector approaches the Γ point ($k_{//} = 0$). Accordingly, the experimental Q factor of the six resonant states monotonously increases from $k_{//} = 0$ towards the BZ boundary. These variations result from the modulation of the intensity profile of the CCW emission by the intensity profile of the single cavity constituent, as explained in details in Ref. [16]. The specific emission profile of the L3 cavity is plotted in Fig. 4.3.6, it follows that the Q factor of the coupled states can be larger or smaller than the Q factor of a single L3 cavity ($Q \sim 4500$) reaching the value larger than 8000 for the state closest to the BZ boundary.

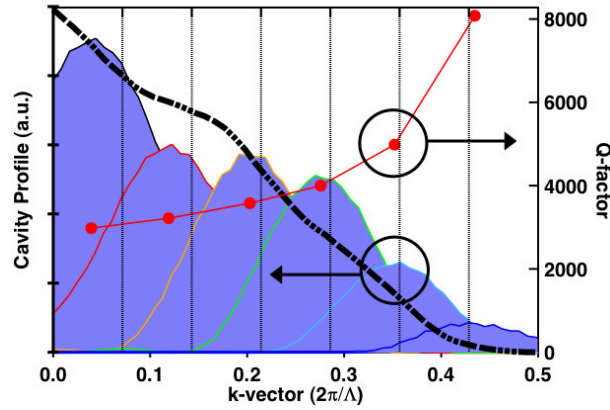


Fig. 4.3.6. Comparison of Q factor of the six-coupled states and their integrated far field profiles (fill-to-zero plots) with the far field profile of a single L3 cavity along $k_{//}$ (dashed black line). Vertical dotted lines indicate the expected k vector positions from the TB theory.

The impact of the frequency dependent out-of-plane loss on the propagation is highlighted in Fig. 4.3.7. Fig. 4.3.7(a) shows the real-space decay of the light propagating along the coupled-cavity chain. In the same way as in Fig. 4.3.5(a), the intensity profiles in real space along the propagation direction have been stacked and plotted versus frequency to achieve the 2D intensity plot. The dashed lines at sample position $0 \mu\text{m}$ and $12.6 \mu\text{m}$ in Fig. 4.3.7(a) show the positions of the first and last cavity in the CCW chain. When excitation wavelength of the coupled state is shorter than 1564 nm , no intensity decay in the propagation direction can be observed. This situation changes at longer excitation wavelengths. *i.e.*, $\lambda > 1564 \text{ nm}$, where an important intensity decay occurs.

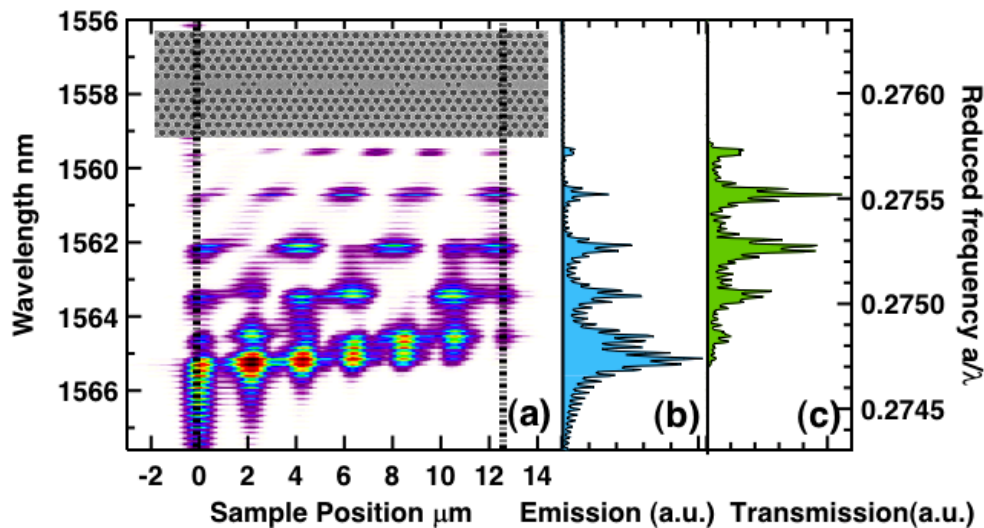


Fig. 4.3.7. (a) Real space emission along the propagation direction as a function of the wavelength for a CCW sample made of 6 cavities with 2-hole barriers. Insert: the SEM top view image. (b) Integrated emission intensity along the light propagation direction. (c) Experimental transmission spectrum.

Figures 4.3.7(b) and 4.3.7(c) show the spatially-integrated emission and in-line transmission spectra of the CCW respectively. The increase of emission intensity, which accounts for a strong radiation loss, is well correlated with the drop of the in-line transmission, except for the mode that has the largest Q factor. Two effects can be at the origin of the low transmission for the high Q resonant mode. One reason is that the input coupling of the light into the mode is non efficient due to an impedance mismatch between the W_1 waveguide and the CCW. The other one is due to the structural disorder, which induces excessive back reflection or in-plane scattering loss.

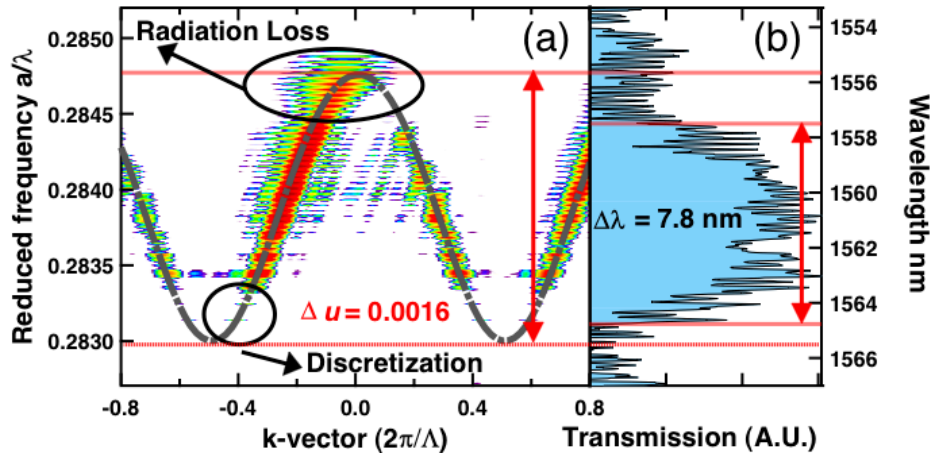


Fig. 4.3.8. (a). Logarithmic scale dispersion curve of a CCW made of 20 L3 cavities with 1-hole barrier design. (b). Corresponding transmission spectrum.

Fig. 4.3.8(a) shows a continuous dispersion curve achieved with a CCW made of $N = 20$ coupled L3 cavities with 1-hole barrier. The measured dispersion curve is plotted in logarithmic scale to visualize the weak signal detected from the Brillouin zone boundary. The continuous dispersion of this CCW device shows negligible intensity variation for almost the entire dispersion bandwidth, except the low frequency band-edge. For the current structure, the periodicity of the coupled cavity chain is $\Lambda = 4a$, which results in a bandwidth of $\Delta u = 0.0016$ ($\Delta\lambda = 7.8$ nm), *i.e.* a bandwidth that is 1.45 times wider than the CCW with two holes in the barriers. The corresponding group index measured in the linear part of the dispersion curve is around 55. In concordance with the previous case, the CCW exhibits the largest out-of-plane radiation losses at the centre of the Brillouin zone with $k = 0$, which is correlated with the linewidth broadening and an abrupt drop in the transmission shown in Fig. 4.3.8(b). At the low frequency band-edge of the CCW band where the dispersion curve approaches the Brillouin zone boundary, the dispersion curve stops being continuous. The transition from continuous to discrete dispersion can be explained by the Q factor variation along k . The number of cavities $N = 20$ is sufficiently large to ensure a continuous transmission only in the linear part of the dispersion curve where the Q-factor of the resonant CCW mode is comparable to the Q of an

isolated cavity. However at the BZ boundary, a strong increase of the Q is expected (see Fig. 4.3.5), as a consequence the mode linewidth ($\delta\omega$) is narrowed in frequency. Such narrowing eventually leads to a no longer fulfilled condition for frequency continuity given by Relation 4.3.3: $mNn_g u > Q$ with same number of cavities at the band-edge.

The in-line transmission plotted in Fig. 4.3.8(b) is continuous and constant over more than half of the overall bandwidth, except for the two CCW band-edge regions. The transmission vanishes at the high frequency band-edge due to the strong out-of-plane loss, while at the low frequency band-edge it gets discretized by the Q factor modulation and finally hindered by inefficient coupling (impedance mismatch) and/or structural residual disorder as explained in Ref. [16].

To summarize this part, an important point to consider with CCW is the interplay of the out-of-plane losses and the coupling, which governs the useful bandwidth of the structure. The out-of-plane losses can be controlled by a proper choice of the single cavity used as unit cell, *i.e.* a properly engineered constituent cavity with a constant intensity distribution along $k_{//}$ vector direction in the far field. Such design could lead to constant out-of-plane losses (regardless of k -vector) and smooth transmission along the entire CCW dispersion band. The control of the structural disorder is mainly a technological issue. The detrimental effects of structural disorder observed in most of the slow light systems, *e.g.*, W_1 PhC waveguides that have been mentioned in section 4.2 [16], were not identified in these two CCW slow light systems. The reason will be discussed in the following theoretical considerations on slow light intrinsic limits.

4.3.4 Delay Bandwidth Product and its upper limit

The periodic nature of a PhC structure imposes a limit between group index and the achievable energy bandwidth that is often overlooked. When discussing a low v_g in a PhC system, two important optical properties need to be considered: the frequency bandwidth of the effect and higher-order dispersion [64]. A fundamental limit to the first of these is the delay–bandwidth product (DBP) [194-196], which affects all approaches to slow light. Although a wide bandwidth is desirable in most applications, it often comes at the price of less delay. The DBP means that the extent to which the group velocity of light is reduced must be balanced with the required bandwidth for the application in mind. Regarding the second issue, the higher–order dispersion that usually occurs in simple slow light PhC W_x waveguides severely distort optical signals. As mentioned before, such distortion can be eliminated either by using dispersion-compensated or zero-dispersion slow-light devices. Here we will discuss the DBP and its upper limits on various slow light PhC systems.

Because of the periodicity of the dispersion curve in the reciprocal space, the wavevectors span that can be used is limited from the zone centre to the Brillouin zone boundary. The maximum bandwidth along k is $\Delta\kappa' \leq \frac{1}{2}$, which leads directly to the maximum accessible bandwidth as a function of the group index :

$$2n_g\Delta u' < 1 \text{ or } 2n_g m\Delta u < 1 \quad (4.3.5)$$

It follows that the normalized delay bandwidth figure of merit, DBP, as defined by Refs. [141, 197, 198] is bounded by its upper limits $\lambda/2\Lambda$:

$$DBP = \frac{n_g\Delta u}{u} = \frac{n_g\Delta u'}{u'} \leq \frac{1}{2u'} = \frac{\lambda}{2ma} = \frac{\lambda}{2\Lambda} \quad (4.3.6)$$

Structure	m	n_g	$\Delta\lambda$ (nm)	Δu	u	DBP ($n_g\Delta u/u$)	$\lambda/2\Lambda$	DBP/($\lambda/2\Lambda$)
W_1 [136]	1	35	10	0.00167	0.2395	0.24	1.82	0.13
CCW_L3/this work	4	55	7.9	0.00161	0.2840	0.31	0.42	0.74
CCW_L3/this work	5	90	6.3	0.00104	0.2753	0.34	0.35	0.97
CCW_hetero[156]	6	105	2.6	0.00042	0.2778	0.18	0.30	0.60
CCW from Ref. [155]	7	120	1.6	0.00028	0.2687	0.13	0.26	0.50

Table 4.3.2. Comparison of experimental demonstrations on slow light PhC structures and their intrinsic limitations.

Table 4.3.2 compares results reported in the literature: the last column lists the ratio between the reported DBP and its upper limit. This ratio is in the range of $0 < DBP/(\lambda/2\Lambda) < 1$, the general design rule for slow light device is to achieve experimental DBP as close as possible to its upper limit, the ultimate case will be $DBP/(\lambda/2\Lambda) = 1$.

The first conclusion we can draw from Table 4.3.2 is that there is still margin for improvement (from 0.13 to 1) on W_x PhC waveguide structures ($m = 1$). However the price to pay is to improve the fabrication induced disorder (*e.g.* hole radius and position variations) in the level of Angstrom (\AA) which is extremely challenging for current state of art technology [16]. Secondly for different types of CCW systems, the lowest ratio of $DBP/(\lambda/2\Lambda)$ is 0.5, which is far beyond the W_1 PhC waveguide cases (0.13). In particular for our CCW device with 2-hole barriers, the ratio is as high as 0.97, which means the experimental achieved DBP is very close to its theoretical limit.

Note that the W_1 PhC waveguide and the CCW PhC devices were exposed with the same EBeam machine, despite the successive dry etching processes were different, the fabrication induced disorders should be still in the same order of magnitude. The large difference in $DBP/(\lambda/2\Lambda)$ between CCW and W_x can be explained as following: the states of the PhC CCW system are formed with localized states that have already averaged the disorder over their large

cavity size ($\Lambda = ma$, typically m is larger than 4). This size averaged disorder feature benefits the PhC CCW systems to be less impacted by the same amount of fabrication disorder. Consequently the CCW systems are robust to disorder whilst larger group index can be achieved than W_x PhC waveguide does. In the W_x PhC waveguide case, the disorder is averaged over the smallest supercell ($\Lambda = a$), which makes it very sensitive to disorders and limits its achievable group index.

In case of PhC CCW systems, both the discretized and continuous designs in Fig. 4.3.5(a) and Fig. 4.3.8(a) show nice dispersions where the wave number k can follow the ideal dispersion relation in the entire bandwidth. On the contrary, in case of PhC W_x system [16], large bandwidth of ‘diffusive regime’ is found where the wave number k cannot follow the ideal dispersion relation anymore. The disappearance of the ‘diffusive regime’ in CCW system is the strong evidence to prove that the CCW is a better slow light candidate than the W_x waveguides.

4.3.5 Summary

In this section, we have presented a slow light system based on coupled photonic crystal cavities. Depending on the constitutive Q factors, both discretized dispersion spots with transmission peaks, and continuous dispersion with flat transmission band have been theoretically presented and experimentally measured. Two types of CCWs with moderated Q-factors have been investigated in detail, in terms of design, simulation, fabrication, and characterization. Group index of n_g of 55 and 90 for different cavity periods have been experimentally achieved. Impacts of out-of-plane radiation loss and structural residual disorder on CCW dispersions have been experimentally investigated and discussed. Radiation losses and Q factor variation along dispersion at CCW band-edges are found to be the most important factor which determines the CCW performance. These investigations give design rules to reduce losses and give fundamental boundaries to what can be expected in CCW and PhC slow light structures.

Chapter 5

5. Experimental investigation of PhC nano-cavity devices in Near Infra-Red

As mentioned in Chapter 4, the second type of passive NIR PhC devices studied under the scope of this PhD thesis is high Quality (Q) factor PhC cavities. The PhC defect cavity is the basic block that constitutes the slow light photonic crystal coupled cavity waveguide. Beside its application in the slow light field, the high quality factor 2D photonic crystal nanocavities are also drawing attentions in various fields, *e.g.*, ultrasmall filters [181, 199, 200], ultrasmall sensors [5], nanolasers [201], single-photon emitters [202], compact optical-buffer memories [203], and quantum information processing [204]. This is due to the fact that the high quality factor 2D photonic crystal nanocavities allow one to trap photons for a long time within an extremely small volume with enhanced light-matter interaction. Therefore besides the fabrication and investigation of coupled cavity waveguides, it is interesting and necessary to study optical properties of the single cavity.

Two types of high Q PhC cavities have been investigated: the conventional PhC cavities and the air-slot cavities. For the conventional PhC cavities, the strong light-matter interaction occurs in the high index material where the maximum of optical field is located. Strong non-linear effects and bistable behaviour have been observed. On the contrary, the air-slot cavities can confine TE polarized modes in the air, thus allowing for a large interaction of the optical field with the low-index medium. Therefore such air-slot cavity can act as a highly sensitive gas index sensor.

This chapter consists of 3 sections. Section 5.1 first starts with the general rules for designing high Q factor cavities using the Fourier transform analysis technique [205-207]. Section 5.2 shows the experimental results of the conventional cavities with maximum optical field localized in the high index region. Q factor as high as 5×10^5 is obtained. Section 5.3 shows the experimental results of the air-slot cavity with maximum optical field localized at the low index region. The high quality factor $\sim 2.6 \times 10^4$ of the air slot cavity allows us to achieve a high experimental sensitivity of 510 nm per refractive index unit (RIU).

5.1 General rules for designing high Q factor cavities

5.1.1 The Gaussian envelope function and the Fourier transform.

The quality factor, or Q factor is a very important parameter that specifies the performance of a resonant cavity [208]. It is determined by the energy stored in the cavity (W) and the dissipated power per cycle (P/ω):

$$Q = \omega \frac{W}{P} \quad (5.1.1)$$

where ω is the resonance frequency. The Q factor can be expressed as:

$$Q = \frac{\nu}{\Delta\omega_c} \quad (5.1.2)$$

Thus the cavity Q factor can be interpreted as the ratio between the resonance frequency ν of the given mode and its linewidth $\Delta\omega_c$. When there is no material absorption or out of plane diffraction, the Q is determined by the reflection loss at the interface between the interior and exterior of the cavity. Total internal reflection (TIR) and/or Bragg reflection are generally used for light confinement. For a cavity with size much larger than the wavelength of light, very high Q result has already been achieved [209]. In that case, the behaviour of light confined in a large cavity obeys ray optics theory, and each ray of light reflected at the interface can be designed to fulfill TIR or Bragg reflection conditions. For much smaller cavities, *i.e.*, cavity size in the wavelength scale, Q is greatly reduced because deviation from ray optics becomes important. In this case the light confined in a very small area consists of numerous plane wave components with wavevectors of different directions due to the localization of light.

2D PhC wavelength-sized nanocavities are good candidates to achieve high Q factors. Such cavities provide in-plane confinement via the PBG effect, while on the third direction: the vertical direction, the confinement is provided by the TIR. However such TIR confinement is normally insufficient, this leads to the fact that the Q factor is limited by vertical radiation loss. The vertical radiation loss is proportional to the radiative fraction of the Fourier transform of the mode profile that lies within the light cone. The relative weight of Fourier components that lies within the light cone has to be minimized in order to achieve a high Q value [205, 210]. In 2003, Susumu Noda's group reported a general design concept for the realization of high-Q nanocavities in 2D PhC slabs: To suppress radiation loss, the envelope of the cavity mode field should follow a Gaussian function, and the field profile should vary smoothly and gently [205]. The strategy is simple: if the cavity mode is concentrated outside the light cone of air in the 2D k space, the cavity mode cannot be coupled to the radiation modes. At the same time the mode is

kept as confined as possible, thanks to the fact that Gaussian function are Fourier transform limited (*i.e.* they realize the minimum of value of $\Delta k \cdot \Delta x < 2\pi$).

In this thesis work, different types of high Q PhC cavities have been reviewed with such design principle, and then they were fabricated and experimentally characterized. Note that apart from the vertical radiation loss, there are some other parameters also play important roles in achieving high Q factor cavities: *e.g.*, the waveguide-cavity coupling conditions, the fabrication imperfections and the non-linear effects.

Here we start from reminding the theoretical background that is used for the design of high Q cavities. The spatial Fourier transform of the field profile in the decomposition of the field on a plane wave with in-plane wavevector $\{k_{//}\}$. If $|k_{//}| \leq k_0$ (where k_0 is the modulus of the wavevector in the cladding, air in case of membrane), this means the mode is no longer confined in the waveguide and leaks out into air, such range is called the “leaky region” or the light cone. On the other hand, for $|k_{//}| > k_0$, the mode is confined in the waveguide by the TIR. Assume that in an ideal long one-dimensional cavity, the electric field profile of the cavity mode has a sinusoid envelope function. Such cavity mode profile will be ideal because after the spatial Fourier transform (FT), there are no components at all in the leaky region. However such mode profile is delocalized in the entire cavity, which leads to a large mode volume (V). When the length of the cavity is reduced, the abrupt changes in the envelope function at both edges will introduce large radiation losses, thus leads to low Q.

In order to realize a high-Q photonic nanocavity, the envelope function should not have low-frequency components in the leaky region but should remain spatially localized, meanwhile, abrupt changes in the envelope function should be avoided. Reports on different ‘gentle confined’ functions, *i.e.*, Lorentzian and the Gaussian envelopes had been investigated, with the conclusion that the envelope of the PhC cavity mode field should have no abrupt changes and should ideally follow a Gaussian function [206].

It has been pointed out that the lower spatial frequency components of the envelope spectrum, with $-k_0 \leq k_{//} \leq k_0$, are transferred to the leaky region. Here we will illustrate the importance of the smoothness in the envelope function, by comparing an ideal long Gaussian envelope function (black curve in Fig. 5.1.1(a)) with a truncated short Gaussian envelope function (red dotted curve in Fig. 5.1.1(a)). For comparison purpose between the truncated Gaussian profile and the simulated E_y field profile, we set 11 lattice constants as the length for both cases. As a consequence, after Fourier transform, such truncated Gaussian envelope function has a large amount of Fourier components in the leaky region (Fig. 5.1.1(b) red curve), due to the abrupt ends in the envelope function. In contrast, the ideal Gaussian envelope function has only a

small amount of Fourier components in the leaky region (Fig. 5.1.1(b) black curve), due to the smooth variation of the envelope function in real space. In terms of radiation losses, the first case suffers much higher radiation losses than the latter one.

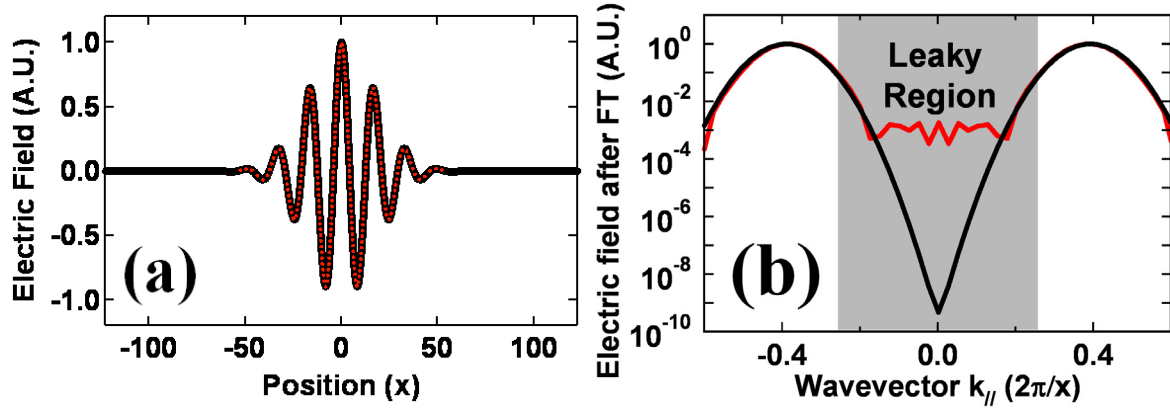


Fig. 5.1.1. (a). Electric field profile of the cavity mode with a Gaussian envelope function. Black curve represent the full Gaussian envelope function, red dotted curve represents the truncated Gaussian envelope function which has the same length (11 periods) as the following simulated E_y field profiles. (b). Respective spatial Fourier transform spectra of full Gaussian envelope function (black) and the truncated one (red). The red one sets the theoretical limitation for our calculation.

For the real 2D PhC nanocavity calculation, the eigenfrequency and the electric field profile of the cavity mode are calculated by the PWE method as mentioned before in Chapter 2. Due to the limited computation capacity, the 2D supercell was set to a maximum length of 11 lattice periods, in order to obtain accurate enough electric field maps. For easy comparison purpose, the length of the cavity field map in this case is as long as the truncated Gaussian profile. The electric field profile of the truncated Gaussian envelope function electric field profile is considered as an effectively ‘ideal’ one, which sets the upper calculation limits for all the forthcoming simulations.

By using the PWE method, we can calculate the E_{xy} field maps for the cavity mode. The y component of the electric field (E_y in Fig. 5.1.2(b)) is the dominant field because it has large amount of low frequency components in the leaky region. On the contrary the x component of the electric field (E_x in Fig. 5.1.2(a)) has few components in the leaky region, which are normally several orders of magnitude lower than the E_y case. This is because the E_x field pattern in real space is antisymmetric about the centerline of the cavity along both the x and y directions, as seen in Fig. 5.1.2(a), leading to the cancellation of light in the far field [206, 211]. The logarithm (Log) scale plots of 2D Fourier transformed spectra of E_x and E_y electric field profiles for an L3 cavity in Fig. 5.1.2(c) and Fig. 5.1.2(d) confirms that the E_x field is negligible for the Q factor

optimization, and E_y components inside the leaky region should be reduced in order to reduce the radiation loss.

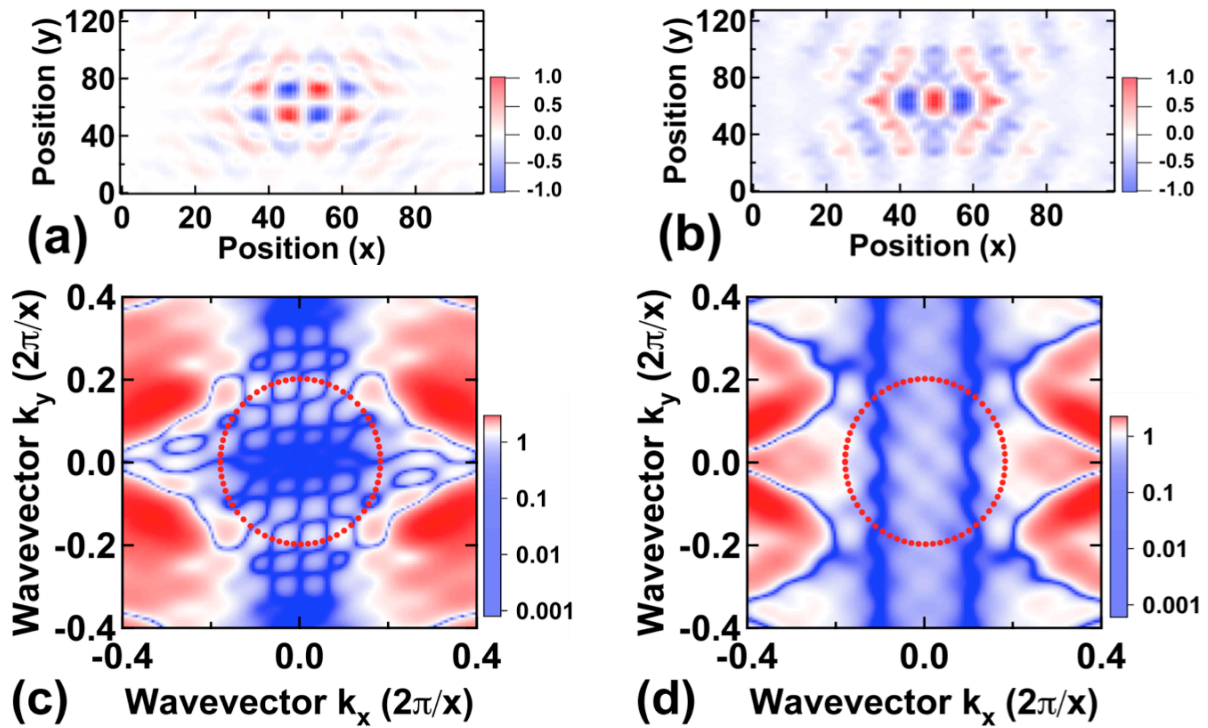


Fig. 5.1.2. (a) and (b). E_x and E_y field distributions of the standard L3 PhC cavity. (c) and (d). Logarithm scale plots of 2D Fourier transform spectra of E_x and E_y electric field profiles for the standard L3 cavity.

5.1.2 High Q factor cavity designs

5.1.2.1 Width modulation on heterostructure PhC cavity

The shifted-hole L3 cavities [205], the multi-heterostructure PhC cavities [210] and the width-modulation PhC cavities [212] achieved very high experimental Q factors. Despite their respectively different forms in terms of photonic crystal engineering: shifting holes near the L3 barrier, gradually tuning the lattice constants and locally tuning the waveguide width, all the designs obtained very similar Gaussian like E_y field profiles.

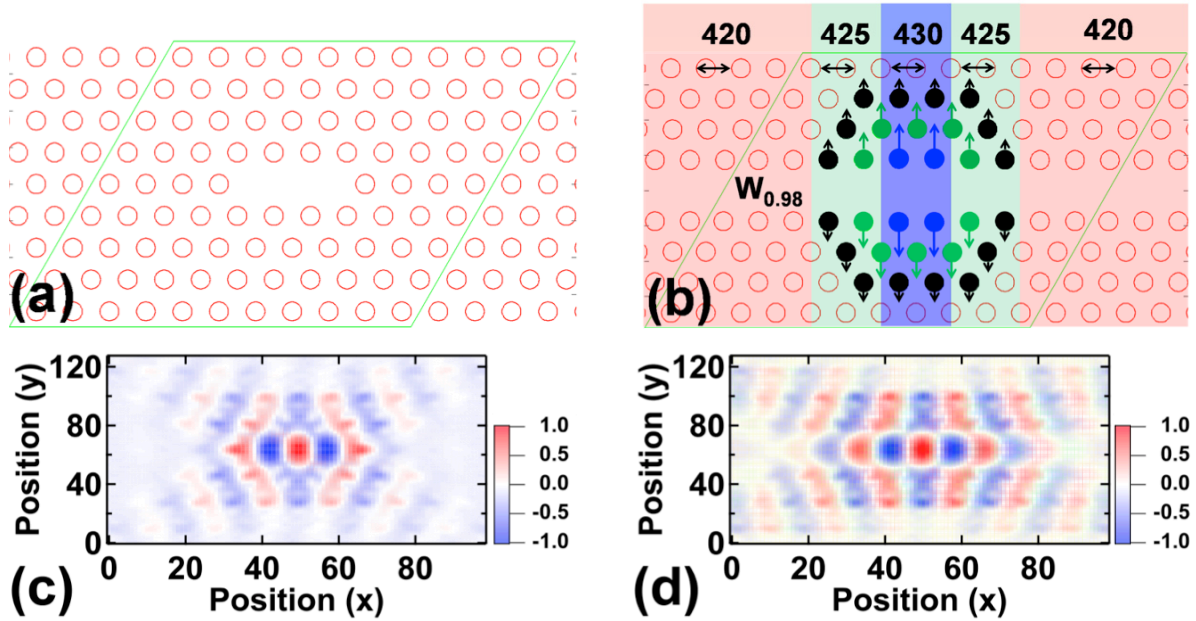


Fig. 5.1.3. (a). Layout of standard L3 PhC cavity. (b). Layout of width modulation on heterostructure PhC cavity. (c). E_y field distribution of the L3 cavity mode. (d). E_y field distribution of the width modulation on heterostructure PhC cavity mode.

Here I propose a new type of PhC nanocavity, by combining the Γ K-direction modification in PhC lattice constant and Γ M-direction modification of waveguide width. Such method is assumed to achieve smooth and gentle confinement of the E_y field profile by superposition the two effects. A standard L3 cavity is also modeled at the same time as a reference cavity, as shown in Fig. 5.1.3(a). The bulk PhC lattice constant was set to 420 nm, the center cavity has a lattice constant modulation as: **420/425/430/425/420 nm**, shown respectively by the colour shadows (Red/Green/Blue) in the layout plot of Fig. 5.1.3(b). Meanwhile, the waveguide width is increased by 4.2/8.4/12.6/8.4/4.2 nm, shown respectively by the filled holes (Black/Green/Blue). Only the E_y mode profiles are plotted in Fig. 5.1.3(c) and Fig. 5.1.3(d) for the L3 and the width modulation on heterostructure cavity. The E_y field distribution of the latter case is more gentle and smoother.

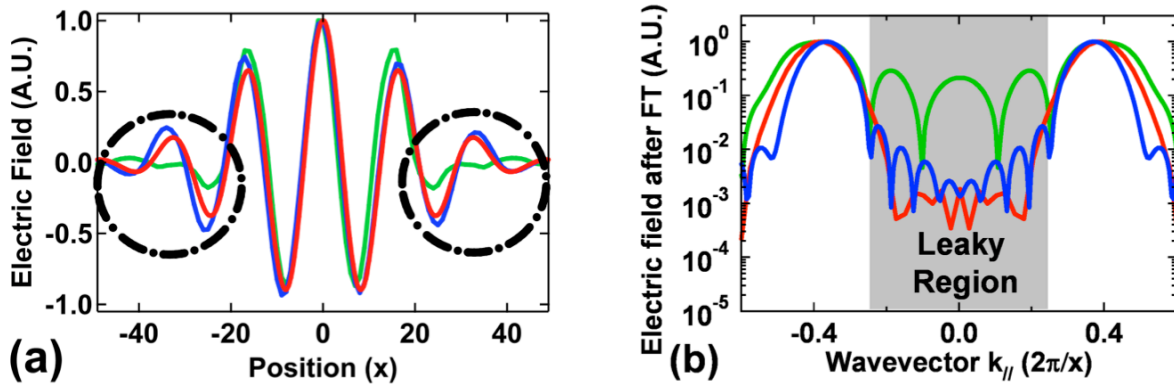


Fig. 5.1.4. (a). The 1D E_y intensity profiles at position $y = 0$ for the L3 cavity and width modulation on heterostructure cavity as green and blue curves,. Red curve represents the truncated Gaussian envelop function cut with the same length with the others. Dashed circles point out the discrepancy with the truncated Gaussian envelop function. (b). The electric fields after performing the spatial Fourier Transform. The green, blue and red curves represent the L3 cavity, the width modulation on heterostructure cavity and the truncated Gaussian envelop profile, respectively.

In Fig. 5.1.4, the 1D E_y field intensity profiles of both cavities at position $y = 0$ are taken from image Fig. 5.1.3(c) and Fig. 5.1.3(d) and plotted as green and blue curves, respectively. The shape discrepancy between the standard L3 profile (green) and the truncated Gaussian envelop function (red) are marked by the dashed circles in Fig. 5.1.4(a). The blue curve represents the electric profile of the width modulation on heterostructure cavity. It shows pretty good agreement with the ideal curve. This means, compared to the standard L3 cavity, the width modulation on heterostructure cavity should exhibit much lower radiation losses, with only a small low frequency component in the leaky region. As a consequence, as shown in Fig. 5.1.4(b), the intensity of the width modulation on heterostructure cavity mode after spatial Fourier Transform is almost as low as the red theoretical calculation minimum (truncated Gaussian), with only less than 5 dB contrast. On the contrary for the non-optimized standard L3 cavity, the low frequency components in the lightcone after spatial Fourier transform are several orders of magnitude higher than the optimized counterpart.

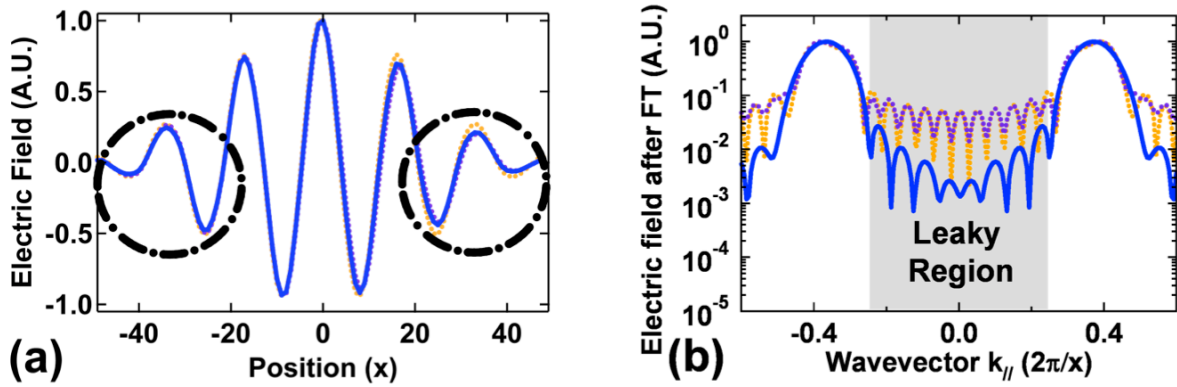


Fig. 5.1.5. (a). The 1D E_y intensity profiles at position $y = 0$ are taken from images in Fig. 5.1.3(c) and Fig. 5.1.3(d) respectively and plotted for the heterostructure cavity and local width modulation cavity as orange and violet dotted curves. Blue curve represents the 1D E_y intensity profile of the width modulation on heterostructure cavity. Dashed circles label the discrepancy between each other. (b). The electric fields after performing the spatial Fourier Transform. The orange, violet and blue curves represent the heterostructure cavity, the local width modulation cavity and the width modulation on heterostructure, respectively.

To compare the width modulation on heterostructure with the reported width modulation cavity and the heterostructure cavity, the linear profiles of the E_y field distribution at position $y = 0$ for all the designs are taken and plotted in Fig. 5.1.5(a). It can be seen that all the three schemes show negligible variations. However, as mentioned before, even small discrepancy can lead to large amount of low frequency component in the leaky region. The comparative plot in Fig. 5.1.5(b) shows the electric field intensity after FT of the three different designs. Although the width modulation cavity and the heterostructure cavity achieved experimental Q factor as large as 10^6 , our new design of width modulation on heterostructure: two dimensional PhC engineering for gentle mode confinement in both ΓK (lattice constant) and ΓM (waveguide width) directions is much better. The intensity of the width modulation on heterostructure cavity mode after spatial Fourier Transform is about 15 dB lower than both of the two reported designs, which implies that the new proposal can further reduce the radiation losses. The 2D Fourier transformed spectra of E_y electric field profile for this width modulation on heterostructure cavity is plotted in Fig. 5.1.6.

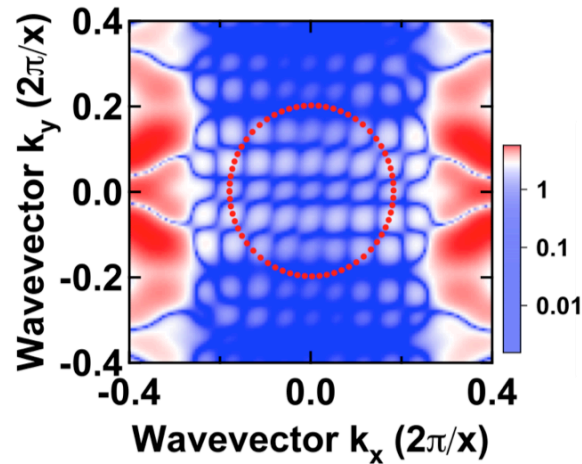


Fig. 5.1.6. 2D Fourier transform spectra of E_y field profiles for the width modulation on heterostructure cavity (E_y field as plotted in Fig. 5.1.3(d)). The leaky region is indicated by the red circle.

5.1.2.2 Local filling factor modulation scheme

Here I propose another method to achieve gentle confined Gaussian mode profile. The cavity design is based on the modulation of local filling factor around the $W_{0.98}$ waveguide. The coupling waveguide which is used to couple the light into this cavity waveguide was set to be $W_{1.05}$. The dispersion of the two waveguides are plotted and compared in Fig. 5.1.7(a). The PhC coupling waveguide is slightly wider in order to achieve efficient light coupling from the fast light part ($W_{1.05}$) to the slow light part ($W_{0.98}$) [212, 213], and eventually lead to the formation of gently confined mode in the cavity.

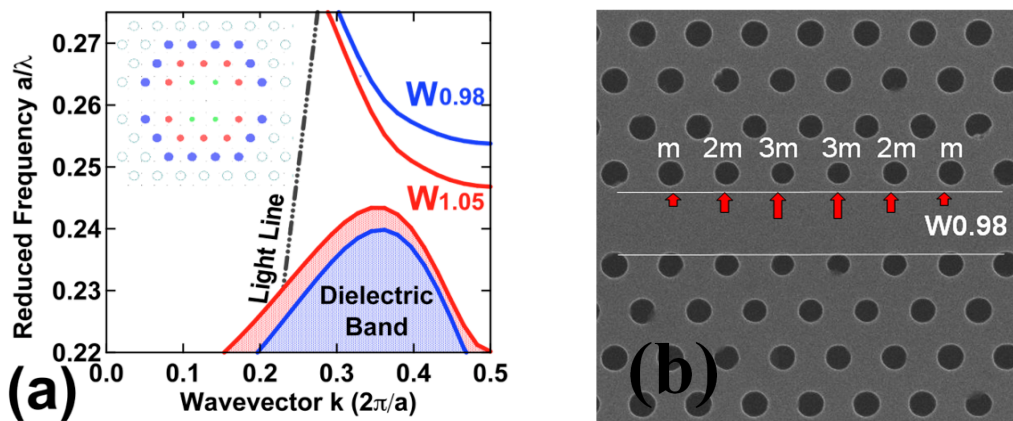


Fig. 5.1.7. (a). PWE calculated waveguide dispersion of different waveguide widths: $W_{1.05}$ (red) and $W_{0.98}$ (blue). Inserts shows the schematic plot of PhC cavity based on the modulation of local filling factor. Blue, red, green holes represent different amount of hole radii shrinking by m , $2m$ and $3m$. Where $m = 4$ nm. The bulk lattice constant is 430 nm. (b) SEM image of the cavity after fabrication.

The sizes of the holes are gradually reduced in the cavity as illustrated in Figs. 5.1.7(a) and 5.1.7(b). Blue, red, green holes represent different shrinking of the hole radius by m , $2m$ and $3m$. Where m is scanned by 3, 4 or 5 nm. The air filling factor (f) is 24% for the holes in bulk PhC region.

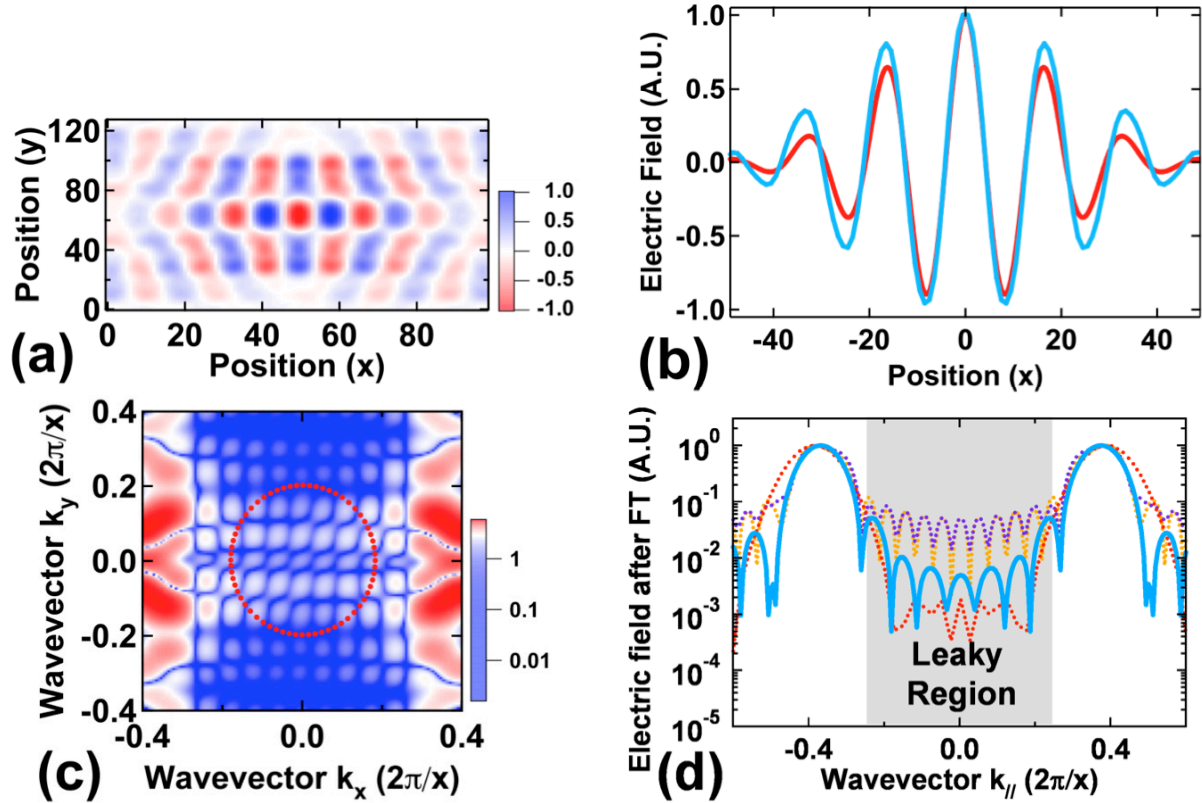


Fig. 5.1.8. (a). E_y field distribution of the local filling factor modulation PhC cavity mode. (b). 1D E_y electric profiles of the local filling factor modulation cavity at position $y = 0$ (light blue curve) and the truncated Gaussian envelop function (red curve). (c). 2D Fourier transform spectrum of the E_y electric field profile for this cavity. The leaky region is indicated by the red circle. (d). Comparison of 1D Fourier transform spectra of E_y electric field profiles for different cavities: the local filling factor modulation cavity (blue), the heterostructure cavity (orange), the local width modulation cavity (violet) and the truncated Gaussian mode profile (red).

The Fourier transform is performed on the E_y field of the cavity based on local filling factor modulation as shown in Fig. 5.1.8. Comparative calculation results show that the local filling factor modulation cavity has smaller components in the leaky region than the other two. This means that the local filling factor modulation cavity should achieve higher quality-factor than the others.

5.2 Experimental investigation of high Q factor PhC cavities

Different types of high Q factor PhC nanocavities were fabricated on SOI material using the Vistech EBP 5000ES EBL system with a resolution of 2.5 nm. The SOI sample was fabricated to the membrane waveguide configuration using the method presented in Chapter 3. At the time of fabrication, the width modulation on heterostructure cavity design had not been proposed yet, thus this type of cavity was not fabricated. The local filling factor modulation cavities and local width modulation cavity were fabricated, and then characterized using the Fourier spacing imaging technique as mentioned in Chapter 4.

5.2.1 Local filling factor modulation cavity

Since this was the first time high-Q PhC cavities were fabricated in EPFL, in order to ensure the sufficient coupling from the waveguide to the cavity and be able to measure the cavity mode in transmission, we selected the waveguide to cavity distance by 4 rows ($R = 4$) for all the local filling factor modulation cavity devices. Moreover, the bulk lattice constant was scanned by 420, 430 and 450 nm in order to ensure the cavity mode wavelength fall down to our measurable wavelength range (1470 – 1600 nm).

The cavity is located in the Γ -M direction from the $W_{1.05}$ waveguide probe waveguide because the cavity mode field decay is most gradual in this direction and thus the cavity-waveguide coupling is easy to control [214]. Fig. 5.2.1(a) shows the design mask (from L-edit) of the cavity. Only light whose wavelength matches the cavity resonance is transmitted to the output waveguide by resonant tunneling. Sharp transmission peaks will be detected for such kind of configuration if there is a cavity mode.

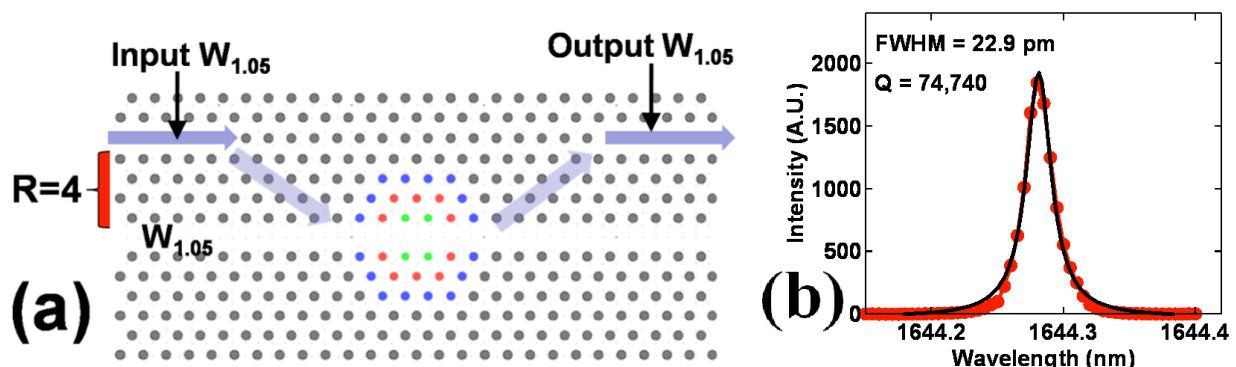


Fig. 5.2.1. (a). Design mask (from L-edit) of local filling factor modulation cavity with 4 rows of separation between the coupling waveguides and the cavity waveguide. (b). Experimental transmission spectrum of the cavity. The bulk lattice constant is 430 nm, $m = 4$ nm, and the red curve with symbols is the experimental data, the black curve is the Lorentzian fitting. The full width half maximum is 22.9 pm, corresponding to a Q factor of 74,740.

Fig. 5.2.1(b) shows the experimental transmission spectra of the local filling factor modulation cavity. The full width half maximum (FWHM) of the transmission peak is 22.9 pm, corresponding to an experimental measured loaded Q factor as high as 7.4×10^4 . However, such value is still about one order of magnitude lower than the other reported cavities: *e.g.*, the width modulation and heterostructures were reported with Q factor as high as 1 million. The main reason that such cavity doesn't achieve extremely high Q is considered to be an over coupling issue: in the fabricated device for such scheme, only 4-row distance is separated between the coupling waveguide and cavity waveguide.

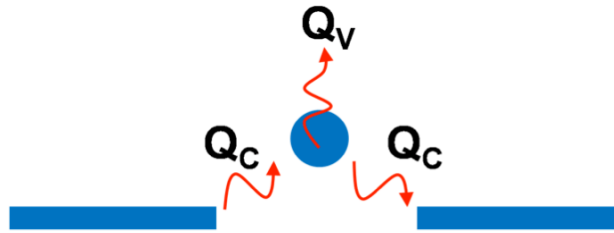


Fig. 5.2.2. Schematic illustration of the waveguide-cavity coupling configuration used for the local filling factor modulation cavity.

In the device shown in Fig. 5.2.2, a single resonator is coupled to two straight waveguides (input and output). Light from the input waveguide can pass through the resonator into the output waveguide by the resonant tunneling process. This tunneling occurs only when the light wavelength matches the resonance wavelength of the cavity. That is, this device works as a resonant tunneling transmission filter [215]. The performance of this device is represented by the transmission Q and transmittance T. The transmission characteristics of these resonance devices can be analyzed by the coupled-mode theory [216]. This analysis confirms that the transmission characteristics can be explained by vertical radiation Q (Q_V) and horizontal coupling (in-plane) Q (Q_C). Q_V is mainly due to decay into the radiation loss from the cavity, that is, the Q of the isolated cavity, if the crystal size is sufficiently large. Q_C is mainly due to decay into the waveguides as a result of coupling. Then total Q (Q_T) is given by:

$$\frac{1}{Q_T} = \frac{1}{Q_V} + \frac{1}{Q_C} \quad (5.2.1)$$

and analysis of the coupled-mode theory leads to energy transmittance (T) expressed as [214, 215, 217-219]:

$$T = \left(\frac{Q_T}{Q_C}\right)^2 = \left(\frac{Q_V}{Q_C + Q_V}\right)^2 \quad (5.2.2)$$

It is important to note that the experimental Q, or total Q factor (Q_T) obtained from the linewidth of the radiation or transmission spectra shown in Fig. 5.2.1(b) is not the intrinsic Q

factor of the cavity itself. The intrinsic Q factor, denoted Q_v , is determined by the coupling loss to free space only. In our first sample, only $R = 4$ rows of holes are selected that actually limits the Q_C to a low value, hence limiting the experimental Q value (Q_T).

It is necessary to mention that there is also another geometry (side coupling) can be used for couple light from waveguide to the cavity. In this case a cavity is placed on one side of a straight waveguide [205, 210]. A dip in the transmission can be observed because it corresponds to the light coupled into the cavity. This geometry allows the measurement of Q_C .

5.2.2 The cavity-waveguide coupling role

Here we will investigate another cavity design by changing the cavity-waveguide coupling Q_C . The waveguide width modulation cavity scheme was also fabricated and characterized together with the previous local filling factor modulation cavity scheme. The waveguide to cavity distance R , was scanned from 4, 5 to 6 rows (as shown in Fig. 5.2.3). By varying the number of rows between the input/output waveguide and the cavity, the waveguide coupling Q_C can be controlled in order to obtain high Q_T .

Fig. 5.2.3(a) shows the design mask (from L-edit) of the local waveguide width modulation cavity with 4/5/6 rows of separation between the input/output coupling waveguides and the cavity waveguide. Fig. 5.2.3(b) is the SEM image of the local waveguide width modulation cavity after fabrication. Red, blue, green circles present different amounts of shifts by $x/3$, $x/2$ and x , where $x = 12/9/6$ nm. The bulk lattice constant is scanned by 420, 430 and 450 nm. The air filling factor is set to be 24% for all the devices.

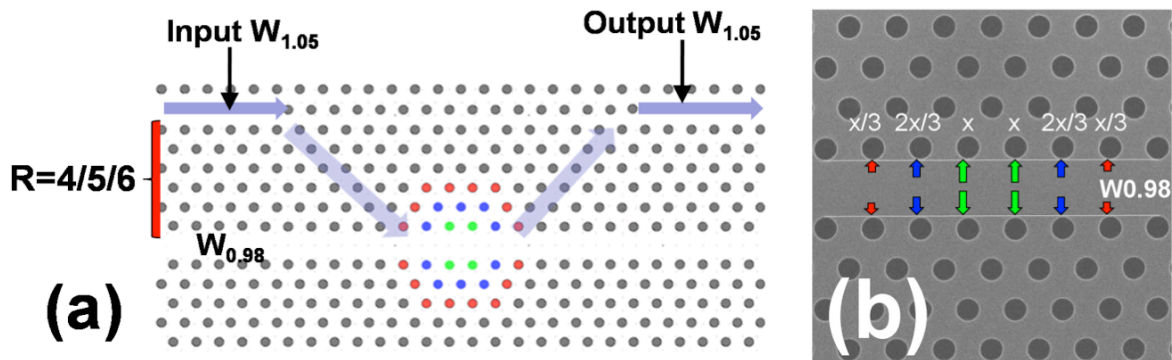


Fig. 5.2.3. (a). Design mask (from L-edit) of the local width modulation cavity with 4/5/6 rows of separation between the input/output coupling waveguides and the cavity waveguide. Red, blue, green circles present different amounts of shifts by $x/3$, $x/2$ and x , ($x = 12/9/6$ nm). The bulk lattice constants are scanned by 420, 430 and 450 nm. (b) SEM image of the local waveguide width modulation cavity after fabrication.

In Fig. 5.2.4, experimental transmission spectra of the waveguide width modulation cavities with different cavity-waveguide coupling Q_C are plotted. For such scheme with $R = 4$, Fig. 5.2.4(a) corresponds to the transmission peak with narrowest cavity linewidth of 35.1 pm (FWHM) and highest Q factor of 4.2×10^4 . Such value is still much lower than the one obtained with the local filling factor modulation design with the same cavity-waveguide coupling Q_C . This proves that the specially designed local filling factor modulation cavity has much higher Q_V than the width modulation cavity under the same coupling conditions.

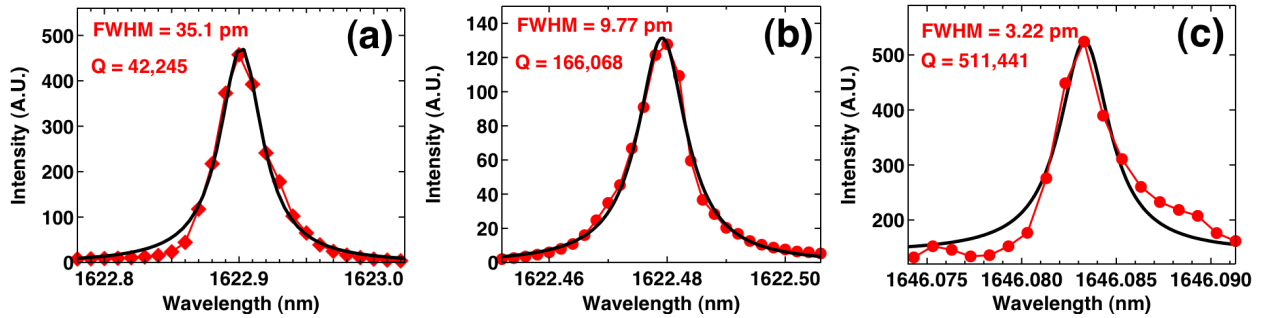


Fig. 5.2.4. Experimental transmission spectra of the local filling factor modulation cavities at different cavity-waveguide coupling Q_C . The waveguide to cavity distances are 4 rows (a), 5 rows (b) and 6 rows (c). The actual PhC cavity parameters in forms of $a/x/R$ are: 420/12/4, 420/12/5 and 430/9/6 for figures (a) (b) and (c), respectively. The 420/12/6 was replaced by 430/9/6 due to a probably device damage (no transmission). The FWHMs from (a) to (c) are respectively 35.1 pm, 9.77 pm and 3.22 pm, corresponding to experimental Q factors of 42,245, 166,068 and 511,441.

However, when the waveguide to cavity distance is increased to 5 or 6 rows, significant increase of the experimental Q factor was observed. The FWHMs after the Lorentzian fitting for the 5 and 6 rows are 9.77 pm and 3.22 pm respectively, corresponding to experimental Q factors of 1.7×10^5 and 5.1×10^5 .

The limited cavity-waveguide coupling Q_C is one of the reasons that such design did not reach values as high as the reported 1 million Q (normally reported with 7-8 rows of separation distance). A second reason can be considered as the minor fabrication disorders which increase scattering loss. Last but not least, the 2 μm BOX layer under the Si core layer was not removed completely (~ 800 nm remaining), which results in a non-perfect membrane waveguide. Consequently this may result in increased roughness with undesired scattering losses and increased coupling from Si core to the remaining cladding and substrate. In this case multi-reflections may build destructive interferences and hence build up an additional vertical loss channel (to substrate) and limit the cavity performance.

5.2.3 Nonlinear and bistable effects

For the experimental transmission measurement of a moderate Q value cavity, when the input power (P_{in}) is increased, the transmission spectrum is changed dramatically due to optical nonlinearity. The cavity is based on the local width modulation scheme with parameter $a/x/R$ (a : lattice constant; x , shift in y ; R , number of rows) of 420/9/5 nm. The laser output power, or the cavity input power (P_{in}) was increased from 0.5 mW to 8 mW. For each measurement the laser was swept from short wavelength to long wavelength, under so called wavelength forward sweep condition.

The nonlinear behaviour that is observed results from both the Kerr effect and the thermo-optic effect [220] induced by two-photon absorption in silicon [214, 221] for this cavity. The resonance peak of this cavity is at 1633.06 nm with FWHM about 70 pm, corresponds to the relatively low experimental Q factor around 2×10^4 . In the wavelength forward sweep case as shown in Fig. 5.2.5, two phenomena can be observed from the spectra: firstly it can be seen that there is a large spectrum broadening effect for longer wavelengths. This broadening is explained by the resonance locking due to the positive feedback between the laser sweeping (wavelength forwardly swept) and the resonance red-shift (caused by the Kerr/thermo-optic effect). Secondly it can be found that there is a sharp drop in transmission at long wavelength ends. The sharp drop in the output power intensity indicates that bistable states are likely to exist [220].

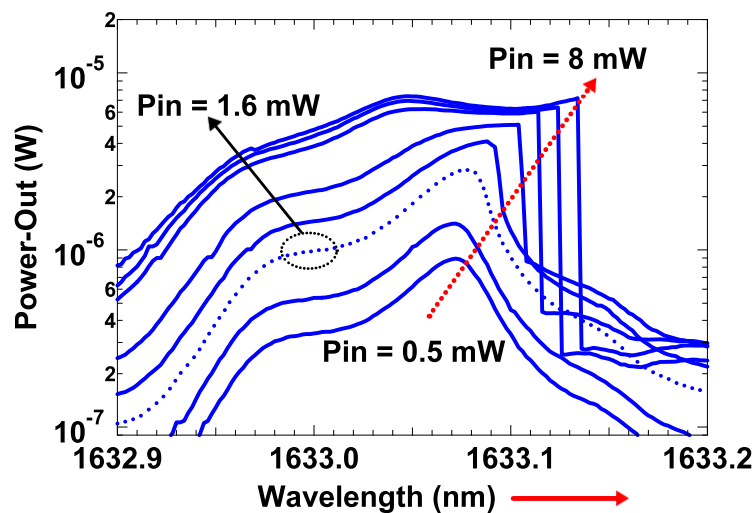


Fig. 5.2.5. Power-dependent (from 0.5 mW to 8 mW) transmission spectra taken by a tuneable laser in the wavelength forward sweep condition (sweep direction indicated by the red arrow at the bottom of the figure). The resonance peak of the cavity is at 1633.06 nm with FWHM about 70 pm. The cavity is based on the local width modulation scheme with parameter of $a/x/R = 420/12/4$ nm. The red dashed arrow indicates the red shift direction of the cavity resonance peaks with increasing input power P_{in} .

The nonlinear effect is observed at input power higher than 1.6 mW for this low Q factor PhC cavity. Note that this value is relatively high as the Q factor of the cavity is only around 2×10^4 . The power needed for the nonlinear effect will be much lower for a high Q cavity.

The laser was then scanned at several fixed wavelengths detuned by δ from the cavity mode to directly observe the bistability. In this case the cavity input power (P_{in}) was swept forward and backward, and meanwhile the output power (P_{out}) was detected and plotted in Fig. 5.2.6. When there is no detuning ($\delta = 0$ pm), Fig. 5.2.6(a) shows linear dependency of the P_{out} and P_{in} . When the wavelength detuning δ is exceeded 40 pm, a clear hysteresis loop was observed between the OFF and ON branches as shown in Fig. 5.2.6(b). The switching contrast is larger than 15dB. This small footprint is of course advantageous for integration, but it is also beneficial for reducing the switching speed because our device is limited by the thermal diffusion process. The relaxation time of our switch is approximately 100 ns [222], which is much shorter than that of conventional thermo-optic switches (\sim msec).

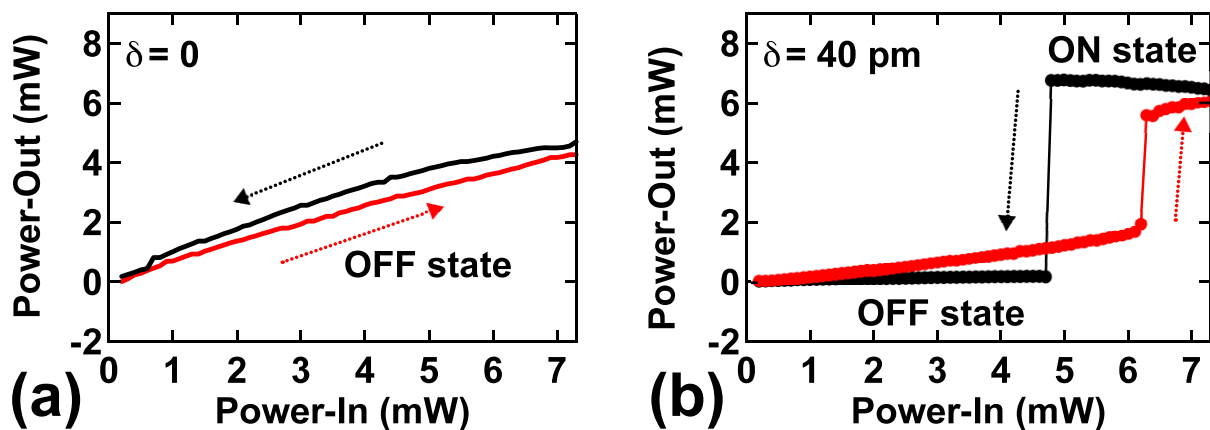


Fig. 5.2.6. (a). Output power (P_{out}) versus input power (P_{in}) for detuning value of $\delta = 0$ pm. The power sweep direction of P_{in} is indicated by arrows. (b). Output power (P_{out}) versus input power (P_{in}) for detuning value of $\delta = +40$ pm. The power sweep direction of P_{in} is indicated by arrows.

Unfortunately because the laser operates in the continuous-wave (CW) condition, the cavity is easily overheated when it is on resonance, in particular in high input power cases. Consequently the cavity became unstable with self pulsing behaviours, and a full set of P_{out}/P_{in} measurement data for various detuning (δ) values cannot be obtained. Moreover, for most of the high Q cavities, we observed the slow self-pulsing effects. This is believed to be mainly a thermal heating/cooling process in time. This behaviour originates from the fact that the two dominating nonlinear refractive index effects - the plasma effect (red shift) and the associated thermal-optic (blue shift [223-226]) refractive index change - have opposite signs and different time constants. Such behaviour may be problematic for the stability of thermal memory and switching operation. On the positive side, it could be used for tunable pulse generation:

optimization of the input power and/or wavelength makes it possible to change both the pulse length and the pulse period.

5.2.4 Summary

To summarize here, we designed, fabricated, and characterized photonic crystal nanocavities with experimental Q factor as high as half a million. We conclude that the achievement of the high Q factor cavity can be hindered by the coupling conditions, the fabrication imperfections, and the complex nonlinear effects. Nonlinear effects and bistable behaviours were observed, however they are all largely impacted by the self-pulsing effect due to the thermal heating. Further optimizations and investigations are needed on the following aspects: cavity design with higher intrinsic Q, fabrication with reduced loss, theoretical and experimental investigations on ultra-fast switching based on nonlinear effects.

5.3 *Air-slot photonic crystal nanocavity**

*The main results in this section are originally published in "Refractive index sensing with an air-slot photonic crystal nanocavity." **Optics Letters** **35** (15), 2523-2525 (2010)

The design, fabrication and characterization of air-slot photonic crystal cavities are investigated in this section. As mentioned before, in typical PhC cavities, the strong light-matter interaction occurs in the high index material where the maximum of optical field is located, making it difficult for precision refractive index sensing [227, 228] purposes: *e.g.*, to efficiently probe the physical properties of analyte found within the hollow part of the cavity. This drawback can be overcome with the use of an air-slot cavity, *i.e.* a photonic crystal cavity with a sub-hundred nanometer-wide air slot designed in the cavity defect region (see Fig. 5.3.1). Due to a large electric field discontinuity at the slot boundaries [229], such a cavity can confine TE polarized modes in the slot, thus allowing for a large interaction of the optical field with the low-index medium. The high quality factor $\sim 2.6 \times 10^4$ of the cavity along with a strong overlap between the resonant mode and the hollow core region allow us to achieve an experimental sensitivity of 510 nm per refractive index unit (RIU). The sensor device has a remarkably low sensing volume of 40 attoliters, holding less than 1×10^6 molecules.

5.3.1 The air-slot waveguide and air-slot cavity

The standard air slot waveguide was theoretically and experimentally reported by M. Lipson and coworkers in 2004 [229, 230]. The proposed structure is a low-index nanometer-wide area embedded in a high-index material medium, *e.g.*, air slot in a Si wire waveguide. In contrast with the leaky modes used in photonic bandgap waveguides with low-index cores, the guiding

mode is an eigenmode of the proposed structure and is therefore fundamentally lossless with very low wavelength sensitivity [230]. The optical field in the low-index material is enhanced because of the discontinuity of the electric field at high index contrast interfaces.

After the introduction of air slot waveguide concept, the air-slot cavity was proposed for the first time in a 1D photonic crystal by Robinson *et al.* [231], followed by several different designs in photonic crystal slabs [232, 233]. However, the full potential of such structures for highly sensitive on-chip sensing has not yet been clearly assessed. Here we present our investigation on a photonic crystal air-slot cavity.

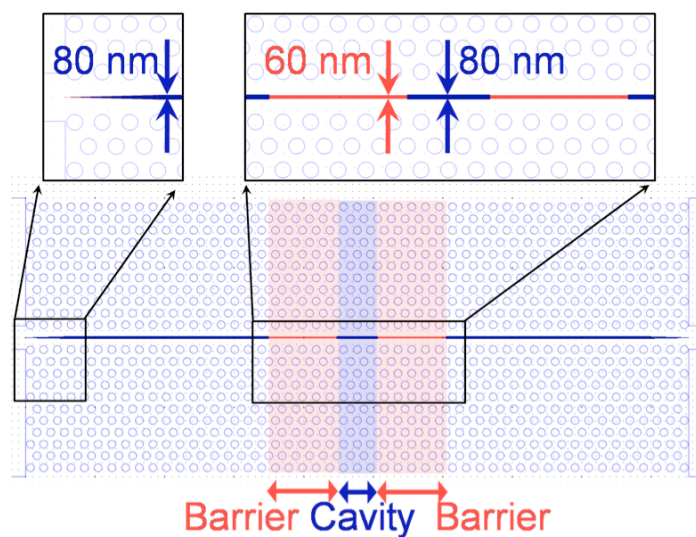


Fig. 5.3.1. Design mask (from L-edit) of the air-slot cavity. Barrier and cavity regions are highlighted by red and blue colors, respectively.

Fig. 5.3.1 shows the design mask of an air-slot photonic crystal cavity, which is based on a W_1 waveguide with an air-slot embedded in the line defect region. To create a cavity, one can either modify the properties of the photonic crystal mirror, or the dimensions of the slot itself. The first approach was adopted by J.T. Robinson and coworkers [231], where the lattice constant of the photonic crystal is locally reduced to create a heterostructure cavity, as well as in the works of Yamamoto *et al.* [233] and Gao *et al.* [234], where the holes adjacent to the slot were transversally shifted to define a width-modulated line-defect cavity. On the contrary, in the present design the photonic crystal lattice is kept unchanged, but the width of the air slot is locally reduced by 20 nm to delimit the volume of the cavity (insert of Fig. 5.3.1). Reduced slit width results in formation of reflective barriers for the cavity mode, as it can be inferred from the dispersion diagram of slot photonic crystal waveguides shown in Fig. 5.3.2. Note that in our EBL and ICP systems, there is always a 40 nm width enlargement during the etching transfer from ZEP520A resist to the Si waveguide, therefore on the mask the width of the slots, as well as the size of the PhC holes are reduced to balance the etching enlargement.

5.3.2 The air-slot cavity modelling, fabrication.

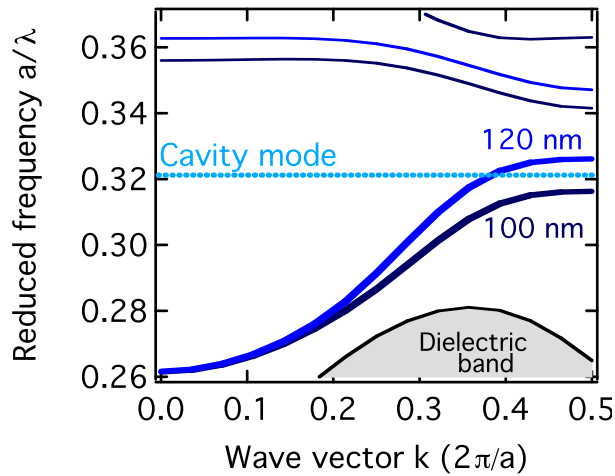


Fig. 5.3.2. Theoretical dispersion curves of 100 and 120 nm wide photonic crystal slot waveguides. The dashed line shows the position of the air-slot cavity mode.

The theoretical dispersion (Fig. 5.3.2) was calculated by guided-mode expansion method [183] for a photonic crystal with a lattice constant $a = 510$ nm and a filling factor $ff = 0.4$. When opening an air-slot inside the W_1 waveguide region, the TE-polarized slot waveguide mode is lifted up from the dielectric band, shifting the mode cut-off to higher frequencies as the width of the slit increases. Consequently, the cut-off of the 120 nm slot waveguide mode lies at slightly higher frequencies than the cut-off of the 100 nm wide one, and hence, the former can support a defect state when sandwiched between two 100 nm wide slot waveguide sections.

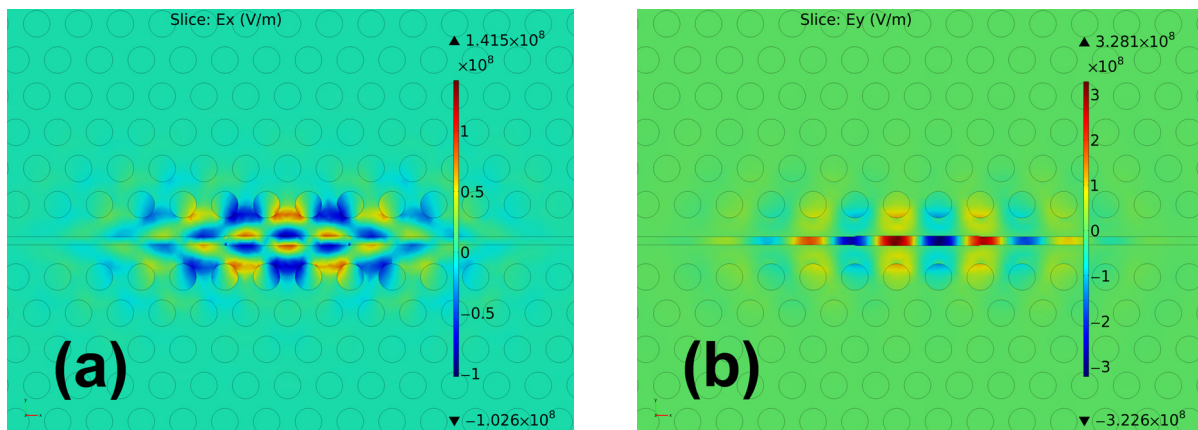


Fig. 5.3.3. (a). E_x field distribution of the air slot cavity mode in the slab (taken at $z = 0$). (b). E_y field distribution of the air slot cavity mode in the slab (taken at $z = 0$).

The cavity length was set to three lattice constants ($L = 3a$) in analogy to the well-known photonic crystal L3 cavity. The resonant state of such a cavity is centred between the cutoffs of the 120 and 100 nm wide slot waveguides. Here we use 3D finite element method (FEM) method to calculate the cavity Q factor and the field distribution. The important parameters in the FEM

model are identical to previously described in Chapter 2, such as: physical properties settings, boundary conditions settings. Very high element quality ($q = 0.6$) meshes were generated, in order to obtain accurate results. The simulation was performed through EPFL ‘SuperB’ cluster, with maximum 121 nodes and more than 1 TB memory available. We set $n_{\text{gas}} = 1$ and $n_{\text{Si}} = 3.47$ in the 3D simulation, and found that the cavity resonance mode at $\lambda = 1609$ nm, with a theoretical Q factor of 2.8×10^4 . The x and y components of the electric field distributions are plotted in Fig. 5.3.3. The localization of E_y field in the slot confirms that the cavity mode is strongly confined within the slot region.

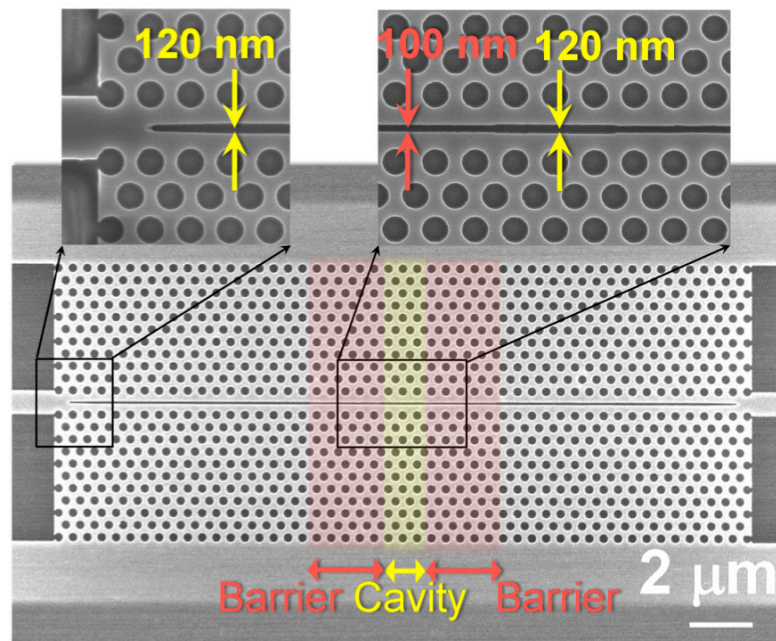


Fig. 5.3.4. Scanning Electron Microscopy (SEM) image of the air-slot cavity. Barrier (100 nm) and cavity (120 nm) regions are highlighted by red and yellow colors, respectively.

To investigate the proposed air-slot cavity experimentally, we fabricated a series of devices with Si membrane configurations with an Ebeam resolution of 2.5 nm using the technique as mentioned in Chapter 3. It has to be stressed that the sample fabrication steps were carefully optimized, and finally we achieved an absolute agreement between the design and the actual parameters with zero errors. The optimized fabrication procedures with EBL system and the ICP etching system can achieve minimum 50 nm of air slots etched down to the BOX layer. In order to have the cavity mode in the 1.5 μm wavelength range, the lattice parameter of the photonic crystal was scanned between 470 and 510 nm, and the slot widths between 80/100 nm to 100/120 nm for the barrier/cavity regions, respectively. All other parameters have their nominal values as in the theoretical simulations presented above. Fig. 5.3.4 shows the SEM image of the cavity in Fig. 5.3.1 after fabrication. The width of the slots are enlarged by 40 nm, thus hitting our simulation target (100/120 nm).

5.3.3 The cavity characterization

The fabricated devices were characterized using a setup combining the endfire and imaging techniques as described before in Chapter 4. Fig. 5.3.5 shows the transmission spectrum measured for an air-slot cavity with the same parameters as previously specified for the theoretical calculations. The cavity barriers are transparent down to approximately 1590 nm, where the mode cutoff of the 100 nm wide slot waveguide is found. 20 nm below the mode cutoff, we can identify a narrow transmission peak that corresponds to the resonant mode of the air-slot cavity. There is a broad and weak resonance observed between the cavity mode and the cut-off at 1580 nm, this is attributed to an evanescent mode that can penetrate through the barriers. The far-field imaging unambiguously confirms the cavity mode identification, even if the transmitted signal is extremely weak or accompanied with spurious resonances that often appear as peaks in the transmission spectrum. The far-field radiation pattern of the cavity mode differs distinctly from the angular emission spectrum of residual resonance peaks, which create a speckle pattern that changes as the excitation wavelength is tuned across the spectral line. This is not the case for the cavity emission, which has a stable, highly symmetric pattern (shown in the inset in Fig. 5.3.5) determined only by geometrical properties of the cavity.

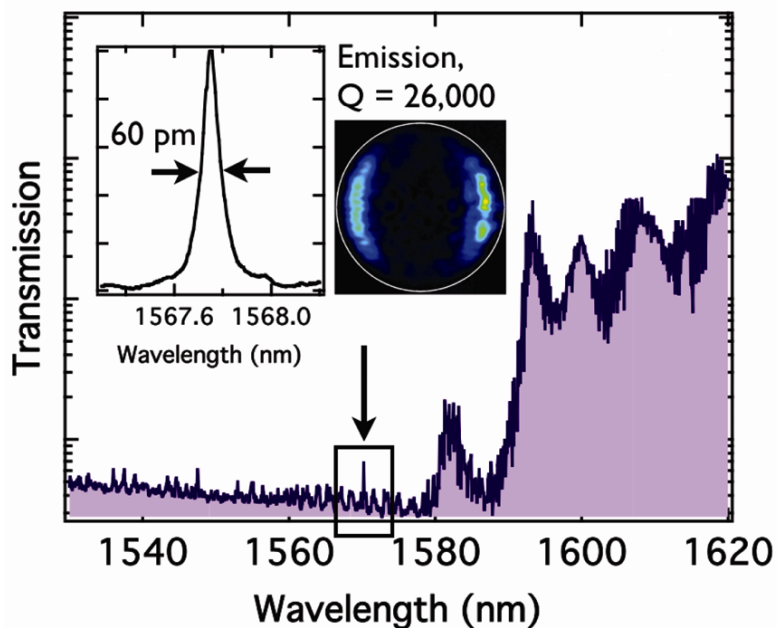


Fig. 5.3.5. Transmission spectrum of the air-slot cavity. Insets show the experimental emission spectrum of the cavity (left) and the far-field image at the cavity resonance (right).

The light radiated from the sample are recorded as a function of the wavelength yields the emission spectrum of the cavity, which is shown in the inset of Fig. 5.3.5. By virtue of careful real-space filtering, such emission spectrum exhibits a better signal to noise ratio as compared to

the transmission measurement and was therefore used to analyze the properties of the cavity resonance. The Lorentzian fit of the emission peak gives the linewidth of 60 ± 1 pm, yielding a loaded quality-factor $Q = 2.6 \times 10^4$. Other cavities with different parameters were investigated and all the observed resonant modes have Q-factors lying in the range of 15,000-26,000.

The effective mode volume [206] is found to be $V_{\text{eff}} = 0.05 \mu\text{m}^3$, and the spatial mode overlap with the gas ambience Γ is as high as 0.83. Knowing the mode field overlap Γ , the first order perturbation theory can be used to estimate the theoretical sensitivity S of the device to the refractive index change Δn inside the cavity [235]:

$$S = \frac{\Delta\lambda}{\Delta n} = \Gamma \frac{\lambda}{n_{\text{eff}}} \quad (5.3.1)$$

where λ is the air-slot cavity resonance wavelength and $n_{\text{eff}} = \sqrt{\Gamma n_{\text{gas}}^2 + (1-\Gamma)n_{\text{Si}}^2}$ is the effective index experienced by the cavity mode. For resonance frequency $\lambda = 1570$ nm, $n_{\text{gas}} = 1$ and $n_{\text{Si}} = 3.47$, we get a sensitivity of $S = 770$ nm per RIU, which is quite remarkable for a sensor with an active sensing volume as low as $0.04 \mu\text{m}^3 = 40$ attoliters.

5.3.4 The gas sensing experiment

In order to assess the sensing potential of the cavities, we expose the sample to gasses of different refractive indices such as air ($n = 1.000265$) [236], nitrogen (N_2 , $n = 1.000270$) [237], helium (He , $n = 1.000032$) [236] and carbon dioxide (CO_2 , $n = 1.000406$) [237]. The refractive index values are given at atmospheric pressure and recalculated for the wavelength $\lambda = 1570$ nm and room temperature $T = 20$ °C using the ideal gas model [238]. During the measurement, the sample is placed in a gas cell that is equipped with a gas inlet, two micrometer-size openings for the optical fibers and an outlet for gas evacuation. The gas is injected into the cell at a constant rate, it fills the volume of the cell and escapes by the outlet opening, thus avoiding the overpressure inside the cell. The flux rate was set to a value just sufficient to entirely fill the cell volume with the test gas by observing the shift of the cavity resonance upon accruing concentration of the gas; when a new increase of the gas flux did not induce further shift in the resonance wavelength, the cell was considered to be completely filled with the analyte. We observed no effect of this weak gas flux on the sample temperature or any vibrations that could have an impact on the coupling efficiency.

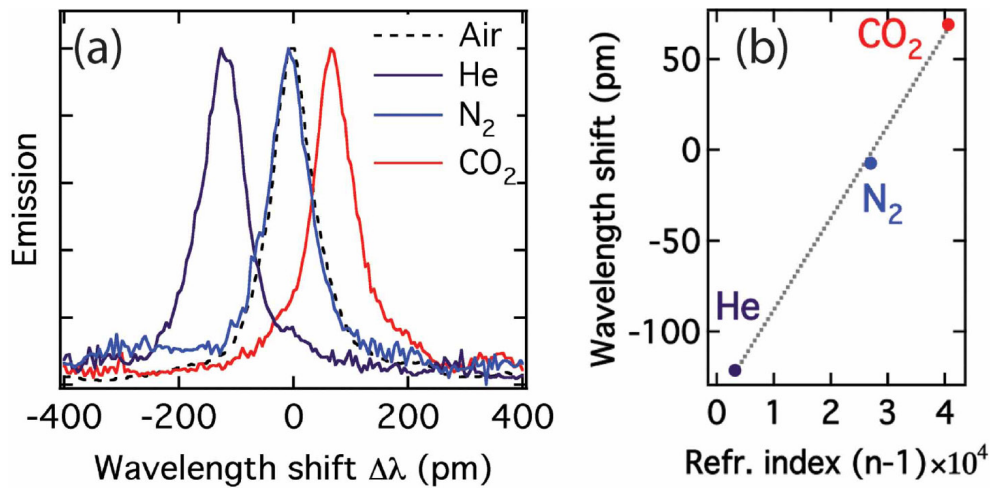


Fig. 5.3.6. (a) Spectral position of the cavity resonance upon exposure to helium, nitrogen and carbon dioxide. Reference peak measured for the air is also shown (dashed line). (b) Wavelength shift of the cavity resonance plotted as a function of the refractive index change of the respective gas. The marker size corresponds to the error bar of ± 3 pm.

The shift of the air-slot cavity resonance in response to the change of the gas refractive index is shown in Fig. 5.3.6. If we consider air as the reference medium, we can observe both blue shift of the resonance peak position for helium, and red shift to higher optical wavelengths for carbon dioxide that exhibits the highest refraction. As plotted in Fig. 5.3.5(b), the dependence of the wavelength shift on the refractive index change is strictly linear and the interpolation of the measured values yields the experimental sensitivity $\Delta\lambda/\Delta n = 510$ nm/RIU, which is in a good agreement with the theoretical value. Repetitive measurements on a longer time scale show that the peak position can be retrieved with a precision of ± 3 pm, which implies the detection limit (DL, defined as the ratio between the resolution and the sensitivity) of the device of 1×10^{-5} RIU. Nevertheless, it should be mentioned that along with the refractive index of the surrounding medium, there are other parameters that can influence the shift in the absolute resonance frequency of the air-slot cavity mode, *e.g.* temperature, air humidity that gets adsorbed as a thin layer at the structure sidewalls, or progressive oxidation of the sample surface. In particular, the latter turns out as the most detrimental as it can induce a shift of the resonance peak by as much as 45 pm per hour. This effect can be compensated by measuring the air-peak position before and after each measurement and taking their time-interpolated value as the reference or by preventing the oxygen to get to the sample surface, *i.e.* by working only with O₂-free gases. All other noise terms mentioned above could be canceled out by using an identical reference structure, thus improving the detection limit.

5.3.5 Summary.

In conclusion, we have presented the design, fabrication and characterization of a high Q factor photonic crystal air-slot cavity. Full 3D simulation shows that the FEM can be used as a powerful tool to simulate the complex structures. Theoretical Q value of the slot cavity as high as 2.8×10^4 was obtained. Such high Q air slot cavity was fabricated with a great precision and reduced disorders using the EBL system, eventually we measured a high experimental Q value of 2.6×10^4 for such cavity, which is very close to the theoretical one. Due to a strong overlap of the cavity mode with the surrounding medium, such a cavity achieved a very high experimental sensitivity ($> 510 \text{ nm/RIU}$) with a detection limit higher than $1 \times 10^{-5} \text{ RIU}$. The major advantage of the cavity is an extremely small sensing volume of 40 attoliters that is possible due to the strong confinement of the optical field in the PhC point-defect cavities. In the potential sensing application, such small volume not only allows to drastically decrease the necessary amount of analyte, but it also makes the sensor suitable for high density integration oriented towards parallel or multiplex detection.

Chapter 6

6. Terahertz Photonic Crystal Quantum Cascade Lasers

Terahertz (THz) light sources in the frequency range of 0.1 - 10 THz, had been long time hindered by the lack of compact laser sources until the first demonstration of THz quantum cascade lasers [239] (QCL) in 2002 [240]. Thanks to the engineering of intersubband optical transitions [239], THz QCLs have experienced improvements on almost every performance, including lower power consumption, longer wavelength, higher output power, operation temperature, and emission directionality control. THz QCLs are showing their great importance in many promising applications, such as spectroscopy, imaging, sensing and environmental monitoring [241].

Photonic band engineering has been proved to be a very efficient way to tailor the emission properties of semiconductor lasers. Thanks to the scaling law between wavelength (λ) and lattice constant (a), concepts of photonic crystal (PhC) semiconductor lasers can be exploited at any frequency [17, 19, 120, 242-245]. For short wavelengths, *e.g.*, UV range, visible range, and near-Infrared, PhC structures commonly suffer from the sub-nanometer fabrication imperfections even with state-of-the-art processing technique, challenging passive devices (as mentioned in Chapter 4) and active devices for practical applications. However, when the wavelength is scaled to longer wavelengths, *e.g.* far infra-red, or THz in frequency, the corresponding critical dimensions required for the PhC devices are in the range of micrometers. Such large dimensions can be easily mastered through standard photolithography.

PhC lasers were reported in two forms, one is the photonic bandgap (PBG) defect mode laser[246] based on resonant cavity mode, the other is the band-edge DFB type laser, either one (1D) or two-dimensional (2D) [66, 247, 248]. At THz frequencies, THz cascade structures are extremely well suited for their use in PhC structures. The double Plasmon (DP) waveguide [249] enables the fabrication of different types of PhC structure with either complete or partial PBG, for pillar type PhC or hole type PhC lasers, respectively. The DP metallic layers can also operate as electrical contacts. Slow light THz PhC QCL lasers can be achieved either with a high index modulation scheme or with a low index scheme, leading to strong PhC or weak PhC effects, respectively. Laser action based on weak PhC effect has been demonstrated with low index

modulation structures that are obtained by patterning the top metallic layer of the laser [19, 250] whilst leaving un-etched the active region. The strong PhC effect, which requires high index modulation can be achieved with deeply etched structures [17, 120, 121] which are sandwiched within the two metallic layers.

The second major aspect of this PhD thesis is to make use of slow light concepts to develop photonic crystal THz light sources. I concentrated the efforts on the generation of laser emission at low THz frequencies (1-3 THz range) on quantum-cascade epilayers. My work is based on the high index modulation scheme. Various types of pillar type PhC slow light lasers at THz frequencies were designed, investigated, fabricated and characterized. Such works were performed under close collaboration with the group of Prof. Jérôme Faist previously at Neuchâtel University and now at Ecole Polytechnique Fédérale de Zurich (ETHZ). Any single research project under this collaboration scheme contains 5 phases: design, simulation, epilayer growth, laser fabrication and characterization. The QCL epilayer growth and device characterization were performed in ETHZ. In EPFL I was in charge of the PhC QCL laser design, simulation and fabrication.

This chapter consists of 5 sections. In Section 6.1, a general and brief literature review of the THz quantum cascade laser is given. The THz applications, the QCL intersubband engineering as well as the waveguides will be briefly discussed. From Section 6.2 and the following sections, specific topics on slow light PhC QCL at THz frequencies will be focused. The fabrication technique has been detailed in Chapter 3, therefore in Section 6.2, a brief introduction of the characterization technique used in ETHZ will be given. Section 6.3 presents an exhaustive record on the investigation of in-plane emitting PhC QCL lasers at 3.3 THz. It will be demonstrated that such photonic crystal lasers strongly improve the performances of THz quantum cascade material in terms of threshold current, waveguide losses, emission mode selection, tuneability and maximum operation temperature. In Section 6.4, we report on a proof-of-principle demonstration of Γ band-edge (refer to the 3rd band near the second bandgap in the dispersion) lasing surface emitting pillar type photonic crystal lasers on quantum cascade material around 1.5 THz. Here, the surface emitting lasing mechanism is introduced. The lasing modes are identified and compared to theoretical modelling. In Section 6.5, I will show the investigation and development of a complex-coupled PhC QCL scheme, where the refractive index and loss can be modulated independently. The laser also operates in a slow-light regime of the pillar type PhC at the Γ band-edge of the third band similar as in Section 6.4. Sub-wavelength holes are introduced in the top plasmon layer, this allows to tailor the light out-coupling through the surface. Very high surface emitting power (31.2 mW) is obtained through such extractors, which is comparable as the standard Fabry-Perot lasers. Elliptical pillars

based photonic crystal brings more mode control on the band-edge degeneracy with single mode operation and can be used to improve the far field emission pattern.

6.1 Introduction of THz quantum cascade lasers

6.1.1 The Terahertz technology.

The terahertz frequency range, as shown in the electromagnetic spectrum Fig. 6.1.1, is loosely defined as the frequencies from 0.1 THz to 10 THz, or the wavelengths from 3 mm to 30 μm . It has historically been characterized by a relative lack of convenient radiation sources, detectors and transmission technology. However, recent technological innovation in photonics and nanotechnology is now enabling THz research to be applied in many more domains with an increasingly wide variety of applications, such as astronomy, information and communications technology, biology and medical sciences; environmental monitoring and security, quality control of food and agricultural products.

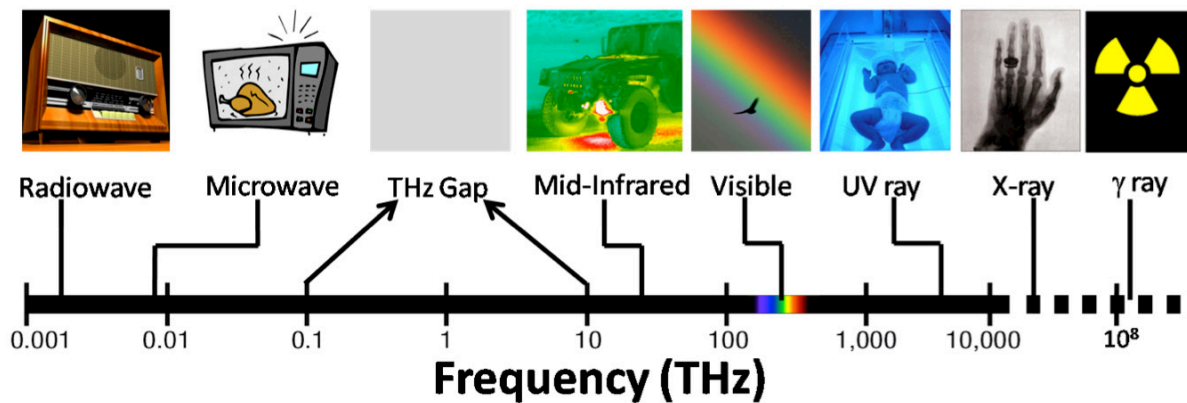


Fig. 6.1.1. A schematic drawing of the THz region within the electromagnetic spectrum. Although there is no strict definition of what qualify as THz waves it is commonly accepted to consider the region between 0.1 THz and 10 THz.

6.1.1.1 THz APPLICATIONS

In recent years, THz technology has been applied to a huge variety of systems both to aid the basic understanding of the material properties, and to demonstrate potential applications in sensing, diagnostics and imaging. The most important two applications of THz technology: Terahertz spectroscopy and Terahertz Imaging will be briefly introduced here.

a) Terahertz spectroscopy

Historically, the major use of THz spectroscopy has been by chemists and astronomers in the spectral characterization of the rotational and vibrational resonances and thermal-emission lines of simple molecules. One of the primary motivations for the development of THz

technology is the potential to extract material characteristics that are unavailable when using other frequency bands. Astronomy and space research has been one of the strongest drivers for THz research because of the vast amount of information that can potentially be collected on the presence of abundant molecules such as oxygen, water and carbon monoxide in stellar dust clouds, comets and planets [251].

Many different methods exist for performing THz spectroscopy, such as Fourier transform spectroscopy (FTS), narrowband spectroscopy, and THz time-domain spectroscopy (THz-TDS [252-254], or called Terahertz Pulse Spectroscopy (TPS) [255]). As the most common technique used for studying molecular resonances, the FTS has the advantage of an extremely wide bandwidth, enabling material characterization from THz frequencies to the infrared. One disadvantage of FTS is its limited spectral resolution. The narrowband spectroscopy system can perform spectral measurements with a much higher resolution. Both FTS and narrowband spectroscopy are also widely used in passive systems for monitoring thermal-emission lines of molecules, particularly in astronomy applications. THz time-domain spectroscopy (THz-TDS) uses short pulses of broadband THz radiation, which are typically generated using ultrafast laser pulses. It has a number of advantages that have given rise to some important recent applications. The transmitted THz electric field is measured coherently, which provides both high sensitivity and time-resolved phase information. A THz-TDS system is described in Fig. 6.1.2(a).

An example of THz-TDS is plotted in Fig. 6.1.2(b). It shows the THz spectral features of the two polymorphic forms (forms 1 and 2 are presented by green and red curves, respectively) of drug ranitidine hydrochloride (HCL). Signature peaks for each form can be identified easily using THz spectroscopy. (reprinted from Ref. [255]).

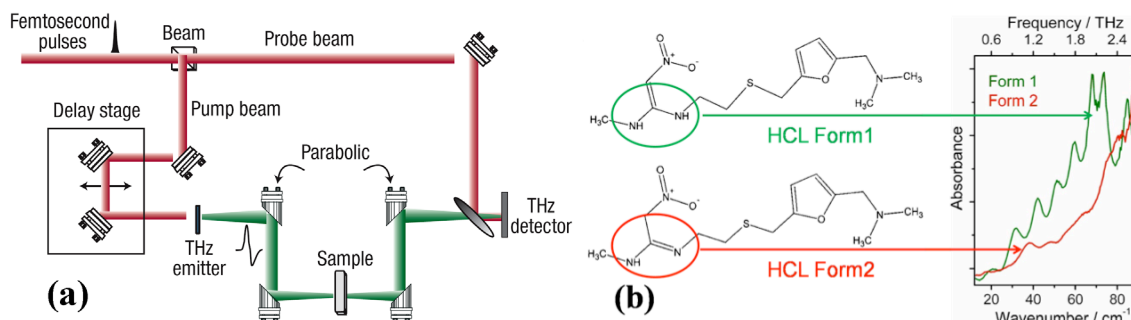


Fig. 6.1.2. (a) Illustration of the most common experimental setup for transmission-type THz-TDS. The ultrafast laser beam is split into pump and probe beams. The pump beam is incident on the THz emitter to generate THz pulses, and the THz pulses are collimated and focused on the target using parabolic mirrors. After transmission through the target, the THz pulse is collimated and re-focused on the THz detector. The optical probe beam is used to gate the detector and measure the instantaneous THz electric field. A delay stage is used to offset the pump and probe beams and allow the THz temporal profile to be iteratively sampled. (reprinted from Ref. [256]). (b) Terahertz spectral features of the drug ranitidine hydrochloride, polymorphic forms 1 and 2. Signature peaks for each form can be identified easily using THz spectroscopy. (reprinted from Ref. [255]).

b) Terahertz Imaging

Pulsed THz-wave imaging, or ‘T-ray imaging’, was first demonstrated by Hu and Nuss [257] in 1995. Many common materials and living tissues are semi-transparent and have ‘Terahertz fingerprints’, permitting them to be imaged, identified, and analyzed. Since its inception it has been used for imaging a wide variety of targets including semiconductors [258], cancerous tissue [259] and flames [260]. The attraction of THz imaging is largely due to the availability of phase-sensitive spectroscopic images, which holds the potential for material identification or ‘functional imaging’. Moreover, the non-ionizing properties of THz radiation are inherently safe for screening application. Although the majority of the work on THz imaging has been performed using broadband ultrafast THz-TDS methods, QC laser sources may have a role to play, as they can deliver higher average powers (milliwatt-level compared with microwatt-level), and narrowband sources can more readily take advantage of the atmospheric transmission windows that are scattered throughout the THz regime [261].

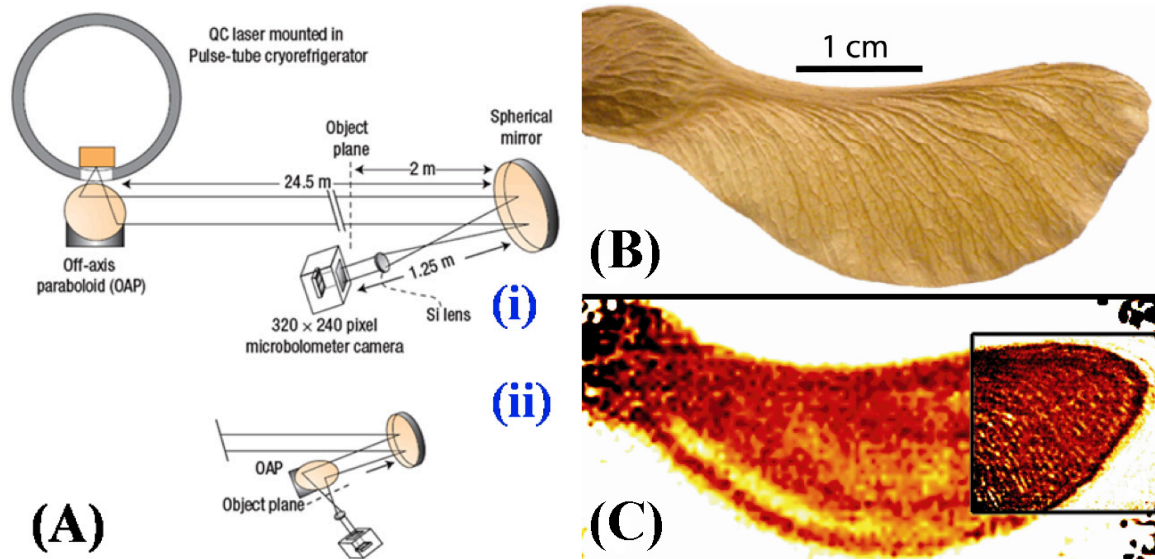


Fig. 6.1.3. Terahertz imaging with a QC laser. (A), Experimental set-up for imaging over a distance of 25 m, where a QC laser mounted in a pulse-tube cryocooler is used as the illumination source, and a room-temperature micro-bolometer focal-plane array camera is used to perform imaging in two possible configurations, (i) and (ii). (B) and (C) show a seed pod visible image, and THz image, respectively, taken with a 1-s integration time in imaging configuration (i). The inset of C shows the THz image from configuration (ii). (reprinted from [241, 261]).

In 2006, Lee and coworkers demonstrated real-time, video-rate, THz imaging using a 4.3 THz QC laser in conjunction with a commercial room temperature micro-bolometer camera [261]. The QCL delivers 50 mW of peak power at a 33% duty cycle, which enabled a video at 20 frames per second, with 20–30 dB signal-to-noise ratios. These are sufficient to enable imaging of pencil writing through envelopes. Atmospheric window at ~ 4.9 THz has low attenuation and therefore is more desirable for long-range imaging. Taking advantage of a transmission window at 4.9 THz, imaging in transmission mode over a 25 m distance was also possible (shown in Fig. 6.1.3, Ref. [261]).

6.1.1.2 THz detectors

THz detectors for time-domain systems were intensively studied in the 1990s, and now GaAs grown at low temperature is often used as a photoconductive antenna. Its unique properties are good carrier mobility, high dark resistivity, and subpicosecond carrier lifetimes [262]. Alternatively, electro-optic sampling techniques are available for ultra wideband time-domain detection. One can measure over 100 THz using a 10-fs-laser and a thin nonlinear crystal such as GaSe [263]. Deuterated triglycine sulphate crystals, bolometers, schottky barrier mixer diodes and superconductor-insulator-superconductor junctions are widely used as conventional THz

detectors [264-266], and their performances have been improved steadily. Further, a THz single-photon detector has been developed using a single-electron transistor [267].

6.1.1.3 THz light sources

There are three major approaches for developing THz sources. The first is optical THz generation, which has spearheaded THz research for the past few decades. The second uses solid-state electronic devices, which are already well established at low frequencies. The last one is the recently developed THz QCL, which is still being refined. Recent advances in nanotechnology have led to the rapid development of semiconductor-based THz sources: the THz-QCL. The current research objectives are targeting high performances at different lasing frequencies, including the following aspects: threshold currents, operational temperatures, tuneable ranges and beam quality. To achieve these goals new designs of structures, gratings and waveguides are being studied intensively. The development of such THz QCL will be presented in the following subsections.

6.1.2 From semiconductor laser to the intersubband engineering

The first semiconductor homojunction diode was demonstrated with coherent light emission by Robert N. Hall in 1962 [268]. The invention of the double heterostructure laser (DHL) shortly thereafter was reported by Kroemer in 1963 [269]. Later on, demonstrations on DHL allow a dramatic reduction of the threshold current density (J_{th}) and hence room temperature continuous wave (CW) operation. The active region of the DHL is sandwiched by other types of semiconductor with larger bandgaps. This creates band discontinuities and confines the injected carriers in the active region. The waveguide is created by the refractive index contrast between the materials, and the light generated by stimulated emission can be guided to propagate parallel to the layers. In 1974 the quantum well (QW) laser was invented by Dingle and Henry [270].

The QW laser is a DHL with multiple QWs at its active region. Population inversion is achieved via electrical pumping when current flows from the valence band to the conduction band. Such transition is also called ‘interband’ transition (as illustrated in Fig. 6.1.4(a)), where photons are generated during the electron-hole recombination across the semiconductor's bandgap. The emission wavelength is determined by the characteristics of the employed material. Small degree of freedom is possible to control the wavelength by active strained structures or by varying the composition and/or thickness of the different layers.

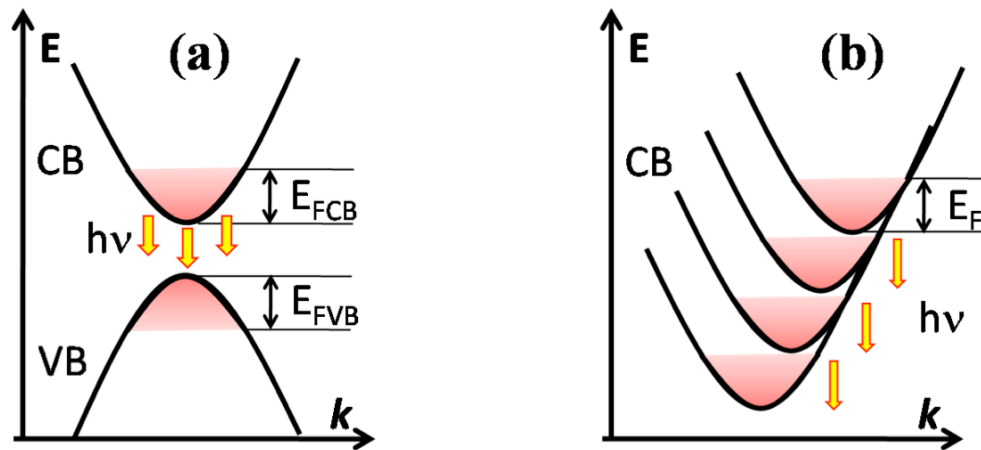


Fig. 6.1.4. (a) and (b), Schematic demonstration of interband and intersubband transitions, respectively.

However it is difficult to find a proper material system to achieve laser emission at low photon energies, *e.g.*, in the Mid-Infrared (MIR) range. Such issue was finally solved with the Quantum cascade laser (QCL). Faist and his co-workers in Bell lab in 1994 demonstrated a QC-laser emitting at 4.3 μm wavelength at cryogenic temperatures [239]. Unipolar transition between intraband states in the conduction band is employed in the QCL, which is intrinsically different from the interband transition in the conventional semiconductor lasers. More precisely, in the case of QW, such intraband transitions consist in ‘intersubband’ transition, *i.e.* transitions between quantized levels or bands originating from the same electronic band. Population inversion in the QCL case is achieved via the intersubband transitions between quantized states in multiple-QW heterostructures. Despite the fact that the carrier relaxation mechanisms within one band of a semiconductor is extremely fast, population inversion of the QCL can be achieved between such states by means of ‘band-structure engineering’ [271]. A schematic demonstration of the differences between conventional interband transition and intersubband transition are plotted in Figs. 6.1.4(a) and 6.1.4(b).

The band diagram of the first QCL [239] is reported in Fig. 6.1.5. The active layer of the laser structure consists of 25 periods of undoped $\text{In}_{0.48}\text{Ga}_{0.52}\text{As}$ QWs and $\text{In}_{0.47}\text{Al}_{0.53}\text{As}$ barriers with lattice matched to InP. It was grown by molecular-beam epitaxy (MBE) [272]. One period consists in an active region and a relaxation-injection region (graded region in Fig. 6.1.5). An external electric field is applied as depicted by the linear slope of the electronic potential. The optical transition occurs in the active region, while the carriers relax after the optical transition and are reinjected in the next period in the relaxation-injection region. The carriers are injected by resonant tunnelling in the state ‘3’, where they can relax to state ‘2’ by means of photon-assisted tunnelling [273] or by scattering, mainly from LO phonon if the condition $E_{32} \geq \hbar\omega_{\text{LO}}$ is satisfied. Population inversion is achieved when the lifetimes (τ) of the electrons in

the quantum states satisfies the relation $\tau_{32} > \tau_2$. The lifetime τ_{32} is increased by employing a transition with a reduced spatial overlap of the wavefunctions, and the lifetime τ_2 is reduced by making the energy E_{21} resonant with an optical phonon energy that is the most efficient energy relaxation mechanism [41]. The injector region is doped, acting as an electron reservoir and preventing the formation of space-charge domains. The cascaded geometry obtained by repeating N times the period allows electron recycling that can be re-injected in the subsequent period after performing the optical transition, thus giving rise to an internal quantum efficiency in principle greater than one and equal to the number of periods: the same electron can emit N photons [274].

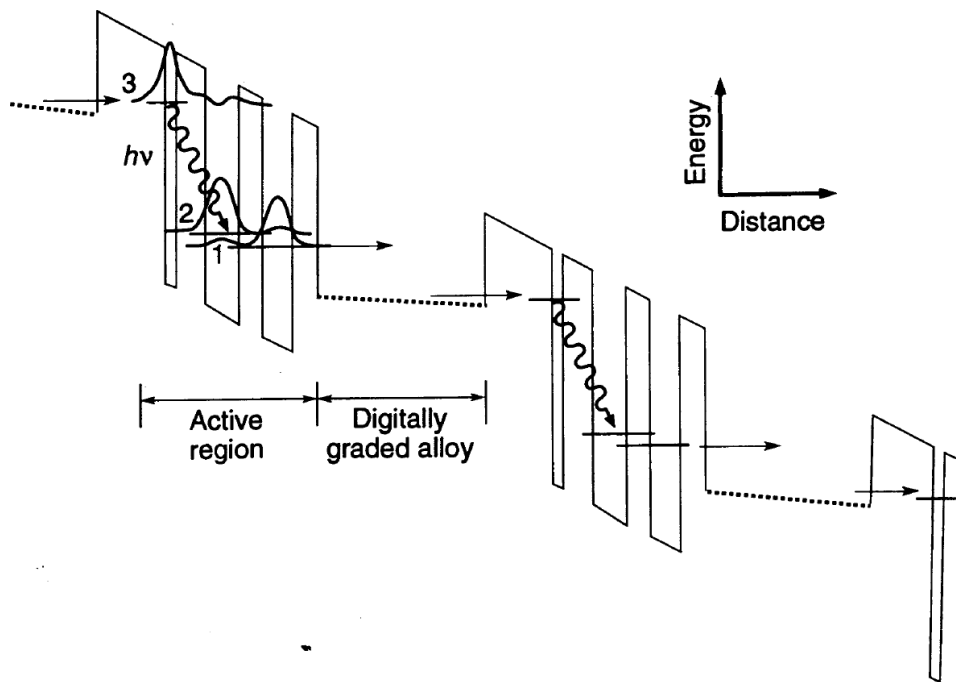


Fig. 6.1.5. Band diagram of the first quantum cascade laser reprinted from Ref. [239]. The structure is aligned for an applied electric field of about 95 kV/cm. Note the diagonal nature of the radiative transition in real space and the energy distance of one LO phonon between states 1 and 2. The digitally graded alloy is where the doping resides (reprinted from Ref. [239]).

The photon energy can be tuned simply by varying the energy spacing between the levels of the QW, *i.e.*, by changing its thickness. Therefore the QCL can generate light with an extremely large frequency range: NIR, MIR, FIR and THz. In the MIR range, QCLs operating between 3.5 μm and 14 μm with high performance have been commercialized. For example, peak power levels are in the Watt range and the operation temperatures for all of these wavelengths can be above room-temperature (RT) for both pulsed and CW conditions [275, 276].

6.1.3 THz QCL Active-region designs

In 2002 the first THz QC laser was reported at 4.4 THz (67 μm) by Köhler *et al.* [240]. The first demonstrated THz QCL lased only in pulsed mode with peak powers of a few milliwatts and ceased lasing above temperatures of several tens of Kelvin. At present, the THz QCLs have been demonstrated in the spectral range of 0.84–5.0 THz (Refs. [261, 277]). The maximum temperatures under the pulsed/CW operation have been achieved up to 220 K/117 K, respectively (Ref. [278]). The maximum output powers under the pulsed/CW operation have been achieved up to 250 mW/130 mW, respectively (Ref. [279]). Fig. 6.1.6 illustrates a survey reprinted from Ref. [241] of the temperature power performance for various types of active regions reported in the literature. The highest operating temperatures are achieved by designs based on resonant-phonon (RP) design. The design of each active region will be briefly introduced in the following text.

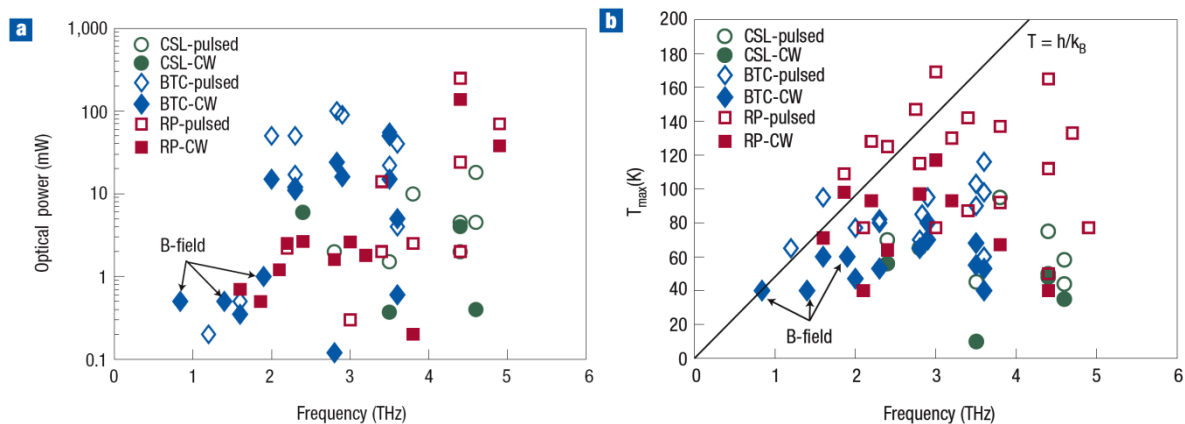


Fig. 6.1.6. Survey of the reported peak performance of THz QC lasers. (a), Peak optical power and, (b), peak operating temperatures are shown as a function of lasing frequency. Data are sorted by pulsed or CW performance and active-region design: RP, BTC or CSL. Several of the low-frequency designs operate with the assistance of a magnetic field (B-field). (reprinted from Ref. [241]).

The design and full examination of the THz QCL active regions are far beyond the scope of this thesis. Nevertheless, we can cite the major THz QCL active region designs as examples to understand the basic working principles behind. The active regions of the QC lasers are commonly grown by MBE in the GaAs/ $\text{Al}_x\text{Ga}_{1-x}\text{As}$ multiple-QW material system. Three major THz active region designs are shown in Fig. 6.1.7 and will be briefly introduced here: chirped superlattice (CSL) design, bound-to-continuum (BTC) design and resonant-phonon (RP) design. Their correspondent conduction-band diagrams are plotted in Fig. 6.1.7. The chirped superlattice demonstrated by Tredicucci *et al.* in 1998 [280] and the bound-to-continuum demonstrated by Faist *et al.* in 2001 [51] both show very good performances originally at low photon energies in

the Mid-IR. They can be also used in the realization of THz QCL.

The CSL design, shown in Fig. 6.1.7(a), is based on the interminiband transitions [281], where the applied electric field is compensated by the quasioelectric field resulting from a gradually varying (chirped) superlattice (SL) [282] period length and average composition. In this way “flat” minibands can be obtained without the need for dopants, which would broaden the optical transition and spoil population inversion at high temperatures [283]. The optical transition (black arrow in Fig. 6.1.7(a)) takes place from the lowest state of the upper miniband ‘2’ to the top state of the lower miniband ‘1’. The population inversion is sustained also at high temperatures because of the scattering of electrons between the tightly coupled states within the miniband (intra-miniband scattering) is favoured over inter-miniband scattering. Thus electrons tend to relax to the bottom of the minibands, leaving the lower radiative state relatively empty. This avoids the backfilling problem that can affect structures based on resonant tunnelling for extraction of the carriers [284].

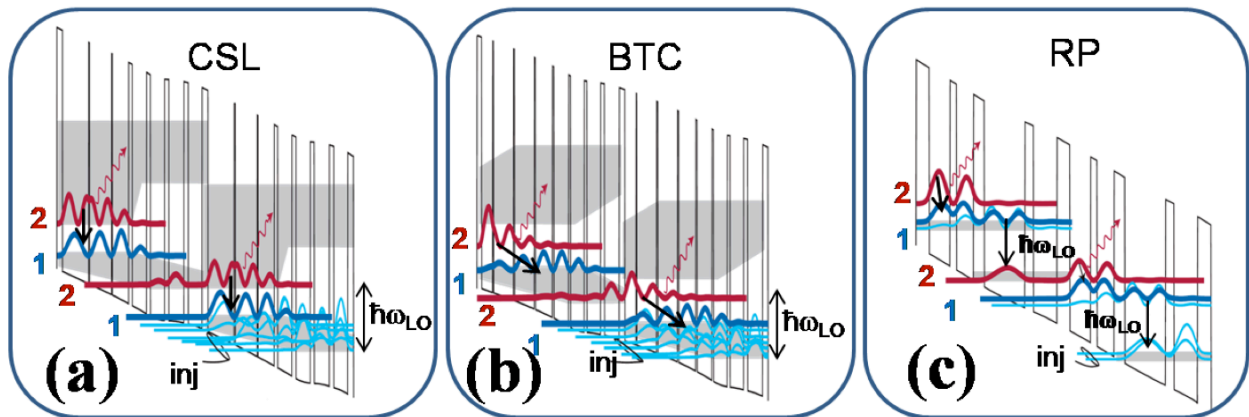


Fig. 6.1.7. Conduction-band diagrams for major THz QCL design schemes. Examples are shown for: a, CSL, b, BTC, c, RP and d, hybrid/interlaced designs. Two identical modules of each are shown here, although typically 100–200 cascaded modules are grown to form active regions 10–15- μm thick. The squared magnitude of the wavefunctions for the various subband states are plotted, with the upper- and lower-radiative state shown in red and blue respectively and the injector states specifically labelled. The grey shaded regions correspond to minibands of states. (reprinted from Ref. [241]).

The bound-to-continuum (BTC) transition, whose band diagram is shown in Fig. 6.1.7(b), is a high performance design based on superlattice design. The lower radiative state and miniband-based depopulation remains the same as in CLS design, but the upper radiative state is an isolated state (‘defect’ state) in the minigap [285, 286]. Such state can be created by inserting a thin well adjacent to the injection barrier, while electron extraction occurs through a lower miniband. The laser transition is diagonal in real space, which maximizes both the injection

efficiency and lifetime ratio (upper to lower state). The miniband transport is employed as an efficient extraction mechanism to minimize the lower state population. As a result, these designs displayed improved temperature and power performance compared with the CSL designs [286, 287] (see Fig. 6.1.6).

The Resonant-phonon-assisted (RP) scheme [288-290], shown in Fig. 6.1.7(c) is a robust depopulation mechanism at high temperatures in THz. Mid-infrared QCLs also use LO-phonon scattering for depopulation, while for THz lasers, the development of THz QCLs turned out to be much more difficult than initially expected [291]. It was difficult to use LO-phonon scattering to depopulate the lower radiative state without also depopulating the upper state [292, 293], because of the narrow subband energy spacing (~ 10 meV). The selectivity of the depopulation scattering on the desired radiative state is achieved through a combination of resonant tunnelling and LO-phonon scattering, hence the term *resonant phonon*. Collector and injector states are designed to be below the lower radiative state '1' by approximately $E_{LO} = 36$ meV, so that electrons in the lower state scatters immediately into the injector states by emitting an LO-phonon. The RP scheme allows a highly selective depopulation of the lower radiative level with a sub-picosecond lifetime, while maintaining a relatively long upper level lifetime (>5 ps) that is due to upper-to-ground-state scattering. The RP scheme is widely used to achieve high operating temperatures [278] and high output powers [279].

6.1.4 The waveguide

A good waveguide for THz light source should possess the following two features: low loss and high overlap. Common dielectric waveguides cannot be used for THz QCL due to the poor confinement factor. Moreover, as losses due to the absorption of radiation by free carriers increase proportionally to the square of the wavelength, waveguides are required that minimize the modal overlap with any doped semiconductor cladding layers. At present, there are two types of waveguides used for THz QC lasers: the semi-insulating surface-plasmon (SP) waveguide, and the double-plasmon (DP) waveguide (also called metal-metal (MM) waveguide). Their schematic demonstrations are shown in Figs. 6.1.8(a) and 6.1.8(b), respectively.

The first demonstrated THz QCL [240] made use of a semi-insulating SP waveguide [47, 294] to confine the optical mode. It suffers heavily from the high optical losses and poor overlap ($\Gamma \sim 0.1-0.5$, shown in Figs. 6.1.8(c) and 6.1.8(e) of the mode with the active region, especially long wavelength. Alternatively, DP waveguide [249] can provide mode confinement factor close to unity ($\Gamma \sim 1$, shown in Figs. 6.1.8(d) and 6.1.8(f)) [249, 278, 295], with reduced optical losses and improved temperature performance, especially at long wavelengths. However, there are two drawbacks of DP waveguide comparing with SP due to the large mode mismatch: one is

lower output power, another one is a poor beam emission diagram in the far field.

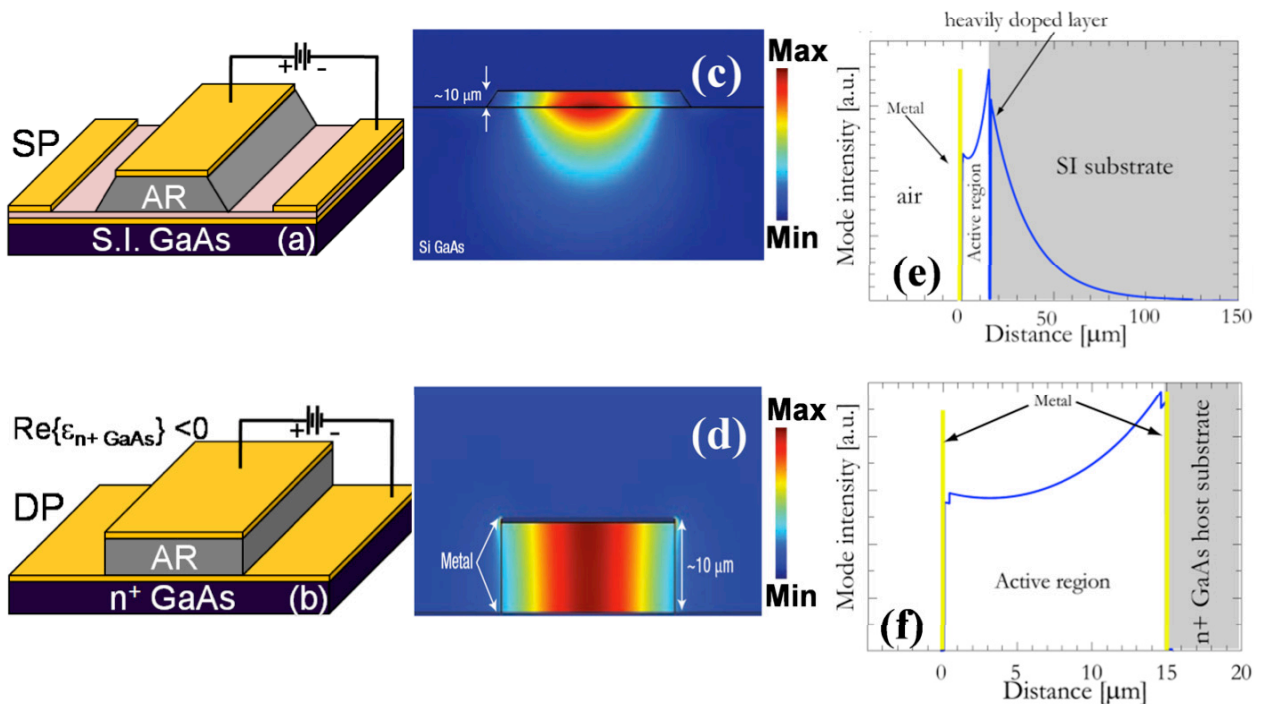


Fig. 6.1.8. Overview of the THz QCL's waveguides. Schematic diagrams (left), typical 2D mode intensity patterns (middle, reprinted from [241]) and 1D mode intensity pattern (right, reprinted from Refs. [240] and [249]) for (a), SP and (b), DP waveguides. n^+ indicates heavily doped region and $\text{Re}(\epsilon) < 0$ indicates that the real part of the permittivity is less than zero.

6.1.5 From Fabry Perot to Slow light photonic crystals.

As mentioned before in section 6.1.1.3, the extended lasing frequencies, lower threshold currents, higher operational temperature, broader tunable ranges and low-divergence beam are desirable for current research objectives of the THz QC lasers. Therefore, apart from the continuous investigation of the intersubband engineering, it is also important to investigate the QCL devices based on different lasing cavities.

The most common structure is the Fabry Perot (FP) cavity laser. The cavity is defined by the cleaved facets and the laser is generally multimode. Low threshold can be achieved, but the mode control is always an issue. The beam quality is heavily distorted by the DP confined narrow active region. Distributed feedback (DFB) structures with in-plane [296, 297] emission have achieved single mode operation, which was accompanied by a reduction of the maximum operating temperature [46]. Additionally, the electrical tuneability of the DFB QCL remains small, in the range of 4 GHz [46]. Micro-disk [298] cavity QC lasers, based on Whispering Gallery mode (WGM), have been reported for their low threshold and low power consumption. Nevertheless, the isotropic in-plane emission property makes them difficult to be utilized.

Recently, Walther *et al.* reported a new type of QC lasers based on coupled micro-cavities which employ the inductor-capacitor (LC) resonant circuit concept [299]. All these reported QC lasers are in-plane emitting lasers. Higher order DFB gratings on FP cavities [46, 300], ring resonators [301, 302], and micro-disk cavities [303] have been reported with vertical emission, however, the surface extraction efficiency and the emission power are not satisfactory.

The first demonstration of PhC QCL was done in 2003 by Colombeli *et al.* at MIR frequency [120]. Such PhC laser utilized deeply etched holes to achieve surface emission on the Γ band which is in the lightcone. Such design cannot fully exploit the potential of PhC, because the hole-type PhC is not a good candidate for TM polarized light. Dunbar *et al.* first demonstrated a pillar type PhC laser in 2005 [304]. Deeply etched pillars were placed adjacent to the FP etched facets, to act as high reflectivity mirrors due to the complete photonic bandgap in TM. The lasing characters are completely controlled by the PhC pillars. After a short period of technology transfer, I started to work on pillar type band-edge PhC QCL, and presented for the first time, a pure in-plane slow light band-edge emitting pillar type PhC QC laser at THz in 2007 [17]. Thanks to the DP waveguide and the BCB planarization technique [305], such photonic crystal lasers strongly improve the performances of THz quantum cascade material in all aspects. Subsequently in 2008, I demonstrated the first surface emission PhC QC lasers with deeply etched pillars operating at the 3rd band (Close to the 2nd bandgap) [306]. While at the same time, other groups were pursuing lasing emission (especially vertical emission) from non-complete PBG structures, such as investigations on patterning PhC holes on the top metal while remain the active region non-etched [19], or deeply etched holes [121].

Surface emission with high beam quality was achieved at Γ band-edge with implantation of a narrow heavily doped absorber [19]. Phase shifter was introduced to enhance the far field emission quality with PhC [307]. I demonstrated special PhC band engineering with elliptical pillar and subwavelength surface extractors with improved far field beam quality [308]. By adding periodic losses to pillar-type PhC system, I achieved an independent refractive index and loss modulation scheme.

In the following sections, I will focus on the experimental achievements and on the investigation of slow light THz PhC QCL lasers. All the PhC lasers investigated are based on strong PhC effect with deeply etched pillars.

6.2 Characterization technology for THz PhC QC lasers

In this section, we will briefly introduce the characterization techniques performed in collaboration with the group in ETHZ.

6.2.1 Electroluminescence and laser emission measurements

All the fabricated PhC QC lasers were characterized within the collaboration of Prof. J. Faist's group in ETHZ. We will briefly introduce the characterization tools that were used, *i.e.* light-current-voltage (LIV) and Fourier transform far-infrared spectral emission (FTIR) measurement. After the bottom contact deposition, the sample was shipped to ETHZ and then cleaved and mounted on a copper holder with conductive glue and bonded with 25 μm gold wires. The typical operating temperature of the THz QCL is below 150 Kelvin, therefore a helium cooled cryostat which allows the coldest temperature of 4 K is used to cool the QCL sample.

For laser emission and power measurement (also called light-current-voltage measurement, abbreviated as LIV), a lightpipe is used to collect the THz emission from the laser facet/surface directly. The light is guided through a polyethylene window, and then a calibrated thermopile (Ophir, SH5) is used to perform the power measurement. For THz spectral emission measurements, a Fourier transform infrared (FTIR) [309, 310] spectrometer has been used. The FTIR consists of a Michelson-Morley interferometer where the resolution is given by the optical path length difference between the two interfering light beams. For electroluminescence (EL) characterization, an under-vacuum home-made FTIR developed at ETHZ has been used. Under vacuum measurement are required because the THz frequencies are strongly absorbed by water vapor [274] and the power emitted from the THz devices may be very low, *e.g.* in the range between picowatts and milliwatts.

A step-scan technique, rather than continuous scan is used to increase the setup sensitivity [274]. The electrical power is provided by a HP-8114A pulse generator, with typical 1 Hz to 15 MHz frequency range and 10 ns to 150 ms pulse width range. The injected current is measured using a calibrated current probe (Model 711 calibrated by American Laser Society). The probe is an electrical transformer placed around the injection current line. The current and the bias on the device are measured by a digital oscilloscope. A phase-sensitive detection scheme is employed, where a lock-in amplifier is synchronized with the pulse generator. Pyroelectric infrared detectors are used, their Noise Equivalent Power is in the $\mu\text{W}/\text{Hz}^{1/2}$ range.

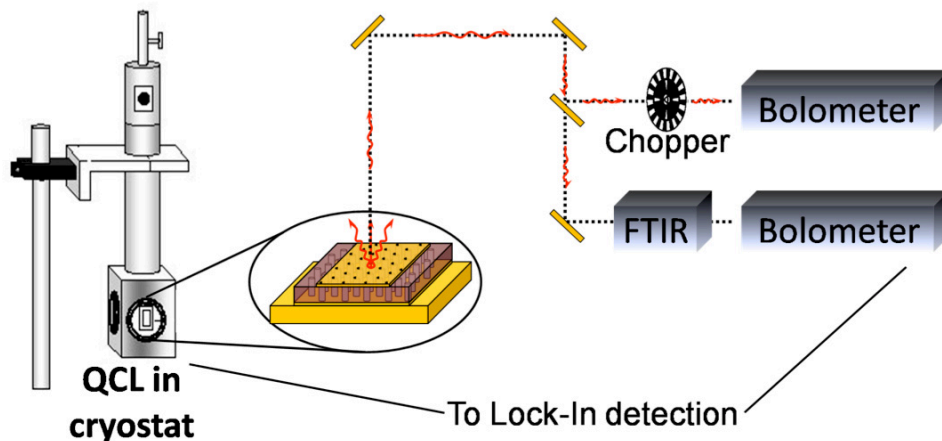


Fig. 6.2.1. Illustration of THz spectra emission measurement setup with an example of surface emitting PhC laser. Radiation path is marked with dashed lines and wavy arrows.

For very low emitting powers, a bolometer, with NEP in the $\text{pW}/\text{Hz}^{1/2}$ range, is used to measure *e.g.* spontaneous emission. Liquid He-cooled Si bolometer is used. The bolometer is intrinsically a slow detector (slow response time) based on a thermal effect over large areas, therefore the injected current is modulated with low frequency long pulses at a repetition rate that matches the bolometer maximum recovery time ($1/\tau_{\text{Sibm}} = 416 \text{ Hz}$ for this Si bolometer). In order to prevent as much as possible device heating, trains of N micro-pulses with a repetition rate of $1/T$ with $NT = \tau_{\text{Sibm}}/2$ are produced. The maximum possible overall duty factor is 50% [274]. Fig. 6.2.1. illustrates the THz spectra emission measurement setup with an example of surface emitting PhC laser.

6.2.2 Far-field characterization

Some of the PhC QCLs can emit very high peak power in the range of tens of milliwatts, which is large enough to allow a far field characterization. The far-field pattern of the laser devices is a key element necessary for the understanding of the lasing mechanism and light extraction, it is also an important feature that characterizes the device performance. A pyroelectric detector mounted on a double rotational stage that allows an angular scan close to 180° on α and β axes correspond to an angular scan in the planes of ΓK and ΓM , respectively [48, 250]. The point $(\pm 90, 0)$ therefore indicates a longitudinal edge emission and point $(0, 0)$ an emission normal to the surface (Fig. 6.2.2).

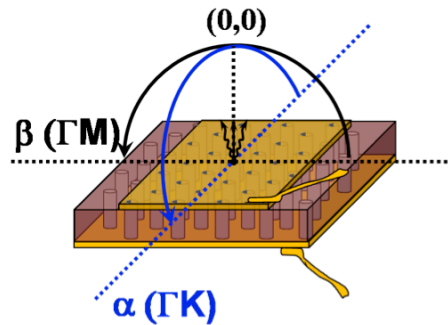


Fig. 6.2.2. Schematic of the angle rotation for the far field measurement.

6.3 Experimental investigation of high performance in-plane emitting terahertz photonic crystal quantum cascade lasers*

*The main results in this section are originally published in "Terahertz Photonic Crystal Quantum Cascade Lasers." Optics Express 15, 16818-16827 (2007).

From this section to the end of this chapter, I will present in detail the experimental investigation results of different pillar type photonic crystal quantum cascade lasers at THz frequency. All the PhC band structure calculations are performed with PWE method as explained in Chapter 2, and all the fabrication procedures are processed with DP waveguide and BCB planarization technique as explained in Chapter 3. Moreover, All the optical-electrical characterization, such as lasing spectra and Electro-Luminescence (EL) spectra measurements, and light-current-voltage (L/I/V) curves against temperature in both pulsed and Continuous-Wave (CW) conditions were performed using the characterization technique as explained in Section 6.2.5.

6.3.1 First band slow light photonic crystal pillars

Our device consists of an active region, patterned into a triangular lattice of pillars, created from the high refractive index semiconductor QCL gain material (Fig. 6.3.1(a)) embedded and planarized in BCB (Fig. 6.3.1(b)). The THz PhC QCL has a complete PBG for TM-polarized light with flat-bands over a large domain in k-space and low-loss band-edge states, and does not rely on defect modes and external mirrors. However, the double plasmon waveguide generates a large impedance mode mismatch that also generates reflection at the tile boundaries (Fig. 6.3.1(b)). Several different lengths (from 600 μm down to 100 μm) rectangular top contacts are used (Fig. 6.3.1(c)).

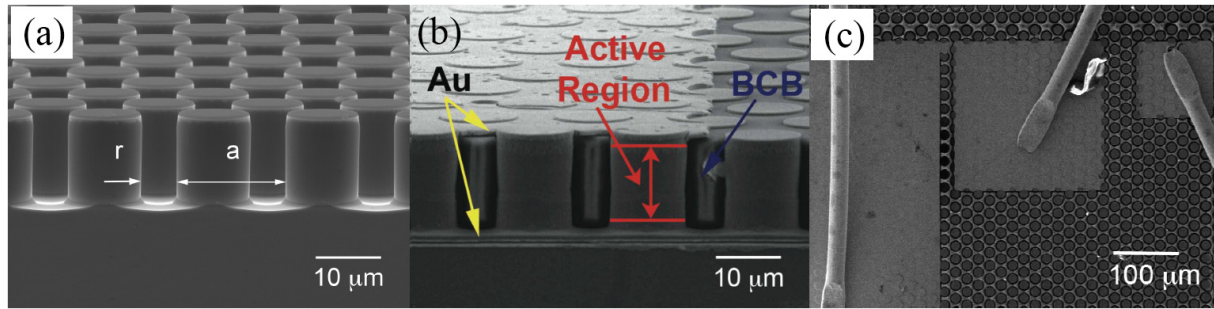


Fig. 6.3.1. Scanning Electron Microscope (SEM) images of THz PhC lasers. a, Cross-section SEM image of PhC pillars after dry etch, showing their high verticality and side-wall smoothness ($\sim 15.5 \mu\text{m}$). b, Side view SEM image of double metal configuration bounding the PhC pillars which are surrounded by BCB. c, Top view SEM image of PhC tile lasers (lengths of square top contacts are $600 \mu\text{m}$, $200 \mu\text{m}$ and $100 \mu\text{m}$) with $25 \mu\text{m}$ diameter bonded gold wire.

The material gain (rectangular blocks) is superimposed onto the PhC dispersion curve of Fig. 6.3.2(a). Patterned blocks show the ranges of the experimentally observed laser or spontaneous emission. 2D Finite Element Method (FEM, [43]) simulation with reflecting boundary condition finds a large number of resonance modes as a consequence of v_g reduction over an extended region of k space between M and K energies. The simulation confirms that the mode spacing is inversely proportional to the size of the PhC tile. The overlap between the calculated peak SE range and the band energy between M and K singularities in Fig. 6.3.2(a) indicates that our PhC tile QCLs with a values between $16 \mu\text{m}$ and $18 \mu\text{m}$ are in the optimum configuration for lasing, because the optical modes are mainly localized in the gain material (dielectric band) and the gain enhancement is maximum in the flat-band region.

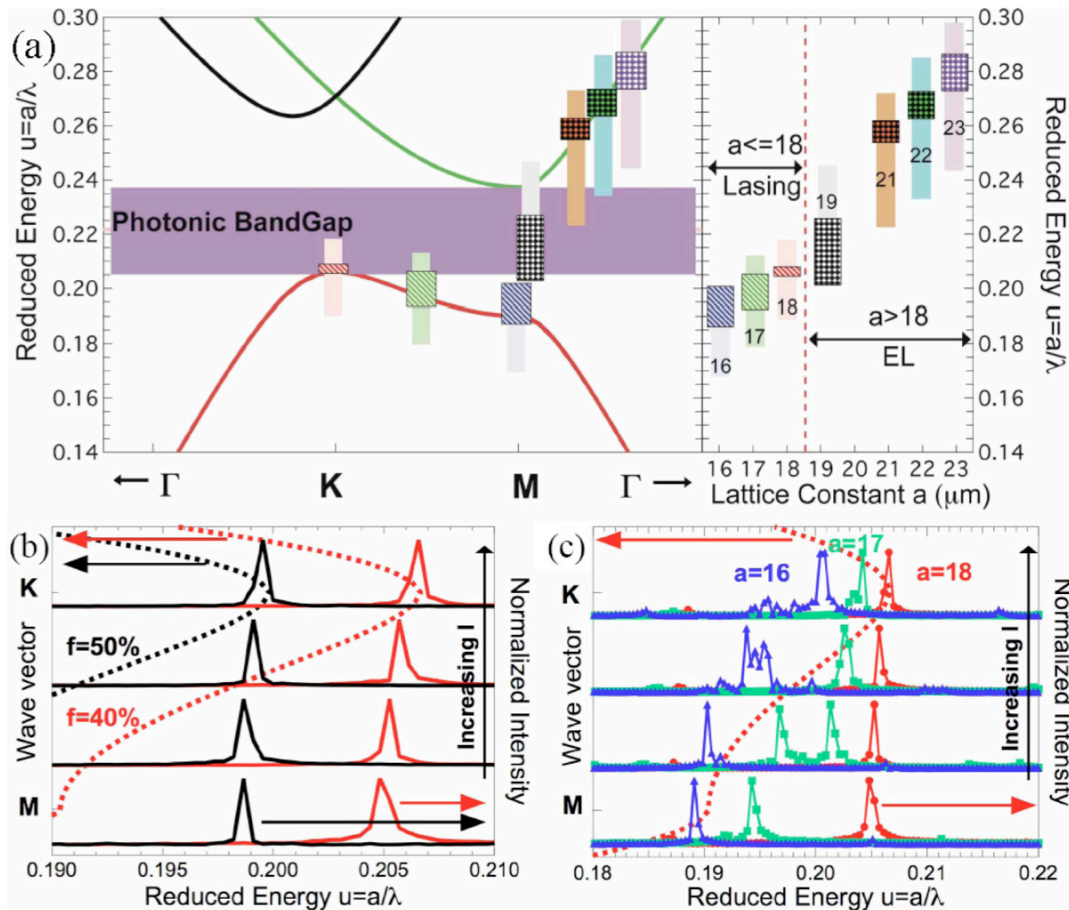


Fig. 6.3.2. Superimposition of material gain and experimentally measured spontaneous and lasing spectra emission ranges onto PhC dispersion curve and lasing emission spectra. a, Left panel shows the material gain range and experimentally measured emission spectra range superimposed onto PhC dispersion curve. Right panel shows the material gain and experimental measurement emission spectra range in reduced energy scale. Solid curves represent the PhC dispersion band diagram; wide patterned blocks represent the ranges of the observed lasers at $a = 16, 17$ and $18 \mu\text{m}$, or spontaneous emission at $a = 19, 21, 22$ and $23 \mu\text{m}$. Narrow rectangular blocks represent material gain. b, Left hand axis: black and red dashed lines represent the simulated PhC first bands for $ff = 50\%$ and 40% between M and K points respectively. Right hand axis: lasing spectra (solid curves) of same lattice constant $a = 18 \mu\text{m}$ at different ' ff ' 50% (black) and 40% (red). A 0.81% (30 GHz) continuously dynamic single mode tuning is observed from $ff = 40\%$ curves. c, Left hand axis: Red dashed curve represents the simulated PhC first band of $ff = 40\%$ between M and K points. Right hand axis: Lasing spectra (solid curves) of $ff = 40\%$ at $a = 16$ (blue), 17 (green) and $18 \mu\text{m}$ (red). A coarse lithographic tuning range of 14.6% (450 GHz) is clearly shown.

The $a = 18 \mu\text{m}$ spectra (Fig. 6.3.2(b)) at pillar filling factor ' ff ' 40% and 50% agree excellently with the corresponding calculated K band-edges. The $a = 16 \mu\text{m}$ spectra

(Fig. 6.3.2(c)) under low current density correspond to the M point. The transition from M saddle point lasing ($a = 16 \mu\text{m}$) to K band-edge lasing ($a = 18 \mu\text{m}$) agrees with the theoretical expectation. The PhC tile QCLs emit predominantly in single mode, except under high injection current. The mode hopping at $a = 17$ and $16 \mu\text{m}$ (Fig. 6.3.2(c)) is caused by the blue shift of the material gain due to the diagonal nature of the bound to continuum transition. The drift continues until the next band-edge point (K) is reached. Note, however, that dispersion along the MK path remains flat and slow light gain enhancement still occurs. For the same lattice constant, PhC lasers with difference size of top contacts show very similar single mode spectral behaviour at localized M or K positions, corroborating the fact that our PhC tile QCLs are lasing as 2D-DFB lasers, which lock in frequencies at the saddle point M and band-edge K. The smallest laser is only 11 periods long ($\sim 2.2 \lambda$). No lasing behaviour was observed for the $100 \mu\text{m}$ long square laser, due to its small size (< 5 periods), which cannot supply sufficient gain enhancement.

As can be seen in Fig. 6.3.2(b), these spectra show that due to cavity pulling the laser emission gradually shifts to higher energies when increasing current density. Note that relying on a cavity pulling effect by the field induced gain shift, the single mode emission can be dynamically and continuously tuned by a value as large as 30 GHz (0.85%), when the lasing frequency approaches the PhC band-edge ($a = 18 \mu\text{m}$). The shift of the observed spectra from M to K points in Fig. 6.3.2(c) corresponds to an emission tuning in reduced energy scale ' u ' between $0.189 \sim 0.201$ (3.55 THz to 3.77 THz) and $0.195 \sim 0.204$ (3.43 THz to 3.60 THz) for $a = 16$ and $17 \mu\text{m}$, respectively. There is a total multimode coarse dynamic tuning range of 220 GHz (6.2%) by varying the injection current to change the properties of QC material, or 450 GHz (14.6%) lithographic tuning range by varying a values to change the properties of PhC.

Emission bandwidth of larger lattice constant tiles ($19 \mu\text{m} < a < 23 \mu\text{m}$) either overlap inside the PBG or the air band whose modes have a limited spatial overlap with the QC material. Consequently only EL was observed. No lasing behaviour at $a = 14$ and $15 \mu\text{m}$ is observed, due to the fact that there is no spectral overlap between the material gain range and the lowest M band singularity.

6.3.2 Electro-Luminescence and lasing measurement.

Figure. 6.3.3(a) shows the lasing or EL spectra of different lattice constants. Lasing behaviours are observed when the lattice constants are smaller than $18 \mu\text{m}$, this is because of the strong overlap between the material gain and the optical mode. When the lattice constants are larger than $18 \mu\text{m}$, only EL can be observed, this is because the frequency is either inside PBG or at air band (mode maximum in the air). This makes the optical mode cannot overlap with the material gain. The weak signals detected in the spectra are the EL from the pillars in the sample

border.

The high resolution spectra measurements were performed again one year after the device fabrication on the single mode laser. No performance degradation was observed. This means the BCB process has the potential to be used for long life-time commercial lasers. Fig. 6.3.3(b) shows the lasing spectra of the PhC QCL at lattice constant $a = 18 \mu\text{m}$ as a function of the injected current in continuous wave operation at a temperature of 25 K. Such frequency ($u \approx 0.206$) corresponds to the K band-edge state referring to the band-edge state shown in Fig. 6.3.2. The single mode emission gradually shifts to higher energies by 30 GHz with increasing current density. Such tuning is achieved via increasing the injection current. The cavity pulling effect and the field induced gain shift [311] allows such significant electrical tuning range [17]. This value is much larger than other types of devices based cavity pulling, such as FP lasers or microdisk lasers [298], or DFB QCLs [46]. The E_z field map of the lasing K band-edge state is shown as insert in Fig. 6.3.3.

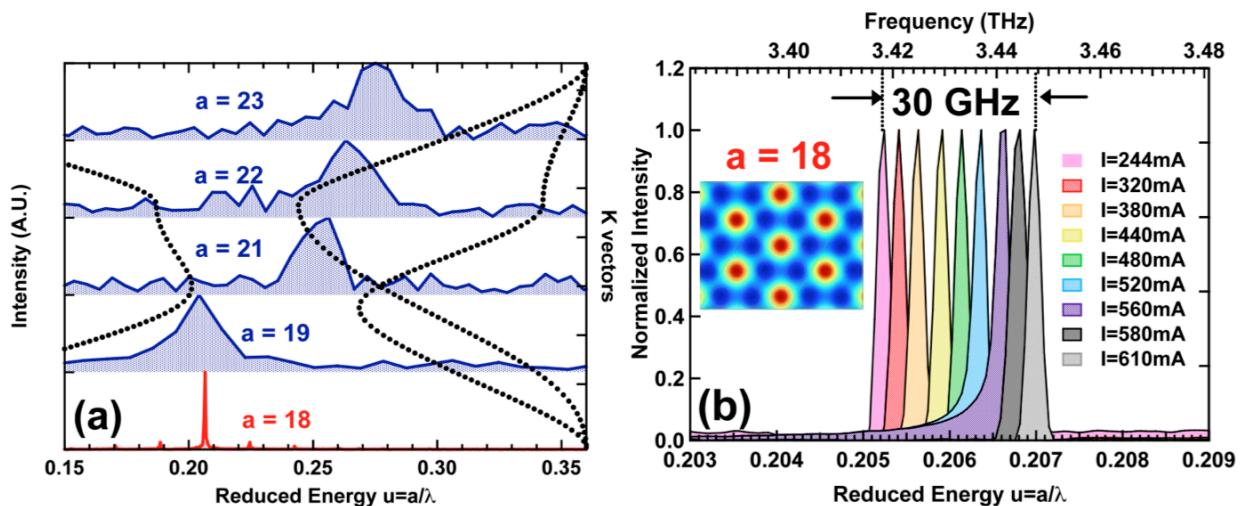


Fig. 6.3.3. Spectra characterization of the PhC QC devices. (a). Comparison of Electro-luminescence (EL, blue curves) and Lasing spectra (red curve) at different lattice constants. When $a \leq 18 \mu\text{m}$, the PhC devices are lasing. When $a \geq 19 \mu\text{m}$, only EL single can be detected. Lasing spectra (solid curves) as a function of the injected current in continuous wave at a temperature of 25 K for a device of lattice constant $a = 18 \mu\text{m}$ at filling factor 'ff' 40%. A 30 GHz continuously dynamic single mode tuning range is observed. Insert is the E_z field map of the corresponding PhC lasing state at bandedge k point.

Fig. 6.3.4(a) illustrates the trend of the light-current (L/I) curves versus lattice constants. The increase of a shows a concomitant decrease of the threshold current, due to the strongest overlap between the material gain peak and the optical mode energy at K band-edge for $a = 18 \mu\text{m}$; this also results in its narrowest dynamic range, because the gain spectrum can only be

shifted into the PBG where no modes can exist. In contrast, the optical mode frequency of smaller a lasers (e.g. $a = 16 \mu\text{m}$) have the potential to span a longer distance between MK path in the wave vector space, and to interact more with the material gain along its blue shifting, thereby giving it broader dynamic ranges.

6.3.3 Measurement results and discussion

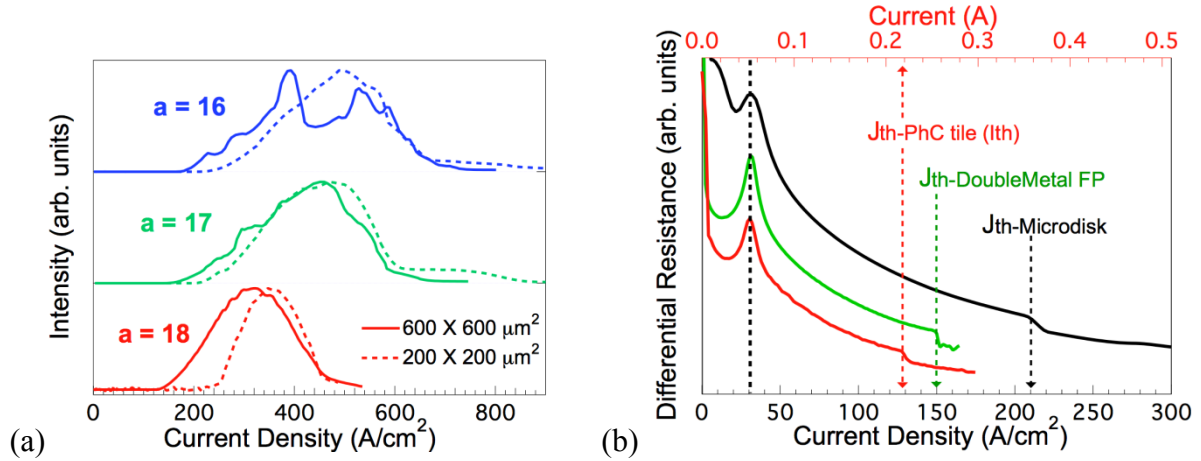


Fig. 6.3.4. Comparison of L/I curves of PhC tile lasers at different lattice constants and differential resistances. (a), L/I characterization of PhC tile lasers at different lattice constants $a = 16$ (blue), 17 (green) and 18 (red) μm under pulsed condition (pulse = 200 ns, duty cycle = 1.3%). Solid lines represent the $600 \times 600 \mu\text{m}^2$ tile lasers, and dashed curves represent the $200 \times 200 \mu\text{m}^2$ tile lasers. (b), Differential resistance versus current density under CW measurement for PhC tile laser ($a = 17 \mu\text{m}$, red, bottom and top axis), double plasmon FP laser ($1400 \times 80 \mu\text{m}^2$, green, bottom axis) and micro-disk laser (radius = $50 \mu\text{m}$, black, bottom axis), the PhC laser has the lowest threshold current density among the others.

It is difficult to obtain the threshold current density for devices based on electrically pumped PhCs precisely and directly, because of the uncertainties on calculating the surface area of the laser and the current spreading [120]. In our case, we circumvent this problem by analysing the miniband electronic transport of the lasing devices. Since all the devices tested show CW operation, we can precisely assess the threshold current density for the PhC tile QCL structures by inspecting the CW electronic transport characteristics of the devices and compare it to reference FP and micro-disk lasers, whose injection surfaces are precisely known. As widely used in electronic transport spectroscopy, we report in Fig. 6.3.4(b) a plot of the differential resistance (dV/dI) versus injected current at 10 K for a PhC tile QCL ($a = 17 \mu\text{m}$), for a micro-disk laser ($50 \mu\text{m}$ radius) and for a double plasmon FP laser fabricated with the same epilayer (N306). We can use the first prominent peaks in the differential resistance (at $J = 31 \text{ A/cm}^2$) for all samples for relative calibration and comparison. All peaks occur at the

same current density, as they are the consequences of misalignment of the injector states from the lower miniband edge state [240]. Note that we defined the current density as the current divided by the cross section of active material, not the pad area, and therefore the "apparent" current density that would for example determine the thermal properties of the device are even lower. In this way current density directly quantifies the excitation of the active material itself and can be used to compare PhC and non-PhC lasers. The lasing threshold is deduced from the discontinuity in the differential resistance due to the onset of stimulated emission. The threshold current density for this tile PhC QCL sample is 128 A/cm^2 which shows a 17 % reduction compared to double metal FP laser, and 41% reduction compared to micro-disk laser.

Threshold reduction in lasers are usually achieved by reducing the relative weight of the out-coupling losses, either with the use of high reflectivity out-coupler or with an increase of the active region area. Similarly, the threshold reduction in band-edge PhC lasers is achieved thanks to an enhancement of the modal gain within the crystal, or, equivalently, a reduction of the out-coupling losses. It is remarkable that, in opposition to a regular FP laser, this is achieved while reducing the volume of the active material, consequently reducing even more the threshold current. Comparison of a PhC tile laser with a FP laser of identical size ($250 \times 400 \text{ }\mu\text{m}^2$ and $1170 \times 100 \text{ }\mu\text{m}^2$ for PhC and FP laser, respectively) shows a moderate reduction of the threshold current density from 155 to 145 A/cm^2 , but a large reduction of the threshold current from 183 mA down to 42 mA . However, previous work on THz QCL have shown, that the 1 mm long, metal-metal waveguide devices, which were used as a reference, have negligible out-coupling losses since the large impedance mismatch between the waveguide and vacuum provides a reflectivity close above 75-80% [47]. The fact that similar thresholds were observed in whispering gallery micro-cavity QCL fabricated with the same material corroborates this point [298]. As the active region is identical, the reduction of the threshold current density should be attributed to a reduction of the waveguide losses by the same amount.

In our metal-metal waveguide, the two components in-plane and perpendicular of the electric field vector generate losses of a different physical origin: the loss of the component normal to the layer will mainly be due to out of resonance intersubband absorption in the injector, the loss of the component in-plane to the layer originates from ohmic losses due to the free in-plane motion both in the active region as well as in the contact and metal layers. The band structure of the injector may be optimized to minimize the amount of losses due to the normal component of the electric field, as shown in Ref. [312], we demonstrate here that the PBG structure may be used to reduce the loss originating from the in-plane component.

In the standing wave pattern of the laser mode, the maximum of the normal and in-plane components of the electric field are shifted by quarter wavelengths. Let us assume for simplicity

a metal-metal waveguide in which a TM mode is propagating in the y direction; z is the confinement direction. The magnetic induction will then have the dependence given by:

$$\vec{B} = (B_x(z)e^{i(\beta y - \omega t)}, 0, 0) \quad (6.3.1)$$

where β is the propagation constant, ω the light angular frequency and $B_x(z)$ the z dependence of the B-field. The time derivative of two components (y and z) of the electric field may be derived from the magnetic field vector using

$$\nabla \times \vec{B} = \epsilon\mu_0 \frac{\partial}{\partial t} \vec{E} \quad (6.3.2)$$

and therefore we have

$$E_z(z) = -\frac{\beta}{\omega\epsilon\mu_0} B_x(z)e^{i(\beta y - \omega t)} \quad (6.3.3)$$

And

$$E_y(z) = \frac{i}{\omega\epsilon\mu_0} \frac{\partial}{\partial z} B_x(z)e^{i(\beta y - \omega t)} \quad (6.3.4)$$

As shown by Eqs. 6.3.3 and 6.3.4, the two components of the electric field exhibit a $\pi/2$ phase shift in respect to each other; the standing wave pattern produced by two such counter-propagating fields will therefore producing standing waves shifted by a quarter wavelength.

In our PhC laser, thanks to the patterning of the active medium the anti-node of the in-plane field occurs in the low-index waveguide section (BCB), which, because it sustains a guided mode with a more rectangular profile. Such rectangular profile is less overlapped with the heavy lossy contact layers in the pillar, hence making itself intrinsically less lossy than the high-index section. This reduction of the losses is a unique feature of our deep etched, strongly confined PhC structure that was not present in previous QCL.

Fig. 6.3.5(a) is the L/IV measurement as a function of temperature. The $a = 17 \mu\text{m}$ PhC tile QCL operates up to 105 K under pulse condition. The dashed line at $J_d = 580 \text{ A/cm}^2$ represents the decay current density J_d for all the temperatures. Such L/I curve shape is caused by the energy mismatch between the material gain and the optical mode which limits the dynamic range.

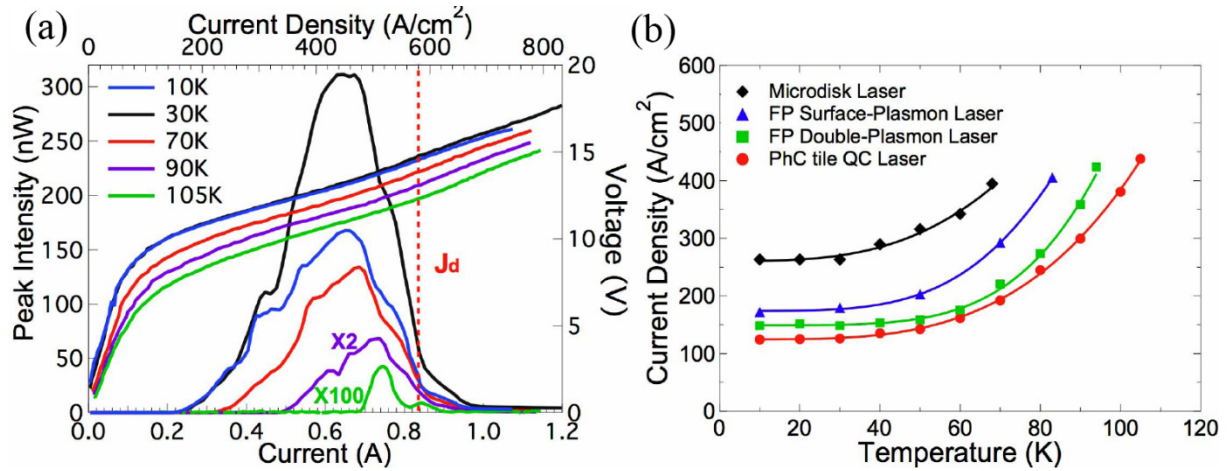


Fig. 6.3.5. *L/I/V* characterization of THz QCL PhC lasers as a function of temperature and the comparison of maximum operation temperature between different material systems. (a), *L/I/V* characterization of peak intensity of the PhC tile laser at lattice parameter $a = 17 \mu\text{m}$ as a function of temperature under pulsed condition (pulse = 200 ns, duty cycle = 1.3%). The lowest threshold current density of this laser is 128 A/cm^2 and the maximum operation temperature is 105 K (intensities at 90 K and 105 K have been scaled by a factor of 2 and 100, respectively). Note that the value of the y scale does not describe the actual emitted power intensity, as the collection efficiency of the setup does not exceed 20%. (b), Comparison of maximum operation temperature between PhC tile laser ($600 \times 600 \mu\text{m}^2$, red circles), double plasmon FP ridge laser ($1170 \times 100 \mu\text{m}^2$, green squares), surface plasmon FP ridge lasers ($2000 \times 200 \mu\text{m}^2$, blue triangles) and micro-disk laser ($50 \mu\text{m}$ radius, black circles). Continuous curves are guide for eye. All devices are processed from the same epilayer.

There is a 17% improvement on the maximum operation temperature respect to the FP laser on the same layer. To further investigate the enhancement of temperature performance, we fit J_{th} versus temperature between PhC tile laser ($600 \times 600 \mu\text{m}^2$), double plasmon FP ridge laser ($1170 \times 100 \mu\text{m}^2$), surface plasmon FP ridge lasers ($2000 \times 200 \mu\text{m}^2$) and micro-disk laser ($50 \mu\text{m}$ radius), as shown in Fig. 6.3.5(b). Note that all of these lasers are fabricated with the same epilayer (N306). Based on its lowest current threshold density, our PhC tile QCL has the highest operating temperature among all the waveguides we were able to realize (and known in literature), including the best double plasmon FP laser with very comparable injected current, this indicates that exploiting PhC band engineering substantially enhances the gain, thus reduces the losses, and improves the temperature performance.

6.3.4 Conclusions

Our THz PhC tile QCLs combine optical dispersion engineering in PhCs and intersubband electronic engineering in QC structures. This is the first time PhC are successfully used to

combine and enhance the key performances on THz QCLs over known FP and micro-disk lasers in all aspects. While remaining single mode, we have shown that employing PhCs allows a substantial reduction of the threshold current and current density due to slow light effects (or band-edge nature) of the lasing mode and we have simultaneously achieved a reduction in waveguide losses by exploiting the peculiarities of the PhC in a metal-metal waveguide. In the QC material used in the present study, a diagonal transition combined with a relatively weak coupling between the injector and the upper states allows a significant electrical tuning over a frequency range of 30 GHz. Such tuning range is achieved at a cost; the quantum design that enabled such a wide tuning due to the electrical tuneability of the gain spectrum is inherently limited to lower operating temperatures. We believe that our approach, mixing PhC and metal-metal waveguide with designs adapted to higher operating temperatures [278] open the way toward low threshold, single mode and high operating temperature THz QCLs.

6.4 Surface emitting pillar type photonic crystal quantum cascade lasers working at Γ band-edge point*

*The main results in this section are originally published in "In-plane and surface emitting high performance THz pillar type photonic crystal lasers with complete photonic bandgaps" art. no. 5192585, CLEO/Europe - EQEC 2009 - European Conference on Lasers and Electro-Optics and the European Quantum Electronics Conference.

6.4.1 Introduction

Surface emission is always a challenging task for semiconductor lasers, especially with quantum cascade (QC) active material operating in the terahertz (THz) range. The transverse magnetic (TM) polarized emission of QCLs makes them intrinsically in-plane emitters. Therefore vertical emission, which is desirable for many applications, needs additional engineering. Second order Distributed Feedback (DFB) lasers [46, 313] and Γ band-edge PhC lasers [19, 121, 250] have been used to achieve surface emission. However the DFB scheme is achieved with 1D index, while the demonstrated Γ band-edge PhC devices do not exploit the full potential of strongly modulated PhC structures with full photonic bandgap (PBG).

In previous sections we have demonstrated THz in-plane emitting PhC QCL and its fabrication techniques. The reported PhC laser works as 2D DFB lasers [17] operating at slow light band-edge state or Van Hove singularities on the first band (*i.e.* first bandgap), due to the slow light signature [66-68]. In contrast to the weak PhC effect lasers, deeply etched PhC pillars were used to generate a strong PhC effect [17, 120, 121, 304] with high index modulation.

In this section, we report a proof-of-principle demonstration of surface emitting pillar type photonic crystal lasers on quantum cascade material around 1.5 THz. The lasers operate in the

slow-light regime between the M saddle state and Γ band-edge state in the reciprocal lattice. The lasing modes are identified and compared with our theoretical calculation. Strong single mode surface emitting behaviour is observed at the Γ band-edge state. A very large lithographic tuning range of 234 GHz is obtained, which accounts to a 17% of the entire tuning range.

6.4.2 Design of surface emitting PhC QCLs with large extractors

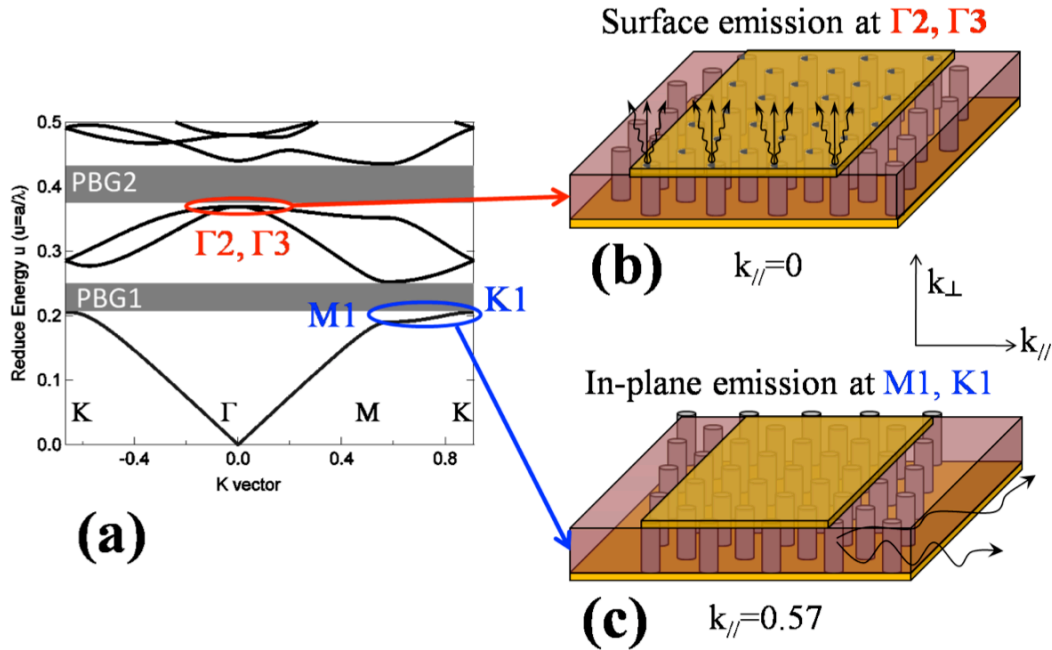


Fig. 6.4.1. Photonic crystal dispersion and sketch plots of the in-plane and surface emitting schemes. (a), Photonic crystal dispersion curves calculated by Plane wave expansion method with two complete bandgaps, PBG1 and PBG2. The pillar filling factor (ff) is 40% in the simulation. (b), Sketch of the lasing mode operation at the bandedges (Γ_2, Γ_3) corresponding to the surface emitting scheme. The pillar height is about $15 \mu\text{m}$ and period range is between $14 - 23 \mu\text{m}$. (c), Sketch of the lasing mode operation at the bandedges (K_1, M_1) corresponding to the inplane emitting scheme.

The PWE method was used to model the planar pillar type PhC as a 2D system in order to calculate the in-plane band structure similar as before (plotted in Fig. 6.4.1(a)). Several complete PBGs can be observed. The slow light regimes, with flat-dispersions over large k-vector ranges and with a large field overlap with the high index medium at the low energy edges of PBG1 and PBG2 are of particular interest. Around the first bandgap (PBG1), the high symmetry K band-edge and M saddle states with large k-vectors allow intrinsic in-plane emission as shown in the sketch plot of Fig. 6.4.1(c). Around the second bandgap (PBG2), the Γ band-edge states with wavevector $k=0$ lie above the light cone, and this allows intrinsic emission in the direction normal to the sample surface [306], as shown in the sketch plot of Fig. 6.4.1(b). The second and

third bands present also the interesting features that their slow light regime extend over a large region in the reciprocal space, which is a necessary condition to achieve small device size of a limited number of lattice constant.

The E_z field distributions of the Γ_2 and Γ_3 band-edge states are plotted in Fig. 6.4.2. The electric fields are antisymmetric with respect to the center of the pillar, where zero intensity is expected. The two states have the same energy ($u = 0.3714$) but with different polarizations.

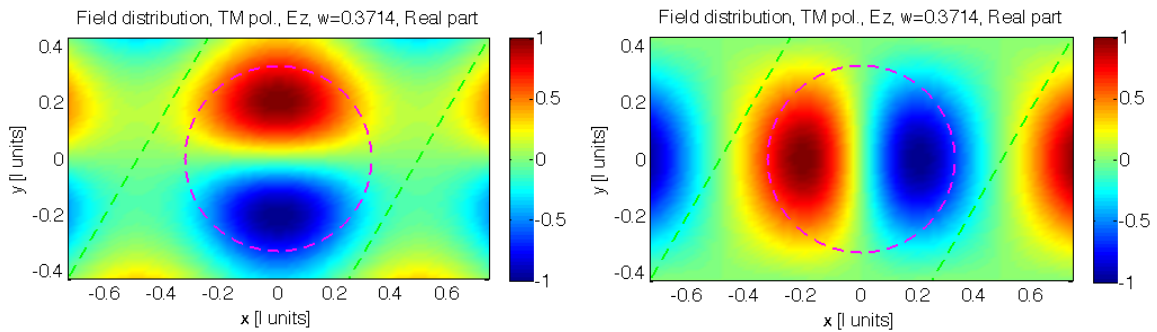


Fig. 6.4.2. The E_z field distributions Γ_2 and Γ_3 band-edge states.

In the presence of complete double-plasmon waveguide, although these states do lie at the Γ point within the light cone and wavevector selection rule allows vertical emission, the coupling factor with a plane wave vanishes because of their odd parity. As a result a small perturbation in the top plasmon layer, on the form of small holes, arranged in a fashion breaking the symmetry of the PhC states is necessary to achieve a finite coupling in the vertical direction. Thanks to the BCB planarization [305] and its associated design flexibility, as a first try of the surface emitting laser extractor, half moon shape holes are designed on the top plasmon layer, in order to out couple the surface emitted light.

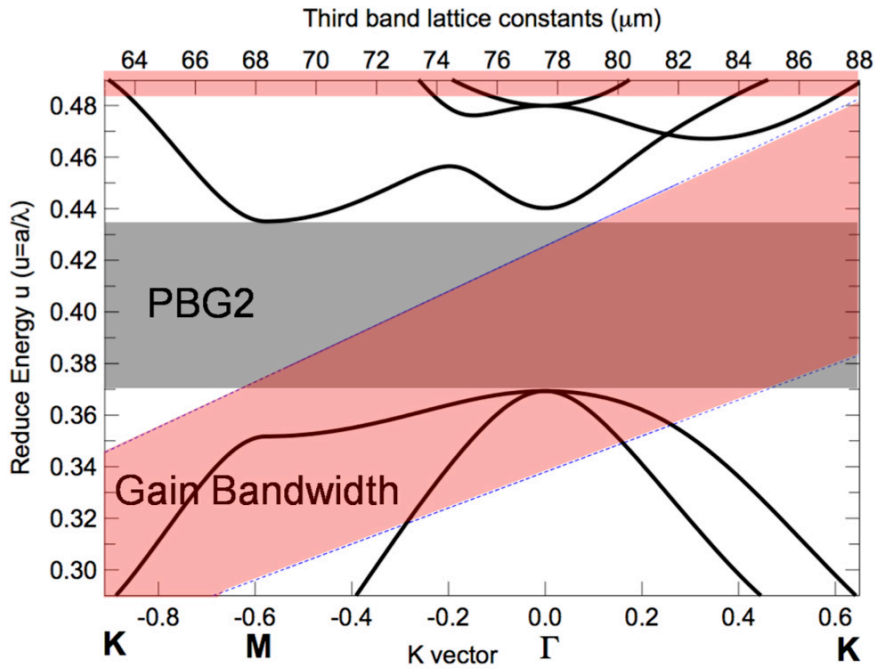


Fig. 6.4.3. Superimposition of material gain bandwidth onto PhC dispersion curve in reduced energy scale. Solid curves represent the simulated PhC dispersion band diagrams with pillar filling factor 40% (Left and Bottom axes). Grey shadow range represents the complete photonic bandgap (PBG, Left and Bottom axes). Red shadow represents the material gain range varied with the increment of lattice constant (Left and Top axes). Lasing effect is expected within the region where the material gain (red shadow) overlaps with the slow light regimes ('flatten dispersion curve' between Γ band-edge point and M saddle point), and light is forbidden to propagate in the region of PBG.

Figure 6.4.3 is a detailed zoom around the PBG2 of PhC dispersion curve with the superposition of the QC material gain bandwidth (182 ~ 230 μm , 5.4 ~ 6.8 meV, red shadow correspond to top axis of lattice constant), which, for such intersubband transitions, is assumed to be identical to the spontaneous emission bandwidth. By scanning a from 64 μm to 88 μm (with 2 μm s step size), the PBG2 can be fully covered. No lasing mode should exist in the PBG2 shadow region. In order to break the band-edge mode symmetry and extract the light from surface, subwavelength (6 μm radius) half-moon shape holes on solid contacts are opened to out couple the intrinsic surface emitted light.

6.4.3 Large surface emitting extractors

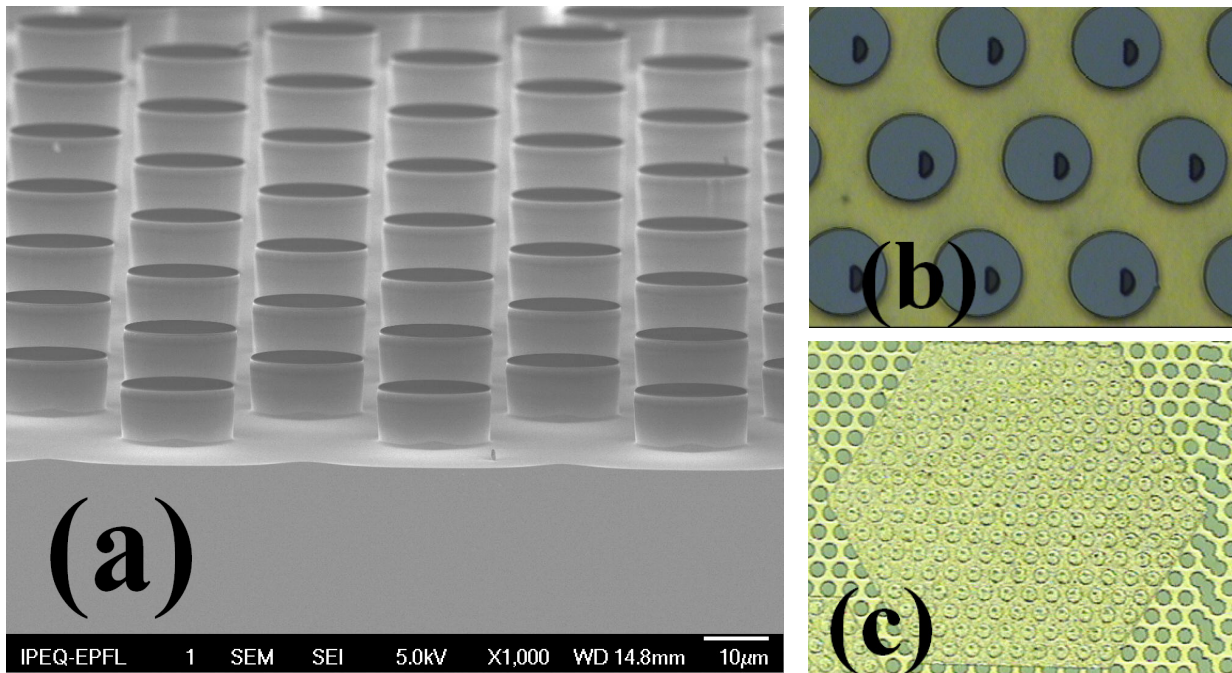


Fig. 6.4.4. (a) Cross-section Scanning Electron Microscope (SEM) image of pillar type PhC structures after dry etch, showing their smooth side-wall. (b) Top view microscope image of detailed half-moon hole opening after top contact developing. (c) Top view microscope image of overview PhC tile lasers whose contact has half-moon holes on individual pillars for light extraction.

The epitaxial layer of the QCL is a repeated 85 periods of GaAs/Al_{0.1}Ga_{0.9}As active layer [314], the center emitting wavelength is 1.5 THz ($\sim 200 \mu\text{m}$ in wavelength). The fabrication process is the same as described in Chapter 3. Subwavelength half-moon shape holes (Fig. 6.4.4(b)) are opened on each of the single pillars during the opening of 600 μm long hexagonal shape top contacts (Fig. 6.4.2(c)).

6.4.4 Experimental results and discussion

The lasing spectra measurements and light-current-voltage (L/IV) measurements at different temperature in pulsed condition were performed using the same characterization technique as explained in subsection 6.2.5.

Fig. 6.4.5(a) shows the comparison of the lasing spectra at different lattice constants in absolute unit (THz frequency scale). The general trend is that with the increasing of lattice constant, the lasing frequency ramps up to lower frequency. However there are exceptions at $a = 70$ and $72 \mu\text{m}$. Things will become clear when we align all the lasing modes with the calculated 3rd band dispersion in reduced energy scale (Fig. 6.4.5(b)). We first distinguish all the lasing spectra into three modes on the slow light regime: M saddle point mode, Γ_2 and Γ_3

band-edge modes at $u = 0.352$, 0.364 and 0.367 , respectively. For small lattice constants, e.g., $a = 68 \mu\text{m}$, due to the gain bandwidth is expanded cross the entire slow light regime, all the possible modes are lasing. There are 3 red curves measured with the increasing injecting current in Fig. 6.4.5(b) shows the mode tuning with respect to the PhC mode symmetries from low energy M to the highest possible energy mode at Γ_3 state. $a = 70 \mu\text{m}$ sample is lasing at M mode only may due to the fabrication imperfection. For $a \geq 72 \mu\text{m}$, all the lasers are lasing at single mode with respect to the dispersion.

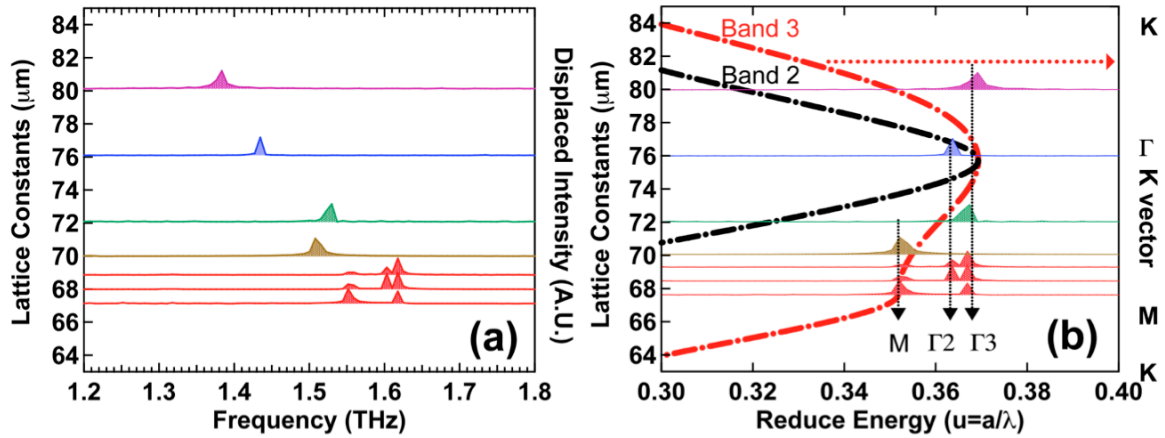


Fig. 6.4.5. (a) Comparison of measured lasing spectra of different lasing lattice constants ($a = [68, 70, 72, 76, 78] \mu\text{m}$) in absolute unit (THz frequency). (b) Comparison of lasing spectra of same lattice constants as in Fig. 6.4.3(a) in relative unit (reduced energy $u = a/\lambda$). It can be seen that all the lasing modes are aligned to $u = 0.352$, 0.364 and 0.367 , respectively. Note that for $a = 68 \mu\text{m}$ there are 3 red curves measured with the increasing injecting current. All the rest curves response to the value on the left axis.

There is a good explanation for the experimental mode splitting behavior between Γ_2 and Γ_3 points. As can be seen in Fig. 6.4.5(b), the Γ point at the second bandgap of the circular pillar structure is doubly degenerated. As these two bands exhibit different slow light enhancement factors [66-68], this would not be an issue in an ideal system and single mode operation would be achieved on the band with slowest group velocity. However, such configuration is a recipe for poor modal control, especially with the inhomogeneously broadened gain experienced in QC active material. Moreover the degeneracy can be lifted, in an uncontrolled manner, by any residual fabrication disorder or anisotropy. Moreover, the extractor itself whose function is to generate outcoupling losses in the vertical direction for the lasing mode will have the counterproductive effect to favour lasing of the not extracted orthogonal mode.

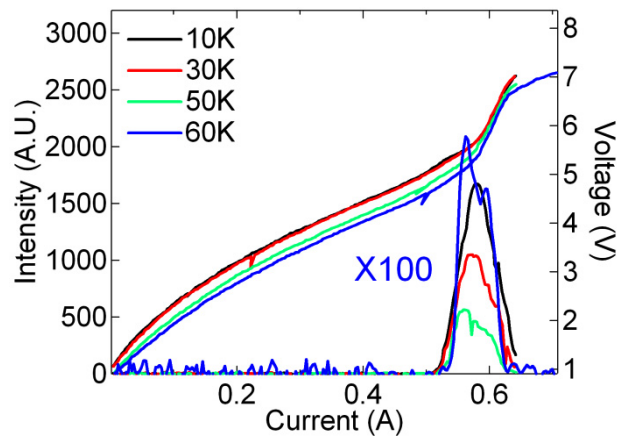


Fig. 6.4.6. L/IV characterization of lasing intensity of the 3rd band THz PhC tile laser at lattice parameter $a = 72 \mu\text{m}$ as a function of temperature under pulsed condition (pulse = 200 ns, duty cycle = 1.3%). The threshold current density of this 3rd band PhC laser is 133 A/cm^2 and the maximum operation temperature is 60 K (Intensities at 60 K has been scaled by a factor of 100).

Due the enlargement of the extractors during the fabrication process, the actual radius of the half-moon shape extractor is around $9 \sim 10 \mu\text{m}$. The increased size of the extractors on top of pillars results in heavy losses to the lasing mode. Moreover, the lasers exhibit very low power, which suggests the large asymmetric half moon holes are low efficiency extractors. The maximum temperature of this surface emitting laser is also lower than the standard FP lasers, this is due to the contamination of the top metal contact by the carbon (during evaporation): the quality of the double plasmon has been demonstrated to be a vital factor which can drastically affect the overall temperature performances [315].

6.4.5 Conclusions

We have successfully demonstrated the first surface emitting pillar type PhC lasers at 1.5 THz. The PhC lasers are lasing at the slow light band-edge regime, with pure 2D DFB feedback scheme. Thanks to the extra design freedom bring by the BCB planarization technique, we have achieved asymmetrical surface holes as extractors. Position of the holes need to be calculated with complex 3D modeling in order to improve the extraction efficiency.

6.5 High Power Surface Emitting Pillar Type Photonic Crystal Terahertz Lasers With Sub-wavelength Extractors*

*The main results in this section are originally presented in "Complex coupled Photonic Crystal Lasers with Independent Loss and Refractive Index Modulation." (Paper in preparation.)

6.5.1 Introduction

In this section, we demonstrate high power surface emitting THz lasers based on the combination of photonic band-structure design and light extraction engineering. Similar to the previous section, this high power pillar type PhC laser also operates in a slow-light regime at the Γ band-edge of the third band (*i.e.* second bandgap). The metal contact also provides vertical confinement as a surface plasmon layer. Sub-wavelength holes are introduced in the top plasmon layer, which allows one to tailor the light out-coupling through the surface. Periodic losses are introduced on a pillar-type PhC pattern, which allows us to tailor independently the refractive index and the losses. Very high surface emitting power (31.2 mW) is obtained through such extractors, which is comparable as the standard Fabry-Perot lasers. Elliptical pillars type photonic crystal brings more mode control on the band-edge degeneracy with single mode operation and can be used to improve the far field emission pattern.

Let's first review the results we have obtained. Our first reported pillar type first band in-plane emitting PhC lasers strongly improve the performances of THz QC material in terms of threshold current, waveguide losses, emission mode selection, tunability and maximum operation temperature [17]. We have achieved surface emission from the 3rd band with large extractors, which are intrinsically lossy and the surface collected power is low. Moreover, as can be seen in Fig. 6.5.1(a), the Γ point at the second bandgap of the circular pillar structure is doubly degenerated. Due to the fabrication disorder or anisotropy, the degeneracy can be lifted in an uncontrolled manner. Moreover the presence of inhomogeneously gain broadening does not contribute the remaining of single mode. The extractor itself whose function is to generate outcoupling losses in the vertical direction for the lasing mode will have the counterproductive effect to favour lasing of the not extracted orthogonal mode.

6.5.2 Solutions on the band splitting

This issue can be solved either with a complex engineering of the extractor with additional losses to prevent lasing on the undesired states. Such approach presents the drawback of an increased lasing threshold. Alternatively this issue can be solved with a proper PhC engineering which lifts the degeneracy with a sufficiently large frequency splitting. This latter approach was selected. Fig. 6.5.1(b) shows the dispersion diagram of an elliptical pillar PhC, where pillar

filling factor is designed to be identical to the circular pillar case in Fig. 6.5.1(a) ($ff = 40\%$). The elliptical pillars have a x/y ratio of 0.8, and are rotated by 30° respective to the horizontal direction. The Γ_2 and Γ_3 band-edge states are successfully lifted as indicated by the arrow. The splitting is about $\Delta u = 0.0224$ in reduced energy, which corresponds to a broad frequency bandwidth of 168 GHz for lattice constant of $a = 40 \mu\text{m}$.

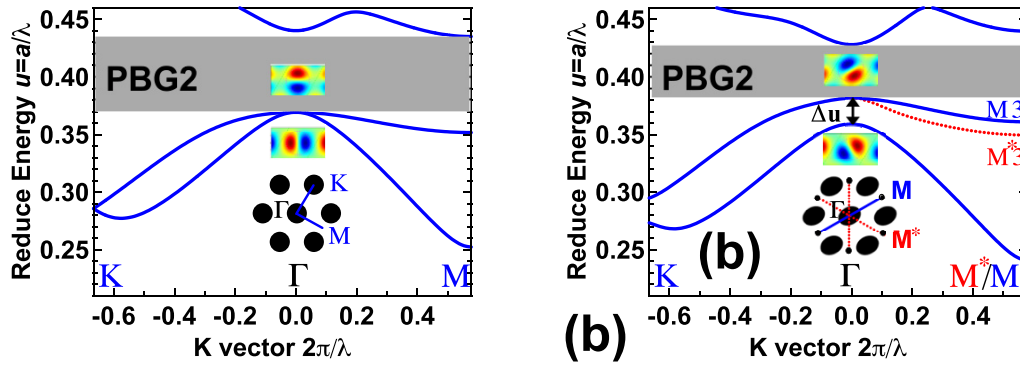


Fig. 6.5.1. Elliptical pillar photonic crystal degeneracy effect. (a), Detailed PhC dispersion of circular pillar around PBG2 from k -vector direction of K - Γ - M . E_z field maps are shown as inserts close the each bandedges (Γ_2 and Γ_3). A hexagonal lattice is inserted with circular pillars configuration. (b), Detailed PhC dispersion of elliptical pillars plotted as in (a). Elliptical pillars are designed with x/y ratio of 0.8, and rotated with 30° angle respective to the horizontal direction. The Γ_2 and Γ_3 band-edge states are successfully degenerated as indicated by the arrow. The splitting is about $\Delta u = 0.0224$ in reduced energy, which corresponds to a broad frequency bandwidth of 168 GHz for lattice constant of $a = 40 \mu\text{m}$. The dashed red dispersion curve between ΓM^* are calculated along corresponds to the specific ΓM^* path as indicated in the insert image of elliptical lattice.

6.5.3 Loss modulation by positioning the extractors

In order to achieve surface emitting light extraction, different extractor patterns are investigated, with either holes-on-pillars or holes-on-BCB based on a triangular lattice. In both cases, the extractor is designed to be $5 \mu\text{m}$ in diameter, which is assumed to have no effect on the current injection. 3D simulation with Finite Element Method (FEM, with Comsol multiphysics) is performed for the two extraction schemes, to model the impact on eigenfrequencies and the modulation on the eigenstate losses [48]. Fig. 6.5.2 shows the modulation on frequency of Γ_3 band-edge state and its losses at different extractor to pillar area ratio. The general rule is that the holes-on-pillars case impacts more dramatically both the frequency and losses than the holes-on-BCB case. With the increase of the extractor size, the band-edge state frequency for holes-on-BCB case shows a negligible shift to the lower frequency; while for holes-on-pillars

case, the frequency is shifted by as large as 100 GHz towards lower frequency for 40% of the extractor/pillar area ratio.

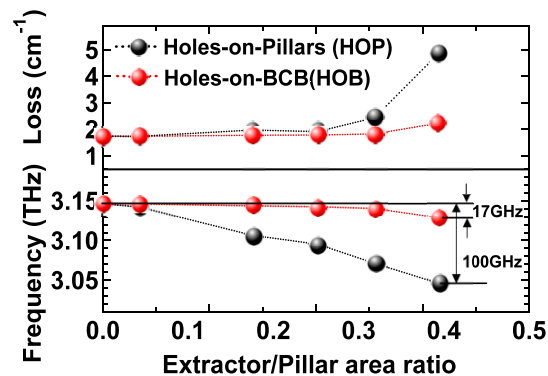


Fig. 6.5.2. Modulation of losses and frequency change by the two extraction schemes. Top panel, modulation of losses on the Γ_3 state when changing the size of the extractor. Bottom panel, modulation of frequency on the Γ_3 state when changing the size of the extractor. For same amount of size change, the holes-on-pillars scheme always modulates the system stronger than the holes-on-BCB scheme.

This result can be understood as follows: the hole-on-pillar configuration generates a strong index perturbation where the field is maximum. This strongly affects the eigenstate and eigenfrequency of the mode itself. On the other hand in the hole-on-BCB configuration the holes are located where the optical field is weak, the index contrast is less and the perturbation is not as dramatic compared to the previous case. Moreover the holes are located where the E-field is parallel to the surface and hence are more suitable to generate a propagating wave in the vertical direction. To summarize the hole-on-BCB configuration is much closer to what we need than the hole-on-pillar configuration.

Both circular pillars and elliptical pillars were designed with different lattice constants in order to ensure the overlap between the gain bandwidth and the band edge-states at the Γ -point. The two types of lasers were fabricated and processed from the same epitaxial layer in order to ease comparison. The emitting wavelength is centred around 3.3 THz, with a gain bandwidth of 900 GHz. Note that rather selecting an optimized active material with narrow gain bandwidth for single mode operation, the active material structure was deliberately selected with a very broad gain bandwidth in order to ensure a proof of principle demonstration as well as a PhC singular points spectroscopy around the second bandgap. The fabrication process and optical-electrical characterization are identical to the previous description in Section 3.4 and Section 6.2, respectively [305]. Owing to the extremely high surface emitting power, the same enables us for the first time, to perform far field characterization of PhC QCL at THz. The far field measurement can be referred to subsection 6.2.5.

6.5.4 Experimental results on circular pillars

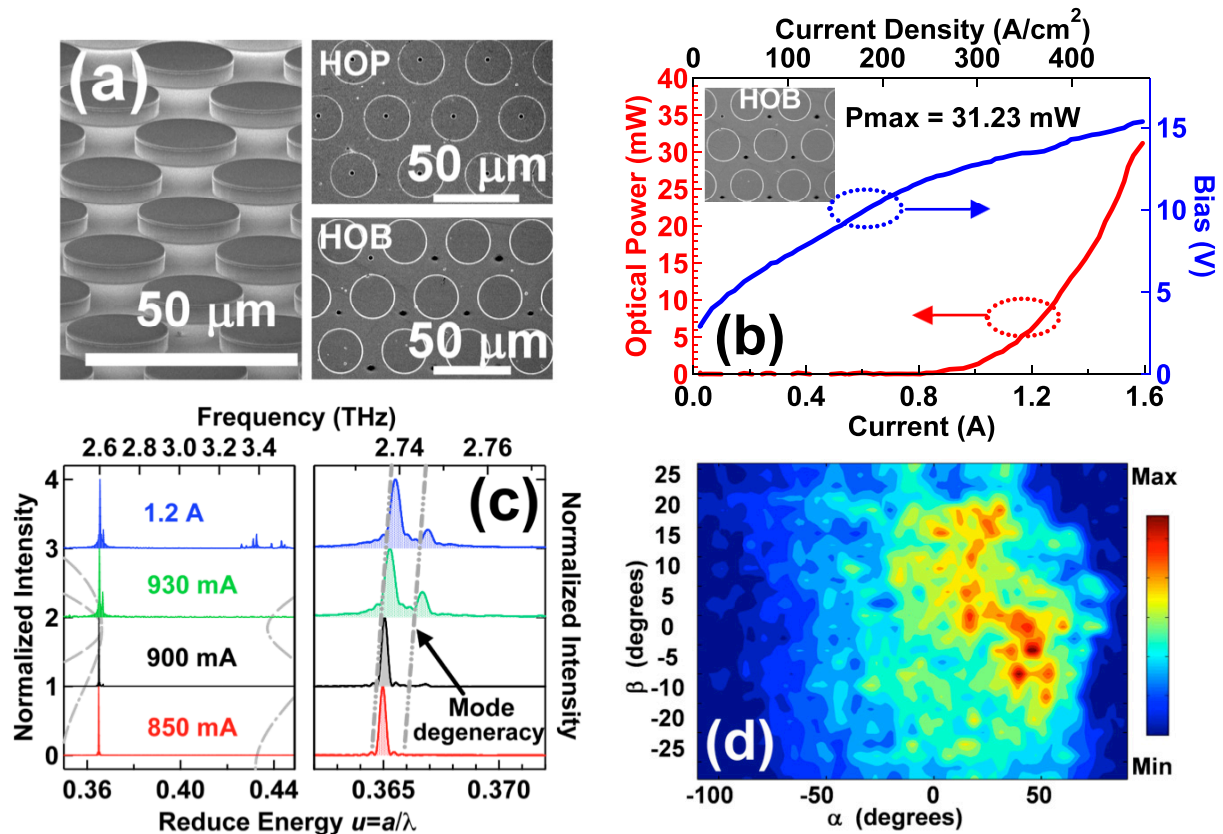


Fig. 6.5.3. Spectral, Light–current–voltage (LIV) and far field characterizations of circular pillar type photonic crystal quantum cascade laser at lattice constant $a = 40 \mu\text{m}$. (a) Left: Sideview SEM of pillars after etching. Right: SEM image of PhC laser with extraction scheme of holes-on-pillars (HOP) and holes-on-BCB (HOB). (b), Light–current–voltage (LIV) characteristics for a circular pillar type photonic-crystal laser with lattice constant $a = 40 \mu\text{m}$, with holes-on-BCB. The maximum power collected from the top of the device exceeds 31 mW. (c), Left panel: superimposition of lasing spectra at different injecting current with PhC dispersion. Multimode behaviour was found at both low injecting current and high injecting current. Right panel: detailed zoom of the mode degeneracy effect at the band-edge with gray dashed lines indication. (d), Far field emission pattern of this laser.

Let's first investigate the circular pillar structures. Fig. 6.5.3(a) shows the combined SEM images of the etched pillars with details of the extractors on different positions after metallization of the top plasmon layer. Fig. 6.5.3(b) shows the LIV for lattice constant $a = 40 \mu\text{m}$, with small holes-on-BCB. The maximum power is 31.25 mW, which is collected from the top of the device via the extractors. Such high surface emitting power is comparable to the standard Fabry-Perot lasers. We must emphasise that such small extractors count only for 3.5% of the active region surface area for lattice constants $a = 40 \mu\text{m}$, this indicates that the

small extractors are working with high efficiency to couple the intrinsic vertical emitted light out. Fig. 6.5.3(c) shows the superimposition of lasing spectra at different injecting current and the PhC dispersion curves. Multimode behaviour was found at both low injecting current and high injecting current. At injection current higher than 900 mA and lower than 1.2 A, the laser exhibits multimode behaviour around $u = 0.365$, which corresponds to the PBG2 lower bandedge. This multimode behaviour illustrates the previously discussed mode degeneracy lifting effect between the Γ_2 and Γ_3 states. Such degeneracy can be lifted off easily by any structural disorders or different boundary conditions. No state is found in the PBG confirming that the PhC dispersion is still controlling the lasing states. At injection current higher than 1.2 A, the cavity pulling induced by the gain shift leads to the laser operates at both lower and higher bandedges of the PBG2. Such multimode behavior eventually results in a complex far field pattern, as shown in Fig. 6.5.3(d).

6.5.5 Experimental results of elliptical pillars

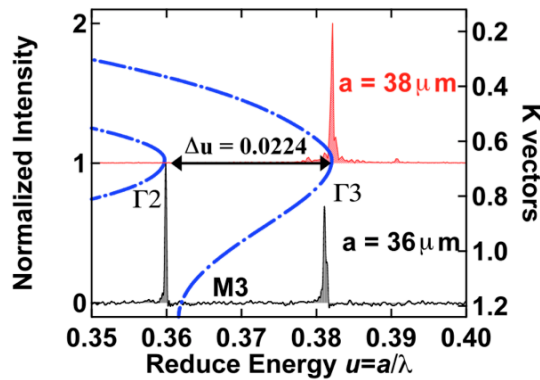


Fig. 6.5.4 Spectral characterizations of elliptical pillar PhC lasers showing the mode splitting effect. (a). Superimposition of lasing spectra at different lattice constants with elliptical pillar PhC dispersion. Lasing spectra of device in elliptical pillar type photonic-crystal lasers with lattice constant $a = 36 \mu\text{m}$ and $a = 38 \mu\text{m}$ are shown as black curves and red curves, respectively, under the holes-on-pillars extraction scheme. The mode splitting between Γ_2 and Γ_3 states correspond well to the calculated $\Delta u = 0.0224$.

In contrast to the standard circular pillars, elliptical pillar PhC lasers show a much more efficient mode control as expected theoretically. Fig. 6.5.4 shows the lasing spectra of elliptical pillar PhC lasers (with holes-on-pillars scheme) at different lattice constants. For smaller lattice constant $a = 36 \mu\text{m}$, where the gain bandwidth is broad enough to excite both the splitted Γ band-edge states, the measured mode splitting energy between Γ_2 and Γ_3 states corresponds well to the calculated $\Delta u = 0.0224$. For larger lattice constant $a = 38 \mu\text{m}$, where the gain shifts to higher frequency in reduced energy, which overlaps with the Γ_3 state only, hence a single mode

lasing is observed. However, these devices are probably damaged since their output power is thousand times reduced with respect to the others, which are not sufficient to perform the far field experiment.

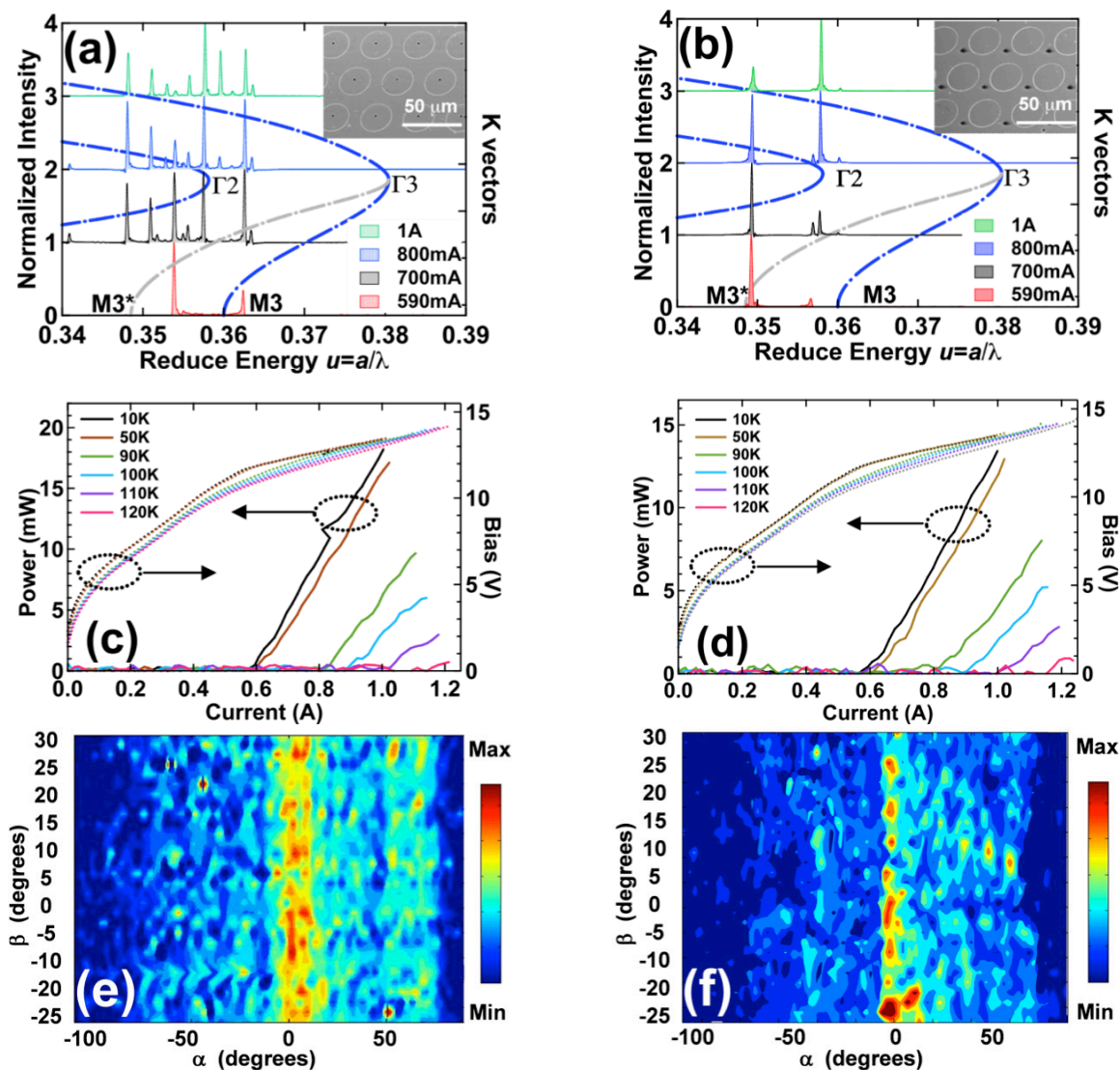


Fig. 6.5.5 Spectral, Light–current–voltage (LIV) and Far field characterizations of elliptical pillar type photonic crystal quantum cascade lasers. (a) and (b), Lasing spectra of elliptical pillar type PhC lasers with lattice constant $a = 32 \mu\text{m}$, with small extractors on top of pillars and on top of BCB, as shown insert SEM images for (a) and (b), respectively. (c) and (d), LIV characteristics as a function of temperature for the two type of elliptical pillar type PhC lasers as shown in (a), and (b). The maximum powers collected from the top of the devices are 18.2 mW and 13.4 mW, for the holes-on-pillars and holes-on-BCB, respectively. The maximum operating temperature for both two devices are 120 K, which is the same as the standard FP ridge lasers (embedded with BCB) fabricated on the same batch with the same material. (e) and (f), Far field emission patterns for elliptical pillar type photonic-crystal lasers with lattice constant $a = 32 \mu\text{m}$, with small holes-on-pillars and holes-on-BCB, respectively.

SEM images of elliptical pillars with extraction scheme of holes-on-pillars and holes-on-BCB are shown in inserts of Fig. 6.5.5(a) and Fig. 6.5.5(b), respectively. The laser spectra shown in Fig. 6.5.5(a) and Fig. 6.5.5(b) are measured at different injection currents from elliptical pillar type photonic-crystal laser devices with lattice constant $a = 32 \mu\text{m}$, with small extractors on pillars and on BCB, respectively. When the injection current is low ($\leq 590 \text{ mA}$ in both cases), both lasers show mode control as expected from the elliptical pillar dispersion. The frequency peaks correspond well to the Γ_2 mode and the M_3^* mode (refers to the elliptical pillar dispersion in Fig. 6.5.1(b)). However for higher injection currents ($> 590 \text{ mA}$ in both cases), the two schemes show different behaviours. Such differences are caused by the previously discussed losses modulation on the eigenmode. The holes-on-pillars scheme turns to multimode rapidly when the injection current is increased. This means the holes-on-pillars scheme introduces more losses to the lasing modes, and eventually increases the losses to a comparable level to the losses of the modes induced by any defect cavity modes or FP like modes. As a consequence the PhC mode control is lost and the laser becomes extremely multimode. On the contrary, in the holes-on-BCB scheme the mode control remains even at very high injection current, which confirms that such extraction scheme disturbs less of the PhC lasing modes. In another word, it introduces less losses to the lasing modes while remaining high extraction efficiency. The LIV curves in Fig. 6.5.5(c) and Fig. 6.5.5(d) show similar threshold current and maximum operation temperature for both cases. The holes-on-pillars scheme achieved slightly higher maximum power (18.2 mW) than the holes-on-BCB (13.4 mW), however the price to pay is the increased mode complexity. Another evidence of the advantage of holes-on-BCB is the far field patterns shown in Fig. 6.5.5(e) and Fig. 6.5.5(f). In general for the elliptical pillars, both the two extractor schemes show beam narrowing to 10° in the horizontal direction, which are improved from the standard pillar case. However for the holes-on-BCB extraction scheme, the case where the mode is better confined shows clearer and narrower far field pattern than the holes-on-pillar. The vertical spots are most probably due to the higher order band-edge states generated by the reflecting boundary.

6.5.6 Conclusion

In conclusion, we have reported on the use of double plasmon photonic crystal lasers operating in the third band to achieve high power surface emission at THz. We have shown the approach of achieving independent refractive index and losses modulation on surface emitting lasers. The idea of introducing small hole extractors on different positions brings extra freedom to the lossy parameter. We have shown that the spectroscopic operation of the PhC is critically dependent on the external losses introduced. We achieved very high surface emission power for the optimum lossy extractor configuration. Our approach can be used as a general tool

for the development of both electrical and optical pumped devices at any frequencies based on index modulation devices. Our modelling has shown that, by playing the size and the position of the holes, the losses can be modulated as a completely free parameter, thanks to the BCB planarization technique. A narrow gain bandwidth active material is needed, in order to achieve mode control and far field emission control by the extractor introduced loss modulation. Future improvement can be achieved based on such scheme by gradually increasing the hole-size until the holes are connected so a top contact can be naturally isolated and defined. This will create a gently defined lossy boundary condition that should benefit the single mode operation and address a sharper far field pattern. Anti-phase complex-coupled lossy holes can be also interesting for more sophisticated photonic crystal engineering.

Chapter 7

7. Conclusions and future works

In this work the slow light behaviours as well as other optical properties of PhCs for both passive devices for integrated optics applications and active devices for light sources have been investigated.

Theoretical calculations of these PhC devices have been performed using PWE method for the dispersion and FEM method for more sophisticated structures. Both the passive PhC slow light devices and nanocavities are operating in the NIR wavelengths. This part of work was first started by the building-up of the entire fabrication platform with state of the art EBL on SOI as well as InP material systems.

For the passive slow light devices, W_1/W_x PhC waveguides based on InP material system have been investigated. In the vicinity of a band-edge, different light transport regimes have been identified by the direct measurement of the dispersion curve in k space. The transition of the guided mode of these regimes has been determined as whether a group velocity, n_g , can be defined from a ω vs. k dispersion relation. Moreover, slow light coupled photonic crystal cavity waveguides have been investigated systematically. Depending on the constitutive Q factors, both discretized dispersion spots with transmission peaks, and continuous dispersion with flat transmission band have been theoretically presented and experimentally measured. Group index n_g of 55 and 90 for different cavity periods have been experimentally achieved. The impact of residual disorder on CCW system has been studied, showing that the CCWs are more robust than slow light line defect waveguides. These investigations give design rules to reduce losses and give fundamental boundaries to what can be expected in CCW and PhC slow light structures.

Two types of passive high Q PhC cavities have been investigated: the conventional PhC cavities and the air-slot cavities. For the conventional PhC cavities, the strong light-matter interaction occurs in the high index material where the maximum of the optical field is located. Q factor as high as half a million has been achieved, however strong non-linear effects and bistable behaviours have also been observed. The air-slot cavities can confine TE polarized modes in the air, thus allowing for a large interaction of the optical field with the low-index medium. It has been shown that the high Q factor $\sim 2.6 \times 10^4$ of the air slot cavity allows us to achieve a high experimental sensitivity of 510 nm per refractive index unit (RIU).

For the active PhC light sources, we have reported the investigation of THz PhC bandedge

emitting lasers based on intersubband active material. Exhaustive records on the investigation of in-plane emitting PhC QCL lasers at 3.3 THz have been presented. Such PhC lasers strongly improve the performances of THz QCL in terms of threshold current, waveguide losses, emission mode selection, tuneability and maximum operation temperature. The investigation and development of a complex-coupled surface emitting PhC QCL schemes have been reported, where the refractive index and loss can be modulated independently. The pillar type PhC lasers also operate in slow-light regime around the Γ band-edge of the third band. Sub-wavelength holes have been introduced in the top plasmon layer, which allows tailoring the light out-coupling through the surface. Very high surface emitting power (31.2 mW) has been obtained through such extractors, which is comparable as the standard Fabry-Perot lasers. Elliptical pillars based photonic crystal brings more mode control on the band-edge degeneracy with single mode operation and can be used to improve the far field emission pattern.

In terms of passive photonic crystal devices, future works can be focused on the study of slow light enhancement on losses: *e.g.*, slow light coupled air slot cavity waveguide filled with specific gases that have sharp absorption lines in the slow light band. Moreover, it can be interesting to further improve the sensitivity of photonic crystal hollow cavities. Furthermore, optical trapping of small particles with photonic crystal cavities under micro-fluidic channels can be also interesting.

In terms of active photonic crystal devices, we should continue our investigation in the direction of deeply etched pillar type PhC QCL at THz to consolidate our leading position in this field. Powerful 3D simulations will be always very helpful for the deep understanding of the complex lasing mechanism and verification of advanced ideas. Small filling factor pillar PhC lasers with large pumping area should contribute to sharp far field pattern with extremely small power consumption. Such devices should also improve the temperature performance due to the diluted pumping area and improved heat generation and dissipation. A narrow gain bandwidth active material is needed, in order to achieve mode control and far field emission control by the extractor introduced loss modulation. The direction of independent index and loss modulation should be continued, due to the intrinsic difficulty in defining a nature absorber. Future improvement can be achieved based on such scheme by gradually increasing the hole-size until the holes are connected so a top contact can be naturally isolated and defined. This will create a gently defined lossy boundary condition that should benefit the single mode operation and address a sharper far field pattern. Anti-phase complex-coupled lossy holes can be also interesting for more sophisticated photonic crystal engineering.

Acknowledgments

Time passed quickly.

I would like to take this opportunity to thank all the people who helped me working on this thesis.

First of all I would like to thank Dr. Romuald Houdré who accepted me for the position in his research group and was my supervisor during my stay in EPFL. He introduced me to the interesting world of photonic crystals and always was an endless source of new ideas and advice which guided me in my work. Romuald is so kind, nice and full of humor, he patiently taught me so many things, and led me to the world of physics. It is really a pleasure to work under his supervision.

A special thank should be given to Dr. Andrea Dunbar. Despite we only worked together at the beginning of my stay in EPFL, these few months were invaluable. She transferred the knowledge and technology of both photonic crystal and quantum cascade laser to me. She is not only a teacher, but also a good friend of mine. All the best to her and Zachary.

I would like also to thank my collaborators: Prof. Jérôme Faist, Dr. Giacomo Scalari and Dr. Lorenzo Sirigu from ETHz. They are truly physicists, pioneers and leaders in the Quantum cascade lasers field. Their deep intuitive understanding of many physical phenomena greatly broaden my scientific experience. I would say that without their invaluable help this PhD work could not have been done.

I also want to thank all members of our group for their invaluable help and the contribution they've made for this work, and for the stimulating and inspiring atmosphere which always supported me. Dr. Nicolas Le Thomas, who great knowledge and hard working spirit impacted me deeply. He helped me a lot in learning the basis of photonic crystals, and his experience in optical characterization of photonic crystal structures allowed us to verify the theoretical results of Si photonic devices. **In principle** and in practical I should thank Dr. Vasily Zabelin. He is a true physicist and theoretician, he helped me a lot on better understanding the physics of photonic crystal. It is really a great pleasure to have such a pretty lady: Jana Jágerská in the group. She is such a smart girl, who came later than me but learnt things faster than me. She is also very sportive and creative, always have nice ideas, not only limited to research. Many many

thanks to Zhaolu Diao, Nicolas Descharmes and Dharanipathy Ulagalandha Perumal. I would say the group has changed a lot since their arrival, in particularly on Tuesday afternoon...

The following people should not be forgotten: Laurence Carlin, Nicolas Leiser, Yoan Trolliet, Damain Trolliet, Maxime Marendaz, Denise Martin, Hans Jörg Buehlmann, Dr. Kevin Lister, Dr. Benjamin Dwir. Without their help and hard working on the lab regulations, nothing can be done.

The following people should also be thanked due to our non-forgettable coffee time, beer time, dinner time, ski time and working time (in Alphabetic order): Agathe Hannebert, Aida Hideo, Dr. Alexei Sirbu, Alessandro Surrente, Alexei Altoukhov, Dr. Andrei Caliman, Dr. Antonino Castiglia, Aota Natsuko, Arai Masayuki, Arun Mohan, Dr. Beilu Shao, Cheng Yu, Christoph Walther, Cyrille Hibert, Dr. Dongfeng Zhang, Dr. Fei Wang, Feng Yang, Fengda Sun, Gael nardin, Georges-André Racine, Dr. Guochu Deng, Dr. Hai Zhan, Dr. Hongyan Bi, Hu Xu, Hui Yang, Dr. Jean-François Carlin, Ji Cao, Jie Luo, Jiang Li, Jing Wang, Julia D'Aloisio, Dr. Julien Dorsaz, Dr. Kirill Atlasov, Dr. Laurent Balet, Le Chen, Li Jin, Li Pu, Dr. Lianhe Li, Liang Qiao, Liangliang Huang, Dr. Lina Huang, Dr. Lukas Mutter, Dr. Maria Amanti, Meng Shen, Dr. Mickaël Guillaumee, Dr. Pascal Gallo, Dr. Pascale El Kallassi, Peiyu Ge, Dr. Peng Xu, Dr. Pierre Lugan, Dr. Philippe Flückiger, Dr. Philipp Ridha, Philippe Langlet, Dr. Qing Zhu, Robert Lockhart, Roland Cerna, Rong Hu, Samuel Clabecq, Shenqi Xie, Dr. Taofiq Paraïso, Dr. Tiankai Zhu, Tomohide Aoyagi, Dr. Valentina Troncale, Verena Kohnle, Dr. Vladimir Iakovlev, Wuzhou Song, Xiuwei Zhang, Yan Yan, Yanjun Zhang, Dr. Yang Yang, Dr. Ye Zhang, Dr. Yu bai, Yu Lu, Yue OuYang, Yunyun Han, Yvan Deillon, Zhixian Yan, Dr. Zhanbing He, Dr. Zhipan Zhang. And all my friends whose name is not in the list should also be thanked.

And of course I want to thank my wife, my mother and my father. They inspired my scientific career and have been supporting it for many years. Despite the 9000 km distance, I always felt their love and care, which helped me in my work towards the PhD degree.

With love.

Hua Zhang

2010-7-19, Lausanne.

张华 2010年七月十九日于洛桑

Glossary and Acronyms (Alphabetical order)

Atomic force microscope	AFM
Beam step size	BSS
Benzocyclobutene	BCB
Bound-to-continuum	BTC
Buried Oxide	BOX
Buffered Hydrofluoric acid	BHF
Brillouin-zone	BZ
Chirped superlattice	CSL
Computer Aided Transcription System	CATS
Conditional Figure Assignment	CFA
Continuous-wave	CW
Coupled cavity waveguide	CCW
Critical Dimension	CD
Deep ultraviolet	DUV
Delay bandwidth product	DBP
Detection limit	DL
Direct writing laser	DWL
Distributed Feedback	DFB
Double plasmon	DP
Double heterostructure laser	DHL
Electroluminescence	EL
Electron Beam	EBeam
Electron Beam lithography	EBL
Electron Beam Pattern Generator	EBPG
Equi-frequency surfaces	EFS
Extreme ultraviolet	EUV
Fabry-perot	FP
Far-infrared spectral emission	FTIR
Finite Difference Time Domain	FDTD
Finite Element Method	FEM
Filling factor	ff
Focused ion beam	FIB
Fourier space	FS
Fourier transform	FT
Fourier transform spectroscopy	FTS
Full width half maximum	FWHM
Group index	n_g
Generic Pattern Format	GPF
Group velocity	v_g
Group velocity dispersion	GVD
Guided mode expansion	GME
Hydrofluoric acid	HF
Inductively coupled plasma	ICP
Integrated circuit	IC

Indium Phosphide	InP
Isopropanol Alcohol	IPA
Lattice constant	a
Linear probe gratings	LPG
Light-current-voltage	LIV
Main field Resolution	MainRes
Mesh quality measure	q
Metal-metal waveguide	MM waveguide
Methyl Isobutyl Ketone	MIBK
Mid-Infrared	MIR
Molecular Beam Epitaxy	MBE
Multiple stepping factor	MSF
Nanoimprint lithography	NIL
Near-Infrared	NIR
Next generation lithography	NGL
Numerical aperture	NA
Photonic crystal	PhC
Photonic band gaps	PBG
Partial differential equations	PDEs
Photolithography	PL
Photonic crystal coupled waveguides	PCCW
Perfectly matched layer	PML
Plane wave expansion	PWE
Plasma Enhance Chemical Vapor Deposition	PECVD
Polymethyl methacrylate	PMMA
Quality factor	Q
Quantum cascade lasers	QCL
Quantum well	QW
Reactive Ion Etching	RIE
Real space	RS
Reduced Energy	u
Refractive index unit	RIU
Resolution	Res
Resonant-phonon	RP
Room-temperature	RT
Scanning electron microscope	SEM
Scanning near field optical microscopy	SNOM
Silicon-On-Insulator	SOI
Single plasmon	SP
Terahertz	THz
THz time-domain spectroscopy	THz-TDS
Tight Binding Approximation	TBA
Total internal reflection	TIR
Transverse Electric/Magnetic	TE/TM
Trapezium field Resolution	TrapRes
Whispering Gallery mode	WGM

References

1. OnlineSource, "http://www.viewsfromscience.com/documents/webpages/natural_photonics_p1.html."
2. S. Kinoshita, and S. Yoshioka, "Structural colors in nature: The role of regularity and irregularity in the structure," *Chemphyschem* **6**, 1442-1459 (2005).
3. OnlineSource, "<http://www.jewelersethicsassociation.com/opals.html>."
4. J. Han, H. L. Su, C. F. Zhang, Q. Dong, W. Zhang, and D. Zhang, "Embedment of ZnO nanoparticles in the natural photonic crystals within peacock feathers," *Nanotechnology* **19**, - (2008).
5. S. John, "Strong localization of photons in certain disordered dielectric superlattices," *Physical Review Letters* **58**, 2486-2489 (1987).
6. E. Yablonovitch, "Inhibited Spontaneous Emission in Solid-State Physics and Electronics," *Physical Review Letters* **58**, 2059-2062 (1987).
7. K. M. Ho, C. T. Chan, and C. M. Soukoulis, "Existence of a Photonic Gap in Periodic Dielectric Structures," *Physical Review Letters* **65**, 3152-3155 (1990).
8. E. Yablonovitch, T. J. Gmitter, and K. M. Leung, "Photonic Band-Structure - the Face-Centered-Cubic Case Employing Nonspherical Atoms," *Physical Review Letters* **67**, 2295-2298 (1991).
9. U. Gruning, V. Lehmann, and C. M. Engelhardt, "2-Dimensional Infrared Photonic Band-Gap Structure-Based on Porous Silicon," *Applied Physics Letters* **66**, 3254-3256 (1995).
10. J. D. Joannopoulos, *Photonic Crystals - Modeling the flow of light* (Princeton, NJ: Princeton University Press, 1995).
11. T. E. Sale, *Vertical cavity surface emitting lasers* (Research Studies Press, Taunton, Somerset, England, 1995).
12. U. Gruning, V. Lehmann, S. Ottow, and K. Busch, "Macroporous silicon with a complete two-dimensional photonic band gap centered at 5 μm ," *Applied Physics Letters* **68**, 747-749 (1996).
13. R. De La Rue, H. Chong, M. Gnan, N. Johnson, I. Ntakis, P. Pottier, M. Sorel, A. M. Zain, H. Zhang, E. Camargo, C. J. Jin, M. Armenise, and C. Ciminelli, "Photonic crystal and photonic wire nano-photonics based on silicon-on-insulator," *New Journal of Physics* **8** (2006).
14. J. Jágorská, H. Zhang, N. Le Thomas, and R. Houdré, "Radiation loss of photonic crystal coupled-cavity waveguides," *Applied Physics Letters* **95**, 111105 (2009).
15. K. Inoue, N. Kawai, Y. Sugimoto, N. Carlsson, N. Ikeda, and K. Asakawa, "Observation of small group velocity in two-dimensional AlGaAs-based photonic crystal slabs," *Physical Review B - Condensed Matter and Materials Physics* **65**, 1213081-1213084 (2002).
16. N. Le Thomas, H. Zhang, J. Jágorská, V. Zabelin, R. Houdré, I. Sagnes, and A. Talneau, "Light transport regimes in slow light photonic crystal waveguides," *Physical Review B* **80**, 125332 (2009).
17. H. Zhang, L. A. Dunbar, G. Scalari, R. Houdré, and J. Faist, "Terahertz photonic crystal quantum cascade lasers," *Optics Express* **15**, 16818-16827 (2007).

18. W. Bogaerts, P. Bienstman, D. Taillaert, R. Baets, and D. De Zutter, "Out-of-plane scattering in photonic crystal slabs," *IEEE Photonics Technology Letters* **13**, 565-567 (2001).
19. Y. Chassagneux, R. Colombelli, W. Mauneult, S. Barbieri, H. E. Beere, D. A. Ritchie, S. P. Khanna, E. H. Linfield, and A. G. Davies, "Electrically pumped photonic-crystal terahertz lasers controlled by boundary conditions," *Nature* **457**, 174-178 (2009).
20. Y. A. T. A. B.-S. S. S. Noda, "High-Q photonic nanocavity in a two-dimensional photonic crystal," *Nature* (2003).
21. H. Benisty, "Modal analysis of optical guides with two-dimensional photonic band-gap boundaries," *Journal of Applied Physics* **79**, 7483-7492 (1996).
22. C. C. Cheng, V. ArbetEngels, A. Scherer, and E. Yablonovitch, "Nanofabricated three dimensional photonic crystals operating at optical wavelengths," *Physica Scripta* **T68**, 17-20 (1996).
23. A. van Blaaderen, "Materials science - Opals in a new light," *Science* **282**, 887-888 (1998).
24. Y. A. Vlasov, X. Z. Bo, J. C. Sturm, and D. J. Norris, "On-chip natural assembly of silicon photonic bandgap crystals," *Nature* **414**, 289-293 (2001).
25. H. Miguez, C. Lopez, F. Meseguer, A. Blanco, L. Vazquez, R. Mayoral, M. Ocana, V. Fornes, and A. Mifsud, "Photonic crystal properties of packed submicrometric SiO₂ spheres," *Applied Physics Letters* **71**, 1148-1150 (1997).
26. A. Blanco, E. Chomski, S. Grabtchak, M. Ibsate, S. John, S. W. Leonard, C. Lopez, F. Meseguer, H. Miguez, J. P. Mondla, G. A. Ozin, O. Toader, and H. M. Van Driel, "Large-scale synthesis of a silicon photonic crystal with a complete three-dimensional bandgap near 1.5 micrometres," *Nature* **405**, 437-440 (2000).
27. P. Lodahl, A. F. Van Driel, I. S. Nikolaev, A. Irman, K. Overgaag, D. Vanmaekelbergh, and W. L. Vos, "Controlling the dynamics of spontaneous emission from quantum dots by photonic crystals," *Nature* **430**, 654-657 (2004).
28. S. A. Rinne, F. García-Santamaría, and P. V. Braun, "Embedded cavities and waveguides in three-dimensional silicon photonic crystals," *Nature Photonics* **2**, 52-56 (2008).
29. A. A. Zakhidov, R. H. Baughman, Z. Iqbal, C. X. Cui, I. Khayrullin, S. O. Dantas, I. Marti, and V. G. Ralchenko, "Carbon structures with three-dimensional periodicity at optical wavelengths," *Science* **282**, 897-901 (1998).
30. S. Y. Lin, J. G. Fleming, D. L. Hetherington, B. K. Smith, R. Biswas, K. M. Ho, M. M. Sigalas, W. Zubrzycki, S. R. Kurtz, and J. Bur, "A three-dimensional photonic crystal operating at infrared wavelengths," *Nature* **394**, 251-253 (1998).
31. K. M. Ho, C. T. Chan, C. M. Soukoulis, R. Biswas, and M. Sigalas, "Photonic Band-Gaps in 3-Dimensions - New Layer-by-Layer Periodic Structures," *Solid State Communications* **89**, 413-416 (1994).
32. K. Aoki, H. T. Miyazaki, H. Hirayama, K. Inoshita, T. Baba, K. Sakoda, N. Shinya, and Y. Aoyagi, "Microassembly of semiconductor three-dimensional photonic crystals," *Nature Materials* **2**, 117-121 (2003).
33. K. Ishizaki, and S. Noda, "Manipulation of photons at the surface of three-dimensional photonic crystals," *Nature* **460**, 367-U378 (2009).
34. Y. V. Miklyaev, D. C. Meisel, A. Blanco, G. von Freymann, K. Busch, W. Koch, C. Enkrich, M. Deubel, and M. Wegener, "Three-dimensional face-centered-cubic photonic crystal templates

- by laser holography: fabrication, optical characterization, and band-structure calculations," *Applied Physics Letters* **82**, 1284-1286 (2003).
35. F. Muller, A. Birner, J. Schilling, U. Gosele, C. Kettner, and P. Hanggi, "Membranes for micropumps from macroporous silicon," *Physica Status Solidi a-Applied Research* **182**, 585-590 (2000).
36. D. C. Meisel, M. Wegener, and K. Busch, "Three-dimensional photonic crystals by holographic lithography using the umbrella configuration: Symmetries and complete photonic band gaps," *Physical Review B* **70**, - (2004).
37. C. Kittel, *Introduction to Solid State Physics* (John Wiley and Sons, New York, 1953).
38. M. Plihal, and A. A. Maradudin, "Photonic Band-Structure of 2-Dimensional Systems - the Triangular Lattice," *Physical Review B* **44**, 8565-8571 (1991).
39. R. D. Meade, A. M. Rappe, K. D. Brommer, J. D. Joannopoulos, and O. L. Alerhand, "Accurate Theoretical-Analysis of Photonic Band-Gap Materials," *Physical Review B* **48**, 8434-8437 (1993).
40. K. Sakoda, "Transmittance and Bragg Reflectivity of 2-Dimensional Photonic Lattices," *Physical Review B* **52**, 8992-9002 (1995).
41. R. Courant, "Variational-Methods for the Solution of Problems of Equilibrium and Vibrations (Reprinted from Bull Am Math Soc, Vol 49, Pg 1, 1943)," *Bull Am Math Soc* **49**, 1 (1943).
42. J. Jin, *The Finite Element method in Electromagnetics* (John Wiley & Sons, Inc, New York, 2002).
43. C. Multiphysics, "COMSOL Multiphysics."
44. H. A. Haus, and W. P. Huang, "Coupled-Mode Theory," *Proceedings of the IEEE* **79**, 1505-1518 (1991).
45. L. Mahler, A. Tredicucci, F. Beltram, C. Walther, H. E. Beere, and D. A. Ritchie, "Finite size effects in surface emitting Terahertz quantum cascade lasers," *Optics Express* **17**, 6703-6709 (2009).
46. S. Kumar, B. S. Williams, Q. Qin, A. W. M. Lee, Q. Hu, and J. L. Reno, "Surface-emitting distributed feedback terahertz quantum-cascade lasers in metal-metal waveguides," *Optics Express* **15**, 113-128 (2007).
47. S. Kohen, B. S. Williams, and Q. Hu, "Electromagnetic modeling of terahertz quantum cascade laser waveguides and resonators," *Journal of Applied Physics* **97**, 1-9 (2005).
48. M. I. Amanti, M. Fischer, G. Scalari, M. Beck, and J. Faist, "Low-divergence single-mode terahertz quantum cascade laser," *Nature Photonics* **3**, 586-590 (2009).
49. K. S. Yee, "Numerical Solution of Initial Boundary Value Problems Involving Maxwells Equations in Isotropic Media," *Ieee T Antenn Propag* **Ap14**, 302-& (1966).
50. A. Taflove, "Application of the Finite-Difference Time-Domain Method to Sinusoidal Steady-State Electromagnetic-Penetration Problems," *Ieee T Electromagn C* **22**, 191-202 (1980).
51. M. Notomi, K. Yamada, A. Shinya, J. Takahashi, C. Takahashi, and I. Yokohama, "Extremely large group-velocity dispersion of line-defect waveguides in photonic crystal slabs," *Physical Review Letters* **87**, 253902-253906 (2001).
52. H. Gersen, T. J. Karle, R. J. P. Engelen, W. Bogaerts, J. P. Korterik, N. F. Van Hulst, T. F.

- Krauss, and L. Kuipers, "Real-space observation of ultraslow light in photonic crystal waveguides," *Physical Review Letters* **94**, 073903 (2005).
53. Y. A. Vlasov, M. O'Boyle, H. F. Hamann, and S. J. McNab, "Active control of slow light on a chip with photonic crystal waveguides," *Nature* **438**, 65-69 (2005).
54. T. F. Krauss, "Slow light in photonic crystal waveguides," *Journal of Physics D: Applied Physics* **40**, 2666-2670 (2007).
55. M. Soljacic, and J. D. Joannopoulos, "Enhancement of nonlinear effects using photonic crystals," *Nature Materials* **3**, 211-219 (2004).
56. T. Asano, K. Kiyota, D. Kumamoto, B. S. Song, and S. Noda, "Time-domain measurement of picosecond light-pulse propagation in a two-dimensional photonic crystal-slab waveguide," *Applied Physics Letters* **84**, 4690-4692 (2004).
57. C. E. Finlayson, F. Cattaneo, N. M. B. Perney, J. J. Baumberg, M. C. Netti, M. E. Zoorob, M. D. B. Charlton, and G. J. Parker, "Slow light and chromatic temporal dispersion in photonic crystal waveguides using femtosecond time of flight," *Physical Review E - Statistical, Nonlinear, and Soft Matter Physics* **73** (2006).
58. T. Baba, and D. Mori, "Slow light engineering in photonic crystals," *Journal of Physics D: Applied Physics* **40**, 2659-2665 (2007).
59. T. Baba, "Slow light in photonic crystals," *Nature Photonics* **2**, 465-473 (2008).
60. N. Le Thomas, R. Houdré, L. H. Frandsen, J. Fage-Pedersen, A. V. Lavrinenko, and P. I. Borel, "Fourier space super-resolution of the dispersion relations of slow light propagating under the light cone," *Physical Review B* **76**, 035103 (2007).
61. A. W. Snyder, and J. D. Love, *Optical waveguide theory* (Chapman & Hall, London, 1983).
62. A. Sakai, G. Hara, and T. Baba, "Propagation characteristics of ultrahigh- Δ optical waveguide on silicon-on-insulator substrate," *Japanese Journal of Applied Physics, Part 2: Letters* **40**, L383-L385 (2001).
63. G. P. Agrawal, *Nonlinear Fiber Optics* (Academic Press, San Diego, CA, USA, 2001).
64. D. Mori, and T. Baba, "Dispersion-controlled optical group delay device by chirped photonic crystal waveguides," *Applied Physics Letters* **85**, 1101-1103 (2004).
65. S. Hughes, L. Ramunno, J. F. Young, and J. E. Sipe, "Extrinsic optical scattering loss in photonic crystal waveguides: Role of fabrication disorder and photon group velocity," *Physical Review Letters* **94** (2005).
66. J. P. Dowling, M. Scalora, M. J. Bloemer, and C. M. Bowden, "The Photonic Band-Edge Laser - a New Approach to Gain Enhancement," *Journal of Applied Physics* **75**, 1896-1899 (1994).
67. S. Nojima, "Optical-gain enhancement in two-dimensional active photonic crystals," *Journal of Applied Physics* **90**, 545-551 (2001).
68. S. Nojima, "Enhancement of optical gain in two-dimensional photonic crystals with active lattice points," *Japanese Journal of Applied Physics Part 2-Letters* **37**, L565-L567 (1998).
69. S. Nojima, "Single-mode laser oscillation in semiconductor gain photonic crystals," *Japanese Journal of Applied Physics, Part 2: Letters* **38** (1999).
70. S. Nojima, "Laser Oscillation due to Light Slowed-Down by Excitons in Photonic Crystals," *Journal of the Physical Society of Japan* **70**, 3432-3445 (2001).

71. S. Nojima, "Theoretical analysis of feedback mechanisms of two-dimensional finite-sized photonic-crystal lasers," *Journal of Applied Physics* **98**, 1-9 (2005).
72. R. A. Soref, and J. P. Lorenzo, "ALL-SILICON ACTIVE AND PASSIVE GUIDED-WAVE COMPONENTS FOR $\lambda = 1.3$ AND $1.6 \mu\text{m}$," *IEEE Journal of Quantum Electronics* **QE-22**, 873-879 (1986).
73. R. A. Soref, and B. R. Bennett, "Kramers-Kronig analysis of E-O switching in silicon," *Proc. SPIE* **704**, 32-37 (1986).
74. B. Schueppert, J. Schmidtchen, and K. Petermann, "Optical channel waveguides in silicon diffused from GeSi alloy," *Electronics Letters* **25**, 1500-1502 (1989).
75. R. A. Soref, J. Schmidtchen, and K. Petermann, "Large single-mode rib waveguides in GeSi-Si and Si-on-SiO₂," *IEEE Journal of Quantum Electronics* **27**, 1971-1974 (1991).
76. B. Jalali, S. Yegnanarayanan, T. Yoon, T. Yoshimoto, I. Rendina, and F. Coppinger, "Advances in silicon-on-insulator optoelectronics," *IEEE Journal on Selected Topics in Quantum Electronics* **4**, 938-947 (1998).
77. P. D. Trinh, S. Yegnanarayanan, and B. Jalali, "Integrated optical directional couplers in silicon-on-insulator," *Electronics Letters* **31**, 2097-2098 (1995).
78. U. Fischer, T. Zinke, and K. Petermann, "Integrated optical waveguide switches in SOI," *IEEE International SOI Conference*, 141-142 (1995).
79. P. D. Trinh, S. Yegnanarayanan, and B. Jalali, "5 X 9 integrated optical star coupler in silicon-on-insulator technology," *IEEE Photonics Technology Letters* **8**, 794-796 (1996).
80. C. Z. Zhao, G. Z. Li, E. K. Liu, Y. Gao, and X. D. Liu, "Silicon on insulator Mach-Zehnder waveguide interferometers operating at $1.3 \mu\text{m}$," *Applied Physics Letters* **67**, 2448-2449 (1995).
81. M. Lipson, "Guiding, modulating, and emitting light on silicon - Challenges and opportunities," *Journal of Lightwave Technology* **23**, 4222-4238 (2005).
82. OnlineSource, "<http://www2.renesas.com/fab/en/index.html>."
83. G. E. Moore, "Cramming more components onto integrated circuits (Reprinted from *Electronics*, pg 114-117, April 19, 1965)," *Proceedings of the Ieee* **86**, 82-85 (1965).
84. Y. Vladimirsky, "*Lithography in Vacuum Ultraviolet Spectroscopy II* (Academic Press, 1998).
85. C. A. Mack, *Field Guide to Optical Lithography* (SPIE Press Book, 2006).
86. C. W. Gwyn, R. Stulen, D. Sweeney, and D. Attwood, "Extreme ultraviolet lithography," in *Papers from the 42nd international conference on electron, ion, and photon beam technology and nanofabrication*(AVS, Chicago, Illinois (USA), 1998), pp. 3142-3149.
87. T. J. N. A. F. (JLab), "X-Ray Lithography towards 15 nm," (2003), pp. Jefferson Lab Technical Note 03-016.
88. C. Wagner, and N. Harned, "EUV lithography: Lithography gets extreme," *Nat Photon* **4**, 24-26 (2010).
89. H. H. Magoon, "Pushing dry 193-nm lithography technology to the limit," *MICRO* **23**, 85-93 (2005).
90. T. Ito, and S. Okazaki, "Pushing the limits of lithography," *Nature* **406**, 1027-1031 (2000).
91. R. F. Service, "EUV lithography: Optical lithography goes to extremes - And beyond:"

- World's smallest transistor," *Science* **293**, 785-786 (2001).
92. G. C. a. M. Wolf, "White paper Smart Cut™ A guide to the technology, the process, the products," (SOITEC, 2003).
93. G. K. Celler, and S. Cristoloveanu, "Frontiers of silicon-on-insulator," *Journal of Applied Physics* **93**, 4955-4978 (2003).
94. X. Q. Feng, and Y. Huang, "Mechanics of Smart-Cut® technology," *International Journal of Solids and Structures* **41**, 4299-4320 (2004).
95. OnlineSource, "http://cmi.epfl.ch/metrology/GES_5E.php."
96. J.Ph.PIEL, "Introduction to ellipsometry," (2008).
97. "Document SOPRA : Fondamentaux de l'ellipsométrie."
98. OnlineSource, "<http://cmi.epfl.ch/metrology/Nanospec.php>."
99. OnlineSource, "<http://cmi.epfl.ch/packaging/Disco.php>."
100. OnlineSource, "<http://www.vistec-litho.com>."
101. K. H. B. F.E. Abboud, V. Chakarian, D.M. Cole, J.P. Daniel, R. Dean, M. Gesley, M. Lu, R. Naber, T. Newman, F. Raymond, D. Trost, M. Wiltse, and W. DeVore, "100-nm OPC Mask Patterning using Raster-scan 50kV Pattern Generation Technology," in *SPIE* (2001), pp. pp. 1-8.
102. V. C. K.H. Baik, R. Dean, M. Lu, R. Naber, T. Newman, M. Wiltse, and F.E. Abboud, "High-Productivity Mask Writer with Broad Operating Range," in *SPIE* (2001), pp. pp. 228-237.
103. OnlineSource, "http://cmi.epfl.ch/ebeam/What_is_an_electron_beam_lithography_tool.php."
104. S. Thoms, and D. S. Macintyre, "Tilt-corrected stitching for electron beam lithography," *Microelectronic Engineering* **84**, 793-796 (2007).
105. OnlineSource, "http://cmi.epfl.ch/ebeam/Ebeam_Resists.php."
106. J. Jágerská, N. Le Thomas, R. Houdré, J. Bolten, C. Moormann, T. Wahlbrink, J. Crtyroky, M. Waldow, and M. Forst, "Dispersion properties of silicon nanophotonic waveguides investigated with Fourier optics," *Optics Letters* **32**, 2723-2725 (2007).
107. OnlineSource, "http://www.microchem.com/products/pdf/PMMA_Data_Sheet.pdf."
108. OnlineSource, "<http://www.zeonchemicals.com/electronicmaterials.aspx?id=11683099>."
109. OnlineSource, "<http://cmi.epfl.ch/etch/AMS200.php>."
110. J. Ohara, K. Kano, Y. Takeuchi, and Y. Otsuka, "Improvement of Si/SiO₂ mask etching selectivity in the new D-RIE process," *Proceedings of the IEEE Micro Electro Mechanical Systems (MEMS)*, 76-79 (2001).
111. F. Ayazi, and K. Najafi, "High aspect-ratio combined poly and single-crystal silicon (HARPSS) MEMS technology," *Journal of Microelectromechanical Systems* **9**, 288-294 (2000).
112. S. A. McAuley, H. Ashraf, L. Atabo, A. Chambers, S. Hall, J. Hopkins, and G. Nicholls, "Silicon micromachining using a high-density plasma source," *Journal of Physics D: Applied Physics* **34**, 2769-2774 (2001).
113. A. A. Ayón, "Etching characteristics and profile control in a time multiplexed inductively coupled plasma etcher," *Solid-State Sensor and Actuator Workshop*, 41-44 (1998).

114. A. A. Ayón, X. Zhang, and R. Khanna, "Anisotropic silicon trenches 300-500 um deep employing time multiplexed deep etching (TMDE)," *Sensors and Actuators, A: Physical* **90**, 381-385 (2001).
115. C. Chang, Y. F. Wang, Y. Kanamori, J. J. Shih, Y. Kawai, C. K. Lee, K. C. Wu, and M. Esashi, "Etching submicrometer trenches by using the Bosch process and its application to the fabrication of antireflection structures," *Journal of Micromechanics and Microengineering* **15**, 580-585 (2005).
116. W. König, J. A. Fan, and D. Seibert, "Recent developments in the extrusion of helical gears," *International Journal of Machine Tools & Manufacture* **33**, 599-614 (1993).
117. M. Ahn, R. K. Heilmann, and M. L. Schattenburg, "Fabrication of ultrahigh aspect ratio freestanding gratings on silicon-on-insulator wafers," *Journal of Vacuum Science & Technology B* **25**, 2593-2597 (2007).
118. S. Deladi, V. Svetovoy, G. J. M. Krijnen, and M. C. Elwenspoek, "Flash release - an alternative for releasing complex MEMS devices," *Journal of Micromechanics and Microengineering* **14**, 1659-1664 (2004).
119. A. Benz, C. Deutsch, G. Fasching, K. Unterrainer, A. M. Andrews, P. Klang, W. Schrenk, and G. Strasser, "Active photonic crystal terahertz laser," *Optics Express* **17**, 941-946 (2009).
120. R. Colombelli, K. Srinivasan, M. Troccoli, O. Painter, C. F. Gmachl, D. M. Tennant, A. M. Sergent, D. L. Sivco, A. Y. Cho, and F. Capasso, "Quantum cascade surface-emitting photonic crystal laser," *Science* **302**, 1374-1377 (2003).
121. O. P. Marshall, V. Apostolopoulos, J. R. Freeman, R. Rungsawang, H. E. Beere, and D. A. Ritchie, "Surface-emitting photonic crystal terahertz quantum cascade lasers," *Applied Physics Letters* **93**, 171112 (2008).
122. OnlineSource, "<http://www.photronics.com/plab/photronics/>."
123. OnlineSource, "<http://www.deltamask.nl/frames.html>."
124. OnlineSource, "<http://www.himt.de/en/home/>."
125. OnlineSource, "http://cmi.epfl.ch/photo/Laser_DWL200/DWL200_introduction.php."
126. OnlineSource, "http://cmi.epfl.ch/threefive/home_threefive.php."
127. OnlineSource, "http://www.oxfordplasma.de/pdf_inst/in100/100%20PECVD%20Install%20v7%20Blue%20PLC.pdf."
128. OnlineSource, "<http://www.oxford-instruments.com/products/etching-deposition-growth/tools/tools/system80plus/Pages/plasmalab80plus.aspx>."
129. OnlineSource, "[http://www.oxfordplasma.de/pdf_inst/in80/80%20Plus%20\(RIE\)%20Install%20v11%20\(Blue%20PLC\).pdf](http://www.oxfordplasma.de/pdf_inst/in80/80%20Plus%20(RIE)%20Install%20v11%20(Blue%20PLC).pdf)."
130. M. L. Povinelli, S. G. Johnson, and J. D. Joannopoulos, "Slow-light, band-edge waveguides for tunable time delays," *Optics Express* **13**, 7145-7159 (2005).
131. M. T. Hill, H. J. S. Dorren, T. de Vries, X. J. M. Leijtens, J. H. den Besten, B. Smalbrugge, Y. S. Oei, H. Binsma, G. D. Khoe, and M. K. Smit, "A fast low-power optical memory based on coupled micro-ring lasers," *Nature* **432**, 206-209 (2004).

132. A. Yariv, Y. Xu, R. K. Lee, and A. Scherer, "Coupled-resonator optical waveguide: A proposal and analysis," *Optics Letters* **24**, 711-713 (1999).
133. T. J. Karle, D. H. Brown, R. Wilson, M. Steer, and T. F. Krauss, "Planar photonic crystal coupled cavity waveguides," *IEEE Journal of Selected Topics in Quantum Electronics* **8**, 909-918 (2002).
134. H. Altug, D. Englund, and J. Vučković, "Ultrafast photonic crystal nanocavity laser," *Nature Physics* **2**, 484-488 (2006).
135. A. Y. Petrov, and M. Eich, "Zero dispersion at small group velocities in photonic crystal waveguides," *Applied Physics Letters* **85**, 4866-4868 (2004).
136. N. Le Thomas, R. Houdré, L. H. Frandsen, J. Fage-Pedersen, A. V. Lavrinenko, and P. I. Borel, "Grating-assisted superresolution of slow waves in Fourier space," *Physical Review B* **76**, 035103 (2007).
137. L. H. Frandsen, A. V. Lavrinenko, J. Fage-Pedersen, and P. I. Borel, "Photonic crystal waveguides with semi-slow light and tailored dispersion properties," *Optics Express* **14**, 9444-9450 (2006).
138. S. Kubo, D. Mori, and T. Baba, "Low-group-velocity and low-dispersion slow light in photonic crystal waveguides," *Optics Letters* **32**, 2981-2983 (2007).
139. N. Le Thomas, V. Zabelin, R. Houdré, M. V. Kotlyar, and T. F. Krauss, "Influence of residual disorder on the anticrossing of Bloch modes probed in k space," *Physical Review B* **78**, 125301 (2008).
140. M. D. Settle, R. J. P. Engelen, M. Salib, A. Michaeli, L. Kuipers, and T. F. Krauss, "Flatband slow light in photonic crystals featuring spatial pulse compression and terahertz bandwidth," *Optics Express* **15**, 219-226 (2007).
141. D. Mori, and T. Baba, "Wideband and low dispersion slow light by chirped photonic crystal coupled waveguide," *Optics Express* **13**, 9398-9408 (2005).
142. R. J. P. Engelen, Y. Sugimoto, Y. Watanabe, J. P. Korterik, N. Ikeda, N. F. Van Hulst, K. Asakawa, and L. Kuipers, "The effect of higher-order dispersion on slow light propagation in photonic crystal waveguides," *Optics Express* **14**, 1658-1672 (2006).
143. M. F. Yanik, W. Suh, Z. Wang, and S. Fan, "Stopping light in a waveguide with an all-optical analog of electromagnetically induced transparency," *Physical Review Letters* **93**, 233903 (2004).
144. D. Mori, S. Kubo, H. Sasaki, and T. Baba, "Experimental demonstration of wideband dispersion-compensated slow light by a chirped photonic crystal directional coupler," *Optics Express* **15**, 5264-5270 (2007).
145. T. Baba, T. Kawasaki, H. Sasaki, J. Adachi, and D. Mori, "Large delay-bandwidth product and tuning of slow light pulse in photonic crystal coupled waveguide," *Optics Express* **16**, 9245-9253 (2008).
146. S. C. Huang, M. Kato, E. Kuramochi, C. P. Lee, and M. Notomi, "Time-domain and spectral-domain investigation of inflection-point slow-light modes in photonic crystal coupled waveguides," *Optics Express* **15**, 3543-3549 (2007).
147. S. Olivier, C. Smith, M. Rattier, H. Benisty, C. Weisbuch, T. Krauss, R. Houdré, and U. Oesterle, "Miniband transmission in a photonic crystal coupled-resonator optical waveguide," *Optics Letters* **26**, 1019-1021 (2001).

148. K. Hosomi, and T. Katsuyama, "A dispersion compensator using coupled defects in a photonic crystal," *IEEE Journal of Quantum Electronics* **38**, 825-829 (2002).
149. A. G. Martínez, A. Sanchis, P. Martí, J., "Group velocity and dispersion model of coupled-cavity waveguides in photonic crystals," *Journal of the Optical Society of America A: Optics and Image Science, and Vision* **20**, 147-150 (2003).
150. W. J. Kim, W. Kuang, and J. D. O'Brien, "Dispersion characteristics of photonic crystal coupled resonator optical waveguides," *Optics Express* **11**, 3431-3437 (2003).
151. T. Fukamachi, K. Hosomi, T. Katsuyama, and Y. Arakawa, "Group-delay properties of coupled-defect structures in photonic crystals," *Japanese Journal of Applied Physics, Part 2: Letters* **43**, L449-L452 (2004).
152. J. B. Khurgin, "Expanding the bandwidth of slow-light photonic devices based on coupled resonators," *Optics Letters* **30**, 513-515 (2005).
153. J. K. S. Poon, L. Zhu, G. A. DeRose, and A. Yariv, "Transmission and group delay of microring coupled-resonator optical waveguides," *Optics Letters* **31**, 456-458 (2006).
154. F. Xia, L. Sekaric, and Y. Vlasov, "Ultracompact optical buffers on a silicon chip," *Nature Photonics* **1**, 65-71 (2007).
155. M. Notomi, E. Kuramochi, and T. Tanabe, "Large-scale arrays of ultrahigh-Q coupled nanocavities," *Nature Photonics* **2**, 741-747 (2008).
156. J. Jágerská, N. Le Thomas, V. Zabelin, R. Houdré, W. Bogaerts, P. Dumon, and R. Baets, "Experimental observation of slow mode dispersion in photonic crystal coupled-cavity waveguides," *Optics Letters* **34**, 359-361 (2009).
157. E. Kuramochi, T. Tanabe, H. Taniyama, M. Kato, and M. Notomi, "Observation of heavy photon state in ultrahigh-Q photonic crystal coupled resonator chain," in *Conference on Quantum Electronics and Laser Science (QELS) - Technical Digest Series*(2007), p. QMG2.
158. M. Bayindir, B. Temelkuran, and E. Ozbay, "Tight-binding description of the coupled defect modes in three-dimensional photonic crystals," *Physical Review Letters* **84**, 2140-2143 (2000).
159. Y. Hara, T. Mukaiyama, K. Takeda, and M. Kuwata-Gonokami, "Heavy photon states in photonic chains of resonantly coupled cavities with supermonodispersive microspheres," *Physical Review Letters* **94**, 203905 (2005).
160. N. Le Thomas, R. Houdré, M. V. Kotlyar, D. O'Brien, and T. F. Krauss, "Exploring light propagating in photonic crystals with Fourier optics," *Journal of the Optical Society of America B: Optical Physics* **24**, 2964-2971 (2007).
161. H. Benisty, C. Weisbuch, D. Labilloy, M. Rattier, C. J. M. Smith, T. F. Krauss, R. M. De la Rue, R. Houdré, U. Oesterle, C. Jouanin, and D. Cassagne, "Optical and confinement properties of two-dimensional photonic crystals," *Journal of Lightwave Technology* **17**, 2063-2077 (1999).
162. R. Ferrini, D. Leuenberger, M. Mulot, M. Qiu, J. Moosburger, M. Kamp, A. Forchel, S. Anand, and R. Houdré, "Optical study of two-dimensional InP-based photonic crystals by internal light source technique," *IEEE Journal of Quantum Electronics* **38**, 786-799 (2002).
163. R. Ferrini, B. Lombardet, B. Wild, R. Houdré, S. Olivier, H. Benisty, A. Djoudi, L. Legouezigou, S. Hubert, S. Sainson, J. P. Chandouineau, S. Fabre, F. Pommereau, and G. H. Duan, "Optical characterisation of 2D InP-based photonic crystals fabricated by inductively coupled plasma etching," *Electronics Letters* **38**, 962-964 (2002).

164. S. I. Bozhevolnyi, V. S. Volkov, T. Sondergaard, A. Boltasseva, P. I. Borel, and M. Kristensen, "Near-field imaging of light propagation in photonic crystal waveguides: Explicit role of Bloch harmonics," *Physical Review B* **66**, 235204 (2002).
165. A. F. Koenderink, M. Kafesaki, B. C. Buchler, and V. Sandoghdar, "Controlling the resonance of a photonic crystal microcavity by a near-field probe," *Physical Review Letters* **95**, 153904 (2005).
166. A. Giannattasio, and W. L. Barnes, "Direct observation of surface plasmon-polariton dispersion," *Optics Express* **13**, 428-434 (2005).
167. S. Massenot, J. Grandier, A. Bouhelier, G. C. des Francs, L. Markey, J. C. Weeber, A. Dereux, J. Renger, M. U. Gonzalez, and R. Quidant, "Polymer-metal waveguides characterization by Fourier plane leakage radiation microscopy," *Applied Physics Letters* **91**, 243102 - 243102 (2007).
168. A. Ishimaru, *Wave Propagation and Scattering in Random Media* (1978).
169. P. Sheng, *Introduction to Wave Scattering, Localization, and Mesoscopic Phenomena* (1995).
170. A. F. Koenderink, and W. L. Vos, "Optical properties of real photonic crystals: Anomalous diffuse transmission," *Journal of the Optical Society of America B: Optical Physics* **22**, 1075-1084 (2005).
171. C. Toninelli, E. Vekris, G. A. Ozin, S. John, and D. S. Wiersma, "Exceptional Reduction of the Diffusion Constant in Partially Disordered Photonic Crystals," *Physical Review Letters* **101**, 123901-123905 (2008).
172. S. Mookherjea, and A. Oh, "Effect of disorder on slow light velocity in optical slow-wave structures," *Optics Letters* **32**, 289-291 (2007).
173. M. Galli, D. Bajoni, M. Patrini, G. Guizzetti, D. Gerace, L. C. Andreani, M. Belotti, and Y. Chen, "Single-mode versus multimode behavior in silicon photonic crystal waveguides measured by attenuated total reflectance," *Physical Review B* **72**, 125322 (2005).
174. C. E. Finlayson, F. Cattaneo, N. M. B. Perney, J. J. Baumberg, M. C. Netti, M. E. Zoorob, M. D. B. Charlton, and G. J. Parker, "Slow light and chromatic temporal dispersion in photonic crystal waveguides using femtosecond time of flight," *Physical Review E* **73**, 016619 (2006).
175. B. Wang, S. Mazoyer, J. P. Hugonin, and P. Lalanne, "Backscattering in monomode periodic waveguides," *Physical Review B* **78**, 245108 (2008).
176. R. J. P. Engelen, D. Mori, T. Baba, and L. Kuipers, "Two Regimes of Slow-Light Losses Revealed by Adiabatic Reduction of Group Velocity," *Physical Review Letters* **101**, 103901 (2008).
177. J. Topolancik, B. Ilic, and F. Vollmer, "Experimental Observation of Strong Photon Localization in Disordered Photonic Crystal Waveguides," *Physical Review Letters* **99**, 253901 (2007).
178. A. Talneau, K. H. Lee, S. Guilet, and I. Sagnes, "Efficient coupling to W1 photonic crystal waveguide on InP membrane through suspended access guides," *Applied Physics Letters* **92**, 061105 (2008).
179. J. W. Goodman, ((Roberts, Greenwood Village, CO, 2007). 2007).
180. P. Sebbah, B. Hu, J. M. Klosner, and A. Z. Genack, "Extended Quasimodes within

- Nominally Localized Random Waveguides," *Physical Review Letters* **96**, 183902 (2006).
181. B. S. Song, S. Noda, and T. Asano, "Photonic devices based on in-plane hetero photonic crystals," *Science* **300**, 1537 (2003).
182. J. Bertolotti, S. Gottardo, D. S. Wiersma, M. Ghulinyan, and L. Pavesi, "Optical Necklace States in Anderson Localized 1D Systems," *Physical Review Letters* **94**, 113903 (2005).
183. L. C. Andreani, and D. Gerace, "Photonic-crystal slabs with a triangular lattice of triangular holes investigated using a guided-mode expansion method," *Physical Review B* **73**, 235114 (2006).
184. D. Leuenberger, R. Ferrini, and R. Houdré, "Ab initio tight-binding approach to photonic-crystal based coupled cavity waveguides," *Journal of Applied Physics* **95**, 806-809 (2004).
185. M. L. Povinelli, and S. Fan, "Radiation loss of coupled-resonator waveguides in photonic-crystal slabs," *Applied Physics Letters* **89**, 191114-191116 (2006).
186. D. P. Fussell, and M. M. Dignam, "Engineering the quality factors of coupled-cavity modes in photonic crystal slabs," *Applied Physics Letters* **90**, 183121-183123 (2007).
187. N. Stefanou, and A. Modinos, "Impurity bands in photonic insulators," *Physical Review B - Condensed Matter and Materials Physics* **57**, 12127-12133 (1998).
188. N. D. M. N. W. Ashcroft, *Solid State Physics* (Saunders college, Philadelphia, 1976).
189. J. Callaway, *Quantum Theory of the Solid State* (Academic Press, Boston 1991).
190. D. LEUENBERGER, "Experimental and numerical investigation of two-dimensional photonic crystals for application in integrated optics," in *PhD Thesis*(ÉCOLE POLYTECHNIQUE FÉDÉRALE DE LAUSANNE, Lausanne, 2004).
191. B. V. Claude Weisbuch, *Quantum Semiconductor Structures: Fundamentals and Applications* (Academic Press, New York, 1991).
192. S. Dutta, H. E. Jackson, J. T. Boyd, R. L. Davis, and F. S. Hickernell, "CO₂ laser annealing of Si₃N₄, Nb₂O₅, and Ta₂O₅ thin-film optical waveguides to achieve scattering loss reduction," *IEEE Journal of Quantum Electronics* **QE-18**, 800-806 (1982).
193. Y. Okamura, A. Miki, and S. Yamamoto, "Observation of wave propagation in integrated optical circuits," *Applied Optics* **25**, 3405-3408 (1986).
194. R. S. Tucker, P. C. Ku, and C. J. Chang-Hasnain, "Slow-light optical buffers: Capabilities and fundamental limitations," *Journal of Lightwave Technology* **23**, 4046-4066 (2005).
195. J. B. Khurgin, "Optical buffers based on slow light in electromagnetically induced transparent media and coupled resonator structures: Comparative and analysis," *Journal of the Optical Society of America B: Optical Physics* **22**, 1062-1074 (2005).
196. D. A. B. Miller, "Fundamental limit to linear one-dimensional slow light structures," *Physical Review Letters* **99**, 066616-066619 (2007).
197. G. Lenz, B. J. Eggleton, C. K. Madsen, and R. E. Slusher, "Optical delay lines based on optical filters," *IEEE Journal of Quantum Electronics* **37**, 525-532 (2001).
198. Z. Wang, and S. H. Fan, "Compact all-pass filters in photonic crystals as the building block for high-capacity optical delay lines," *Phys Rev E* **68**, 066616-066619 (2003).

199. S. Noda, A. Chutinan, and M. Imada, "Trapping and emission of photons by a single defect in a photonic bandgap structure," *Nature* **407**, 608-610 (2000).
200. H. Takano, Y. Akahane, T. Asano, and S. Noda, "In-plane-type channel drop filter in a two-dimensional photonic crystal slab," *Applied Physics Letters* **84**, 2226-2228 (2004).
201. O. Painter, R. K. Lee, A. Scherer, A. Yariv, J. D. O'Brien, P. D. Dapkus, and I. Kim, "Two-dimensional photonic band-gap defect mode laser," *Science* **284**, 1819-1821 (1999).
202. P. Michler, A. Kiraz, C. Becher, W. V. Schoenfeld, P. M. Petroff, L. Zhang, E. Hu, and A. Imamoglu, "A quantum dot single-photon turnstile device," *Science* **290**, 2282-2285 (2000).
203. M. F. Yanik, and S. Fan, "Stopping Light All Optically," *Physical Review Letters* **92**, 839011-839014 (2004).
204. K. Hennessy, A. Badolato, M. Winger, D. Gerace, M. Atatüre, S. Gulde, S. Föllt, E. L. Hu, and A. Imamoglu, "Quantum nature of a strongly coupled single quantum dot-cavity system," *Nature* **445**, 896-899 (2007).
205. Y. Akahane, T. Asano, B. S. Song, and S. Noda, "High-Q photonic nanocavity in a two-dimensional photonic crystal," *Nature* **425**, 944-947 (2003).
206. T. Asano, B. S. Song, Y. Akahane, and S. Noda, "Ultrahigh-Q nanocavities in two-dimensional photonic crystal slabs," *IEEE Journal on Selected Topics in Quantum Electronics* **12**, 1123-1134 (2006).
207. Y. Tanaka, T. Asano, and S. Noda, "Design of photonic crystal nanocavity with Q-factor of $\sim 10^9$," *Journal of Lightwave Technology* **26**, 1532-1539 (2008).
208. O. Svelto, *Principles of Lasers* (Springer, 2009).
209. D. K. Armani, T. J. Kippenberg, S. M. Spillane, and K. J. Vahala, "Ultra-high-Q toroid microcavity on a chip," *Nature* **421**, 925-928 (2003).
210. B. S. Song, S. Noda, T. Asano, and Y. Akahane, "Ultra-high-Q photonic double-heterostructure nanocavity," *Nature Materials* **4**, 207-210 (2005).
211. S. G. Johnson, S. Fan, A. Mekis, and J. D. Joannopoulos, "Multipole-cancellation mechanism for high-Q cavities in the absence of a complete photonic band gap," *Applied Physics Letters* **78**, 3388-3390 (2001).
212. E. Kuramochi, M. Notomi, S. Mitsugi, A. Shinya, T. Tanabe, and T. Watanabe, "Ultrahigh-Q photonic crystal nanocavities realized by the local width modulation of a line defect," *Applied Physics Letters* **88**, 041112 (2006).
213. M. Notomi, A. Shinya, K. Yamada, J. Takahashi, C. Takahashi, and I. Yokohama, "Structural tuning of guiding modes of line-defect waveguides of silicon-on-insulator photonic crystal slabs," *IEEE Journal of Quantum Electronics* **38**, 736-742 (2002).
214. M. Notomi, A. Shinya, S. Mitsugi, G. Kira, E. Kuramochi, and T. Tanabe, "Optical bistable switching action of Si high-Q photonic-crystal nanocavities," *Optics Express* **13**, 2678-2687 (2005).
215. M. Notomi, A. Shinya, S. Mitsugi, E. Kuramochi, and H. Y. Ryu, "Waveguides, resonators and their coupled elements in photonic crystal slabs," *Optics Express* **12**, 1551-1561 (2004).
216. C. Manolatou, M. J. Khan, S. H. Fan, P. R. Villeneuve, H. A. Haus, and J. D. Joannopoulos, "Coupling of modes analysis of resonant channel add-drop filters," *IEEE Journal of Quantum Electronics* **35**, 1322-1331 (1999).

217. G. H. Kim, Y. H. Lee, A. Shinya, and M. Notomi, "Coupling of small, low-loss hexapole mode with photonic crystal slab waveguide mode," *Optics Express* **12**, 6624-6631 (2004).
218. S. Mitsugi, A. Shinya, E. Kuramochi, M. Notomi, T. Tshchizawa, and T. Watanabe, "Resonant tunneling wavelength filters with high Q and high transmittance based on photonic crystal slabs," in *Conference Proceedings - Lasers and Electro-Optics Society Annual Meeting-LEOS(2003)*, pp. 214-215.
219. Y. Akahane, T. Asano, B. S. Song, and S. Noda, "Fine-tuned high-Q photonic-crystal nanocavity," *Optics Express* **13**, 1202-1214 (2005).
220. H. M. Gibbs, *Optical bistability* (Academic Press Orlando, 1985).
221. H. K. Tsang, C. S. Wong, T. K. Liang, I. E. Day, S. W. Roberts, A. Harpin, J. Drake, and M. Asghari, "Optical dispersion, two-photon absorption and self-phase modulation in silicon waveguides at 1.5 μm wavelength," *Applied Physics Letters* **80**, 416 (2002).
222. M. Notomi, T. Tanabe, A. Shinya, E. Kuramochi, H. Taniyama, S. Mitsugi, and M. Morita, "Nonlinear and adiabatic control of high-Q photonic crystal nanocavities," *Optics Express* **15**, 17458-17481 (2007).
223. C. Husko, A. De Rossi, S. Combrie, Q. V. Tran, F. Raineri, and C. W. Wong, "Ultrafast all-optical modulation in GaAs photonic crystal cavities," *Applied Physics Letters* **94**, 021111 (2009).
224. T. Tanabe, M. Notomi, E. Kuramochi, A. Shinya, and H. Taniyama, "Trapping and delaying photons for one nanosecond in an ultrasmall high-Q photonic-crystal nanocavity," *Nature Photonics* **1**, 49-52 (2007).
225. Q. F. Xu, and M. Lipson, "Carrier-induced optical bistability in silicon ring resonators," *Optics Letters* **31**, 341-343 (2006).
226. T. Uesugi, B. S. Song, T. Asano, and S. Noda, "Investigation of optical nonlinearities in an ultra-high-Q Si nanocavity in a two-dimensional photonic crystal slab," *Optics Express* **14**, 377-386 (2006).
227. M. Lončar, A. Scherer, and Y. M. Qiu, "Photonic crystal laser sources for chemical detection," *Applied Physics Letters* **82**, 4648-4650 (2003).
228. X. D. Fan, I. M. White, S. I. Shopoua, H. Y. Zhu, J. D. Suter, and Y. Z. Sun, "Sensitive optical biosensors for unlabeled targets: A review," *Anal Chim Acta* **620**, 8-26 (2008).
229. V. R. Almeida, Q. F. Xu, C. A. Barrios, and M. Lipson, "Guiding and confining light in void nanostructure," *Optics Letters* **29**, 1209-1211 (2004).
230. Q. F. Xu, V. R. Almeida, R. R. Panepucci, and M. Lipson, "Experimental demonstration of guiding and confining light in nanometer-size low-refractive-index material," *Optics Letters* **29**, 1626-1628 (2004).
231. J. T. Robinson, C. Manolatou, L. Chen, and M. Lipson, "Ultrasmall mode volumes in dielectric optical microcavities," *Physical Review Letters* **95**, 143901 (2005).
232. A. Di Falco, L. O'Faolain, and T. F. Krauss, "Chemical sensing in slotted photonic crystal heterostructure cavities," *Applied Physics Letters* **94**, 063503 (2009).
233. T. Yamamoto, M. Notomi, H. Taniyama, E. Kuramochi, Y. Yoshikawa, Y. Torii, and T. Kuga, "Design of a high-Q air-slot cavity based on a width-modulated line-defect in a photonic crystal slab," *Optics Express* **16**, 13809-13817 (2008).

234. J. Gao, J. F. McMillan, M. C. Wu, J. J. Zheng, S. Assefa, and C. W. Wong, "Demonstration of an air-slot mode-gap confined photonic crystal slab nanocavity with ultrasmall mode volumes," *Applied Physics Letters* **96**, 051123 (2010).
235. N. A. Mortensen, S. S. Xiao, and J. Pedersen, "Liquid-infiltrated photonic crystals: enhanced light-matter interactions for lab-on-a-chip applications," *Microfluid Nanofluid* **4**, 117-127 (2008).
236. *L'Air Liquide-Division Scientifique* (Elsevier, Amsterdam/New York 1976).
237. A. C. Simmons, "The refractive index and Lorentz-Lorenz functions of propane, nitrogen and carbon-dioxide in the spectral range $15\ 803\text{-}22\ 002\ \text{cm}^{-1}$ and at $944\ \text{cm}^{-1}$," *Optics Communications* **25**, 211-214 (1978).
238. Y. Clergent, C. Durou, and M. Laurens, "Refractive index variations for argon, nitrogen, and carbon dioxide at $\lambda = 632.8\ \text{nm}$ (He-Ne laser light) in the range $288.15\ \text{K} \leq T \leq 323.15\ \text{K}$, $0 < p < 110\ \text{kPa}$," *Journal of Chemical and Engineering Data* **44**, 197-199 (1999).
239. J. Faist, F. Capasso, D. L. Sivco, C. Sirtori, A. L. Hutchinson, and A. Y. Cho, "Quantum cascade laser," *Science* **264**, 553-556 (1994).
240. R. Kohler, A. Tredicucci, F. Beltram, H. E. Beere, E. H. Linfield, A. G. Davies, D. A. Ritchie, R. C. Iotti, and F. Rossi, "Terahertz semiconductor-heterostructure laser," *Nature* **417**, 156-159 (2002).
241. B. S. Williams, "Terahertz quantum-cascade lasers," *Nature Photonics* **1**, 517-525 (2007).
242. S. Riechel, C. Kallinger, U. Lemmer, J. Feldmann, A. Gombert, V. Wittwer, and U. Scherf, "A nearly diffraction limited surface emitting conjugated polymer laser utilizing a two-dimensional photonic band structure," *Applied Physics Letters* **77**, 2310-2312 (2000).
243. M. Scharrer, A. Yamilov, X. H. Wu, H. Cao, and R. P. H. Chang, "Ultraviolet lasing in high-order bands of three-dimensional ZnO photonic crystals," *Applied Physics Letters* **88**, 201103 (2006).
244. M. Imada, S. Noda, A. Chutinan, T. Tokuda, M. Murata, and G. Sasaki, "Coherent two-dimensional lasing action in surface-emitting laser with triangular-lattice photonic crystal structure," *Applied Physics Letters* **75**, 316-318 (1999).
245. A. Chen, S. J. Chua, G. C. Xing, W. Ji, X. H. Zhang, J. R. Dong, L. K. Jian, and E. A. Fitzgerald, "Two-dimensional AlGaInP/GaInP photonic crystal membrane lasers operating in the visible regime at room temperature," *Applied Physics Letters* **90**, 011113 (2007).
246. O. Painter, J. Vuckovic, and A. Scherer, "Defect modes of a two-dimensional photonic crystal in an optically thin dielectric slab," *Journal of the Optical Society of America B-Optical Physics* **16**, 275-285 (1999).
247. M. Meier, A. Mekis, A. Dodabalapur, A. Timko, R. E. Slusher, J. D. Joannopoulos, and O. Nalamasu, "Laser action from two-dimensional distributed feedback in photonic crystals," *Applied Physics Letters* **74**, 7-9 (1999).
248. H. Y. Ryu, S. H. Kwon, Y. J. Lee, Y. H. Lee, and J. S. Kim, "Very-low-threshold photonic band-edge lasers from free-standing triangular photonic crystal slabs," *Applied Physics Letters* **80**, 3476-3478 (2002).
249. B. S. Williams, S. Kumar, H. Callebaut, Q. Hu, and J. L. Reno, "Terahertz quantum-cascade laser at lambda approximate to 100 mu m using metal waveguide for mode

- confinement," *Applied Physics Letters* **83**, 2124-2126 (2003).
250. L. Sirigu, R. Terazzi, M. I. Amanti, M. Giovannini, J. Faist, L. A. Dunbar, and R. Houdré, "Terahertz Quantum Cascade Lasers based on two-dimensional photonic crystal resonators," *Optics Express* **16**, 5206-5217 (2008).
251. W. S. Holland, J. S. Greaves, B. Zuckerman, R. A. Webb, C. McCarthy, I. M. Coulson, D. M. Walther, W. R. F. Dent, W. K. Gear, and I. Robson, "Submillimetre images of dusty debris around nearby stars," *Nature* **392**, 788-791 (1998).
252. P. Y. Han, M. Tani, M. Usami, S. Kono, R. Kersting, and X. C. Zhang, "A direct comparison between terahertz time-domain spectroscopy and far-infrared Fourier transform spectroscopy," *Journal of Applied Physics* **89**, 2357-2359 (2001).
253. D. H. Auston, K. P. Cheung, J. A. Valdmanis, and D. A. Kleinman, "Cherenkov radiation from femtosecond optical pulses in electro-optic media," *Physical Review Letters* **53**, 1555-1558 (1984).
254. C. Fattinger, and D. Grischkowsky, "Point source terahertz optics," *Applied Physics Letters* **53**, 1480-1482 (1988).
255. P. F. Taday, I. V. Bradley, D. D. Arnone, and M. Pepper, "Using Terahertz pulse spectroscopy to study the crystalline structure of a drug: A case study of the polymorphs of ranitidine hydrochloride," *Journal of Pharmaceutical Sciences* **92**, 831-838 (2003).
256. B. Ferguson, and X. C. Zhang, "Materials for terahertz science and technology," *Nature Materials* **1**, 26-33 (2002).
257. B. B. Hu, and M. C. Nuss, "Imaging with terahertz waves," *Optics Letters* **20**, 1716-1718 (1995).
258. D. M. Mittleman, R. H. Jacobsen, and M. C. Nuss, "T-ray imaging," *IEEE Journal on Selected Topics in Quantum Electronics* **2**, 679-692 (1996).
259. T. Löffler, T. Bauer, K. J. Siebert, H. G. Roskos, A. Fitzgerald, and S. Czasch, "Terahertz dark-field imaging of biomedical tissue," *Optics Express* **9**, 616-621 (2001).
260. R. A. Cheville, and D. Grischkowsky, "Far-infrared terahertz time-domain spectroscopy of flames," *Optics Letters* **20**, 1646-1648 (1995).
261. A. W. M. Lee, Q. Qin, S. Kumar, B. S. Williams, and Q. Hu, "Real-time terahertz imaging over a standoff distance (> 25 meters)," *Applied Physics Letters* **89**, 3 (2006).
262. H. Němec, A. Pashkin, P. Kužel, M. Khazan, S. Schnull, and I. Wilke, "Carrier dynamics in low-temperature grown GaAs studied by terahertz emission spectroscopy," *Journal of Applied Physics* **90**, 1303-1306 (2001).
263. C. Kübler, R. Huber, and A. Leitenstorfer, "Ultrabroadband terahertz pulses: Generation and field-resolved detection," *Semiconductor Science and Technology* **20** (2005).
264. A. J. Miller, A. Luukanen, and E. N. Grossman, "Micromachined antenna-coupled uncooled microbolometers for terahertz imaging arrays," *Proceedings of SPIE - The International Society for Optical Engineering* **5411**, 18-24 (2004).
265. T. Yasui, A. Nishimura, T. Suzuki, K. Nakayama, and S. Okajima, "Detection system operating at up to 7 THz using quasioptics and Schottky barrier diodes," *Review of Scientific Instruments* **77** (2006).
266. S. Ariyoshi, C. Otani, A. Dobroiu, H. Sato, K. Kawase, H. M. Shimizu, T. Taino, and H. Matsuo, "Terahertz imaging with a direct detector based on superconducting tunnel junctions,"

Applied Physics Letters **88** (2006).

267. S. Komiyama, O. Astafiev, V. Antonov, T. Kutsuwa, and H. Hiral, "A single-photon detector in the far-infrared range," *Nature* **403**, 405-407 (2000).

268. R. N. Hall, R. O. Carlson, T. J. Soltys, G. E. Fenner, and J. D. Kingsley, "Coherent Light Emission from Gaas Junctions," *Physical Review Letters* **9**, 366-& (1962).

269. H. Kroemer, "A Proposed Class of Heterojunction Injection Lasers," *Proceedings of the Ieee* **51**, 1782-& (1963).

270. R. Dingle, W. Wiegmann, and C. H. Henry, "Quantum States of Confined Carriers in Very Thin $\text{Al}_x\text{Ga}_{1-x}\text{As}$ -Gaas- $\text{Al}_x\text{Ga}_{1-x}\text{As}$ Heterostructures," *Physical Review Letters* **33**, 827-830 (1974).

271. F. Capasso, "Band-Gap Engineering - from Physics and Materials to New Semiconductor-Devices," *Science* **235**, 172-176 (1987).

272. A. Y. Cho, "Advances in Molecular-Beam Epitaxy (Mbe)," *Journal of Crystal Growth* **111**, 1-13 (1991).

273. K. Unterrainer, *Photon-assisted tunneling in semiconductor quantum structures*. (Academic Press, San Diego, 2000).

274. G. Scalari, "Magneto-spectroscopy and development of terahertz quantum cascade lasers," in *PhD Thesis*(Université de Neuchâtel, Neuchâtel, 2005).

275. OnlineSource, "http://www.alpeslasers.ch/products.html#products_top."

276. OnlineSource, "<http://sales.hamamatsu.com/en/products/laser-group/QCL.php>."

277. G. Scalari, C. Walther, J. Faist, H. Beere, and D. Ritchie, "Electrically switchable, two-color quantum cascade laser emitting at 1.39 and 2.3 THz," *Applied Physics Letters* **88** (2006).

278. B. S. Williams, S. Kumar, Q. Hu, and J. L. Reno, "Operation of terahertz quantum-cascade lasers at 164 K in pulsed mode and at 117 K in continuous-wave mode," *Optics Express* **13**, 3331-3339 (2005).

279. B. S. Williams, S. Kumar, Q. Hu, and J. L. Reno, "High-power terahertz quantum-cascade lasers," *Electronics Letters* **42**, 89-91 (2006).

280. A. Tredicucci, F. Capasso, C. Gmachl, D. L. Sivco, A. L. Hutchinson, and A. Y. Cho, "High performance interminiband quantum cascade lasers with graded superlattices," *Applied Physics Letters* **73**, 2101-2103 (1998).

281. G. Scamarcio, F. Capasso, C. Sirtori, J. Faist, A. L. Hutchinson, D. L. Sivco, and A. Y. Cho, "High-power infrared (8-micrometer wavelength) superlattice lasers," *Science* **276**, 773-776 (1997).

282. L. Esaki, and R. Tsu, "Superlattice and Negative Differential Conductivity in Semiconductors," *Ibm Journal of Research and Development* **14**, 61-& (1970).

283. J. Faist, F. Capasso, C. Sirtori, D. L. Sivco, A. L. Hutchinson, S. N. G. Chu, and A. Y. Cho, "Narrowing of the Intersubband Electroluminescent Spectrum in Coupled-Quantum-Well Heterostructures," *Applied Physics Letters* **65**, 94-96 (1994).

284. J. Faist, Capasso, F., Sirtori, C., Sivco, D. & Cho, A., *Photon-assisted tunneling in semiconductor quantum structures*. (Academic Press, San Diego, 2000).

285. J. Faist, M. Beck, T. Aellen, and E. Gini, "Quantum-cascade lasers based on a

- bound-to-continuum transition," *Applied Physics Letters* **78**, 147-149 (2001).
286. G. Scalari, L. Ajili, J. Faist, H. Beere, E. Linfield, D. Ritchie, and G. Davies, "Far-infrared (λ similar or equal to 87 μm) bound-to-continuum quantum-cascade lasers operating up to 90 K," *Applied Physics Letters* **82**, 3165-3167 (2003).
287. J. Alton, S. Barbieri, C. Worrall, M. Houghton, H. E. Beere, E. L. Linfield, and D. A. Ritchie, "Optimum resonant tunnelling injection and influence of doping density on the performance of THz bound-to-continuum cascade lasers," *Proceedings of SPIE - The International Society for Optical Engineering* **5727**, 65-73 (2005).
288. B. S. Williams, H. Callebaut, S. Kumar, Q. Hu, and J. L. Reno, "3.4-THz quantum cascade laser based on longitudinal-optical-phonon scattering for depopulation," *Applied Physics Letters* **82**, 1015-1017 (2003).
289. Q. Hu, B. S. Williams, S. Kumar, H. Callebaut, S. Kohen, and J. L. Reno, "Resonant-phonon-assisted THz quantum-cascade lasers with metal-metal waveguides," *Semiconductor Science and Technology* **20**, S228-S236 (2005).
290. M. A. Stroschio, M. Kisin, G. Belenky, and S. Luryi, "Phonon enhanced inverse population in asymmetric double quantum wells," *Applied Physics Letters* **75**, 3258-3260 (1999).
291. M. Helm, P. England, E. Colas, F. Derosa, and S. J. Allen, "Intersubband Emission from Semiconductor Superlattices Excited by Sequential Resonant Tunneling," *Physical Review Letters* **63**, 74-77 (1989).
292. B. S. Williams, B. Xu, Q. Hu, and M. R. Melloch, "Narrow-linewidth terahertz intersubband emission from three-level systems," *Applied Physics Letters* **75**, 2927-2929 (1999).
293. B. Xu, Q. Hu, and M. R. Melloch, "Electrically pumped tunable terahertz emitter based on intersubband transition," *Applied Physics Letters* **71**, 440-442 (1997).
294. M. Rochat, L. Ajili, H. Willenberg, J. Faist, H. Beere, G. Davies, E. Linfield, and D. Ritchie, "Low-threshold terahertz quantum-cascade lasers," *Applied Physics Letters* **81**, 1381 (2002).
295. K. Unterrainer, R. Colombelli, C. Gmachl, F. Capasso, H. Y. Hwang, A. M. Sergent, D. L. Sivco, and A. Y. Cho, "Quantum cascade lasers with double metal-semiconductor waveguide resonators," *Applied Physics Letters* **80**, 3060 (2002).
296. L. Mahler, R. Kohler, A. Tredicucci, F. Beltram, H. E. Beere, E. H. Linfield, D. A. Ritchie, and A. G. Davies, "Single-mode operation of terahertz quantum cascade lasers with distributed feedback resonators," *Applied Physics Letters* **84**, 5446-5448 (2004).
297. L. Ajili, J. Faist, H. Beere, D. Ritchie, G. Davies, and E. Linfield, "Loss-coupled distributed feedback far-infrared quantum cascade lasers," *Electronics Letters* **41**, 419-421 (2005).
298. L. A. Dunbar, R. Houdré, G. Scalari, L. Sirigu, M. Giovannini, and J. Faist, "Small optical volume terahertz emitting microdisk quantum cascade lasers," *Applied Physics Letters* **90** (2007).
299. C. Walther, G. Scalari, M. I. Amanti, M. Beck, and J. Faist, "Microcavity Laser Oscillating in a Circuit-Based Resonator," *Science* **327**, 1495-1497 (2010).
300. O. Demichel, L. Mahler, T. Losco, C. Mauro, R. Green, J. H. Xu, A. Tredicucci, F. Beltram, H. E. Beere, D. A. Ritchie, and V. Tamosiunas, "Surface plasmon photonic structures in terahertz quantum cascade lasers," *Optics Express* **14**, 5335-5345 (2006).

301. L. Mahler, M. I. Amanti, C. Walther, A. Tredicucci, F. Beltram, J. Faist, H. E. Beere, and D. A. Ritchie, "Distributed feedback ring resonators for vertically emitting terahertz quantum cascade lasers," *Optics Express* **17**, 13031-13039 (2009).
302. E. Mujagić, S. Schartner, L. K. Hoffmann, W. Schrenk, M. P. Semtsiv, M. Wienold, W. T. Masselink, and G. Strasser, "Grating-coupled surface emitting quantum cascade ring lasers," *Applied Physics Letters* **93** (2008).
303. L. Mahler, A. Tredicucci, F. Beltram, C. Walther, J. Faist, B. Witzigmann, H. E. Beere, and D. A. Ritchie, "Vertically emitting microdisk lasers," *Nature Photonics* **3**, 46-49 (2009).
304. L. A. Dunbar, V. Moreau, R. Ferrini, R. Houdré, L. Sirigu, G. Scalari, M. Giovannini, N. Hoyler, and J. Faist, "Design, fabrication and optical characterisation of quantum cascade lasers at terahertz frequencies using photonic crystal reflectors," *Optics Express* **13**, 8960-8968 (2005).
305. H. Zhang, G. Scalari, J. Faist, L. A. Dunbar, and R. Houdré, "Design and fabrication technology for high performance electrical pumped THz photonic crystal bandedge lasers with complete photonic band gap," Submitted to *Journal of Applied Physics* (Unpublished).
306. H. Zhang, G. Scalari, R. Houdré, and J. Faist, "In-plane and surface emitting high performance THz pillar type photonic crystal lasers with complete photonic bandgaps," in *CLEO/Europe - EQEC 2009 - European Conference on Lasers and Electro-Optics and the European Quantum Electronics Conference*(Munich, 2009), p. D.O.I. 5192585.
307. Y. Chassagneux, R. Colombelli, W. Maineult, S. Barbieri, S. P. Khanna, E. H. Linfield, and A. G. Davies, "Graded photonic crystal terahertz quantum cascade lasers," *Applied Physics Letters* **96** (2010).
308. H. Zhang, G. Scalari, R. Houdré, and J. Faist, "Complex Coupled Photonic Crystal Lasers with Independent Loss and Refractive Index Modulation," To be submitted (Unpublished).
309. B. C. Smith, *Fundamentals of Fourier transform infrared spectroscopy* (CRC Press LLC, New York, 2000).
310. B. H. Stuart, *Infrared spectroscopy: fundamentals and applications* (John Wiley & Sons Ltd., Chichester, 2004).
311. A. Yariv, in *Quantum Electronics* (Saunders College Publishing, 1991), p. 181.
312. C. Walther, G. Scalari, J. Faist, H. Beere, and D. Ritchie, "Low frequency terahertz quantum cascade laser operating from 1.6 to 1.8 THz," *Applied Physics Letters* **89** (2006).
313. J. A. Fan, M. A. Belkin, F. Capasso, S. Khanna, M. Lachab, A. G. Davies, and E. H. Linfield, "Surface emitting terahertz quantum cascade laser with a double-metal waveguide," *Optics Express* **14**, 11672-11680 (2006).
314. C. Walther, M. Fischer, G. Scalari, R. Terazzi, N. Hoyler, and J. Faist, "Quantum cascade lasers operating from 1.2 to 1.6 THz," *Applied Physics Letters* **91**, 3 (2007).
315. M. A. Belkin, J. A. Fan, S. Hormoz, F. Capasso, S. P. Khanna, M. Lachab, A. G. Davies, and E. H. Linfield, "Terahertz quantum cascade lasers with copper metal-metal waveguides operating up to 178 K," *Optics Express* **16**, 3242-3248 (2008).

List of Publications and Presentations

List of Publications

1. **H. Zhang**, G. Scalari, J. Faist, L. A. Dunbar and R. Houdré "Design and fabrication technology for high performance electrical pumped THz photonic crystal band-edge lasers with complete photonic band gap." (Paper accepted for publication in **Journal of Applied Physics**.)
2. **H. Zhang**, G. Scalari, J. Faist, and R. Houdré "Complex coupled Photonic Crystal Lasers with Independent Loss and Refractive Index Modulation." (Paper in preparation.)
3. **H. Zhang**, J. Jágerská, N. Le Thomas and R. Houdré, "Experimental investigation of slow light photonic crystal coupled cavity waveguides and their intrinsic limitations". (Paper in preparation.)
4. J. Jágerská, **H. Zhang**, Z. Diao, N. Le Thomas and R. Houdré, "Refractive index sensing with an air-slot photonic crystal nanocavity ". **Optics Letters** **35** (15), 2523-2525 (2010).
5. N. Le Thomas, **H. Zhang**, J. Jágerská, V. Zabelin, R. Houdré, I Sagnes and A. Talneau, "Light transport regimes in slow light photonic crystal waveguides", **Physical Review B** **80** (12), 125332 (2009).
6. J. Jágerská, **H. Zhang**, N. Le Thomas and R. Houdré, "Radiation loss of photonic crystal coupled-cavity waveguides", **Applied Physics Letters** **95** (11), 111105 (2009).
7. **H. Zhang**, L. A. Dunbar, G. Scalari R. Houdré and J. Faist, "Terahertz photonic crystal quantum cascade lasers," **Optics Express** **15** (25), 16818-16827 (2007).
8. R. De La Rue, H. Chong, M. Gnan, N. Johnson, I. Ntakis, P. Pottier, M. Sorel, A. M. Zain, **H. Zhang**, E. Camargo, C. J. Jin, M. Armenise, and C. Ciminelli, "Photonic crystal and photonic wire nano-photonics based on silicon-on-insulator," **New Journal of Physics** **8** (2006).

List of presentations and posters

1. **H. Zhang**, G. Scalari, J. Faist and R. Houdré, "Third band surface emitting THz photonic crystal quantum cascade band-edge lasers". 9th Workshop on Photonic and Electromagnetic Crystal Structures (PECSIX), Granada, Spain, 2010.
2. N. Le Thomas, **H. Zhang**, J. Jágerská, and R. Houdré, " Numerical challenges posed by experimental investigations of the slow light regime in photonic crystal waveguides," Photonics

North, Niagara Falls, Canada, 2010, invited communication.

3. J. Jágerská, **H. Zhang**, Z. Diao, N. Le Thomas and R. Houdré, "Air-Slot Photonic Crystal Cavity for High Precision Refractive Index Sensing". 9th Workshop on Photonic and Electromagnetic Crystal Structures (PECSIX), Granada, Spain, 2010.

4. **H. Zhang**, G. Scalari, J. Faist and R. Houdré, "In-plane and Surface Emitting High Performance THz Pillar Type Photonic Crystal Lasers with Complete Photonic Bandgaps," Oral presentation on CLEO/Europe-EQEC Conference, Munich, June, 2009.

5. J. Jágerská, **H. Zhang**, N. Le Thomas and R. Houdré, "Dispersion Properties of Photonic Crystal Coupled-Cavity Waveguides," Oral presentation on CLEO/Europe-EQEC Conference, Munich, June, 2009.

6. N. Le Thomas, J. Jágerská, **H. Zhang**, V. Zabelin, and R. Houdré, "Dispersion properties of photonic waveguide structures," Photonics North, Québec, Canada, 2009, invited communication.

7. N. Le Thomas, J. Jágerská, **H. Zhang**, V. Zabelin, and R. Houdré, "Limits of slow light in actual photonic crystals structures," International Laser Physics Workshop (LPHYS'09), Barcelona, Spain, 2009, invited communication.

8. N. Le Thomas, J. Jágerská, **H. Zhang**, and R. Houdré, "Light transport and limits of slow light in real photonic crystal structures in the presence of residual disorder," 11th International Conference on Transparent Optical Networks (ICTON2009), Azores, Portugal, 2009 (ICTON Tech. Dig.), invited communication.

9. N. Le Thomas, J. Jágerská, **H. Zhang**, and R. Houdré, "Limits of slow light in real photonic crystals structures," 8th Workshop on Photonic and Electromagnetic Crystal Structures (PECSVIII), Sydney, Australia, 2009.

10. **H. Zhang**, L. A. Dunbar, G. Scalari R. Houdré and J. Faist, "High Performance Pillar Type Photonic Crystal Quantum Cascade Lasers at THz Frequency," Oral presentation on International Quantum Cascade Lasers School & Workshop Monte Verita, Sept. 2008.

11. **H. Zhang**, J. Jágerská, N. Le Thomas R. Houdré, G. Scalari, J. Faist, "Advanced Photonic crystal structures in THz frequency and in telecommunication wavelength," Poster presentation on General Assembly of NCCR Quantum Photonics, Montreux, Switzerland, June, 2007.

12. **H. Zhang**, L. A. Dunbar, R. Houdré G. Scalari, J. Faist, "Fabrication, Simulation, Electrical and Optical Characterization of Terahertz Microdisk Quantum Cascade Lasers," Poster presentation on Epixnet Winter School - Applications of Photonic Integration, Pontresina, Switzerland, March 2007.

13. **H. Zhang**, M. Gnan, N. Johnson, and R. M. De la Rue, "Ultra-Small Mach-Zehnder Interferometer Devices In Thin Silicon-on-Insulator," Oral presentation on Integrated Photonics Research and Applications Topical Meeting, UncasvilleCT, 24–26 April. 2006, paper ItuB3 (2006).

14. R. De La Rue, M. Sorel, N. Johnson, F. Rahman, C. Ironside, L. Cronin, I. Watson, R. Martin, C. Jin, P. Pettier, H. Chong, M. Gnan, A. Jugessur, E. Camargo, G. Erwin, A. M. Zain, I. Ntakis, L. Hobbs, **H. Zhang**, M. Armenise, C. Ciminelli, and D. Coquillat, "Photonic crystal and photonic wire device structures," Proceedings of SPIE - on Optics and Optoelectronics, Warsaw, Poland, 5950, pp. 1-12. , Oct. 12, 2005.

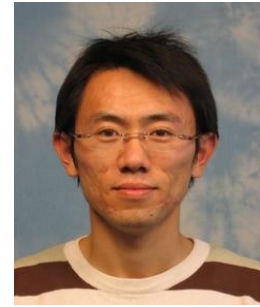
Curriculum Vitae

Hua Zhang

Nationality : Chinese

Date of Birth : 18, 09, 1982

Email: amd008@gmail.com



Self-assessment

- Diversified background in software engineering, micro/nano technology and physics.
- 6 years of hands on experience in world leading research universities (U.K. and Swiss) for integrated-circuit manufacturing (such as lasers, LEDs).
- Conducted several independent consulting projects for a private venture capitalist, such as Market-entrance cases, Mergers&Acquisitions as well as oversea Market strategies.
- Able to work under time pressure.
- Good communication and presentation skills (> 50 oral presentations during the past 4 years)
- Strong analytical and problem solving skills (via a long list of publications, available upon request).
- Team working, respect and responsibility.
- Strong leadership skills (can be proved by the extra-curricular activities and select Honors and Awards).

Work Experience

2006/10- 2010/09: Swiss Federal Institutes of Technology Lausanne (EPFL) Laboratory of Quantum opto-electronics. Position: PhD research assistant.

EPFL 's engineering ranks **NO.1** in Europe. During my PhD research assistant time, I

- Built up the 3rd generation lithography (Electron Beam Lithography) fabrication platform for the group, replaced the samples that purchased from Univ. St-Andrews (U.K.) and IMEC (Belgium) (2007-2009).
- Invented world's first high performance surface emitting laser with independent modulation on refractive index and loss (2009).
- Invented world's first surface emitting photonic crystal quantum cascade laser at 1.5 THz (2008).
- Invented world's first pillar type photonic crystal quantum cascade laser at 3 THz (2007).

Consulting Achievements:

During the past 3 years, I have conducted the following consulting projects for a venture capitalist:

- Market-entrance: Solar cell industry, including the entrance with the amorphous Si technique and commercialization of Dye sensitized solar cell (DSSC) technique.
 - Mergers&Acquisitions study of an Infra-red detection security system manufacturing company.
 - Market-entrance: Investment research on social networking sites based on small residential communities who share the same real estate agency.
 - Market-entrance and Increase sales strategies: I have been helping a small company to translate their brochures into English, French, Japanese and Korea. It is a mineral company who wants to sell its products overseas. I have investigated and analyzed the oversea market size, competitor situations etc. I have provided the oversea marketing strategy.
-

2006/01- University of Glasgow, U.K. Department of Electronics and Electrical Engineering.

2006/09: Position: Academic visitor.

I designed and achieved the world's smallest Mach-Zehnder Interferometer on Silicon-on-Insulator.

2004/04- Neusoft Co. Ltd. China. Position: Software Engineer (Internship)

2004/07: I designed and achieved a knowledge document management system based on Java Script (2004).

Education Background

2006/10 -- 2010/09: **Swiss Federal Institutes of Technology Lausanne (EPFL) | Photonics | Doctor**

2004/07 -- 2005/12: **University of Glasgow (U.K.) | Electronics and Electrical Engineering | Master**

2000/09 -- 2004/07: **Dalian Jiaotong University | Software Engineering | Bachelor**

Language Skills

English: reading&writing expert | listening&speaking expert

French: reading&writing basic | listening&speaking average

Japanese: reading&writing basic | listening&speaking basic

Special skills

I have 6 years fabrication experience on lasers and SOI devices in cleanroom. I am a operator of Electron Beam lithography (EBL) and photolithography, dry etching (RIE/ICP) and wet etching, PECVD, evaporation and sputtering, wafer bonding, polishing and packaging, wafer diffusion and ion-implantation, scanning electron microscopy (SEM). Familiar with FEM, FDTD, good at simulation, layout, fabrication, optical characterization. Knowledge of MBE, MOCVD, AFM, TEM, LED, microfluidic and biosensing.

Honors & rewards

Personal:

Swiss Federal Institutes of Technology Lausanne PhD full scholarship(2006-2010);

Excellent Freshmen of Dalian JiaoTong Univ.(2000);

4 years of scholarship of the specialty study(2000-2004);

Excellent Student Cadre of Dalian City(2002-2003);

Team working:

As class monitor, I led my class to win the following Awards:

Advanced branch of the communist youth league of Dalian City(2001-2002);

Advanced Class of Dalian City(2001-2002);

Advanced Class of LiaoNing Province(2001-2002);

Interests & hobbies

Love skiing, like hiking. Watch CNN 'Quest means business' if possible every day. Read articles regularly on the following websites: Wall street journal, the Economist, Barrons, CNN money, Bloomberg, etc.

Extra-curricular activities:

- 2001-2002, I founded the Youth Volunteer Association (> 100 members) of Dalian JiaoTong Univ. I was the first Chairman and organized voluntary social activities monthly.
- 2002-2004, I founded the Association Federation of Software Technology Institute, Dalian JiaoTong Univ. It consists in 12 individual associations (> 1000 members). I organized regular activities, searched for funding and sponsorships.